

Abstract

RANDALL, TRAVIS JOHN. Characterizing the Ductile Response of Brittle Semiconductor Materials to Dynamic Contact Processes. (Under direction of Ronald O. Scattergood.)

It has been well documented that single crystal silicon and germanium exhibit plastic flow with the generation of high pressure on the surface by contact processes such as micro-indentation, scribing, and single point diamond turning. A high pressure phase transformation (HPPT) of the near surface region from the brittle, highly covalent diamond cubic (dc) structure to a metallic β -tin phase is thought to be responsible for the anomalous plastic flow behavior during contact loading processes. The scope of this investigation is the study of the response of single crystal silicon and germanium to dynamic contact processes such as scratching and single point diamond turning.

Plastic flow in silicon was noted for scribing experiments in SEM observation for various cutting directions on different crystal orientations. The both the ductile response and fracture behavior was shown to be greatly influence by the combination of cutting direction and tip geometry. Residual stress was measured by wafer deflection and quantified as a dipole force. The cutting direction and tip dependence of the fracture behavior was qualitatively explained using a stress model (modified from a model used for diamond turning of these materials) showing the directional propensity for fracture based on imparted tensile stresses on a certain set of fracture planes. Raman measurements to identify remnant phases indicative of HPPT in the scribe regions showing intense plastic behavior and the generated debris were inconclusive.

Low RMS (1-9 nm,) optical quality surfaces were generated by diamond turning silicon and germanium at low feed rates (1-5 um/rev.) Symmetric damage patterns noted at

high feed rates are partially explained using a damage orientation model based on elasticity theory developed from previous diamond turning work with these materials. Raman measurements of the machined areas showed signature of a near surface amorphous layer, perhaps remnant of the high pressure β -tin transformation, in both silicon and germanium samples. TEM observation of collected debris indicated dc structure perhaps to recrystallization of the amorphous material by heating. The implication of the ductile behavior is that using careful machining conditions, normally brittle materials such as single crystal silicon or germanium (and similar dc semiconductors) may be machined in the ductile regime to create high quality optics and substrates without intensive processing steps.

Characterizing the Ductile Response of Brittle Semiconductor Materials to Dynamic Contact Processes

By:

Travis Randall

A thesis submitted to the Graduate Faculty of
North Carolina State University
In partial fulfillment of the
requirements for the Degree of
Masters of Science

DEPARTMENT OF MATERIALS SCIENCE AND ENGINEERING

Raleigh

2004

Approved by:

Chair of Advisory Committee

Biography

Originally from Ann Arbor, MI, Travis spent most of his life in upstate Elmira, New York. He received his BS in Ceramic Engineering/Materials Science from Alfred University in Alfred, NY in May 2002. He started working at the Precision Engineering Center at North Carolina State in August 2002. His thesis research, *Characterizing the Ductile Response of Brittle Semiconductors to Dynamic Contact Processes*, culminated in his thesis defense in June of 2004.

Acknowledgements

The completion of this research is due in large part to the following people to whom I am very grateful...

- **Dr. Ron Scattergood**, whose guidance, wisdom, and patience were greatly appreciated, his support made my graduate experience more than worth while.
- **Dr. Thomas Dow**, for the privilege of being able to work in a world class research setting.
- **Dr. Nadia El-Masry and Dr. John MacKenzie**, for serving on my defense committee.
- **Alex Sohn**, for his knowledge of what seems like everything under the sun. His patience and advice on any problem made my life that much easier.
- **Ken Gerrard**, for his knowledge and time spent on everything computer.
- **Jen Heuning**, her expert Raman work brought this research all together.
- **Dr. Robert Nemanich**, for his support during this research.
- **Nobu Negishi, Stuart Clayton, Patrick Morrissey, David Hood, and Witoon Panusittikorn**, for making my time in the PEC that much more interesting.
- **Lara Bodenhamer and Laura Underhill**, who were both very kind and helpful.

I would also like to thank my family for all their support during my academic career.

Finally, I would like to thank my girlfriend, Stephanie, whose care and support has made this past year of my life wonderful.

Table of Contents

List of Figures	vi
List of Tables	xiii
1 Introduction	1
1.1 Background.....	1
1.2 Present Work.....	2
2 Properties of Silicon	4
2.1 Atomic and Crystallographic Structure.....	4
2.2 Mechanical Properties.....	5
2.2.1 Surface Energy and Elastic Parameters.....	6
2.2.2 Hardness.....	9
2.2.3 Fracture Toughness.....	10
3 Literature Review on Theory and Experimentation	13
3.1 Modeling Material Mechanics of Contact Processes.....	13
3.2 Experiments and Modeling of Ductile Regime Machining.....	18
3.3 Plasticity and High Pressure Phase Transformation.....	21
3.3.1 Indentation.....	22
3.3.2 Scribing and Diamond Turning.....	26
4 Single Point Scribing of Silicon	30
4.1 Scope and Objectives.....	30
4.2 Experimental Setup.....	31
4.2.1 Sample Creation.....	31
4.2.2 Scribing with a Dynatex Tip.....	32
4.2.3 Interferometric Analysis.....	34
4.2.4 Characterization.....	35
4.2.5 Measurement of Bend Deflection.....	36
4.3 Experimental Results.....	37
4.3.1 Scribing Behavior.....	37
4.3.2 Residual Stress Generation and Measurement.....	62
4.3.3 Raman Measurement of Scribe Regions and Debris.....	75
4.4 Discussion.....	78
4.4.1 Material Response to Scribing.....	78
4.4.2 Directional Dependency of Cutting Behavior.....	80
4.4.3 Raman Measurement of Scribe Regions and Debris.....	86
4.5 Conclusions and Suggested Future Work.....	90

5	Diamond Turning of Silicon and Germanium	93
5.1	Scope and Objectives.....	93
5.2	Aside: SPDT Material Removal in Si and Ge.....	94
5.3	Aside: Materials Consideration- Germanium.....	97
5.4	Experimental Setup.....	97
5.4.1	Diamond Turning.....	97
5.4.2	Characterization.....	99
5.5	Experimental Results and Discussion (Silicon).....	100
5.5.1	Machining Behavior/ Material Response.....	100
5.5.2	Raman Measurement of Machined Surface.....	122
5.6	Experimental Results and Discussion (Germanium).....	126
5.6.1	Machining Behavior/ Material Response.....	126
5.6.2	Raman Measurement of Machined Surface.....	153
5.7	Experimental Results and Discussion (TEM analysis of Si and Ge debris)....	156
5.8	Conclusions and Suggested Future Work.....	158
6	References	161
7	Appendices	165
A.	“Residual Stress Bend Effect Due to Diamond Tip Scribing of an Al ₂ O ₃ -TiC Composite Ceramic” B.W. Austin, R.O. Scattergood, T.J. Randall.....	165
B.	“Crystal Orientation Dependence of Machining Damage- A Stress Model” W.S. Blackley and R.O. Scattergood. J. Am. Ceram. Soc. 73 [10] (1990) 3113.....	178

List of Figures

2.1	(a) Diagram of Si unit cell atomic arrangement. (b) Schematic of crystallographic planes of common wafer orientation.[6].....	5
2.2	Directional dependency of (a.) Elastic (Young's) Modulus and (b.) Shear Modulus for (100) wafer.....	9
2.3	Variation of fracture toughness with orientation for (a.) (100), (b.) (110) and (c.) (111) planes. [7]	12
3.1	Evolution of crack systems during loading and unloading of sharp contact. [17].....	15
3.2	Crack formation as a single point tool is moved along the surface of a brittle material. (a) side view. (b) front on view [19].....	15
3.3	Formation of plastic zone and subsequent cracking with scribing. Typical crack patterns include median, lateral, and radial cracking. [20].....	16
3.4	Yoffe's "blister" field model. (a.) Hypothesized yield zone under indenter. (b.) force double to model stress field in indentation [20].....	17
3.5	Diagram showing chip removal area and damage region. Critical chip thickness is shown. [27].....	18
3.6	Line force loading P applied to an elastic half space. [26].....	20
3.7	(a.) σ_{\max} vs ω for diamond turning of (100) wafer. (b.) Schematic of pitting damage seen on a wafer face turned at the brittle-ductile transition. Dark regions are those of pitting while white regions where plastically turned. [Adapted, 26].....	20
3.8	(a.)TEM image of spherical indent at 80mN. (b.) diffraction pattern of region 1, showing amorphization. (c.) diffraction pattern on region 2, showing crystalline nature. [43].....	24
3.9	Scanning electron micrograph of Vickers indentation (1-N) showing extruded plastic material. [44].....	24
3.10	Schematic of phase transformations thought to occur during contact loading. [5].....	25
3.11	(a) Load vs. displacement curves. (b) Contact pressure vs. depth curve. (c) Raman corresponding to indentation region for each discontinuity event. [48]...	26
3.12	TEM cross-section of diamond turned Si. Depth of cut: (a.) 100 nm and (b.) 500 nm. [52].....	27
3.13	SEM images of (a.)ductile scribe created with Vickers indenter. (b.) the onset of microcracks at the critical depth to induce ductile to brittle trasnition. [53]...	28
4.1	Schematic of sample orientation indicating scribing direction of interest.....	31
4.2	Schematic of (a.) Dynatex Tip [54] (b.) scribing setup [54] and (c.) flattened pyramid [54].....	32
4.3	(a.) Schematic of geometry of tip to sample surface [54] and (b.) (b.) SEM of area encircled in Fig. 4.1(a).....	34
4.4	Image of Zygo GPI Laser interferometer.....	34
4.5	Oblique plot of bend angle effect generated in Metroporo.....	36
4.6	2-D profile of bend effect showing line fit to flat portions and bend angle [2]...	37
4.7	General material responses to scribing with Dynatex Tip.....	38

4.8	(a.) and (b.) Micrographs of plastically extruded debris typically seen from the material response of Figure 4.7(b.) <i>Bar = 2 um</i>	39
4.9	Optical micrograph of scribing range of (100)[100] for sharp geometry.....	40
4.10	Optical micrograph of scribing range of (100)[100] for blunt geometry.....	41
4.11	(a.) SEM and (b.) AFM image of sharp scribe for (100)[100] within the ductile regime. (a.) <i>Bar = 2 um</i>	41
4.12	(a.) SEM and (b.) AFM image of blunt scribe for (100)[100] within the ductile regime. (a.) <i>Bar = 2 um</i>	41
4.13	AFM profile of (a.) sharp and (b.) blunt scribe on (100) in [100] direction in ductile regime.....	42
4.14	Effect of Sharp vs. Blunt geometry on depth of cut for (100)[100].....	43
4.15	Optical micrograph of scribing range of (100)[011] for sharp geometry.....	45
4.16	Optical micrograph of scribing range of (100)[011] for blunt geometry.....	45
4.17	(a.) SEM and (b.) AFM image of sharp scribe for (100)[011] within the ductile regime. (a.) <i>Bar = 2 um</i>	45
4.18	(a.) SEM and (b.) AFM image of blunt scribe for (100)[011] within the ductile regime. (a.) <i>Bar = 2 um</i>	46
4.19	AFM profile of (a.) sharp and (b.) blunt scribe on (100) in [011] direction in ductile regime.....	47
4.20	Effect of Sharp vs. Blunt geometry on depth of cut for (100)[011].....	48
4.21	Optical micrograph of scribing range of (111)[1-10] for sharp geometry.....	49
4.22	Optical micrograph of scribing range of (111)[1-10] for blunt geometry.....	49
4.23	(a.) SEM and (b.) AFM image of sharp scribe for (111)[1-10] within the ductile regime. (a.) <i>Bar = 2 um</i>	50
4.24	(a.) SEM and (b.) AFM image of blunt scribe for (111)[1-10] within the ductile regime. (a.) <i>Bar = 2 um</i>	50
4.25	AFM profile of (a.) sharp and (b.) blunt scribe on (111) in [1-10] direction in ductile regime.....	51
4.26	Effect of Sharp vs. Blunt geometry on depth of cut for (111)[1-10].....	52
4.27	Optical micrograph of scribing range of (111)[-1-12] for sharp geometry.....	53
4.28	Optical micrograph of scribing range of (111)[-1-12] for blunt geometry.....	53
4.29	(a.) SEM and (b.) AFM image of sharp scribe for (111)[-1-12] within the ductile regime. (a.) <i>Bar = 2 um</i>	54
4.30	(a.) SEM and (b.) AFM image of blunt scribe for (111)[-1-12] within the ductile regime. (a.) <i>Bar = 2 um</i>	54
4.31	AFM profile of (a.) sharp and (b.) blunt scribe on (111) in [-1-12] direction in ductile regime.....	55
4.32	Effect of Sharp vs. Blunt geometry on depth of cut for (100)[-1-12].....	56
4.33	Optical micrograph of scribing range of (111)[11-2] for sharp geometry.....	57
4.34	Optical micrograph of scribing range of (111)[11-2] for blunt geometry.....	58
4.35	(a.) SEM and (b.) AFM image of sharp scribe for (111)[11-2] within the ductile regime. (a.) <i>Bar = 2 um</i>	58
4.36	(a.) SEM and (b.) AFM image blunt scribe for (111)[11-2] within the ductile regime. (a.) <i>Bar = 2 um</i>	58
4.37	AFM profile of (a.) sharp and (b.) blunt scribe on (111) in [11-2] direction in ductile regime.....	59

4.38	Effect of Sharp vs. Blunt geometry on depth of cut for (100)[11-2].	61
4.39	Illustration of expansion of constrained plastic zone and resulting deflection....	63
4.40	Line-force dipole model. [54].....	64
4.41	(a.) Graph of Dipole Strength B vs Scribe Load W for (100)[100] and (b.-d.) Micrographs corresponding to points encircled in (a).....	66
4.42	(a.) Graph of Dipole Strength B vs Scribe Load W for (100)[011] and (b.-d.) Micrographs corresponding to points encircled in (a).....	67
4.43	(a.) Graph of Dipole Strength B vs Scribe Load W for (111)[1-10] and (b.-d.) Micrographs corresponding to points encircled in (a).....	68
4.44	(a.) Graph of Dipole Strength B vs Scribe Load W for (111)[-1-12] and (b.-d.) Micrographs corresponding to points encircled in (a).....	69
4.45	(a.) Graph of Dipole Strength B vs Scribe Load W for (111)[11-2] and (b.-d.) Micrographs corresponding to points encircled in (a).....	70
4.46	(a.) Graph of Dipole Strength B vs Scribe Load W comparing residual stress of sharp and blunt cutting for (100)[100] and (b.-d.) Micrographs corresponding to points encircled in (a).....	71
4.47	(a.) Graph of Dipole Strength B vs Scribe Load W comparing residual stress of sharp and blunt cutting for (111)[1-10] and (b.-d.) Micrographs corresponding to points encircled in (a).....	72
4.48	(a.) Graph of Dipole Strength B vs Scribe Load W comparing residual stress of sharp and blunt cutting for (111)[-1-12] and (b.-d.) Micrographs corresponding to points encircled in (a).....	74
4.49	Typical Raman scans taken from the outside to the center of scribe region for the sharp geometry interaction on Si.....	75
4.50	Typical Raman scans taken from the outside to the center of scribe region for the sharp geometry interaction on Si.....	76
4.51	(a.) Raman spectra of Si debris taken at various power levels (decreasing from top) and (b.) graph of power level versus peak position.....	77
4.52	Speculated profile of scribe made with sharp indenter within ductile regime....	78
4.53	Speculated profile of scribe made with blunt indenter within ductile regime....	80
4.54	Line force loading P applied to an elastic half space. [26].....	81
4.55	Point force stress model showing crystallographic dependence of fracture propensity for (100) surface as evaluated from maximum normal stress on {111} planes.	83
4.56	Point force stress model showing crystallographic dependence of fracture propensity for (111) surface as evaluated from maximum normal stress on {111} planes.....	83
4.57	Point force stress model showing crystallographic dependence of fracture propensity for (100) surface as evaluated from maximum normal stress on {100} planes.....	85
4.58	Point force stress model showing crystallographic dependence of fracture propensity for (111) surface as evaluated from maximum normal stress on {110} planes.....	85
4.59	Raman spectra showing phases indicative of HPPT seen in other research for various indenter types. [54].....	87
4.60	Raman spectra obtained for plastically generated debris matching that	

attributed by others to nanocrystalline Si in an amorphous matrix.....	90
4.61 Raman spectra (b in figure) obtained for plastically generated debris found around a scribe and attributed by others to nanocrystalline Si in an amorphous matrix. [54].....	90
5.1 Illustration of chip formation during diamond turning pass. [Adapted, 58].....	94
5.2 Diagram showing chip removal area and damage region. [26].....	95
5.3 Theoretical diamond turned surface generation. [59].....	96
5.4 Variation of surface from theoretical due to deformation and spring back of surface. [59].....	96
5.5 Rank Pneumo ASG 2500 DTM used in diamond turning experiments.....	98
5.6 Close-up view of a wafer vacuum chucked to the DTM spindle.....	98
5.7 Illustration of fracture pattern on (100) Si machined with a -30° rake angle tool. White areas indicate no pitting. Grey scale indicates severity of pitting...	101
5.8 (a.) Collage of micrographs depicting surface of (100) Si diamond turned at various feed rates (um/rev) with -30° rake angle tool. (Path 1) (b.) Collage of micrographs depicting surface of (100) Si diamond turned at various feed rates (um/rev) with -30° rake angle tool. (Path 2).....	102
5.9 Illustration of fracture pattern on (100) Si machined with a -30° rake angle tool.....	103
5.10 (a.) Collage of micrographs depicting surface of (100) Si diamond turned at various feed rates (um/rev) with -45° rake angle tool. (Path 1) (b.) Collage of micrographs depicting surface of (100) Si diamond turned at various feed rates (um/rev) with -45° rake angle tool. (Path 2).....	104
5.11 Illustration of fracture pattern on (111) Si machined with a -30° rake angle tool.....	105
5.12 (a.) Collage of micrographs depicting surface of (111) Si diamond turned at various feed rates (um/rev) with -30° rake angle tool. (Path 1) (b.) Collage of micrographs depicting surface of (111) Si diamond turned at various feed rates (um/rev) with -30° rake angle tool. (Path 2) (c.) Collage of micrographs depicting surface of (111) Si diamond turned at various feed rates (um/rev) with -30° rake angle tool. (Path 3).....	106
5.13 Illustration of fracture pattern on (111) Si machined with a -45° rake angle tool. White areas indicate no pitting. Grey scale indicates severity of pitting....	108
5.14 (a.) Collage of micrographs depicting surface of (111) Si diamond turned at various feed rates (um/rev) with -45° rake angle tool. (Path 1) (b.) Collage of micrographs depicting surface of (111) Si diamond turned at various feed rates (um/rev) with -45° rake angle tool. (Path 2) (c.) Collage of micrographs depicting surface of (111) Si diamond turned at various feed rates (um/rev) with -45° rake angle tool. (Path 3).....	109
5.15 Stress orientation factor accompanied by a schematic representation of pitting damage observed by Blackley for (100) wafer. [26].....	111
5.16 Stress orientation factor accompanied by a schematic representation of pitting damage observed by Blackley for (111) wafer. [26].....	112
5.17 Digital image showing (100) Si wafer with fracture pattern shifted 45° from normal (previous results [24, 26, 57] with same tool.).....	112
5.18 Profile of (100) Si surface machined at 15 um/rev feed with -45° tool.....	114

5.19	Profile of (100) Si surface machined at 5 um/rev feed with -45° tool.....	114
5.20	Profile of (100) Si surface machined at 2 um/rev feed with -45° tool.....	115
5.21	Profile of (100) Si surface machined at 15 um/rev feed with -30° tool.....	115
5.22	Profile of (100) Si surface machined at 5 um/rev feed with -30° tool.....	116
5.23	Profile of (100) Si surface machined at 2 um/rev feed with -30° tool.....	116
5.24	Profile of (111) Si surface machined at 15 um/rev feed with -45° tool.....	117
5.25	Profile of (111) Si surface machined at 5um/rev feed with -45° tool.....	117
5.26	Profile of (111) Si surface machined at 2um/rev feed with -45° tool.....	117
5.27	Profile of (111) Si surface machined at 15 um/rev feed with -30° tool.....	118
5.28	Profile of (111) Si surface machined at 5um/rev feed with -30° tool.....	118
5.29	Profile of (111) Si surface machined at 2um/rev feed with -30° tool.....	118
5.30	Comparison of PV values achieved during machining experiments of (111) Si with those obtained theoretically with Equation 5.1.....	119
5.31	RMS versus feed rate and machining direction for a (100) Si wafer machined with a -45° rake angle tool.....	120
5.32	RMS versus feed rate and machining direction for a (100) Si wafer machined with a -30° rake angle tool.....	121
5.33	RMS versus feed rate and machining direction for a (111) Si wafer machined with a -45° rake angle tool.....	121
5.34	RMS versus feed rate and machining direction for a (111) Si wafer machined with a -30° rake angle tool.....	122
5.35	Raman spectra taken of a ductile turned (100) Si surface at various feed rates machined with a -30° tool.....	123
5.36	Raman spectra taken of a ductile turned (100) Si surface at two feed rates machined with a -45° tool.....	124
5.37	Raman spectra taken of a ductile turned (111) Si surface at two feed rates machined with -30° and -45° tools.....	125
5.38	Illustration of fracture pattern on (100) Ge machined with a -30° rake angle tool.....	126
5.39	(a.) Collage of micrographs depicting surface of (100) Ge diamond turned at various feed rates (um/rev) with -30° rake angle tool. (Path 1) (b.) Collage of micrographs depicting surface of (100) Ge diamond turned at various feed rates (um/rev) with -30° rake angle tool. (Path 2)	127
5.40	Illustration of fracture pattern on (100) Ge machined with a -45° rake angle tool.....	128
5.41	(a.) Collage of micrographs depicting surface of (100) Ge diamond turned at various feed rates (um/rev) with -45° rake angle tool. (Path 1) (b.) Collage of micrographs depicting surface of (100) Ge diamond turned at various feed rates (um/rev) with -45° rake angle tool. (Path 2).....	129
5.42	Illustration of fracture pattern on (110) Ge machined with a -30° rake angle tool.....	131
5.43	(a.) Collage of micrographs depicting surface of (110) Ge diamond turned at various feed rates (um/rev) with -30° rake angle tool. (Path 1) (b.) Collage of micrographs depicting surface of (110) Ge diamond turned at various feed rates (um/rev) with -30° rake angle tool. (Path 2) (c.) Collage of micrographs depicting surface of (110) Ge diamond turned at various feed rates (um/rev)	

with -30° rake angle tool. (Path 3).....	132
5.44 Illustration of fracture pattern on (110) Ge machined with a -45° rake angle tool.....	134
5.45 (a.) Collage of micrographs depicting surface of (110) Ge diamond turned at various feed rates (um/rev) with -45° rake angle tool. (Path 1) (b.) Collage of micrographs depicting surface of (110) Ge diamond turned at various feed rates (um/rev) with -45° rake angle tool. (Path 2) (c.) Collage of micrographs depicting surface of (110) Ge diamond turned at various feed rates (um/rev) with -45° rake angle tool. (Path 3).....	135
5.46 Illustration of fracture pattern on (111) Ge machined with a -30° rake angle tool.....	137
5.47 (a.) Collage of micrographs depicting surface of (111) Ge diamond turned at various feed rates (um/rev) with -30° rake angle tool. (b.) (Path 1) Collage of micrographs depicting surface of (111) Ge diamond turned at various feed rates (um/rev) with -30° rake angle tool. (c.) (Path 2) Collage of micrographs depicting surface of (111) Ge diamond turned at various feed rates (um/rev) with -30° rake angle tool. (Path 3).....	138
5.48 Illustration of fracture pattern on (111) Ge machined with a -45° rake angle tool.....	140
5.49 (a.) Collage of micrographs depicting surface of (111) Ge diamond turned at various feed rates (um/rev) with -45° rake angle tool. (b.) (Path 1) Collage of micrographs depicting surface of (111) Ge diamond turned at various feed rates (um/rev) with -45° rake angle tool. (c.) (Path 2) Collage of micrographs depicting surface of (111) Ge diamond turned at various feed rates (um/rev) with -45° rake angle tool. (Path 3).....	141
5.50 Stress orientation factor accompanied by a schematic representation of pitting damage observed by Blackley for (110) wafer. [26].....	143
5.51 Typical profile of Ge surface machined at high feed with -45° tool. (10 um/rev feed).....	144
5.52 Typical profile of Ge surface machined at low feed with -45° tool. (5 um/rev feed).....	144
5.53 RMS versus feed rate and machining direction for a (100) Ge wafer machined with a -45° rake angle tool.....	145
5.54 RMS versus feed rate and machining direction for a (110) Ge wafer machined with a -45° rake angle tool.....	146
5.55 RMS versus feed rate and machining direction for a (111) Ge wafer machined with a -45° rake angle tool.....	146
5.56 RMS versus feed rate and machining direction for as a function of wafer orientation wafer machined with a -45° rake angle tool.....	147
5.57 Typical profile of Ge surface machined at high feed with -30° tool. (10 um/rev feed).....	148
5.58 Typical profile of Ge surface machined at low feed with -30° tool. (5 um/rev feed).....	148
5.59 RMS versus feed rate and machining direction for a (100) Ge wafer machined with a -30° rake angle tool.....	149
5.60 RMS versus feed rate and machining direction for a (110) Ge wafer machined	

with a -30° rake angle tool.....	150
5.61 RMS versus feed rate and machining direction for a (111) Ge wafer machined with a -30° rake angle tool.....	150
5.62 RMS versus feed rate and machining direction for as a function of wafer orientation wafer machined with a -45° rake angle tool.....	151
5.63 Comparison of PV values achieved during machining experiments of different Ge orientations with those obtained theoretically with Equation 5.1.....	152
5.64 Raman spectra taken of ductile turned (100) Ge surface at two feed rates machined with a -30° and -45° tool in separate machining runs.....	153
5.65 Raman spectra taken of ductile turned (110) Ge surface at two feed rates machined with a -30° and -45° tool in separate machining runs.....	154
5.66 Raman spectra taken of ductile turned (111) Ge surface at two feed rates machined with a -30° and -45° tool in separate machining runs.....	155
5.67 TEM image of Si chip generated in the ductile regime. [ORNL] <i>Bar = 2 um</i>	156
5.68 Diffraction pattern of Si chip indexed as crystalline dc-Si. [ORNL].....	156
5.69 TEM image of Ge chip generated in the ductile regime. [ORNL] <i>Bar = 0.5 um</i> .	157
5.70 Diffraction pattern of Ge chip indexed as crystalline dc-Ge. [ORNL].....	157

List of Tables

2.1	Surface energy values for single crystal silicon planes. [10].....	7
4.1	Cutting behavior for (100) Si wafer.....	62
4.2	Cutting behavior for (111) Si wafer.....	62
4.3	Elastic moduli used for determining dipole strength B from equation 4.2.....	65
5.1	Experimental matrix of 20 Raman scans for comparison of wafer orientation, tool rake angle, and feed rate (low/high.).....	99

1. Introduction

1.1 Background

Into the 21st century, silicon has remained the most technologically important semiconducting material for use in electronics. In addition to being used in microelectronics as transistors, rectifiers, and other electronic solid-state devices, silicon has more recently found function in energy and mechanical applications such as optics, electro-optics and micro-electro-mechanical (MEMS) devices. [1] As a result, substantial interest has been placed into improving machining of silicon to produce flatter, higher quality substrates and high precision form optical components, as well as the intricate shapes necessary in MEMS design. [2]

A major limitation of machining or grinding a brittle material such as silicon is that material removal processes can generate subsurface fracture damage. Such fracture damage reduces part quality and lifetime, and diminishes part efficiency in precision applications. This damage is typically removed by costly processes such as etching and chemical mechanical polishing with further manufacturing steps such as epilayer deposition or annealing treatments depending on the device application. Currently, processes associated with damage removal have difficulty achieving the required shape accuracy without substantial cost. [3] It is therefore important to reduce fracture damage during machining or grinding in order to increase device quality at lowered production costs.

It is generally acknowledged that single crystalline silicon (diamond cubic dc/Si-I) exhibits brittle nature at ambient temperature. However, this material has been shown to exhibit a plastic flow under contact loading when the deformation volume is adequately small. [4] Large non-hydrostatic and shear stresses are common during contact

loading as material undergoes machining processes. During such loading, various response mechanisms such as dislocation induced plasticity, microfracture, or even amorphization and high pressure phase transformations (HPPT) can affect a materials behavior. [5]

If the mechanisms driving ductile behavior in a brittle material can be better understood, one may be able to determine the conditions necessary to maintain this anomalous plasticity during a machining process, enhancing the machinability of these materials. Eliminating subsurface damage during machining will reduce cost and environmental considerations caused by CMP and etching post processing, as well as allow for the production of high quality ultraprecision optical, mechanical and electronic parts.

1.2 Present Work

The present work is concerned with the response of single crystal silicon to dynamic contact forces during machining processes such single point scribing and diamond turning operations. The response will be characterized by the nature of material removal (plastic versus fracture,) the creation of residual stress, and the presence of indicative phase transformations in the processed region.

Crystallographic direction, applied load, and tool tip geometry will be considered for scribing tests performed on single crystal silicon. Distortion created in the wafer due to residual stress after cutting is measured using interferometry. A model is being developed to relate the magnitude of the residual stress signature as it related to the distortion. The use of Raman will aide in understanding the role of HPPT in ductile behavior and the generation of residual stress and fracture initiation in the scribe region. Raman is a nondestructive characterization technique that characterizes the structure of the material and will be used to indicate whether the transformation has taken place. SEM imaging, optical microscopy, and

AFM measurement afford a look at the nature of the material removal and will determine whether a set of experimental parameters produces the desired ductile cut.

Crystallographic direction, rake angle, and feed rate will be considered for diamond turning operations. Surface characterization using interferometry will be done on machined surfaces. Raman will be used to characterize the turned regions and collected chips for sign of possible phase transformation. A TEM investigation of the debris generated during cutting will be carried out.

Stress models qualitatively explaining directional dependencies on material removal behavior seen during the two contact operations are developed. The models predict directions of easiest fracture based the resolved tensile stress on planes of high cleavage created by the stress conditions (whether by the tool or residual stress) induced by the contact process.

This research will attempt to investigate the effects of different parameters of both operations as each relates to inducing plastic flow in this nominally brittle material. The role, if any, of the high pressure phase transformation in plastic flow will also be discussed.

2. Properties of Silicon

This chapter will present a brief study of the mechanical properties of silicon; as such a study is necessary to acquire insight into its machining behavior. Single crystal silicon is a highly brittle and anisotropic material. As a result it is very difficult to model the response of silicon to contact processes. A discussion of the atomic and crystallographic structure of silicon is presented that explains the brittle nature of silicon and shows the anisotropy of its mechanical properties. An extension of these characteristics to machining is made as an exercise to show that many considerations are present and can become confounded in trying to explain the response of this material to contact processes.

2.1 Atomic and Crystallographic Structure

Silicon has an atomic number of 14, possessing 14 electrons with the energy level configuration of $1s^2 2s^2 sp^6 3s^2 3p^2$ as an isolated atom. The four unpaired electrons in the 3s and 3p energy levels are hybridized in a sp^3 orbital to form four covalent bonds in which electrons are shared with neighboring atoms. Movement within the structure is necessary for plasticity by dislocation motion and shear. Because covalent bonds are highly directional in nature and resist such movement, a brittle material results.

A single Si atom will bond in a tetrahedral configuration with other Si atoms. Bonding several of the tetrahedral molecules together yields a diamond cubic atomic structure, such as is the structure of single crystal silicon in its normal semiconducting state. A diagram of the crystal unit cell is shown in Figure 2.1 along with views of atomic planes as seen from different directions. [6]

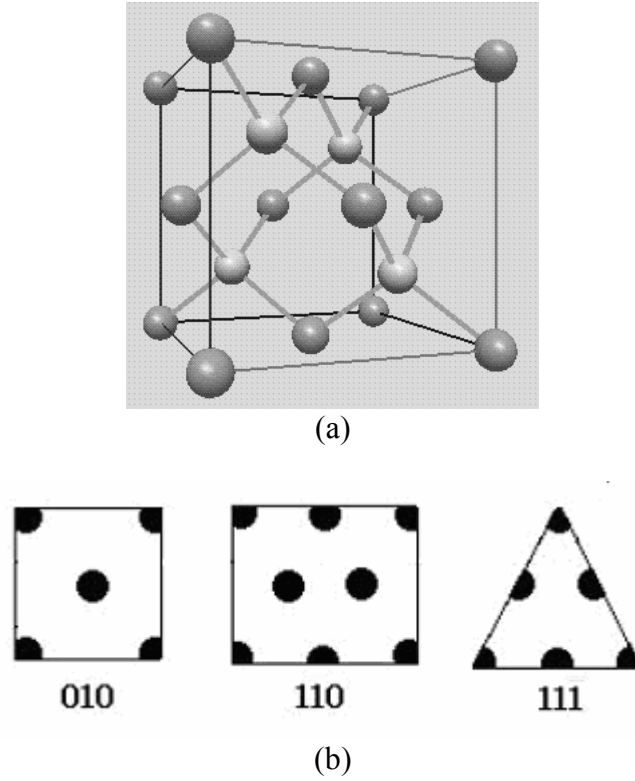


Figure 2.1: (a) Diagram of Si unit cell atomic arrangement. (b) Schematic of crystallographic planes of common wafer orientation. Arrows indicate equivalent planes. [6]

The anisotropic nature of the mechanical properties of single crystal silicon is governed by the atomic structure and crystallography. Si wafers used commercially feature either the (100), (110), or (111) crystal plane as the wafer face. Each plane (and its corresponding direction) features different structuring of the Si atoms giving markedly different material properties. Crystallographic directions with the same structuring of atoms are called equivalent and posses the same material properties. Non-equivalent orientations give rise to anisotropy.

2.2 Mechanical Properties

The anisotropic nature of the mechanical properties is of particular interest to this investigation. Presented in this section are the crystallographic orientation-dependent properties thought to affect the machining behavior of silicon. This discussion is mainly to

point out the difficulty in predicting machining behavior due to the anisotropic nature of these properties. This is further complicated by the formation of a speculated HPPT region at small deformation volumes near the tool tip.

2.2.1 Surface Energy and Elastic Parameters

In *Fracture of Brittle Solids- 2nd Edition*, Lawn states that for anisotropic materials, the dependence of elastic parameters (elastic and shear modulus) and surface energy on crystallographic direction complicates the issue of predicting fracture and plastic deformation behavior during contact processes. [7]

Assuming elastic fracture as the material removal mechanism, the theoretical strength to create two new surfaces (crack propagation) is dependent on the elastic modulus by:

$$2\gamma \cong \frac{2Ea}{\pi^2} \quad (2.1)$$

where γ is the cleavage energy, E is the elastic modulus and a is atomic spacing. This simple argument states that fracture is more likely to be seen between planes with large atomic spacing, low elastic modulus, and low surface energy. [8]

Lawn found that the quantity H/E (hardness/elastic modulus) is an important parameter for elastic-plastic contacts and could be used as an effective measure of brittleness.

[7] A high H/E corresponds to lower residual field intensity.

Shear modulus is an important parameter effecting plastic properties such as slip and yielding in single crystals. As ductility is the preferred material removal mechanism in scratching or machining of this material, the anisotropy of shear modulus should be considered (assuming HPPT does not dominate entirely as the mechanism of plasticity.) The critical shear stress that causes irreversible plastic deformation of the lattice is given by

$$\tau_c = \frac{G_{ij}a}{2\pi d} \quad (2.2)$$

where τ_c is the critical shear stress, G_{ij} is the shear modulus, a is the interatomic spacing, and d is the spacing between slip planes.

Surface energy is a measure of the energy of unsatisfied surface bonds. [9] The release of strain energy and work applied to the systems are competing energies with crack formation. Cracking generates new surfaces and increases the overall number of unsatisfied bonds, thus relieving strain energy and work done to the system. Table 2.1 reports surface energy values for various crystallographic planes after Hesketh *et al.* [10]

Table 2.1. Surface energy values for single crystal silicon planes. [10]

Crystal Plane	Surface Energy(J/m ²)	Crystal Plane	Surface Energy(J/m ²)	Crystal Plane	Surface Energy(J/m ²)
(100)	1.99	(110)	1.41	(111)	1.15
(210)	1.78	(310)	1.89	(410)	1.94
(211)	1.63	(311)	1.80	(411)	1.94
(221)	2.00	(331)	1.72	(320)	1.80
(322)	1.65	(433)	1.45	(522)	1.46

On an atomic scale, macroscopic elastic strain is created by small changes in interatomic spacing by the stretching of bonds. The magnitude of the elastic modulus is a measure of the resistance of adjacent planes to separate. The magnitude of the shear modulus is a measure of the resistance to moving one plane of atoms over another. The resistance to separation and shear are governed by interatomic forces. [9] These forces are dependent on atomic spacing, so it stands to reason that non-equivalent planes will have different atomic spacing, and therefore will have differing interatomic forces. As a result, elastic parameters are dependent on crystallographic orientation.

Wortman and Evans [11] used an approach by Nye [12] to create surfaces and curves to illustrate the directional elastic anisotropy of silicon. A simplified version of Hooke's Law states that for small deformations where nonpermanent (elastic) deformation occurs, stress (σ_{ij}) and strain (ε_{ij}) are proportional by the stiffness (c_{ijkl}) and compliance (s_{ijkl}) constants as:

$$\sigma_{ij} = c_{ijkl} \varepsilon_{kl} \quad (2.3)$$

$$\varepsilon_{kl} = s_{ijkl} \sigma_{ij} \quad (2.4)$$

Using this generalized form of Hooke's Law, elastic coefficients were determined from rotation transformations of the compliance constants about a general crystal axis for a particular orientation. The result is a dimensional surface or curve which illustrates the anisotropy of the elastic parameters. The author refers the reader to the reference [11, 12] or to a tutorial [13] explaining how the surfaces and curves are formed.

Figures 2.2(a.) and (b.) are examples of such a curves showing the anisotropic nature of the elastic and shear modulus of the (100) crystal face of silicon. It possesses a four-fold geometry for both moduli. The (110) crystal orientation possesses a two-fold geometry of the elastic and shear modulus and a (111) orientation interestingly possesses no directional dependency (isotropic) of either modulus. [13] The author refers the reader to Ebrahimi *et al.* [14] for a complete listing of the elastic parameter values (reported from similar calculation) for various crystallographic directions on the (100), (011), and (111) crystal orientation.

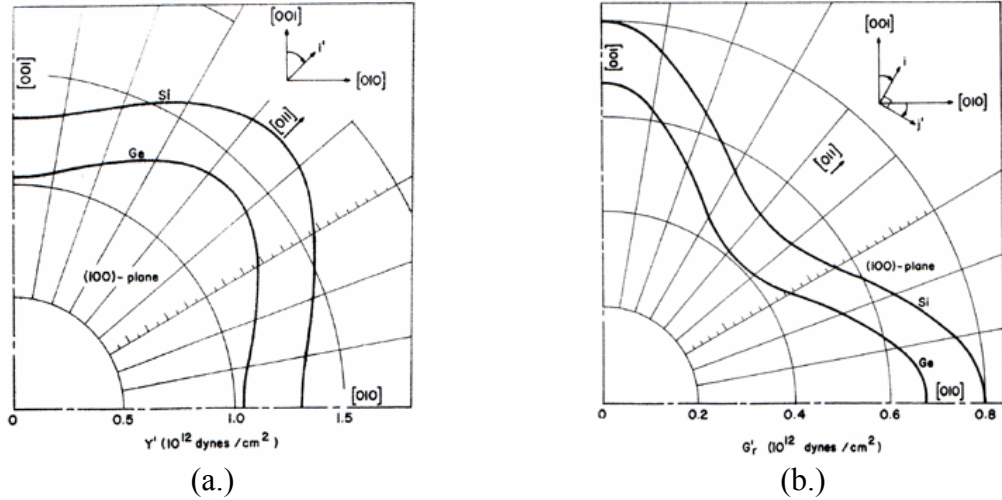


Figure 2.2. Directional dependency of (a.) Elastic (Young's) Modulus and (b.) Shear Modulus for (100) wafer

2.2.2 Hardness

Hardness is the measure of the ability of a material to withstand deformation by surface indentation or abrasion. [9] Harder materials present greater difficulty to machine. The accommodation of an indenter during a hardness test is discussed in Chapter 3 (Figure 3.1). For small scale deformations, the plasticity of the material usually governs the hardness of the material. Each of the commercially used wafer orientations exhibits a slight variation in measured hardness. The nature of this anisotropy is thought to be governed by the orientation of the primary slip systems that aid dislocation-induced plasticity during indentation within the resulting stress field, but this argument is clouded by the effects of the possible HPPT that may occur. Crystallographic orientations that promote the lowest value of effective resolved shear stress on these slip systems ($\{111\} <110>$ for silicon) are found to be the hardest. The effective resolved shear stress is given as

$$\tau_e = \frac{F}{2A}(\cos\psi + \sin\gamma)\cos\alpha\cos\lambda \quad (2.5)$$

where F is the applied load, A is the area supporting the load, ψ is the angle between the indenter face and the rotation axis of the slip system, γ is the angle between the indenter face and the slip direction, α is the angle between the axis of the applied load and the normal vector to the slip plane, and λ is the angle between the axis of the applied load and the slip direction.

[15]

Direct evidence on the directional dependence hardness on a given crystal orientation (wafer face) has not been fully researched for silicon and is highly complicated by the possibility of HPPT. The variation in hardness between each of the commercially available wafer orientations is established. Nihara *et al.* reports a hardness approximately 25-30% higher for (100) faces than for (110) and smaller disputed (depending on testing method) difference in hardness between (100) and (111). [16]

2.2.3 Fracture Toughness

While plasticity is the dominant mechanism of material removal in ductile-regime machining, fracture toughness is a key parameter said to influence the transition from ductile to brittle removal. Fracture toughness is the critical value of the stress intensity for which crack extension occurs. Fracture toughness K_{Ic} , is defined by

$$K_c = \psi \sigma_c \sqrt{a\pi} \quad (2.6)$$

where ψ is a constant dependent on crack geometry, a is the crack length and σ_c is the critical stress for crack propagation. [9]

The combined anisotropy of surface energy, elastic constants, and plastic deformation creates the dependency of fracture toughness on crystallographic orientation. The crack path depends on differences of elastic energy release rate and surface energy with orientation.

Based on the Griffith criteria, planes in which the elastic energy release rate reaches twice that of the surface energy tend to crack first. It is proposed that if suitably oriented to the stress field, a high surface energy plane may cleave in preference to a low surface (closely packed) energy plane. [14] In a definitive study by Ebrahimi, it was reported that silicon can cleave on many crystallographic planes, including high index planes. The intent of the study was to report the fracture toughness for the {110}, {100}, and {111} "intended" fracture planes. Intended planes are those that experience the highest tensile stress values during contact processes. There is a huge variation in reports for the fracture toughness values for these planes, depending on the method of testing. See Table 6 in reference [14] for a summary. The variation of fracture toughness with direction on various orientations was found by indenting and measuring the resultant crack length and indentation sizes. The dependency of fracture toughness on direction is shown in Figure 2.3(a.), (b.) and (c.) for the (100), (110), and (111) wafers respectively. Ebrahimi reported a variation in fracture toughness along the various orientations that was consistent with the symmetry axis of the indent plane (wafer face.) It was concluded that the variation in fracture toughness is due mainly to a change in crack length. No distinct conclusion on the effect of elastic modulus on fracture toughness could be made.

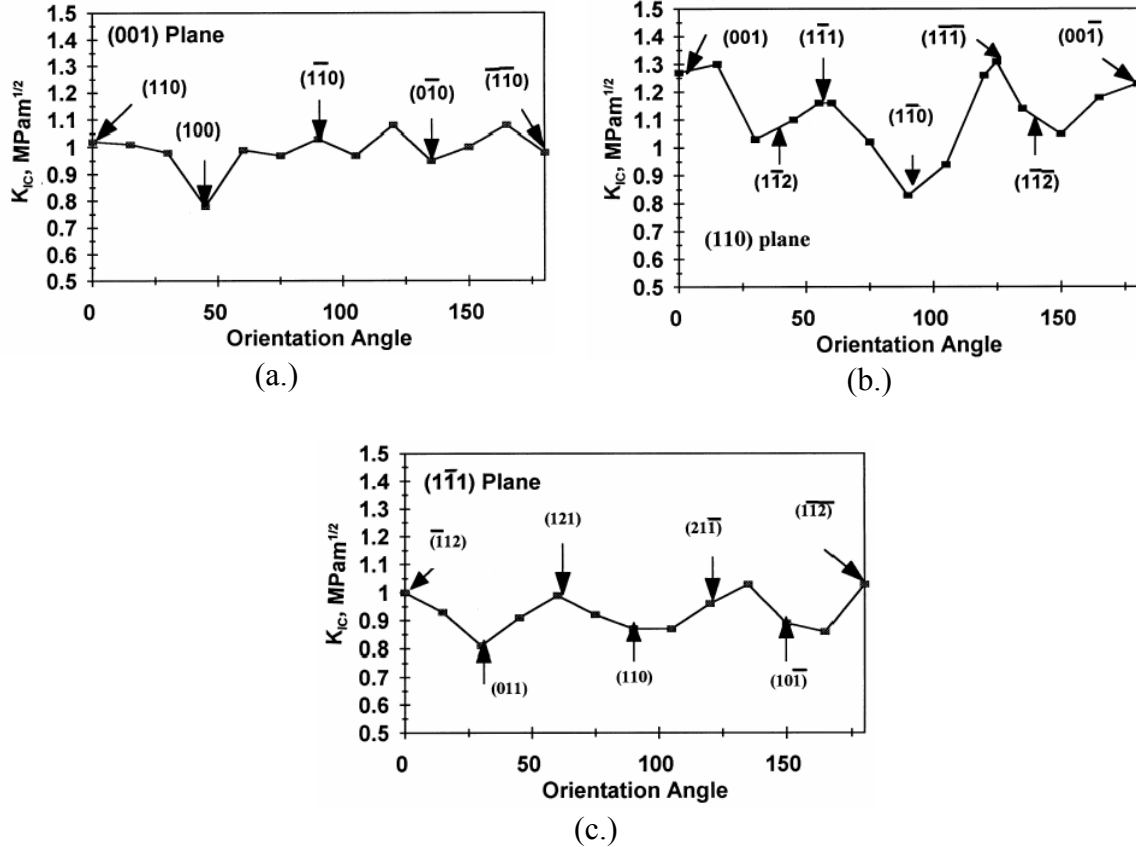


Figure 2.3. Variation of fracture toughness with orientation for (a.) (100), (b.) (110) and (c.) (111) planes. [7] The indices in parentheses are the planes in which fracture is thought to occur as the orientation angle of the indenter is changed.

The study also found that for the (110) indent plane, {1-11} planes are the preferred cleavage planes and for the (111) indent plane, the preferred cleavage plane was the {110} family. No conclusion was drawn for (100) planes. Ebrahimi further concluded that fracture path may be different than the “intended” paths however that fracture path was confounded by not by surface energy (and fracture toughness) anisotropy considerations, but the extent of plasticity in the indent and the inclination of cleavage planes relative to the indent plane. [14]

3. Literature Review on Machining Theory and Experimentation

The machining and grinding of brittle materials concerns the cutting action of a contact area such as a sharp tool tip or abrasive grains into the material. Understanding the interaction between the material and the contact force is essential in understanding material removal processes.

Due to its significance to electronic and mechanical applications, silicon is the most studied and documented material with thousands of research papers written annually. There is however, very little published on the response of silicon under contact loading similar to that seen in machining and grinding processes. As a result it is difficult to understand the mechanisms creating the ductile-to-brittle transition seen in several experiments to be discussed. [5] This section is intended for the brief discussion of the various developed theories and experimental findings in research of Si response to contact forces of scribing and diamond point turning. First, a simplified model of the response of a brittle material to indentation from a fracture mechanics standpoint is given followed by the introduction of an analytical model of stress fields caused by sliding microindentation (scribing). Critical parameters and crystallographic dependencies of diamond turning behavior are then discussed. Lastly, the theory of High Pressure Phase Transformation (HPPT) is discussed as a mechanism for aiding the plasticity seen during indentation, microcutting, and precision machining operations as it is a special interest of the present research.

3.1 Modeling Material Mechanics of Contact Process

Models interpreting the response of a material to contact processes, namely indentation and sliding indentation (scribing) are largely based on fracture mechanics approaches. Fracture mechanics focuses on the initiation and propagation of cracks through

a material. Initiation of a crack during contact processes originates at points of high tensile stress concentration in the contact field, which is dependent on tip geometry and path. Cracks tend to initiate and propagate as the size deformation volume (indentation or depth of cut) increases. [17] However, if the size of the deformation volume is small enough [18], plastic deformation becomes more energetically favorable over crack initiation and propagation to avert a stress singularity. [17]

Lawn [17] outlined the evolution of the response of a brittle material to loading with a sharp contact point shown in Figure 3.1: (i.) the sharp point induces irreversible deformation of the material as the contact size (and field) is below a critical value; (ii) at a critical point, a flaw within the deformation field is unstable and a median crack is formed; (iii.) the median crack propagates with increased loading; (iv.) as the compressive load is removed the median crack closes; (v.) relaxation of the plastically deformed material causes a residual stress build up that is relieved by lateral cracking; (vi.) the expansion of lateral cracks continues until indenter removal is complete.

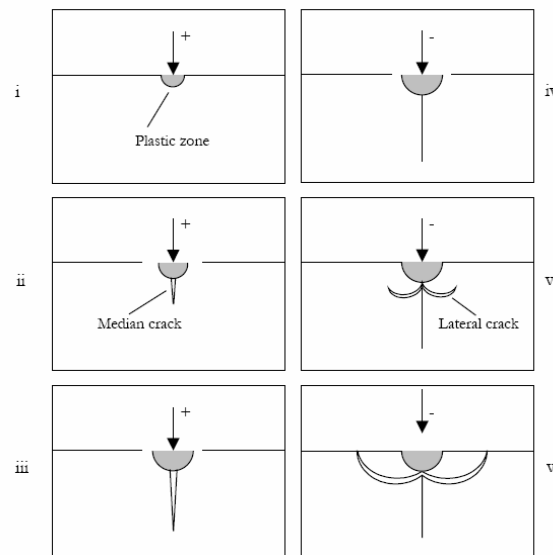


Figure 3.1 Evolution of crack systems during loading and unloading of sharp contact. [17]

Diamond turning and scribing processes are not as well modeled but are thought to be similar in nature. Swain [19] concluded that the crack system also propagates in the wake of tool motion for sliding microindentation with a sharp indenter. Figure 3.2 illustrates how Swain proposed that median and lateral crack systems propagated behind the moving tool. Median and lateral cracking are both damage processes said to be associated with brittle material strength and material removal (pitting), respectively.

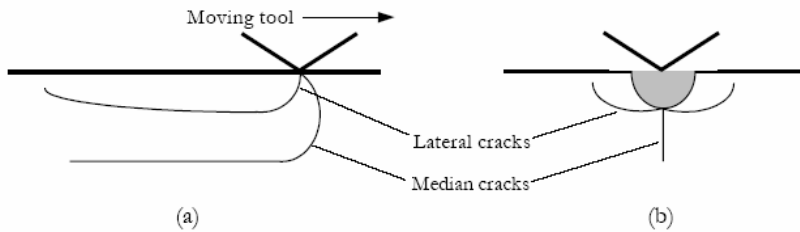


Figure 3.2. Crack formation as a single point tool is moved along the surface of a brittle material. (a) side view. (b) front on view [19]

Ahn *et al.* proposed the response seen in Figure 3.3 of a brittle material to sliding microindentation. At small deformation volumes the material responds to the scribing operation with the generation of a plastic zone within the elastic matrix. As the material is released from load it acts to push on the elastic half-space of the surrounding material. If the residual stress is great enough cracking can initiate from the plastic/elastic interface to relieve some of the strain energy of the elastic matrix. Growth of these cracks occurs in the elastic region. It was assumed that the tensile stresses which are incurred in the elastic region surrounding the expanding plastic material initiate and propagate the crack patterns illustrated in Figure 3.3. [20]

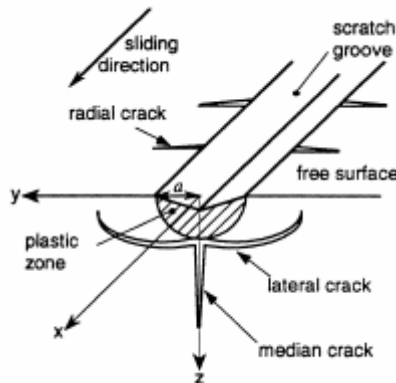


Figure 3.3. Formation of plastic zone and subsequent cracking with scribing. Typical crack patterns include median, lateral, and radial cracking. [20]

Because the residual stresses imprinted by the plastically deformed material are thought play a key role in determining final crack lengths, analyses of stress fields produced by microindentation and sliding microindentation were sought. Chiang et al [21] and Yoffe [22] provided stress field analyses (and corresponding stress equations) of indentation stress fields in elastic/plastic materials. Each likened the stresses exerted by the plastically deformed region to the expansion of a pressurized cavity. Yoffe explained this expansion generates residual stress due to an elastic/plastic constraint. The result of the analysis is a solution called a “blister,” a surface perturbation which produces a residual stress field. The stress distribution is obtained as a superposition of two stress fields, a “doublet force system,” consisting of a point center of expansion in an infinite elastic solid with and additional force to satisfy the free surface stress boundary condition. Figure 3.4 shows (a.) the hypothesized yield area and (b.) the force doublet used for the blister field.

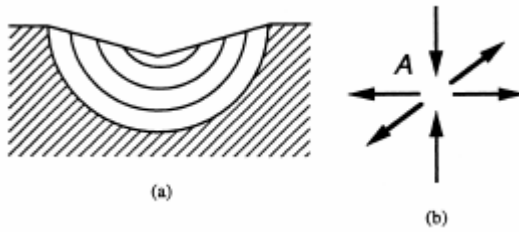


Figure 3.4. Yoffe’s “blister” field model. (a.) Hypothesized yield zone under indenter. (b.) force double to model stress field in indentation [20]

The strength of the blister is related to the volume increase of the inelastic zone and varies with the applied force of the indenter. [22] The prediction of origin and growth of the different crack types from this model has shown consistency with experimental observations. [20]

Ahn *et al.* [20] extended the model created by Yoffe to describe the stress field and fracture caused by sliding microindentation (scribing) of a brittle material. The stress field is approximated as a superposition of applied normal and tangential forces [23] with the blister-field prediction of localized inelastic deformation at the tip. It was concluded that lateral cracking is the result of the blister stress field while median cracking resulted from the forces applied by the tip. The numerical results provided by quantitative analysis that the model provides compared well with experimental observations. It was shown that the model provided reasonably good description of the crack patterns observed in soda lime silicate glasses and other brittle materials. The analysis, based on the assumption that lateral cracking is initiated and propagated by the tensile stresses adjacent to the inelastic zone, accounted for the occurrence of lateral cracking above an observed load threshold. The author refers the reader to the reference [22] for a complete explanation of the model and corresponding stress analysis.

3.2 Experiments and Modeling of Ductile Regime Machining

Considerably less is understood about the response of silicon and similar materials to diamond turning processes. Early work in ductile regime machining used fracture mechanics models to explain machining behavior. Research primarily focused on determining machining parameters that induced ductile regime machining. The mechanisms of plasticity were still accepted as a dimensional effect in which as the scale of deformation increases, plastic deformation become more energetically favorable than fracture. [18]

Blake and Scattergood were among the first to demonstrate that silicon and germanium could be diamond turned in a regime where material removal was by plastic flow without introduction of fracture into the surface. Blake defined a critical chip thickness where above which the damage, in the form of pitting due to lateral cracking, created by a tool pass could not be cleaned up by subsequent passes. It was shown that the critical chip thickness (Figure 3.5) was a function of feed rate, crystal orientation and tool rake angles. [24]

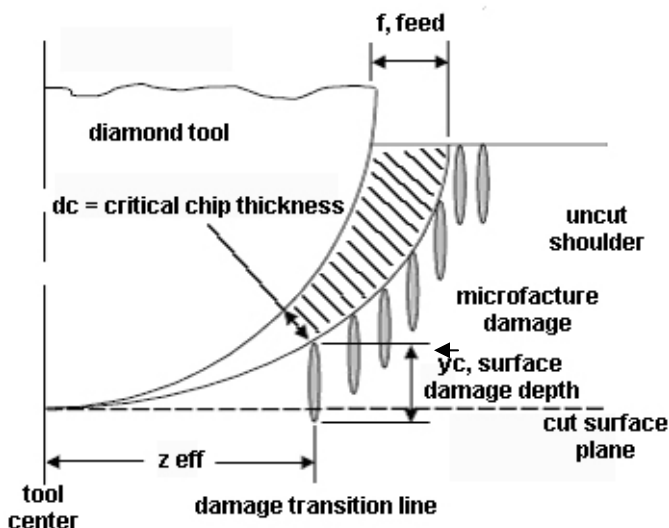


Figure 3.5 Diagram showing chip removal area and damage region. Critical chip thickness is shown. [26]

Work by Bifano used fracture mechanics models and experimental data to determine critical chip thickness for grinding in the ductile regime. The plasticity of Si was modeled as a function of important materials parameters such as elastic modulus, hardness, and fracture toughness. Bifano showed that experimental data gave good agreement with the analytical model. The model assumed an isotropic material and was not directionally dependent. Critical chip thickness was found to be

$$d_c \propto \left(\frac{E}{H} \right) \left(\frac{K_c}{H} \right)^2 \quad (3.1)$$

where E is elastic modulus, H is hardness, and K_c is fracture toughness. [35]

Blackley and Scattergood later introduced a model for diamond turning of these materials in the ductile regime and showed the crystallographic directional dependency of the operation. They predicted the variation of damage with crystallographic orientation using a line force stress model (Figure 3.6.) The model, which will be applied to the current investigation, uses stress and rotation transformations to find the maximum tensile stress resolved on the planes of easiest fracture. The model showed good agreement (Figure 3.7) with experimental results for (100) and (111) directions. [26]

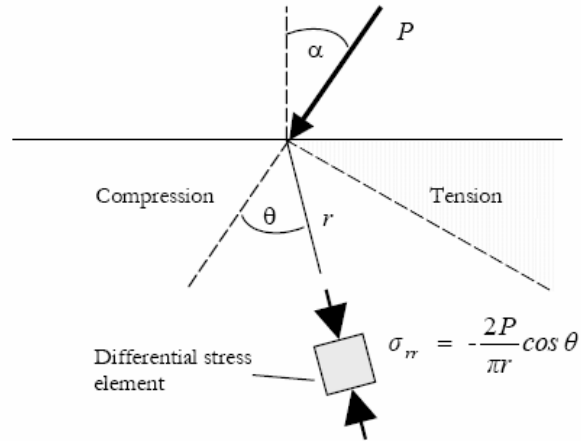


Figure 3.6 Line force loading P applied to an elastic half space. [26]

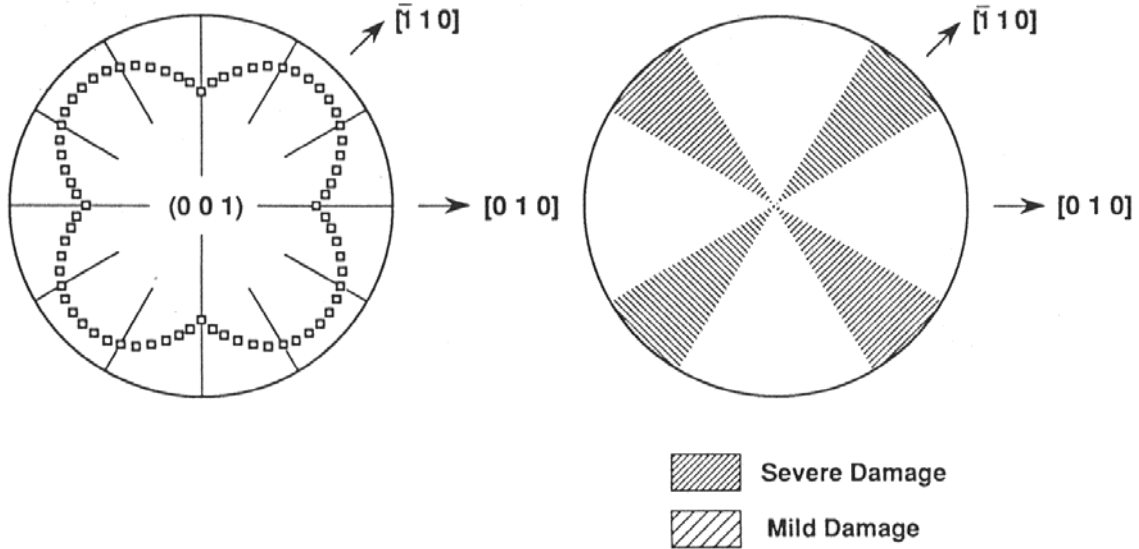


Figure 3.7 (a.) σ_{max} vs ϕ for diamond turning of (100) wafer. (b.) Schematic of pitting damage seen on a wafer face turned at the brittle-ductile transition. Dark regions are those of pitting while white regions where plastically turned. [26]

Shibata *et al.* carried out diamond turning on (100) and (111) wafers. The work showed agreement with that of Blackley and Scattergood for depths of cut of 1um. However, the damage pattern was shifted 45° (pitting damage went from [011] to [100] dependence) at 100 nm depth of cut. It was reasoned that the difference in material removal mechanism between plastic deformation and brittle fracture was responsible. It was shown through TEM

characterization of the $\{111\}<110>$ slip systems that the orientation dependence of the surface features was related to the ease of which these systems were activated. A slip orientation factor model based on the Schmid factor for a given slip system was developed and proved useful for describing the ductile-regime turning mechanism. [27]

3.3 Plasticity and High Pressure Phase Transformation

The mechanisms involved in causing plastic deformation in a brittle material are highly debated. While plasticity could be the result of dislocation and slip mechanisms of the covalent material brought on by intense shear stresses, researchers were looking to another possible explanation. It has been well documented in two survey papers in the area of High Pressure Surface Science that single crystal silicon (diamond cubic-dc) is thought to undergo a phase transformation to a metallic β -tin phase (Si-II) with the generation of large pressure on the surface by micro-indentation, scratching and ultra precision machining. It is believed that the metallic nature of this transformation facilitates the generation and motion of dislocations and slip behavior near the tool tip. While this transformation has yet to be observed *in-situ*, early research on phase transformation of silicon from pressure cell experiments coupled with analytical modeling of static and dynamic loading have led researchers to believe that the hydrostatic and nonhydrostatic components of stress induced by contact loading are thought to be high enough to induce the transformation. Popular theory among high pressure surface scientists seems to state that the metallic nature of the high pressure β -tin phase is thought to play a role in ductile cutting behavior by facilitating plastic deformation mechanisms. The microstructure of the plastically flowed material from contact loading experiments has been examined by several methods including x-ray diffraction, Raman spectroscopy, transmission electron microscopy, and various other

methods. Phases said to be indicative of the β -tin transformation including amorphous or a combination of rhombohedral and body-centered cubic (Si-XII and Si-III, respectively) crystal structures were seen depending on experimental conditions. These phases are known back-transformations from β -tin seen in pressurization experiments, thought to exist in material subjected to contact loading as the kinetics may prohibit the return transformation to dc structure upon unloading. [5, 28]

Experiments performed in indenting, single point diamond scratching, and ultra-precision cutting have indicated agreement with high pressure cell experiments of inducing phase transformation to the metallic β -tin. [5] The indicative phases discussed in the following brief literature review are pertinent to this investigation. Previous results from scribing and single point diamond turning cutting experiments are of particular interest to this investigation. Indentation experiments are also discussed as such research provides the foundation for the hypothesis that phase transformation is responsible for plastic behavior during contact loading.

3.3.1 Indentation

Early attempts to explain apparent plasticity in Si indentation experiments were rooted in dislocation-induced models. Trefilov explained that in low temperature, the theoretical shear strength was exceeded locally during indentation and dislocations arose to due to block slip. [29] Other theories proposed where the role of quantum properties of dislocations [30] and the creation of dislocation loops with climb. [31] TEM studies by Nikitenko [32] and Rowcliff [33] reported dislocation and defect formations in the vicinity of indents made at low temperature. Theories based on dislocation generation and motion, however, are said to

give poor explanation of observed behaviors of hardness or flow stress in dc silicon at low temperature. [5]

Grindeva *et al.* [34] first proposed the idea of pressure-induced metallization by correlating the measured hardness of Si at low temperature with the pressure needed to induce the β -tin transformation in high-pressure cell experiments. The group later performed conductivity measurements that were verified by others using different indenter geometries. [35-37] A drop in resistance coupled with the theoretical pressure was hypothesized to indicate metallization had occurred under the tip.

TEM studies done by several groups have shown the presence of amorphous [35, 38-40] and metastable crystalline phases [41-43] in regions below an indenter, depending on experimental conditions such as tip geometry and unloading rate. Some experiments showed other phenomena such as slip bands or dislocation arrays beneath the transformation region depending on conditions (which are hypothesized to be secondary responses to densification in the transformation region.) [39] Among the proposed explanations for this region included: (i) the amorphous phase is created as β -tin transforms back to dc with insufficient release time or (ii) the amorphous phase is a direct result of localized high pressure upon loading dc-Si. [35] Figure 3.8 [43] illustrates one such example of TEM work showing the transformation region created by a spherical indenter.

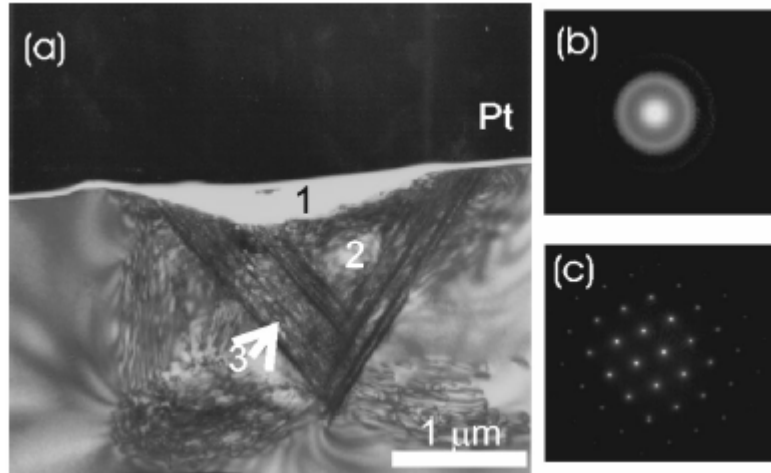


Figure 3.8. (a.)TEM image of spherical indent at 80mN. (b.) diffraction pattern of region 1, showing amorphization. (c.) diffraction pattern on region 2, showing crystalline nature. [43]

SEM imaging often shows a very high-ductility material extruded from indenting experiments providing additional support for the phase transformation to a metallic state during indentation. Figure 3.9 shows a typical example of an SEM image from indentation testing on single crystal silicon. [44]

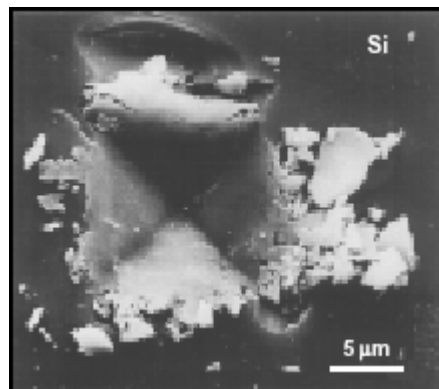


Figure 3.9. Scanning electron micrograph of Vickers indentation (1-N) showing extruded plastic material. [44]

Extensive indentation studies performed by Gogotsi *et al.* concluded that silicon can undergo a series of phase transformations during static contact loading and subsequent annealing seen in Figure 3.10. Raman micro spectroscopy scans were taken in regions immediately around and within the indentation region. Annealing experiments were

performed by adjusting the Raman laser intensity during scans. The major conclusion was that for fast unloading rates silicon was solely observed within indentation, while for slow unloading rates a combination of Si-XII and Si-III metastable crystalline structures were found. (Loading rate is thought to be a function of penetration depth and indenter geometry.) The authors concluded that transformation to metastable crystalline phases required a sufficiently slow pressure release for the formation of the crystalline phases. Upon subsequent annealing however, the crystalline phases eventually amorphize and finally return to the original dc structure. [5, 44]

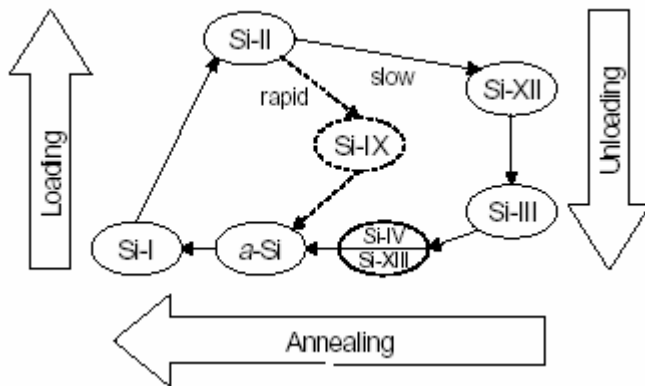


Figure 3.10. Schematic of phase transformations thought to occur during contact loading. [5]

Raman stress mapping was used by Gogotsi and Gardner to show that indentation performed in the ductile regime induced residual stress fields around indents. The researchers were also able to map the amount of Si-XII present in a Vickers indent by normalizing its characteristic band with that of the Si-I characteristic peak at each point within the indent. [45]

The appearance of discontinuities in applied load vs. indenter depth curves were studied by several groups. [46-48] Theoretical calculations of the pressures at which discontinuities in loading and unloading curves occurred were made. [46, 47] These values

matched up well to pressures shown to induce the phase transformations of interest in high pressure cell experiments. The presence of the phases thought to cause each discontinuity was verified by Raman measurements. [48] Figure 3.11 shows that for indent cycles creating a “pop-out” discontinuity, Si-III and Si-XII were present in the indents. For an “elbow” discontinuity, amorphous phase was seen within the indent. The calculated pressure at which the two discontinuities occurred matches pressure cell experiments. [48]

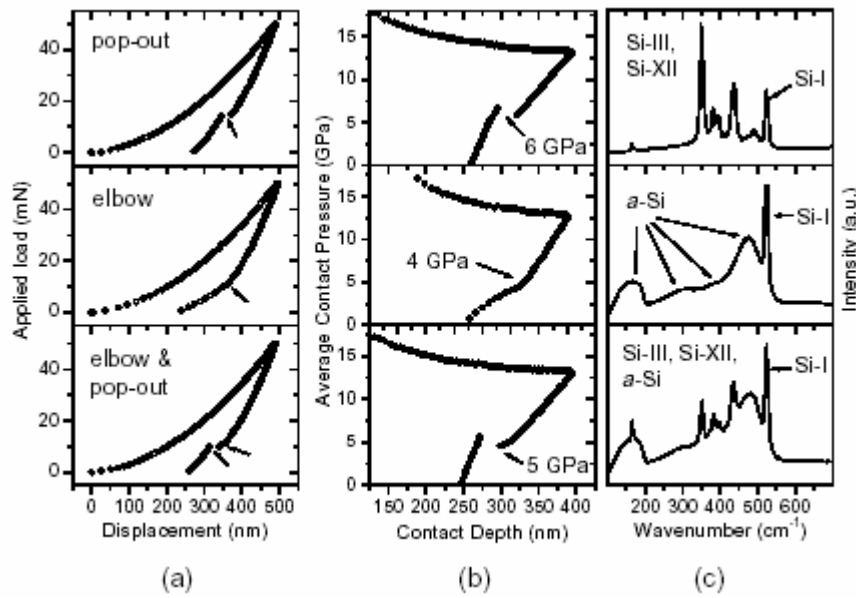


Figure 3.11. (a) Load vs. displacement curves. (b) Contact pressure vs. depth curve. (c) Raman corresponding to indentation region for each discontinuity event. [48]

3.3.2 Scribing and Diamond Turning

Considerably less work has been done in the effect of dynamic contact loading on inducing phase transformation in nominally brittle materials, most of which having been done on silicon wafers.

TEM studies of scribing operations performed on silicon wafers with Rockwell (rounded) and Vickers (pyramidal) verified the creation of a thin amorphous zone within the scribe traces. The amorphous zone was surrounded by a dislocated and micro-cracked region.

[49] Tanikella *et al.* reported that Raman analysis of scribing with Vickers indenters showed that material within the scribe appeared amorphous, while debris on the surface was thought to be nanocrystalline Si-I domains subjected to tensile stresses within a less dense amorphous matrix. [50]

Raman characterization of a diamond turned surface performed by Duduch *et al.* indicated findings of Si-I domains in an amorphous surrounding on the surface. Morris *et al.* concluded that a high pressure phase transformation created variation in critical chip thickness depending on rake angle, feed rate, and crystal orientation. [51] TEM work done on diamond turned Si showed that the machined surface produced from the operation had a damage layer (2-3 um) beneath a thin layer (~150 nm) of amorphous material. In addition, the chips formed were shown to be completely amorphous. Figure 3.12 shows the cross sectional TEM images of the turned samples. The upper layer was shown to be amorphous by electron diffraction, while the lower layer was shown to be highly dislocated crystalline material. [52]

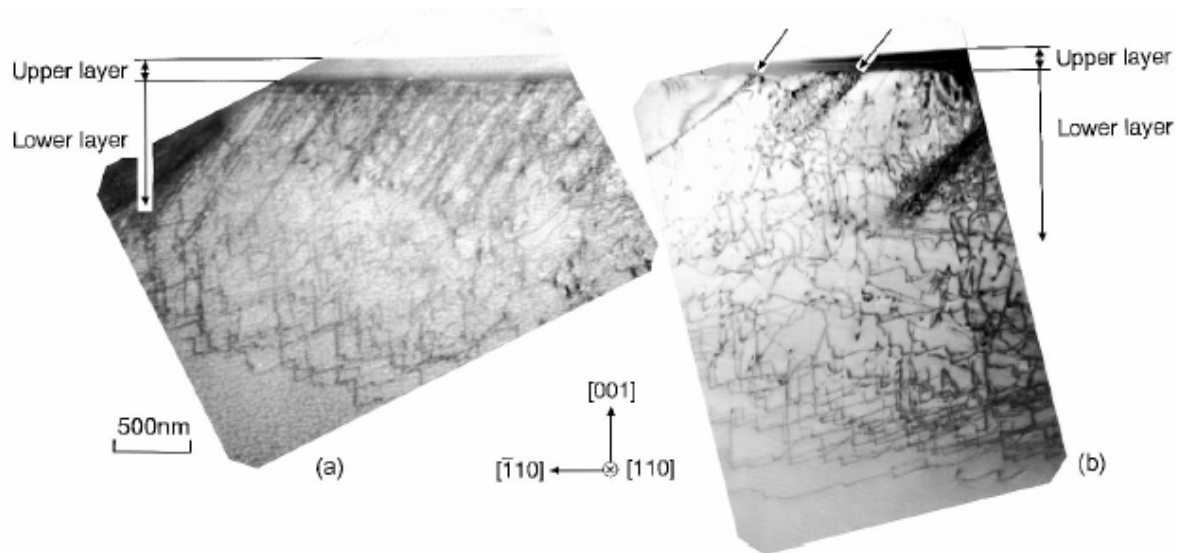


Figure 3.12. TEM cross-section of diamond turned Si. Depth of cut: (a.) 100 nm and (b.) 500nm. [52]

Yan demonstrated the correlation between amorphization and undeformed chip thickness in diamond turning via Raman spectroscopy. It was found that the intensity for amorphous material increased as the chip thickness increased within the ductile regime. The maximum amorphous intensity was near the ductile-brittle transition. When pitting occurred, the Raman spectra depended highly on the location at which it was taken. Non-fractured areas showed amorphization, while fractured areas (within the pits) were crystalline. [53]

Gogotsi *et al.* provided the most thorough study of scribing of single crystal silicon and the appearance of phase transformation to date. By gradually controlling the depth of indenter penetration, a critical depth of cut was established as a transition from ductile to brittle response (~250nm for both indenter types.) The authors also noted morphological features (deformation bands, pile ups and debris) thought only to exist as an artifact of the ductile response. Figure 3.13 is an SEM micrograph of scribes created below and just above the ductile to brittle transition.

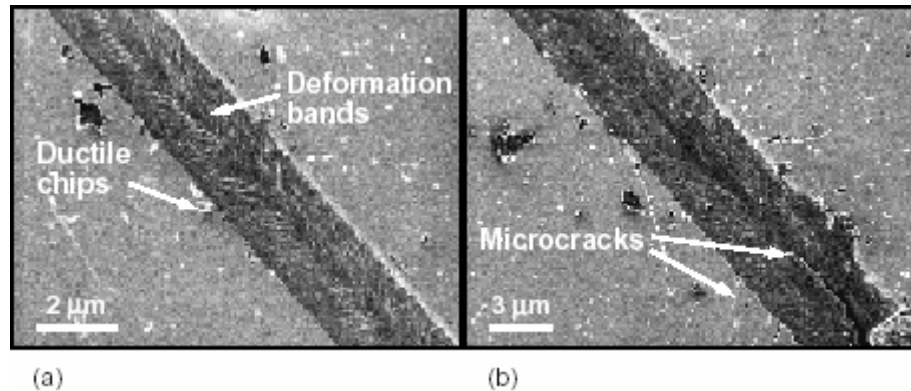


Figure 3.13. SEM images of (a.) ductile scribe created with Vickers indenter. (b.) the onset of microcracks at the critical depth to induce ductile to brittle transition. [54]

The $\text{dc} \rightarrow \beta\text{-tin}$ transformation was said to be confirmed by the presence of Si-XII/III at deeper depths of cut, while the scribes with a smaller depth of cut were shown to be amorphous. The authors hypothesized that large depth of cuts had a slower rate of release

due to high residual stress (constraint) resulting in atomic reordering to crystalline structures. Smaller depths of cut were rapidly released resulting in disorder. Raman stress mapping showed that increasing depth of cut resulted in increasing residual stress within the ductile regime. Upon fracture initiation, cracking released local strain creating variation in stress.

[54]

4. Single Point Scribing of Silicon

4.1 Scope and Objectives

The scope of this investigation is the study of the stresses generated and to determine the presence of HPPT within scribe grooves of single crystal silicon in order to further understanding of the nature of material removal during machining. Scribing tests act to model the grinding and polishing process by replicating the material deformation behavior of an individual grinding or polishing particle.

During the investigation, scribing data was obtained for various directions on (100) and (111) crystallographic planes of silicon. Scribing along the $<100>$ and $<110>$ will be studied for the (100) orientation. $<110>$ and $<112>$ directions will be studied for the (111) orientation. Various loads with in the ductile range and extending into the fracture region are tested for two different geometries of tip interaction with the surface. Residual stresses resulting from the elastic constraint on the plastically deformed and displaced material create distortion in a flat plat geometry sample. This bending distortion can be used to corroborate the residual stress model that has tensile dipole forces to predict the bend effect. [54] Scribes are studied with scanning electron microscopy to determine the nature of material removal within the scribe trace and to observe the fracture behavior/plastic deformation in relation to crystallography. Atomic Force Microscopy allows for depth of cut measurements as well as reinforces SEM study. The dependence of fracture behavior on scribing direction is discussed qualitatively with a stress orientation model. Raman spectroscopy will be used to identify differences in structure between the untouched silicon and that within the scribe to better understand the nature of the observed plasticity. It is hoped that either crystalline or

amorphous phases of silicon that are indicative of β -tin phase transformation can be identified within the transformation zone. What is not known however, is the role of high pressure phase transformation (HPPT) in the generation of residual stress.

To facilitate explanation, experimental results are presented, followed by a separate discussion section. It is necessary to present all the data first as each part adds to the final ideas extracted from the data.

4.2 Experimental Setup

4.2.1 Sample Creation

Four inch P-type Si wafers of both (100) and (111) orientation were sent to Valley Design Corp of Santa Cruz, CA to be diced into several 1 cm x 2 cm rectangular pieces. The wafers were diced so as to have the crystallographic directions of interest orientated along the short axis of the sample as seen in Figure 4.1.

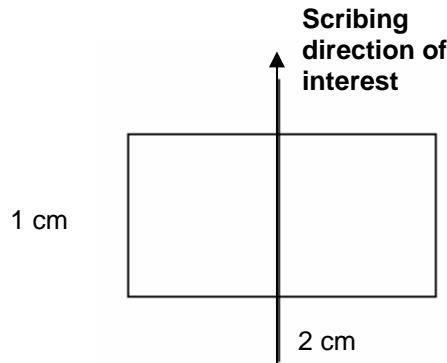


Figure 4.1 Schematic of sample orientation indicating scribing direction of interest.

[100] and [110] directions were of interest for the (100) wafer face and [1-10] and [11-2] and [-1-12] directions were of interest for the (111) wafer. [11-2] and [-1-12] have the same scribing axis, due to the three fold symmetry of the (111) face, produces different scribing

behavior. [11-2] is distinguished from [-1-12] by reversing the direction of the scribe in the opposite direction.

4.2.2 Scribing with a Dynatex Tip

A Zwick micro hardness tester is fitted with a Dynatex diamond tip (Figure 4.2(a.)) in a custom holder as pictured in Figure 4.2(b.) The tip is manufactured by Dynatex International using synthetic diamond for scribing wafers in the semiconductor industry. The tools are approximately 25mm long, 4mm diameter, stainless steel shaft containing a faceted diamond tip at one end. The tip is in the shape of a square based pyramid, with the point flattened into a square table as pictured in Figure 4.2(c.) The angle of each of the four sides with reference to the table is 45° . The angle of the edge where two sides meet is 35.3° from the table, and 54.7° from the axis of the tool.

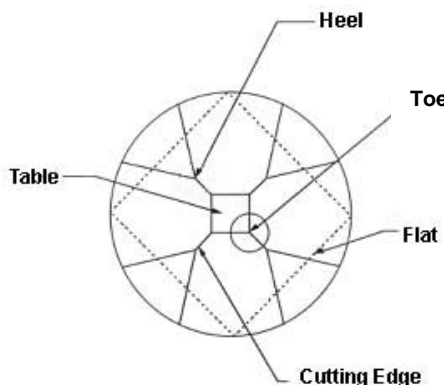


Figure 4.2(a.) Dynatex Tip [54]

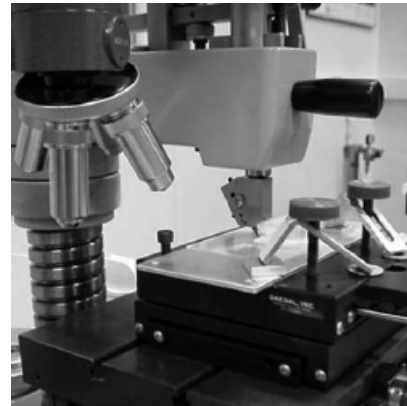


Figure 4.2(b.) Picture of scribing setup [54]

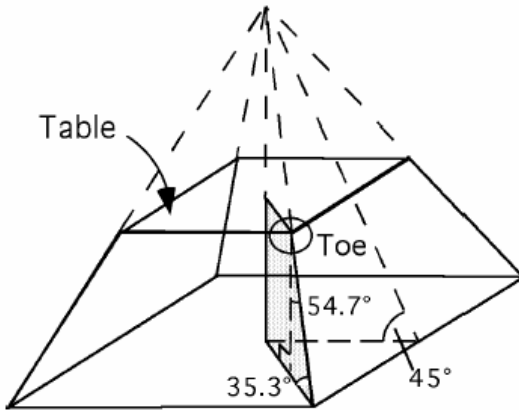


Figure 4.2(c.) Illustration of flattened pyramid [54]

To produce a scribe, the sample is translated under the diamond tip such that either the cutting edge or table is oriented in the scribe direction, depending on the desired tip geometry. The samples are held firmly in place between two metal slides mounted to a custom stage with the desired crystallographic direction orientated in the translation direction. This motorized stage is used to create translation at a constant rate of 0.250 mm per second. Samples are scribed at various loads ranging from 20-250 mN by placing a series of masses on the loading sleeve of the micro hardness tester. Multiple, evenly spaced (50-100 um) scribes are placed at the center of the long axis of the 2 cm x 1 cm sample. An odd number of multiple scribes are used to generate measurable deflection (the effects of multiple scribes are additive to the bend) and to produce a more statistically significant measurement than that of a single scribe.

A tool holder was designed to hold the cutting edge of the diamond tip at an angle of 3.3° from the sample surface as shown in Figure 4.3(a.) Figure 4.3(b.) is an SEM image of the area enclosed in the circle in Figure 4.3(a.) The tip orientation allows for two different geometric interactions with the surface depending on which way the stage is translated. Translating in one direction creates a plowing action of the table into the surface, which is

nominally termed “blunt” cutting. Translating in the opposite direction creates a slicing action of the cutting edge which is nominally termed “sharp” cutting. The two different geometric interactions create vastly different responses in the material.

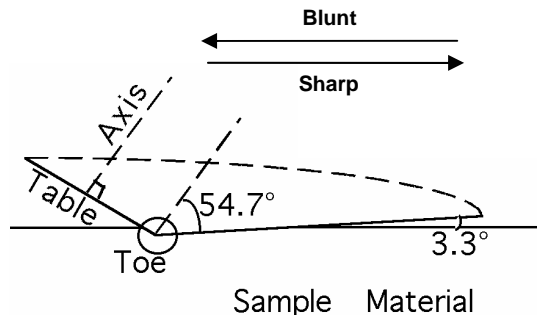


Figure 4.3(a.) Geometry of tip to sample surface [54]

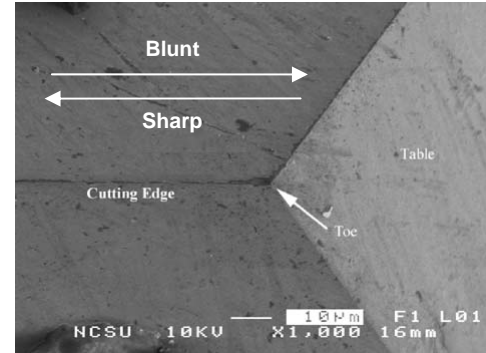


Figure 4.3(b.) SEM of area encircled in Fig. 4.1(a.)

4.2.3 Interferometric Analysis

Topographic data is collected for an as-received 1cm x 2cm x 525 μm Si sample using a Zygo GPI Laser interferometer pictured in Figure 4.4. The sample is measured again using the interferometer after scribing.



Figure 4.4. Image of Zygo GPI Laser interferometer

MetroPro, the software suite used to analyze the interferometer data, allows the user to subtract the data collected before scribing from that collected after scribing. The resulting profile created is the net bending effect. The data collected from the Zygo is then converted with a utility to an ASCII format. The Y and Z data for an X approximated as the center of the long axis is then used to create a plot of the bend profile. Microsoft Excel is used to graph these values. The generated plot is then used to approximate the angle of deflection from the initial state. The deflection angle data is then correlated to the residual stresses created by scribing using a bend effect model.

4.2.4 Characterization

Optical Microscopy

Optical micrographs using a Nomarski filter were taken with an Olympus BH2-UMA to determine the quality and topography of the machined surface.

Raman Spectroscopy

Characterization of the scribe region was accomplished with Micro-Raman spectroscopy done at room temperature using an ISA U-1000 scanning monochromator. Raman excitation was done with the 514.5 nm line of an Argon-ion laser, with a spot size of approximately 3 to 4 μm in diameter. Laser focus was produced by an Olympus BH-2 optical microscope. Raman spectra were taken in the 200-600 cm^{-1} range which contains the characteristic peaks normally associated with crystalline, amorphous, and various metastable crystalline phases seen in other research. A spectral resolution of $\approx 4 \text{ cm}^{-1}$ was utilized, and the laser power was $\approx 5 \text{ mW}$.

Scanning Electron Microscopy

SEM was carried out using a Hitachi S-3200N is a Scanning Electron Microscope operating at 20 keV at varied working distances. The Everhart-Thornley detector was used for topographic imaging of the scribes. Digital image capture was done using NIH Image collection.

Atomic Force Microscopy

AFM was done with a VISTA-100 Scanning Probe Microscope. A low stiffness cantilever was used to perform contact mode measurements of the sample surface. Image studio 3.0 was used to capture images as well as interpret data.

4.2.5 Measurement of Bend Deflection

The bend profile as generated by MetroPro is represented by a 3-D oblique plot as shown in Figure 4.5. The data is then converted to a line plot format with a conversion utility. An X is selected that is estimated to be the center of the long axis. The Y and Z data for that X is used to generate a 2-D profile in which the flat portions of the profile can be fit to lines and the angle of the deflection from the flat position can be calculated. Figure 4.6 illustrates an example of a 2-D bend profile generated with fitted lines.

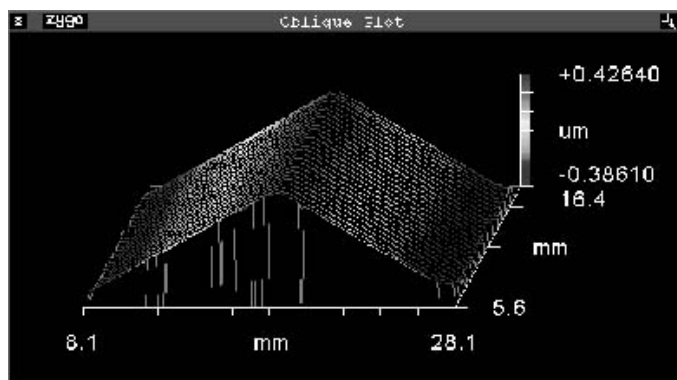


Figure 4.5. Oblique plot of bend angle effect generated in Metropro.

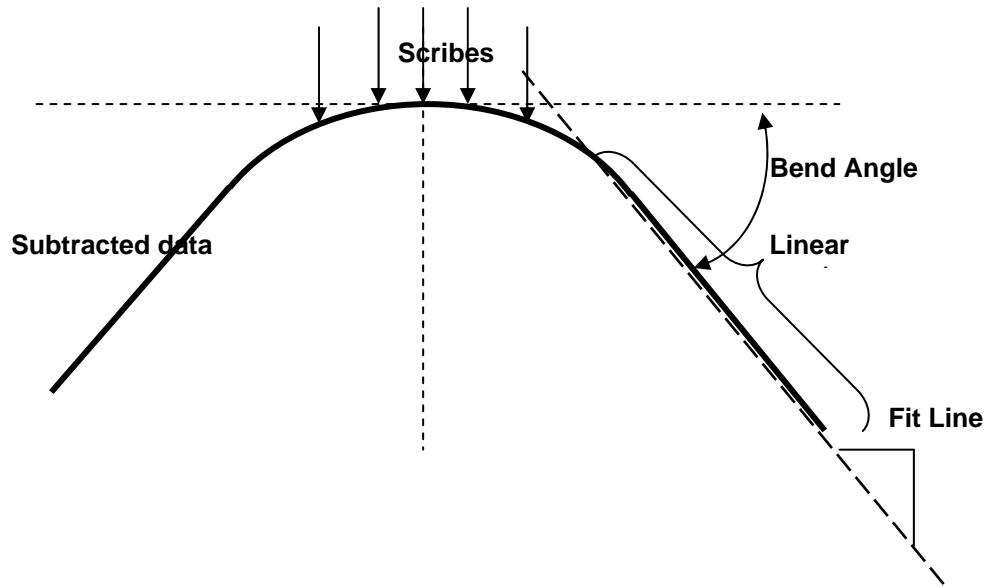


Figure 4.6. 2-D profile of bend effect showing line fit to flat portions and bend angle [2].

4.3 Experimental Results

4.3.1 Scribing Behavior

General Material Responses

Figures 4.7 (a.)-(d.) show SEM images of the four general material responses seen due to scribing with the Dynatex tip. Scribe widths were found to be on the order of a few microns, increasing as the load applied increased. Figures 4.7(a.) and (b.) are of ductile cuts generating no debris and debris, respectively. Figure 4.7(c.) and (d.) displays the two commonly seen fracture responses (geometry dependent.) It is important at this point to distinguish between a purely ductile and the combination of ductile/elastic fracture as a response to scribing. Each sample was viewed under an optical microscope to make an initial observation on material removal processes. If no chipping is present along the scribe traces (by either means seen in Figure 4.7(c.) or (d.),) it is reasoned that the material removal is mostly by plastic mechanisms. If chipping is apparent, it is reasoned that the material

removal is influenced by elastic fracture mechanisms, and that the plastically deformed material will be removed in the process.

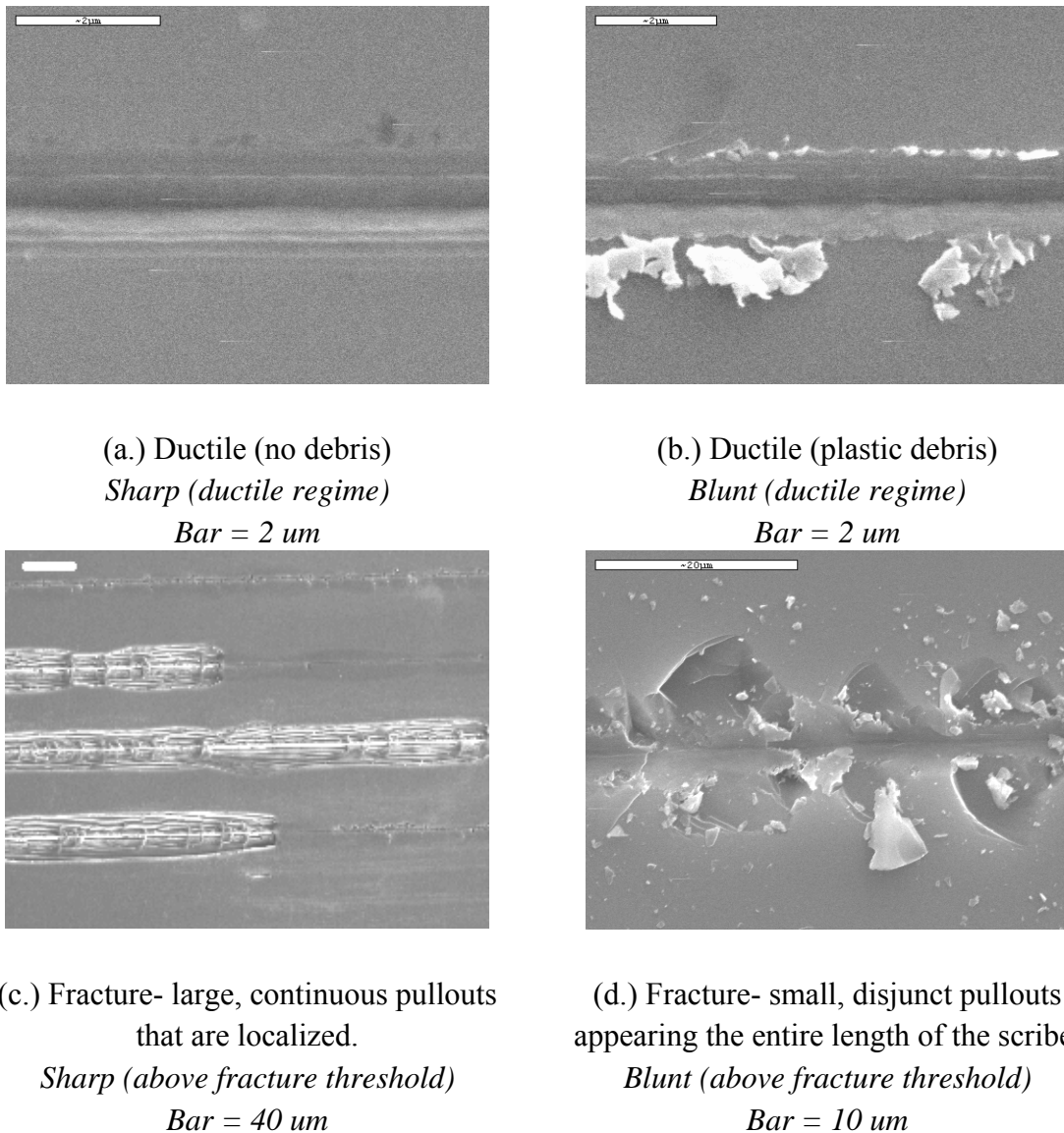


Figure 4.7. General material responses to scribing with Dynatex Tip

Ductile responses shown in Figure 4.6(a.) and (b.) were seen when scribing **within the ductile regime** for a particular direction. The “ductile- no debris” response seen in Figure 4.6(a.) was created by translating the stage to cause the sharp geometry interaction while translation in the blunt geometry direction would elicit the “ductile-plastic debris”

response in Figure 4.7(b.). The debris from this response is shown in Figures 4.8(a.) and (b.) Figure 4.7(c.) is a typical fracture response created when scribing above a particular direction's fracture threshold with the sharp geometry. The pullouts are large and continuous, localized along the scribe, with widths on the order of tens of microns. Figure 4.7(d.) is a typical fracture response seen during scribing above the fracture threshold with the blunt geometry. The pullouts tend to be much smaller and disjunct appearing over the entire length of a scribe. The resultant crystalline debris is thrown around the scribe, and tends to have sizes on the order of a few microns.

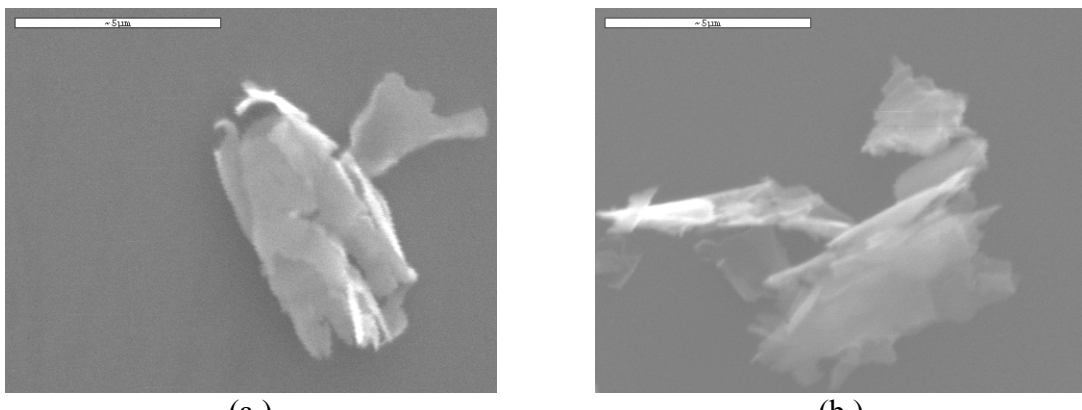


Figure 4.8(a. and b.) Micrographs of plastically extruded debris typically seen from the material response of Figure 4.7(b.) *Bar = 2 um*

Geometry/Cutting Direction

A set of scribes was made for each direction of interest for both the (100) and (111) wafers, varying the load from 1-15g in increments of 1g for both geometry directions. The fracture threshold load was determined for each condition and the material response was noted using optical microscopy. Selected scribes within the ductile regime are viewed with SEM. AFM results are also shown to give a three dimensional feel as well as provide profiles and depths of cuts for the scribe.

(100)[100] Figures 4.9 and 4.10 are optical micrographs of scribes made in the load range tested for scribing in the [100] direction on (100) samples for sharp and blunt geometries, respectively. In Figure 4.9, the scribes appear to be similar in nature to those seen in Figure 4.7a (ductile- no debris) within the ductile regime (1-7g applied load.) Figures 4.11(a.) and (b.) are an SEM and AFM image of such a scribe in the ductile regime cut with sharp geometry. No debris is present, and no chipping is apparent until the fracture threshold which occurs around 9g of applied load. Above 7g of applied load, large pull outs, most likely due to lateral cracks reaching the surface, appear periodically along the scribe trace (similar to Figure 4.7c.) In Figure 4.10, the scribes appear to be similar in nature to those seen in Figure 4.7b (ductile- plastic debris) within the load range tested. Figures 4.12(a.) and (b.) are a SEM and AFM image of a typical scribe within the ductile regime cut with the blunt geometry. The fracture threshold is out of the load range that could be tested with the experimental setup. The debris along the side appears plastic in nature and is present for all the loads tested. This same debris is shown in Figure 4.8.

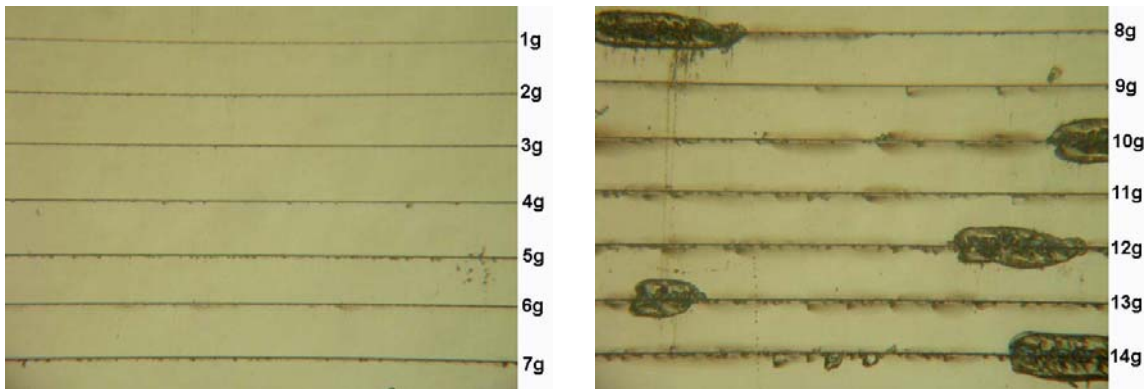


Figure 4.9. Optical micrograph of scribing range of (100)[100] for sharp geometry. Fracture threshold occurs at approximately 8g of applied load. (15g omitted for presentation)

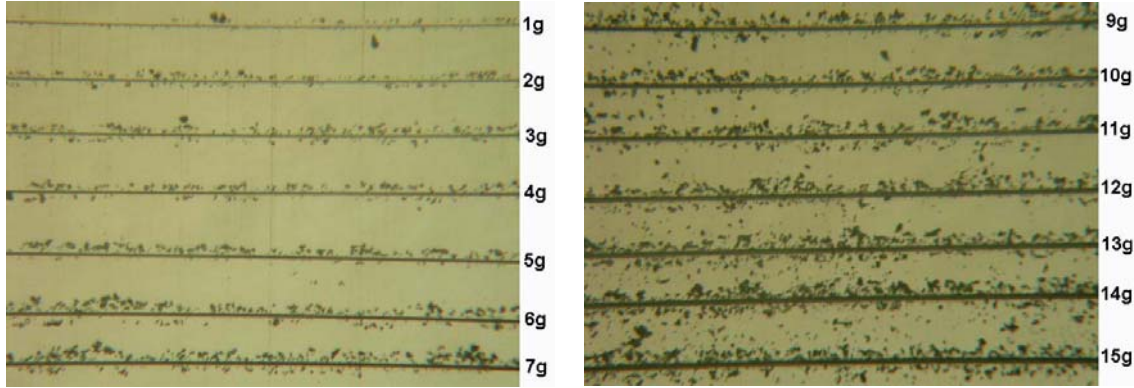


Figure 4.10. Optical micrograph of scribing range of (100)[100] for blunt geometry. Fracture threshold was not reached in the load range tested. Plastic debris is heavily present along the sides of the scribes. (8g omitted for presentation)

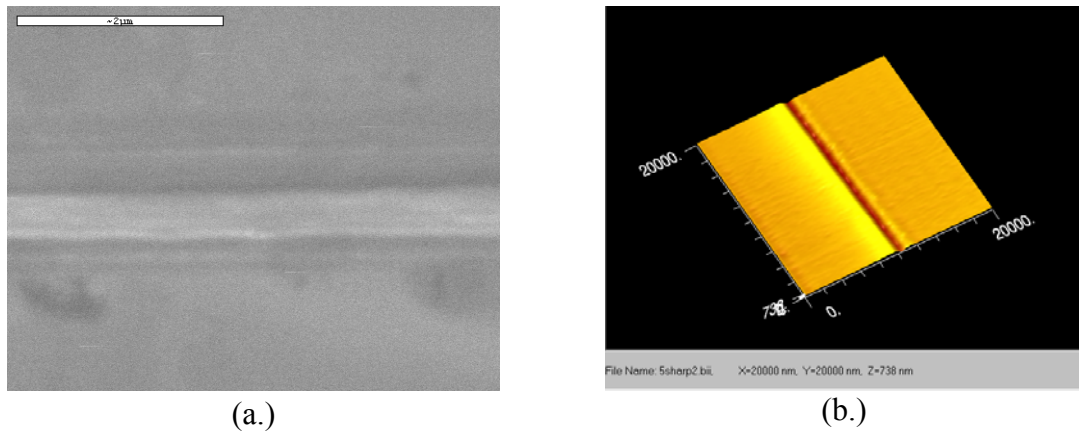


Figure 4.11. (a.) SEM and (b.) AFM image of sharp scribe for (100)[100] within the ductile regime. (a.) Bar = 2 μ m

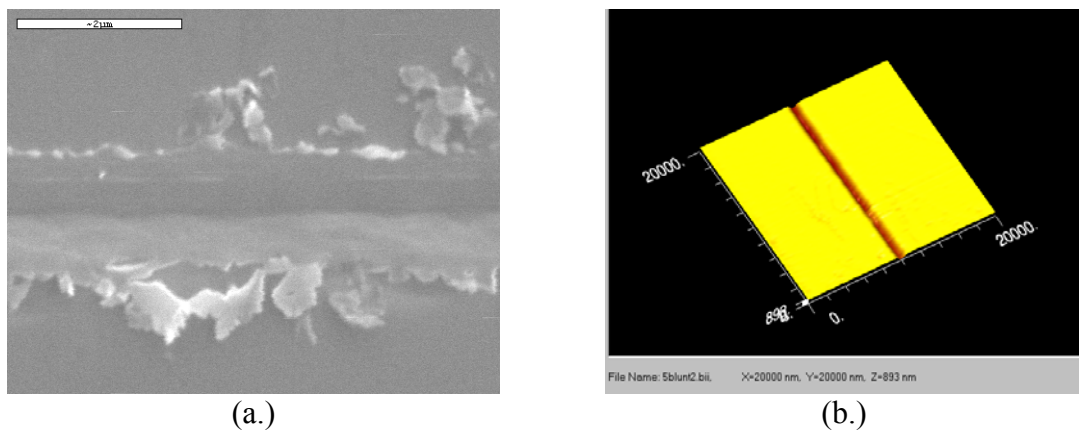
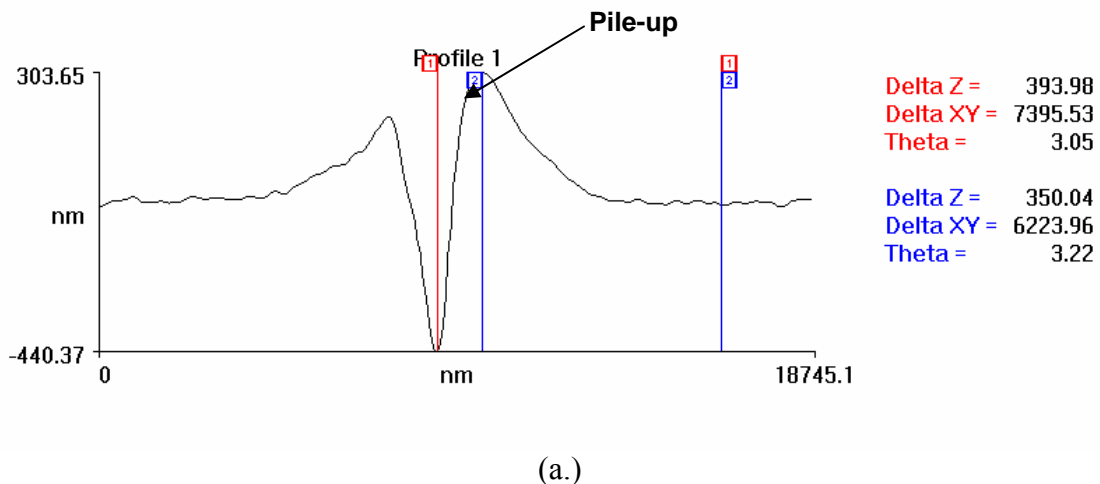


Figure 4.12. (a.) SEM and (b.) AFM image of blunt scribe for (100)[100] within the ductile regime. (a.) Bar = 2 μ m

Figures 4.13(a.) and (b.) are profiles of scribes made in the ductile regime (5g loading) for both sharp and blunt geometries, respectively. These profiles are typical of those made in the ductile regime. AFM measurements taken on scribes made with the sharp geometry above the fracture threshold were performed in regions where pullouts had not occurred (the pullouts tended to be localized and there were regions unaffected by fracture.)

For the blunt geometry, depths of cut tended to be much greater than for sharp. Profiles for the sharp geometry tended to have large “pile-ups” on the sides of the scribe trace as plastic material was thought to be displaced around the tip, but not removed onto the surface. These pile-ups would measure several hundred nanometers in height on some occasions. Scribing with the blunt geometry tended to eliminate the appearance or reduce the height considerably of these features.



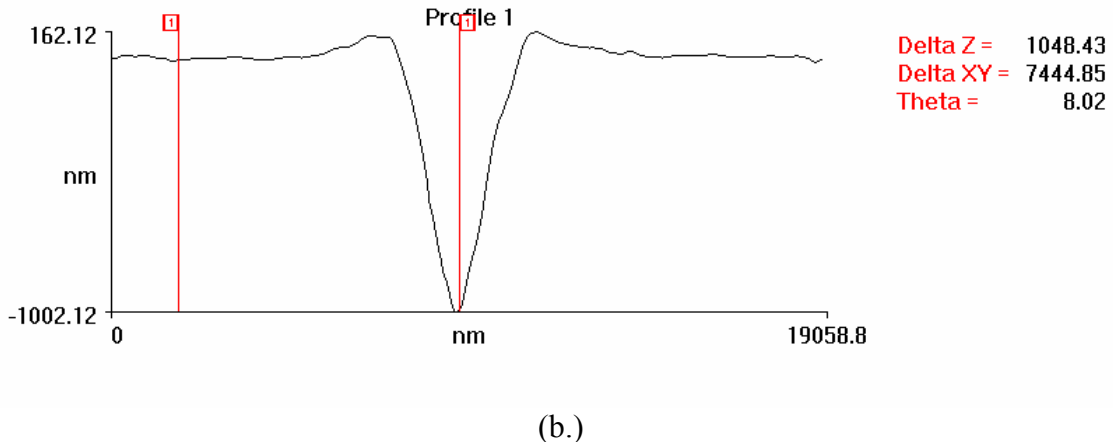


Figure 4.13. AFM profile of (a.) sharp and (b.) blunt scribe on (100) in [100] direction in ductile regime.

Figure 4.14 shows the depths of cuts for both sharp and blunt geometries as a function of applied load. There seemed to be a steady increase of depth of cut for both indenters as load increased.

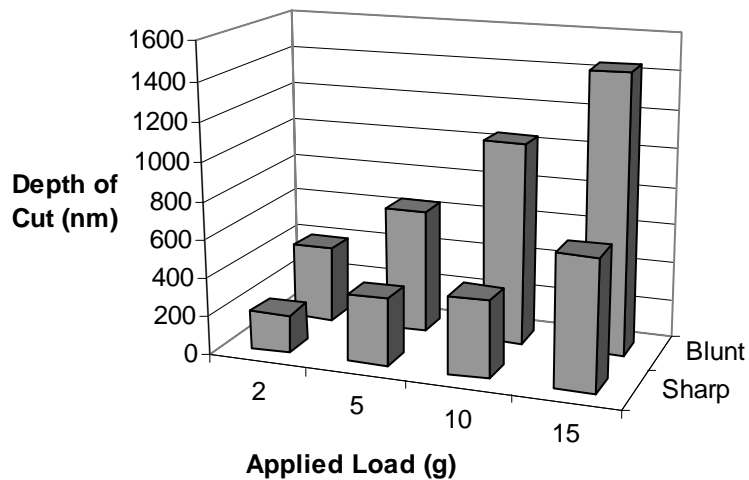


Figure 4.14. Effect of Sharp vs. Blunt geometry on depth of cut for (100)[100].

(100)[011] Figure 4.15 and 4.16 are optical micrographs of scribes made in the load range tested for scribing in the [011] direction on (100) samples for sharp and blunt geometries, respectively. In Figure 4.15, the scribes appear to be similar in nature to those seen in Figure 4.7a (ductile- no debris) within the ductile regime (1-13g applied load.) Figures 4.17(a.) and (b.) are an SEM and AFM image of such a scribe in the ductile regime cut with the sharp geometry. No debris is present, and no chipping is apparent until the fracture threshold which occurs around 14g of applied load. Above 13g of applied load, large pull outs, most likely due to lateral cracks reaching the surface, appear periodically along the scribe trace (similar to Figure 4.7c.) For blunt geometry cutting shown in Figure 4.16, scribes below the fracture threshold (as shown SEM and AFM images of Figure 18(a.) and (b.)) appear similar to that in Figure 4.b (ductile- plastic debris,) but generating less debris than seen for the [100] scribing direction (Figure 4.10.) The fracture threshold is relatively low, with the first sign of pitting appearing at 5g in a few areas and becoming more frequent as the load increases. The scribes are similar in nature to those seen in Figure 4.7d (fracture-small, disjunct pullouts) within the load range tested. The debris along the side appears crystalline in nature and is present where fracture occurred.

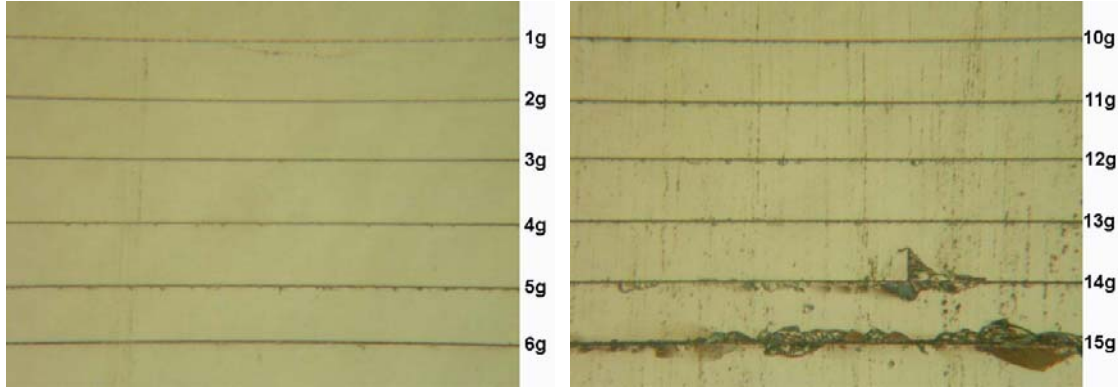


Figure 4.15. Optical micrograph of scribing range of (100)[011] for sharp geometry. Fracture threshold occurs at approximately 14g of applied load. (7-9g omitted for presentation)

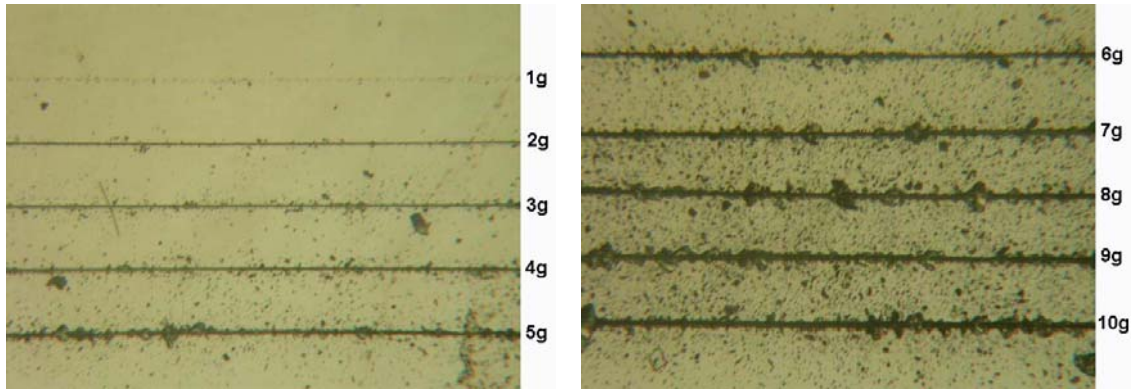


Figure 4.16. Optical micrograph of scribing range of (100)[011] for blunt geometry. Fracture threshold occurs between 5-6g of applied load. Debris is plastic below the fracture threshold, changing to small crystalline fracture above it.

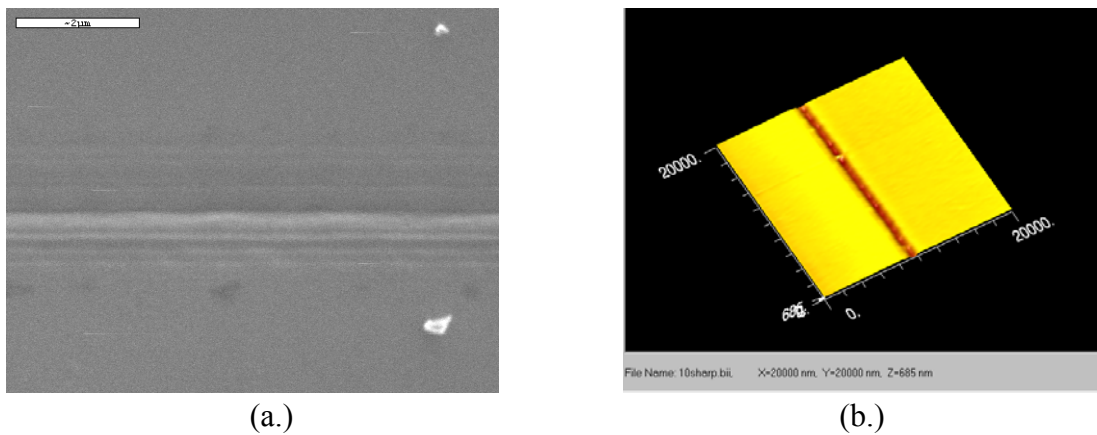


Figure 4.17. (a.) SEM and (b.) AFM image of sharp scribe for (100)[011] within the ductile regime. (a.) Bar = 2 μ m

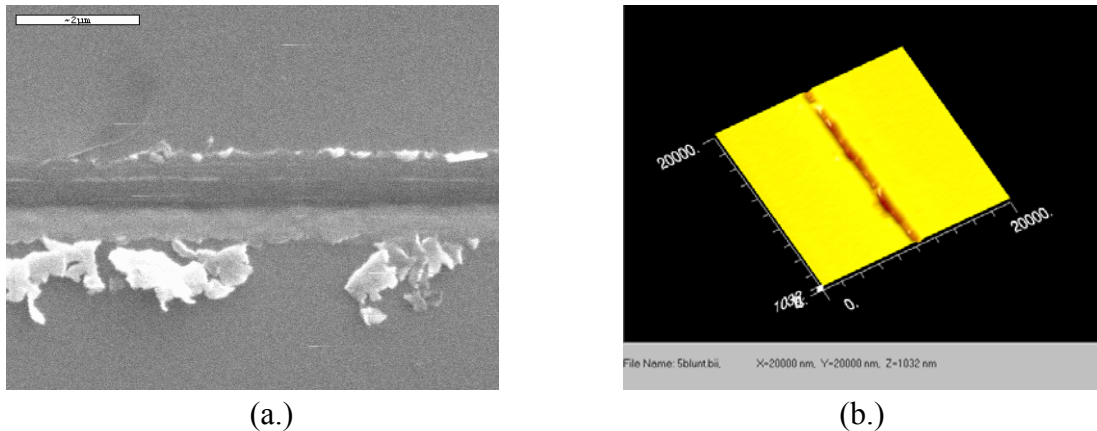


Figure 4.18. (a.) SEM and (b.) AFM image of blunt scribe for (100)[011] within the ductile regime. (a.) *Bar = 2 um*

Figures 4.19(a.) and (b.) are profiles of scribes made in the ductile regime (5g loading) for both sharp and blunt geometries, respectively. These profiles are typical of those made in the ductile regime.

For the blunt geometry, depths of cut tended to be much greater than for sharp within the ductile regime. As well, profiles for the sharp geometry tended to have large “pile-ups” on the sides of the scribe trace as plastic material was thought to be displaced around the tip, but not removed onto the surface. These pile-ups would measure several hundred nanometers in height on some occasions. Scribing with the blunt geometry tended to eliminate the appearance or reduce the height considerably of these features at low loads. As this scribing direction was easily fractured with the blunt geometry, measurements were effected by large removal of crystalline material.

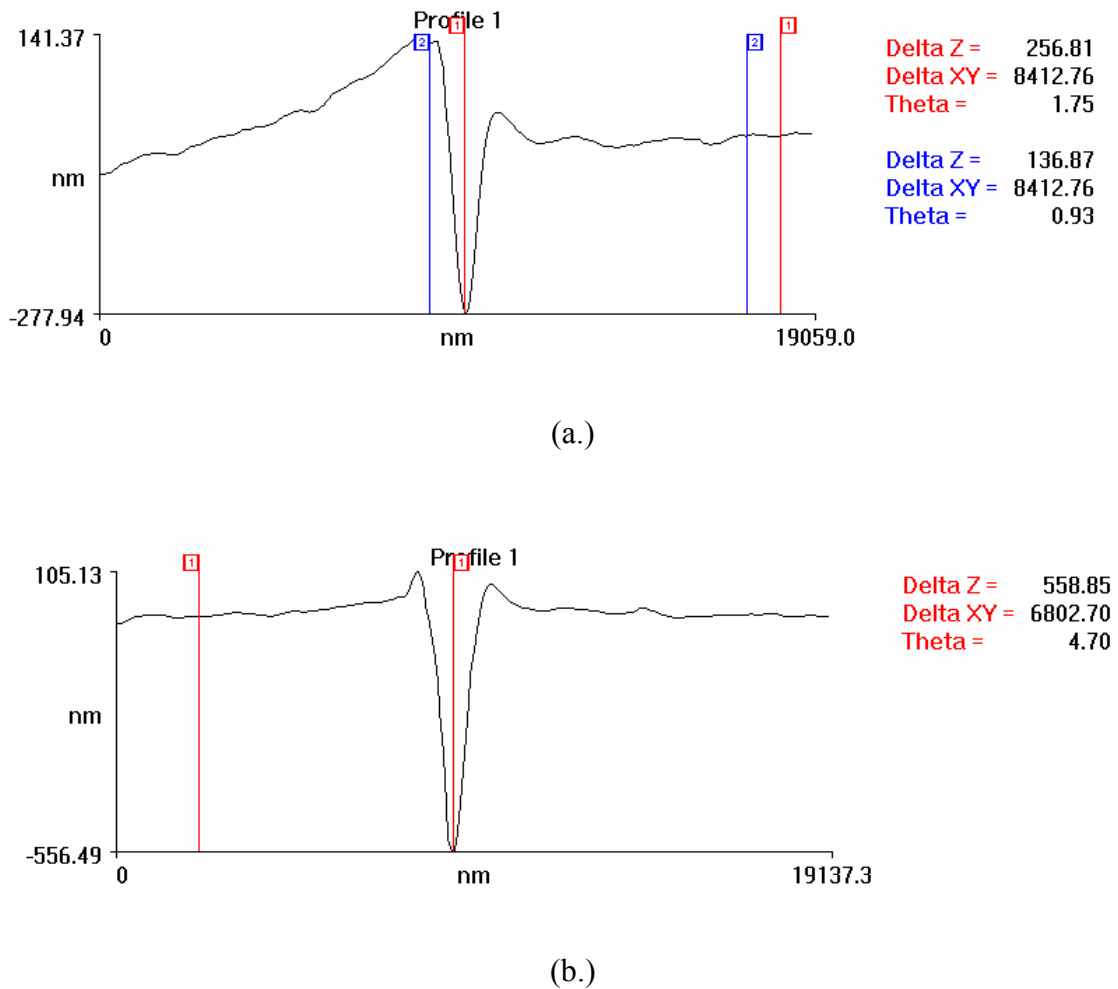


Figure 4.19. AFM profile of (a.) sharp and (b.) blunt scribe on (100) in [011] direction in ductile regime.

Figure 4.20 shows the depths of cuts for both sharp and blunt geometries as a function of applied load. There seemed to be a steady increase of depth of cut for the sharp indenter as load increased. The depth of cut for the blunt geometry however would spike from a couple hundred nanometers to several microns with the onset of fracture as large amounts of material were removed by fracture.

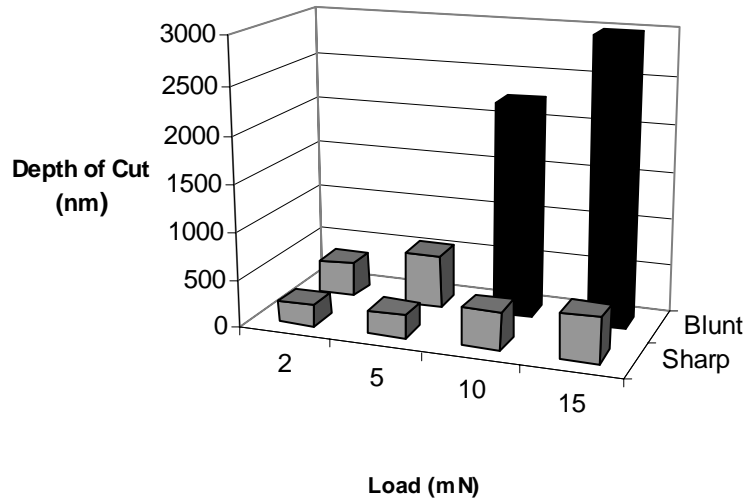


Figure 4.20. Effect of Sharp vs. Blunt geometry on depth of cut for (100)[011]. The black bars indicate the presence of heavy fracture.

(111)[1-10] Figure 4.21 and 22 are optical micrographs of scribes made in the load range tested for scribing in the [1-10] direction on (111) samples for sharp and blunt geometries, respectively. In Figure 4.21, the scribes appear to be similar in nature to those seen in Figure 4.7a (ductile- no debris) within the ductile regime (1-6g applied load.) SEM and AFM images of a scribe made in the ductile regime with the sharp geometry appear in Figures 4.23(a.) and (b.). No debris is present, and no chipping is apparent until the fracture threshold which occurs around 7g of applied load. Above 6g of applied load, large, lateral crack-induced pullouts appear periodically along the scribe trace (similar to Figure 4.7c.) In Figure 4.22, the scribes appear to be similar in nature to those seen in Figure 4.7b (ductile- plastic debris) within the load range tested. SEM and AFM images for a scribe representative blunt geometry cutting in the ductile regime appear in Figures 4.24(a.) and (b.) The fracture threshold is out of the load range that could be tested with the experimental setup. The debris along the side appears plastic in nature and is present for all the loads tested. The geometric

dependency of the scribing behavior is similar to that seen when scribing in the [100] direction on a (100) wafer (Figures 9 and 10.)

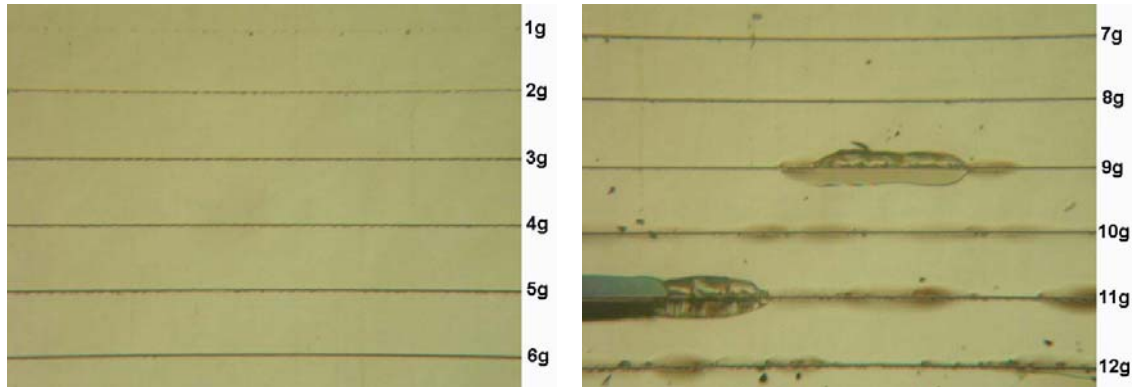


Figure 4.21. Optical micrograph of scribing range of (111)[1-10] for sharp geometry. Fracture threshold occurs at approximately 9g of applied load. (12-15g omitted for presentation.)

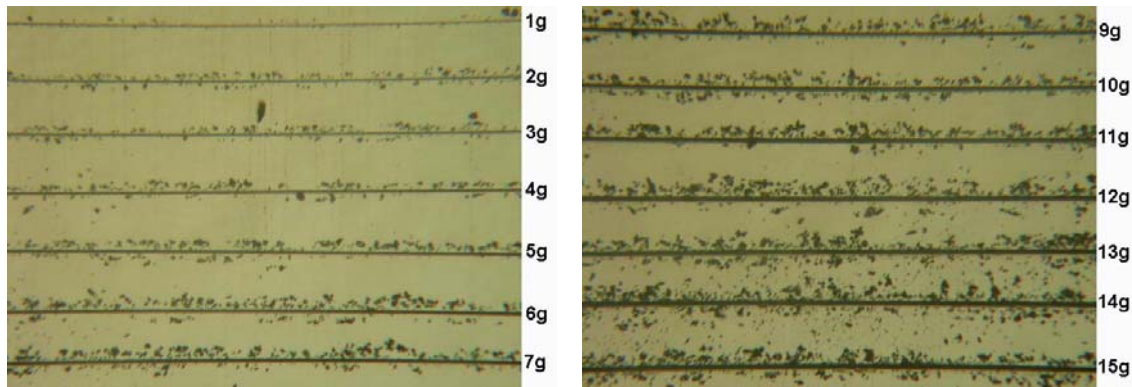


Figure 4.22. Optical micrograph of scribing range of (111)[1-10] for blunt geometry. Fracture threshold was not reached in the load range tested. Plastic debris is heavily present along the sides of the scribes. (8g omitted for presentation.)

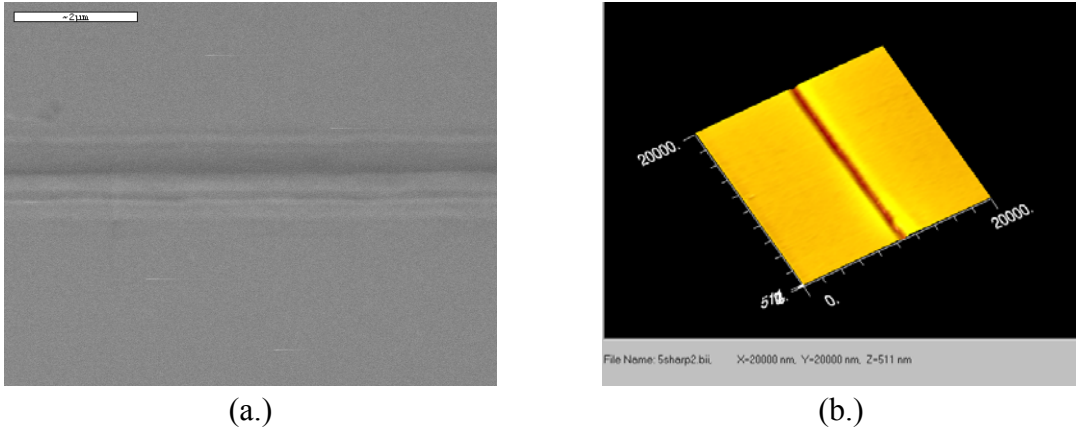


Figure 4.23. (a.) SEM and (b.) AFM image of sharp scribe for (111)[1-10] within the ductile regime. (a.) Bar = 2 μ m.

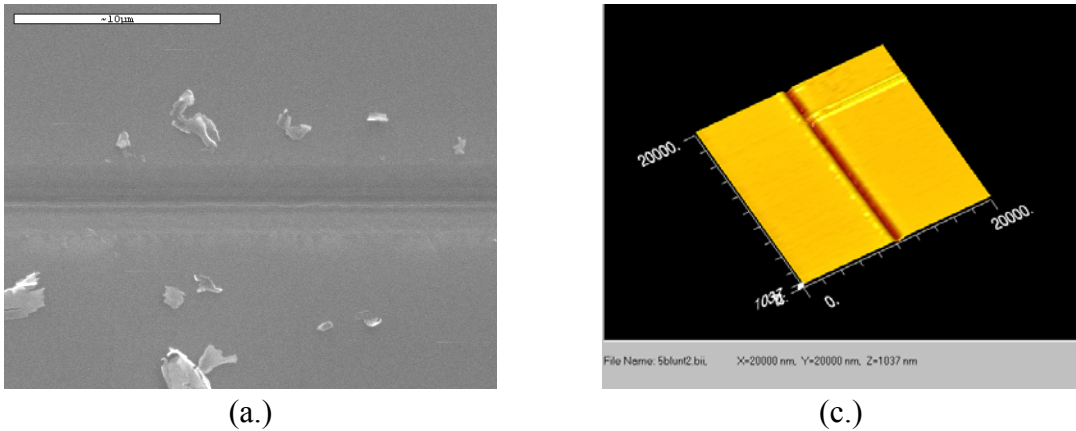


Figure 4.24. (a.) SEM and (b.) AFM image of blunt scribe for (111)[1-10] within the ductile regime. (a.) Bar = 2 μ m.

Figures 4.25(a.) and (b.) are profiles of scribes made in the ductile regime (5g loading) for both sharp and blunt geometries, respectively. These profiles are typical of those made in the ductile regime. AFM measurements taken on scribes made with the sharp geometry above the fracture threshold were performed in regions where pullouts had not occurred (the pullouts tended to be localized and there were regions unaffected by fracture.)

For the blunt geometry, depths of cut tended to be much greater than for sharp. Again, the profiles for the sharp geometry tended to have large “pile-ups” on the sides of the scribe trace measuring several hundred nanometers in height on some occasions. Scribing

with the blunt geometry tended to eliminate the appearance or reduce the height considerably of these features.

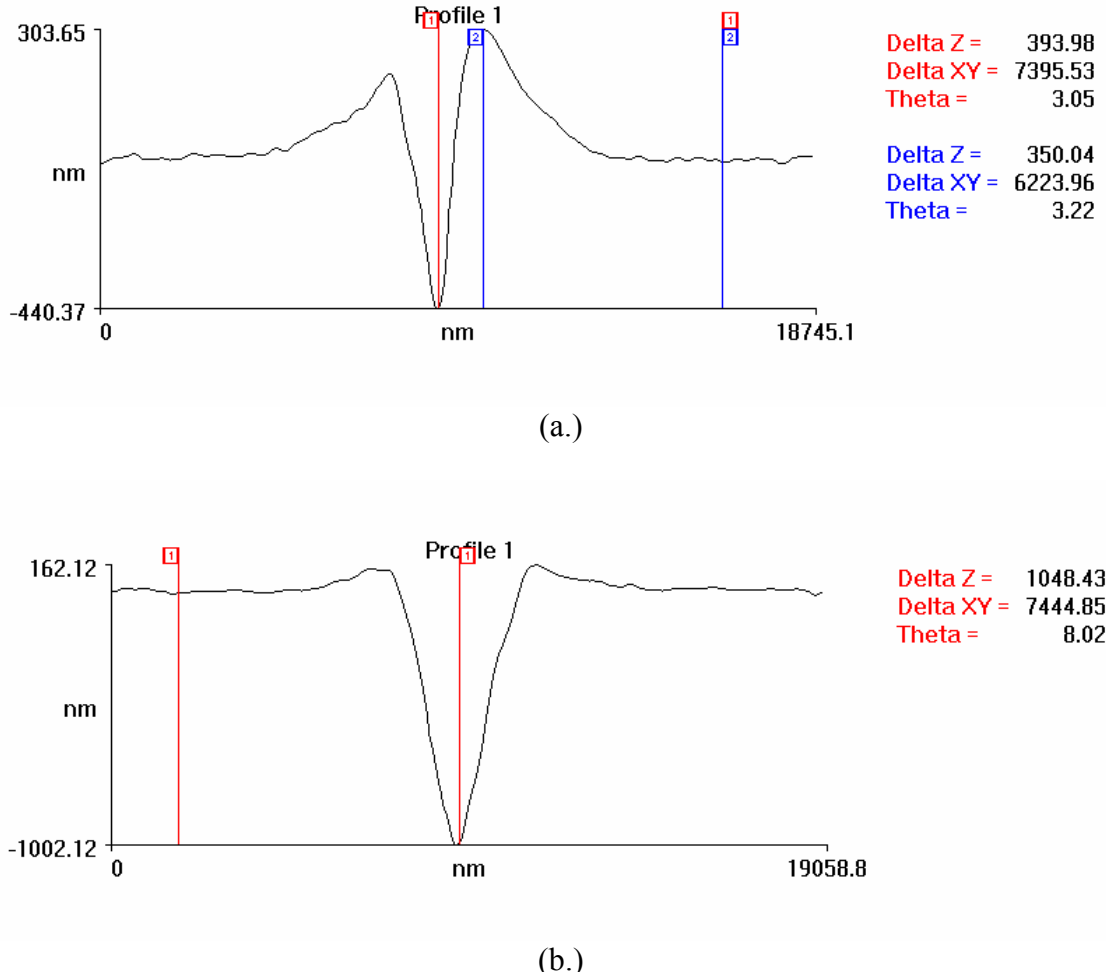


Figure 4.25. AFM profile of (a.) sharp and (b.) blunt scribe on (111) in [1-10] direction in ductile regime.

Figure 4.26 shows the depths of cuts for both sharp and blunt geometries as a function of applied load. There seemed to be a steady increase of depth of cut for both indenters as load increased.

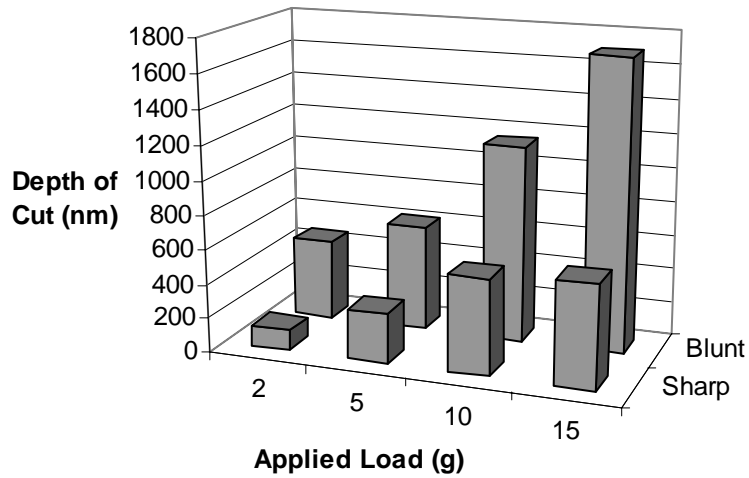


Figure 4.26. Effect of Sharp vs. Blunt geometry on depth of cut for (111)[1-10].

(111)[-1-12] Figure 4.27 and 28 are optical micrographs of scribes made in the load range tested for scribing in the [-1-12] direction on (111) samples for sharp and blunt geometries, respectively. In Figure 4.27, for sharp cutting, the scribes appear to be similar in nature to those seen in Figure 4.7a (ductile- no debris) within the ductile regime (1-15g applied load.) Such a scribe is shown in Figures 29(a.) and (b.) in SEM and AFM images. No debris is present, and no chipping is apparent until the fracture threshold which occurs around limitedly at 15g of applied load. Above 15g of applied load, large pull outs (similar to Figure 4.7c,) most likely due to lateral cracks reaching the surface, appear periodically along the scribe trace. For blunt cutting shown in Figure 4.28, scribes below the fracture threshold (characteristic of that in SEM and AFM images of Figure 30(a.) and (b.)) appear similar to that in Figure 4.b (ductile- plastic debris,) but with less debris than seen for the [1-10] scribing direction. The fracture threshold is relatively low, with the first sign of pitting appearing at 6-7g in a few areas and becoming more frequent as the load increases. The scribes are similar in nature to those seen in Figure 4.7d (fracture- small, disjunct pitting)

above the threshold. The pullouts are small, and the debris along the side appears crystalline in nature and is present where fracture occurred. The geometric dependency of the scribing behavior is similar to that seen when scribing in the [011] direction on a (100) wafer (Figures 4.15 and 4.16.)

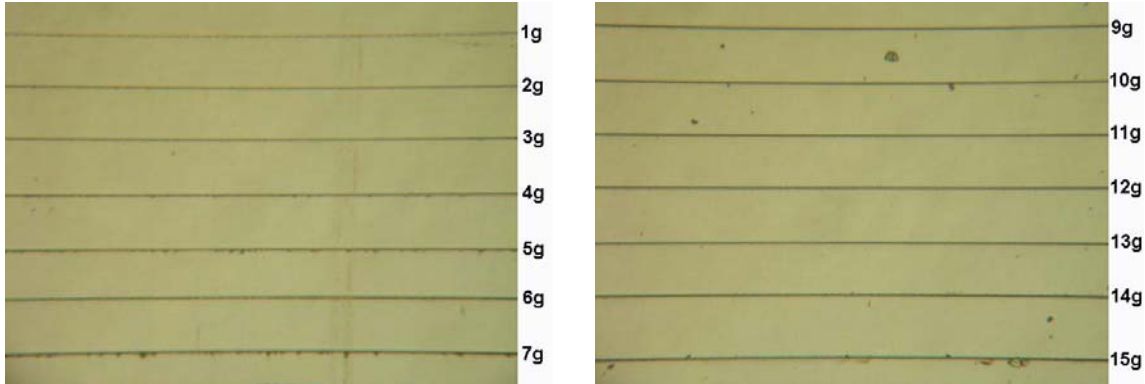


Figure 4.27. Optical micrograph of scribing range of (111)[-1-12] for sharp geometry. Fracture threshold occurs between 15-16g of applied load. (8g scribe omitted for presentation)

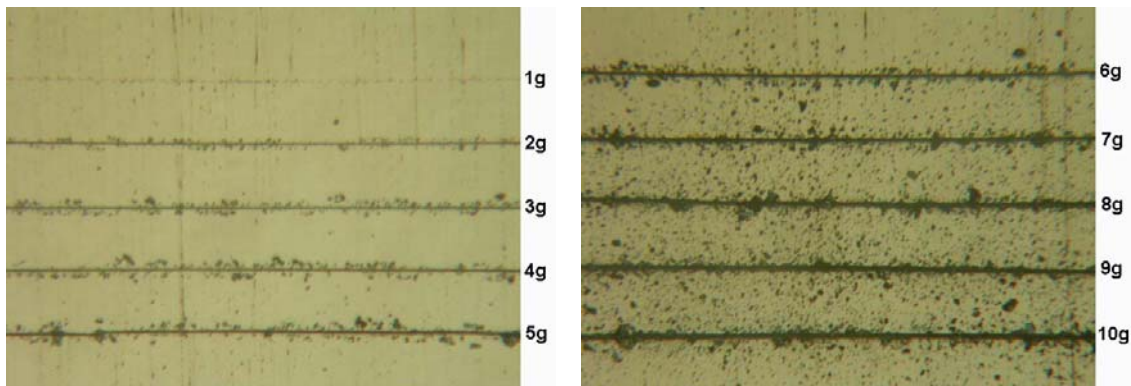


Figure 4.28. Optical micrograph of scribing range of (111)[-1-12] for blunt geometry. Fracture threshold occurs between 6-7g of applied load. Debris is plastic below the fracture threshold, changing to small crystalline fracture above it.

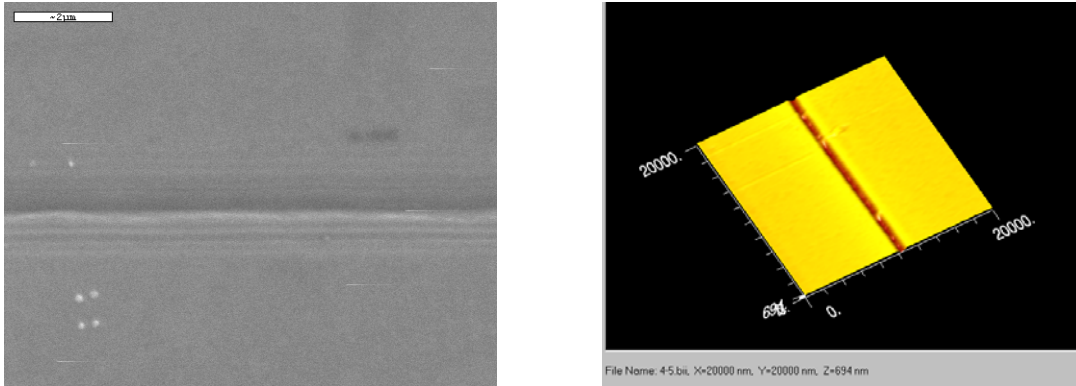


Figure 4.29. (a.) SEM and (b.) AFM image of sharp scribe for (111)[-1-12] within the ductile regime. (a.) Bar = 2 μ m

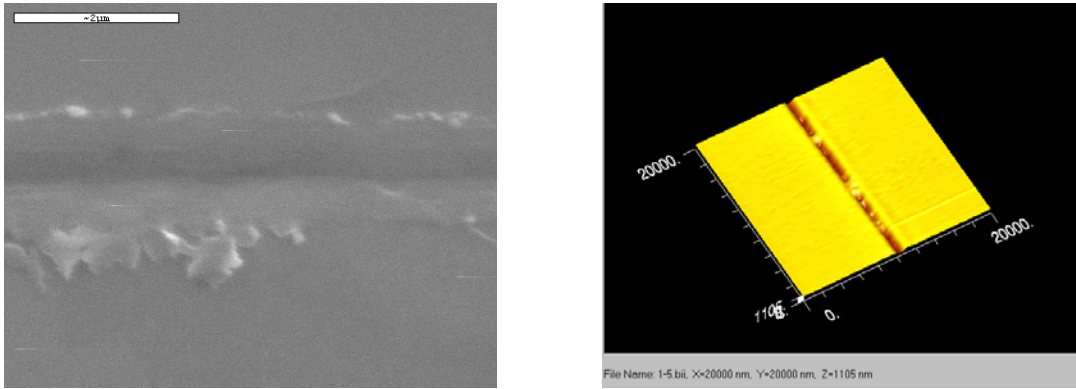


Figure 4.30. (a.) SEM and (b.) AFM image of blunt scribe for (111)[-1-12] within the ductile regime. (a.) Bar = 2 μ m

Figures 4.31(a.) and (b.) are profiles of scribes made in the ductile regime (5g loading) for both sharp and blunt geometries, respectively. These profiles are typical of those made in the ductile regime.

For the blunt geometry, depths of cut still tend to be much greater than for sharp within the ductile regime. Again, profiles for the sharp geometry tended to have large “pile-ups” on the sides of the scribe measuring several hundred nanometers in height on some occasions. Scribing with the blunt geometry tended to eliminate the appearance or reduce the height considerably of these features at low loads. At higher loads, this scribing direction

was easily fractured with the blunt geometry, effecting measurements by large removal of crystalline material.

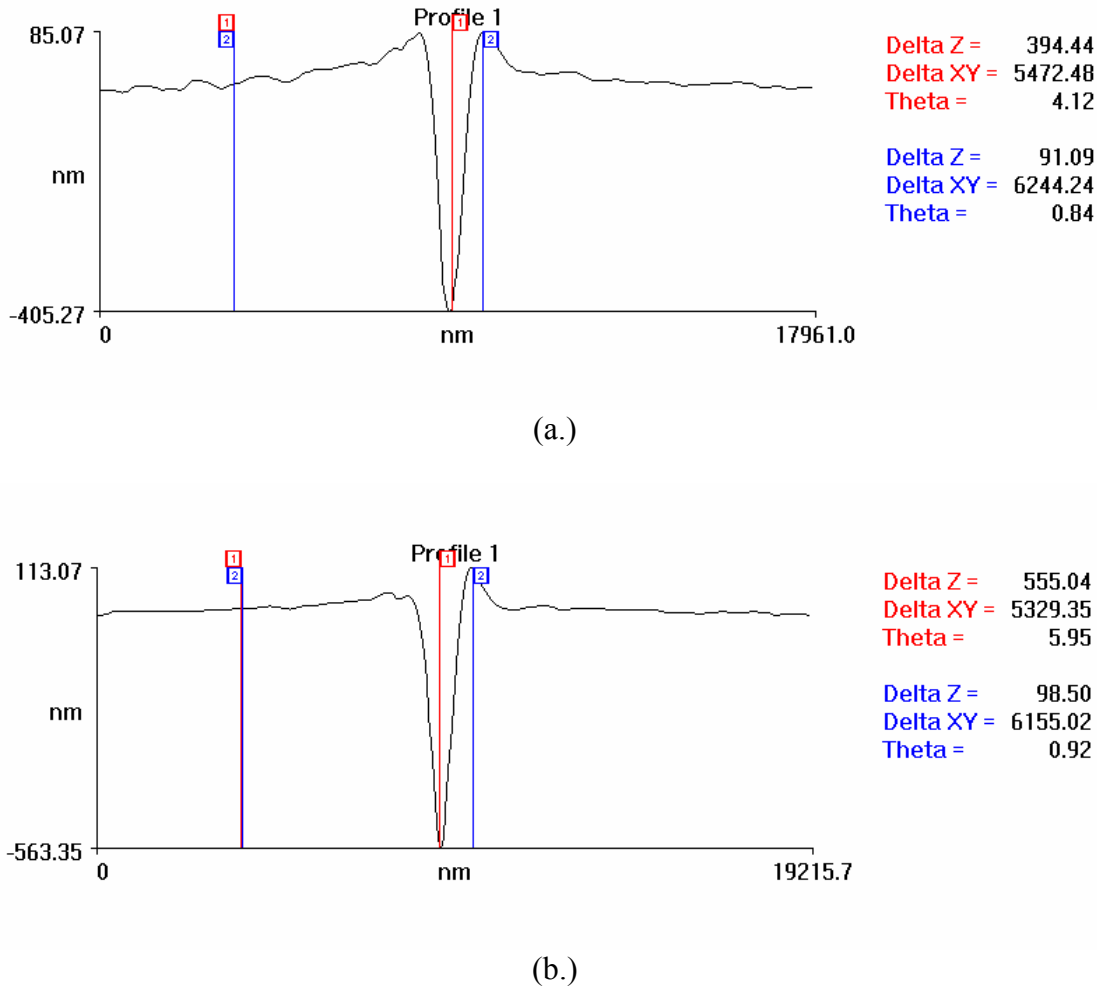


Figure 4.31. AFM profile of (a.) sharp and (b.) blunt scribe on (111) in [-1-12] direction in ductile regime.

Figure 4.32 shows the depths of cuts for both sharp and blunt geometries as a function of applied load. There seemed to be a steady increase of depth of cut for the sharp indenter as load increased. Similar to that seen for (100)[011], depth of cut for the blunt geometry however would spike from a couple hundred nanometers to several microns with the onset of fracture as large amounts of material were removed by fracture.

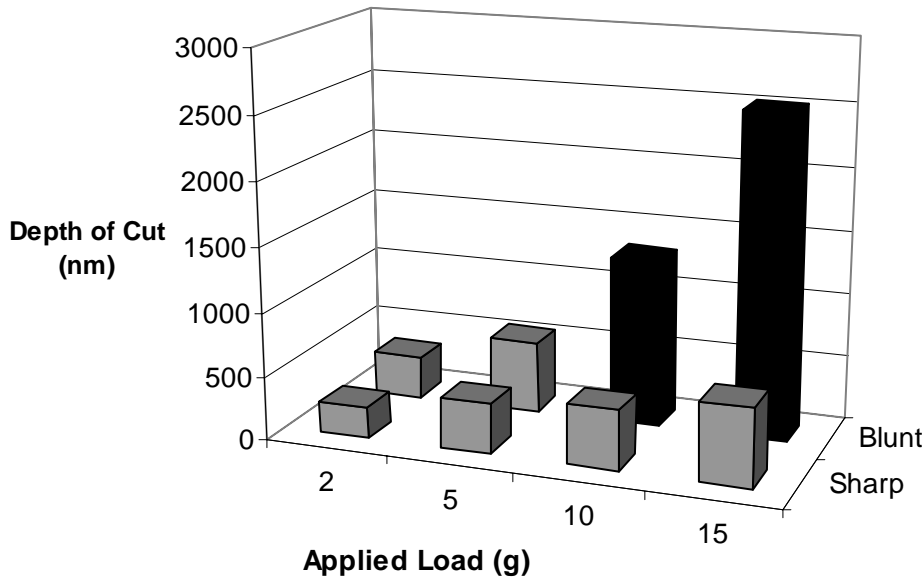


Figure 4.32. Effect of Sharp vs. Blunt geometry on depth of cut for (100)[-1-12]. The black bars indicate the presence of heavy fracture.

(111)[11-2] Figure 4.33 and 4.34 are optical micrographs of scribes made in the load range tested for scribing in the [11-2] direction on (111) samples for sharp and blunt geometries, respectively. (The [11-2] is the reverse translation of the [-1-12] direction, and due to a three-fold symmetry produces different scribing behavior.) In Figure 4.33, the scribes appear to be similar in nature to those seen in Figure 4.7a (ductile- no debris) within the ductile regime (1-7g applied load.) A typical scribe made within the ductile regime with the sharp geometry is shown in Figures 35(a.) and (b.) as an SEM and AFM image. No debris is present, and no chipping is apparent until the fracture threshold which occurs around limitedly at 8g of applied load. Above 8g of applied load, large pull outs, most likely due to lateral cracks reaching the surface, appear periodically along the scribe trace (similar to Figure 4.7(c.)). Upon close inspection of Figure 4.16, scribes below the fracture threshold with the blunt geometry (typical of that seen in SEM and AFM images in Figure 4.36(a.) and (b.)) appear similar to that in Figure 4.7(b.) (ductile- plastic debris,) but generating less debris than seen

for the [1-10] scribing direction (Figure 4.22.) The fracture threshold is relatively low, with the first sign of pitting appearing at 6-7g in a few areas and becoming more frequent as the load increases. The scribes are similar in nature to those seen in Figure 4.7c (fracture) above the threshold. The pullouts are considerably smaller than those seen in Figure 4.33. The debris along the side appears crystalline in nature and is present where fracture occurred. The geometric dependency of the scribing behavior is similar to that seen when scribing in the [011] direction on a (100) wafer (Figures 11 and 12) and [-1-12] on a (111) wafer, but with a lower fracture threshold than both.

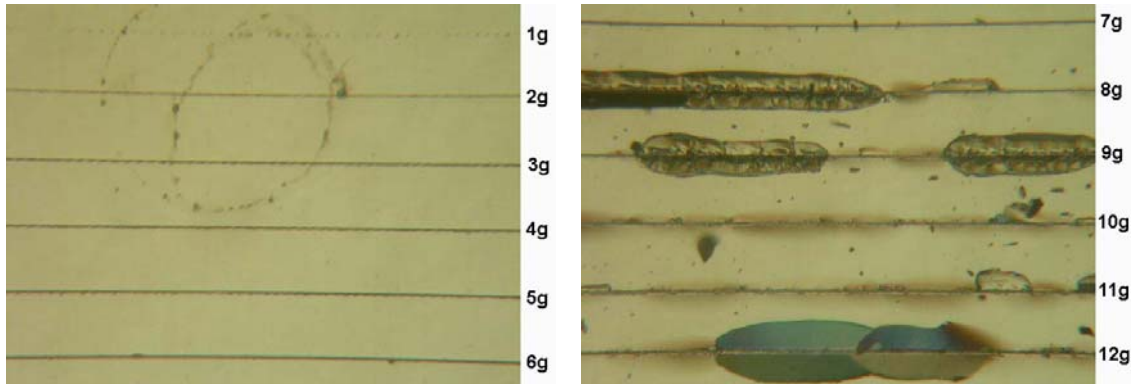


Figure 4.33. Optical micrograph of scribing range of (111)[11-2] for sharp geometry. Fracture threshold occurs at approximately 8g of applied load. (13-15g omitted for presentation.)

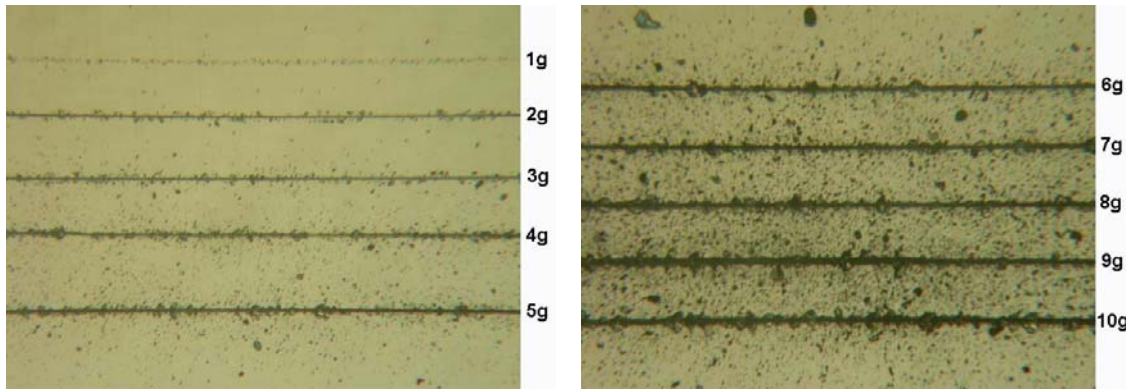


Figure 4.34. Optical micrograph of scribing range of (111)[11-2] for blunt geometry. Fracture threshold occurs around 5g of applied load. Debris is plastic below the fracture threshold, changing to small crystalline fracture above it.

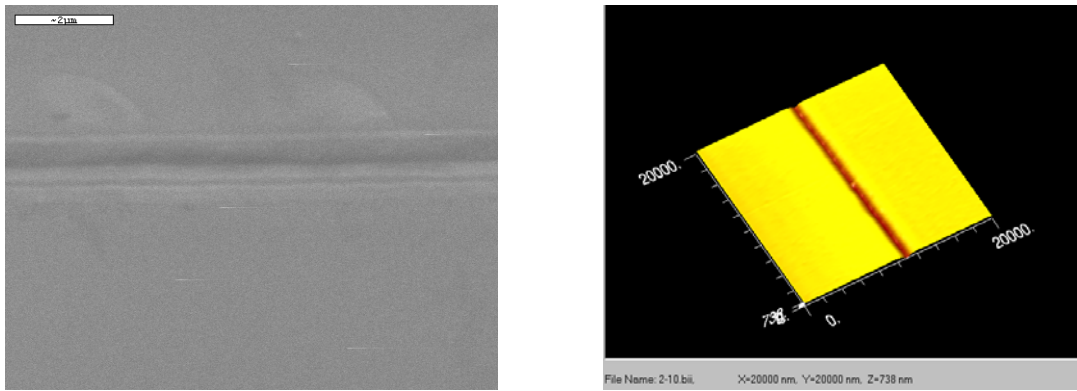


Figure 4.35. (a.) SEM and (b.) AFM image of sharp scribe for (111)[11-2] within the ductile regime. (a.) Bar = 2 μm .

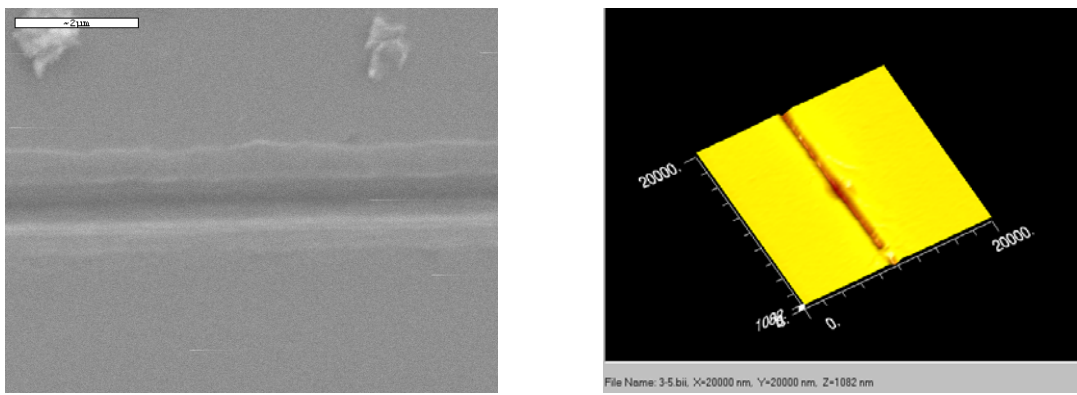
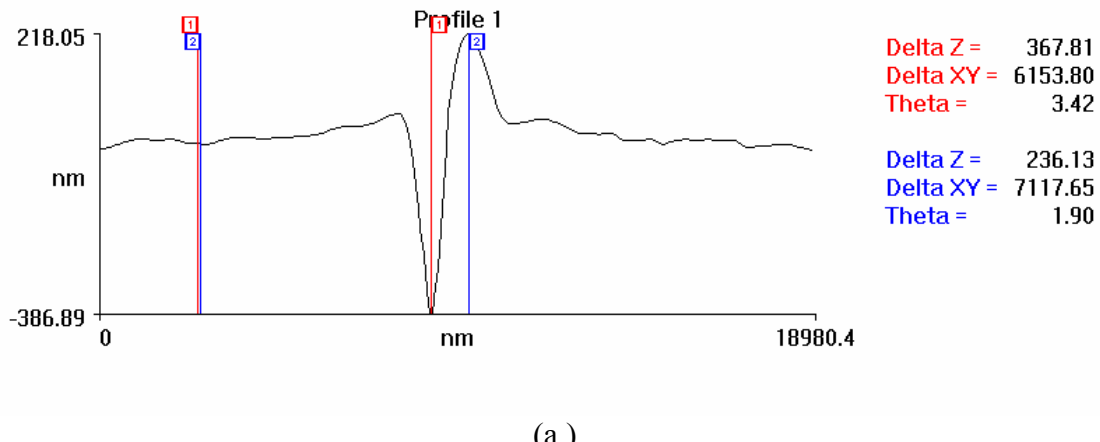


Figure 4.36. (a.) SEM and (b.) AFM image blunt scribe for (111)[11-2] within the ductile regime. (a.) Bar = 2 μm .

Figures 4.37(a.) and (b.) are profiles of scribes made in the ductile regime (5g loading) for both sharp and blunt geometries, respectively. These profiles are typical of those made in the ductile regime.

As seen for every direction tested, depths of cut still tend to be much greater than for the blunt geometry than the sharp within the ductile regime. Again, profiles for the sharp geometry tended to have large “pile-ups” on the sides of the scribe measuring several hundred nanometers in height on some occasions. It is a little less clear in Figure 4.36(b.) that scribing with the blunt geometry reduced the appearance of these features at low loads. At higher loads, this scribing direction was easily fractured with the blunt geometry, effecting measurements by large removal of crystalline material.



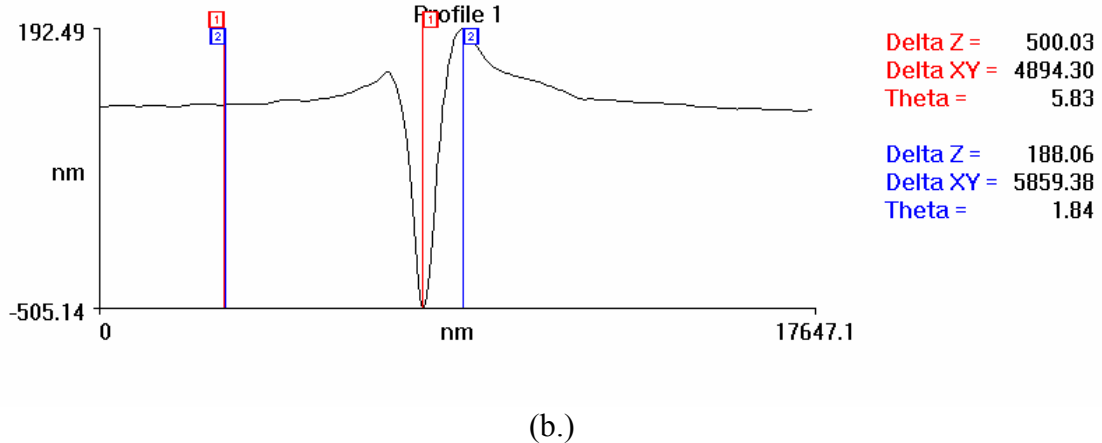


Figure 4.37. AFM profile of (a.) sharp and (b.) blunt scribe on (111) in [11-2] direction in ductile regime.

Figure 4.38 shows the depths of cuts for both sharp and blunt geometries as a function of applied load. There seemed to be a steady increase of depth of cut for the sharp indenter as load increased. Similar to that seen for (100)[011] and (111)[-1-12], depth of cut for the blunt geometry however would spike from a couple hundred nanometers to several microns with the onset of fracture as large amounts of material were removed by fracture.

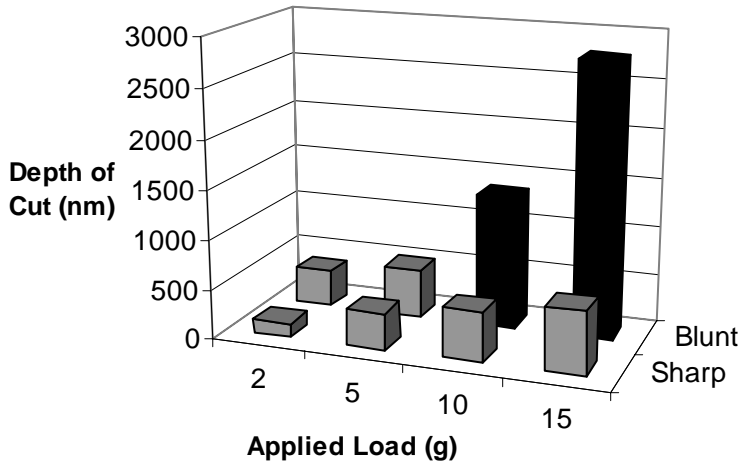


Figure 4.38. Effect of Sharp vs. Blunt geometry on depth of cut for (100)[11-2]. The black bars indicate the presence of heavy fracture.

To facilitate future discussion, it is important at this point to distinguish between what will be termed a “good cutting” direction and a “poor cutting” direction. A good cutting direction for a given tip geometry is that which creates ductile cutting with no fracture through a range of loads that is larger than alternate cutting directions for a given wafer. In other words, a good cutting direction will exhibit a larger fracture threshold than a bad cutting direction. On the other hand, a poor cutting direction will create fracture at a relatively low loads rather than a ductile response.

For example, given a (100) Si wafer, scribing with the blunt geometry interaction in the [100] direction created ductile scribes from 1-15g of applied load (a large range), and scribing in the [011] direction created ductile scribes from 1-4g of applied load (short range.) So for the blunt geometry, the [100] direction is termed good cutting and the [011] direction is termed poor cutting. Oppositely, scribing with the sharp geometry interaction would reverse the response making [011] a better cutting direction than [100].

A similar effect was noted in a (111) wafer; the blunt geometric interaction gave the opposite cutting behavior than that of the sharp. Tables 4.1 and 4.2 summarize the general cutting behavior as a function of direction and tip geometry on (100) and (111), respectively.

Table 4.1. Cutting behavior for (100) wafer

	Blunt	Sharp
[100]	Good	Poor
[011]	Poor	Good

Table 4.2. Cutting behavior for (111) wafer

	Blunt	Sharp
[1-10]	Good	Poor
[-1-12]	Poor	Good
[11-2]	Poor	Good

4.3.2 Residual Stress Generation and Measurement

As a scribe is created within the ductile regime the plastically generated material, whether driven by the β -tin metallic phase or not, is either removed (debris) or displaced into the surrounding elastic material. The material displaced into the surrounding elastic material creates residual stress on the surface of the sample. This stress is due to the elastic-plastic constraint associated with the expanding plastic material against the elastic boundary placing the boundary under large tensile stress. The difference in stress states between the opposing faces generates the deflection in the sample geometry. Figure 4.39 depicts the expansion of the constrained plastic zone, creating the resulting distortion of a flat wafer due to the difference in stress states between the two wafer faces. [2]

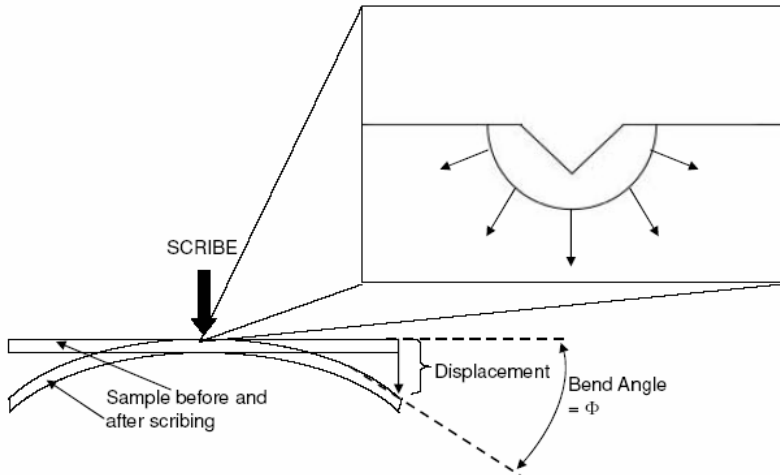


Figure 4.39. Illustration of expansion of constrained plastic zone and resulting deflection.

A model shown in previous work [54] to accurately reflect the bend effect generated by the line-force dipoles created from a scribe will be used to characterize residual stress in the single crystal silicon. A line-force dipole, shown in Figure 4.40, will be used to model the elastic-plastic deformation zone along a scribe path. The dipole forces act outward from the scribe trace since the surrounding elastic material is forced outward by the plastically deformed material region after unloading. The line-force dipole model was extended from a model created by Yoffe [22] in which orthogonal dipole forces acting on an elastic half space describe residual forces left by indentation. The line-force dipole model is derived by the superposition of the dipole “blister” fields proposed by Yoffe. Standard elasticity solutions [23] are used to obtain the line-force dipole stresses for a limiting case of infinitesimal dipole spacing. By applying the line-force dipole stresses to a beam bending problem the stresses will be then be approximated as a function of bend angle. The parameter derived from the bend effect model, force dipole strength is a direct measure of the magnitude of the residual stresses produced by scribing. The author refers the reader to the Appendix A for a paper outlining the derivation of the model.

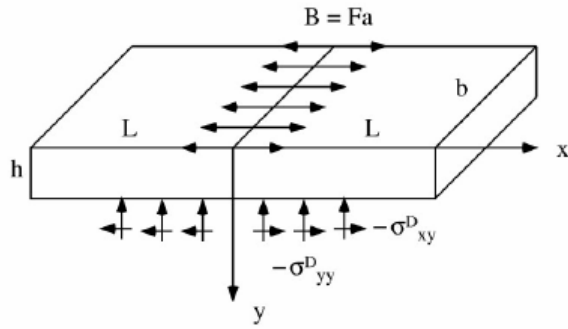


Figure 4.40. Line-force dipole model. [54]

From the reference in Appendix A equation 4.1 is used to obtain the residual stress parameter dipole strength B (N) from the angle of deflection ϕ (radians). Equation 4.1 is

$$\phi(X) = \frac{6B}{\pi Eh^2} f(X) \quad (4.1)$$

where $\phi(X)$ is bend angle (radians), B is dipole strength (N), E is elastic modulus (N/m^2) of the bend axis, h is sample thickness, and $f(X)$ is the bend-angle function. The bend-angle function can be approximated as $\pi/2$ because the bending effect appears as a localized “hinge” Equation 4.1 becomes

$$B = \frac{\phi(X) * Eh^2}{3} \quad (4.2)$$

As the elastic modulus for single crystal silicon is directionally dependent for a (100) wafer, selection of the proper elastic modulus is important in calculating the dipole strength. For calculations on samples made from a (100) the correct direction (bend axis) for determining modulus was perpendicular to the scribe direction as seen in figure 4.40. Due to the four-fold symmetry, the modulus in the scribing direction is the same as that of the bend axis direction. (111) wafers are isotropic in nature so the elastic modulus is the same in each

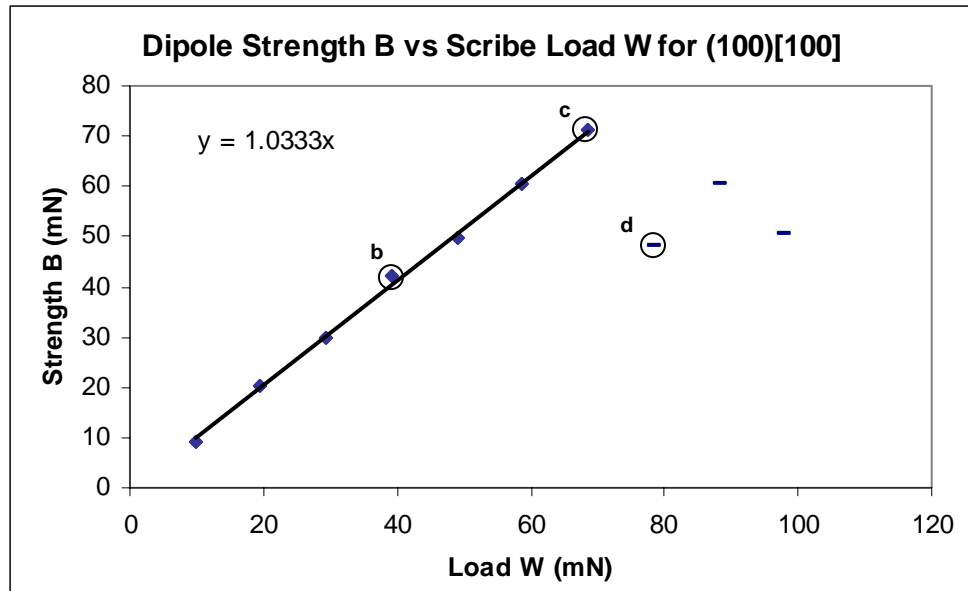
direction. Table 4.3 lists the various moduli used for the combinations of wafer orientation and scribing direction tested.

Table 4.3. Elastic moduli used for determining dipole strength B from equation 4.2.

Orientation/Scribe Direction	Elastic Modulus
(100)[100]	169.20 Gpa
(100)[011]	130.40 Gpa
(111)[1-10]	169.20 GPa
(111)[11-2]	169.20 Gpa
(111)[-1-12]	169.20 Gpa

Scribing with the sharp geometry seemed to produce the most interesting results. Within the ductile regime, scribes produced with the sharp geometry show a linear dependence of the parameter dipole strength B, which is the measure of residual stress, on the applied load W. Upon initiation of fracture however, dipole strength no longer showed any direct correlation with applied load. The resultant dipole strength would drop from the expected trend. This seemed to be true for each direction tested. Each direction was tested with a brand new tip, with the tool tip well aligned in the scribing direction.

Figures 4.41-45(a.) show the correlation of dipole strength B to applied load W for the various combinations of scribing direction and wafer orientation tested. (Parentheses indicate wafer orientation and brackets indicate scribing direction) The diamonds indicate loads at which the scribes appeared to have negligible fracture damage. The dashes indicate loads at which considerable fracture was seen. Figures 4.41-45(b.), (c.) and (d.) are micrographs of the produced scribes corresponding to the encircled points on their respective figures. These are points of interest including ductile regime, sub- fracture threshold, and fracture. The intercept of the trend lines in each figure has been forced to zero (there should be no stress with zero load applied.)

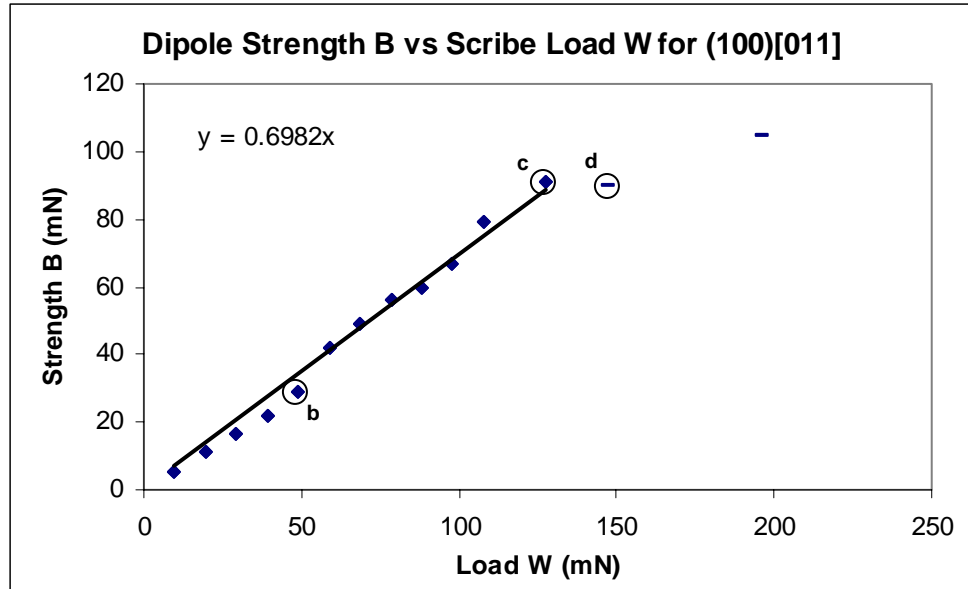


(a.) Dipole Strength B vs Scribe Load W. Diamonds indicate no sign of fracture (purely ductile response) while dashes indicate presence of fracture.



Figure 4.41. (a.) Graph of Dipole Strength B vs Scribe Load W for (100)[100] and (b.-d.) Micrographs corresponding to points encircled in (a.)

For scribing with the sharp geometry in the [100] direction on a (100) wafer, ductile cutting was seen until fracture initiation at around 80 mN (8g) of applied load. Within the ductile regime, the dipole strength scaled directly with applied load until fracture.

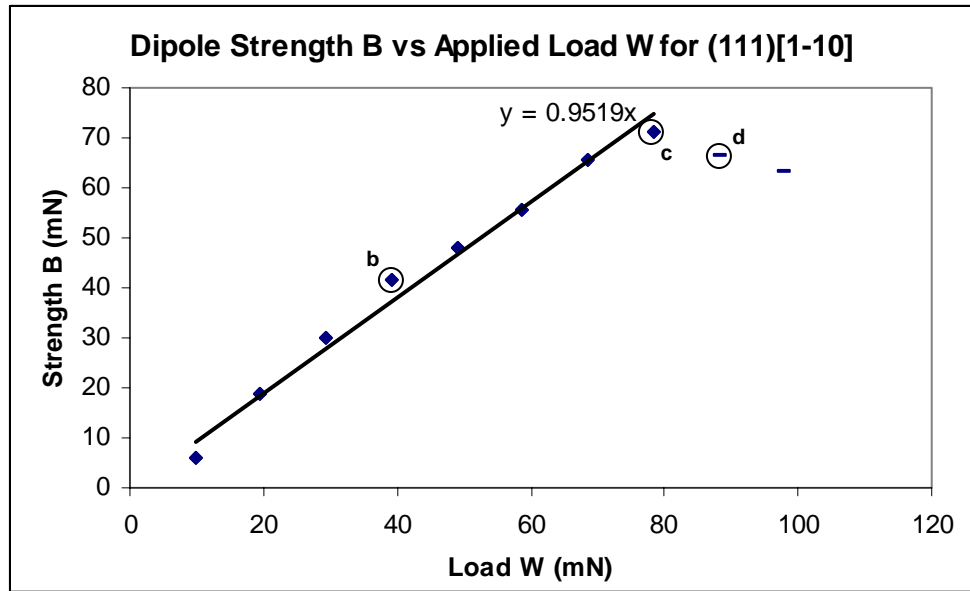


(a.) Dipole Strength B vs Scribe Load W. Diamonds indicate no sign of fracture (purely ductile response) while dashes indicate presence of fracture.



Figure 4.42. (a.) Graph of Dipole Strength B vs Scribe Load W for (100)[011] and (b.-d.) Micrographs corresponding to points encircled in (a.)

For scribing with the sharp geometry in the [011] direction on a (100) wafer, ductile cutting was seen until fracture initiation at around 150 mN (13g) of applied load. Similarly, the dipole strength scaled directly with applied load until fracture within the ductile regime.



(a.) Dipole Strength B vs Scribe Load W. Diamonds indicate no sign of fracture (purely ductile response) while dashes indicate presence of fracture.

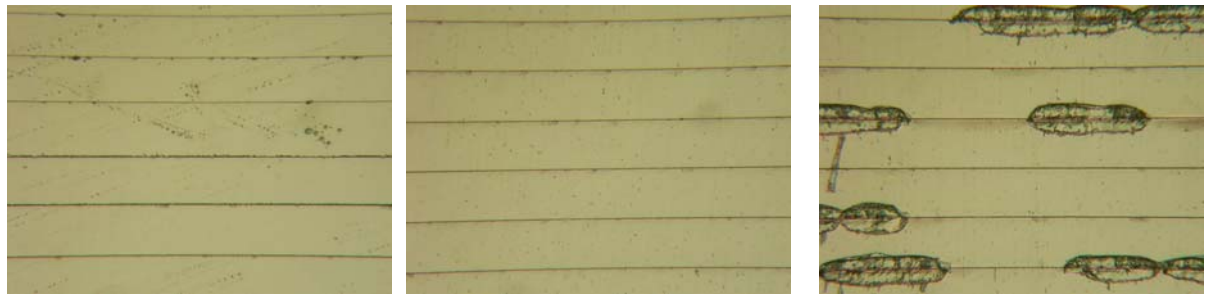
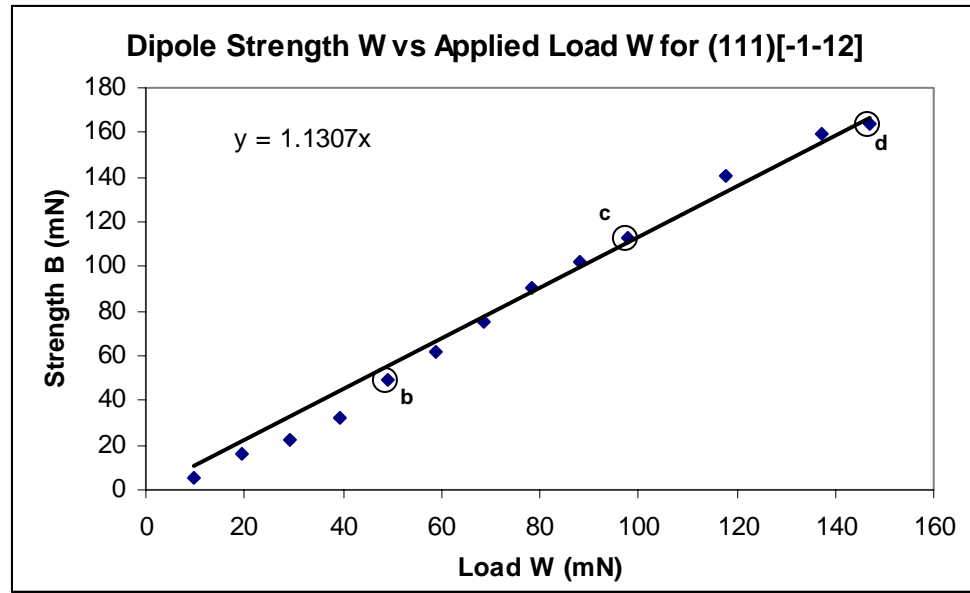


Figure 4.43. (a.) Graph of Dipole Strength B vs Scribe Load W for (111)[1-10] and (b.-d.) Micrographs corresponding to points encircled in (a.)

For scribing with the sharp geometry in the [1-10] direction on a (111) wafer, ductile cutting was seen until fracture initiation at around ~90 mN (9g) of applied load. Again, the dipole strength scaled directly with applied load until fracture within the ductile regime.



(a.) Dipole Strength B vs Scribe Load W. Diamonds indicate no sign of fracture (purely ductile response) while dashes indicate presence of fracture.



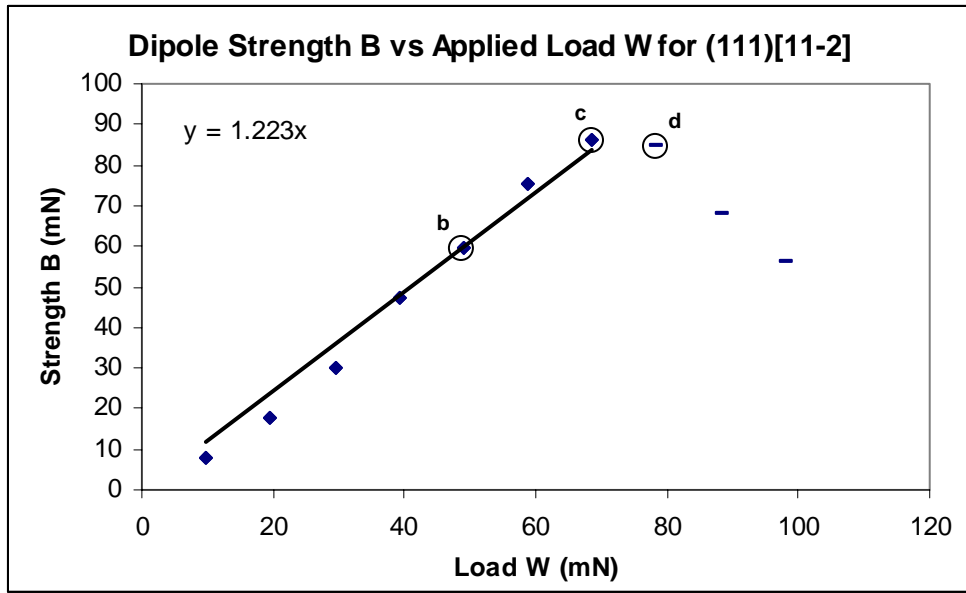
(b.) Ductile (50 mN)

(c.) Ductile (100 mN)

(d.) Approaching fracture threshold (~150 mN)

Figure 4.44. (a.) Graph of Dipole Strength B vs Scribe Load W for (111)[-1-12] and (b.-d.) Micrographs corresponding to points encircled in (a.)

For scribing with the sharp geometry in the [-1-12] direction on a (111) wafer, ductile cutting was seen throughout the load range tested. Negligible fracture was seen at 150mN (15g.) The fracture threshold is thought to be slightly above 150mN but was out of the test range. Again, the dipole strength scaled directly with applied load within the ductile regime.



(a.) Dipole Strength B vs Scribe Load W. Diamonds indicate no sign of fracture (purely ductile response) while dashes indicate presence of fracture.

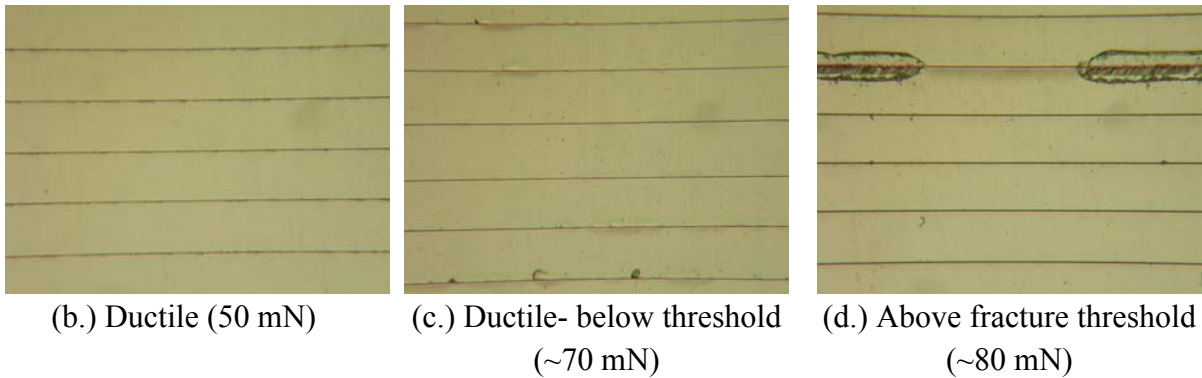
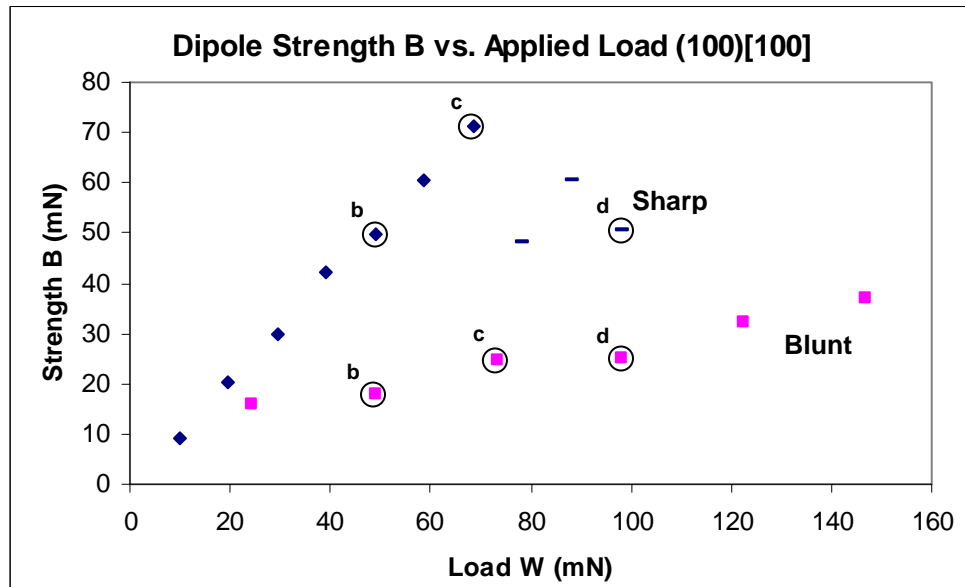


Figure 4.45. (a.) Graph of Dipole Strength B vs Scribe Load W for (111)[11-2] and (b.-d.) Micrographs corresponding to points encircled in (a.)

For scribing with the sharp geometry in the [11-2] direction on a (111) wafer, ductile cutting was seen until fracture initiation at around ~80 mN (8g) of applied load. As with each of the directions tested, the dipole strength scaled directly with applied load until fracture within the ductile regime.

The fracture threshold for each scribing direction as noted in the bend effect experiments matched up well with the approximate values found during the material response experiments.

Figures 4.46-48(a.) compare dipole strength B for sharp versus blunt cutting for selected crystal orientation/cutting direction combinations. Figures 4.46-48(b.), (c.) and (d.) are optical micrographs of the produced scribes corresponding to the encircled points on their respective figures. These are points of interest including ductile regime, sub-fracture threshold, and fracture. Figures 4.46 and 4.47 are for the two combinations of crystal orientation/cutting direction of those tested which produce similar material response to the cutting geometry parameter. Both combinations produced good cutting in the blunt direction and poor cutting in the sharp direction. Figure 4.48 is for one of the three other combinations of those tested that produced poor cutting in the blunt direction and good cutting in the sharp direction.



(a.) Dipole Strength B vs Scribe Load W. Diamonds indicate no sign of fracture (purely ductile response) while dashes indicate presence of fracture.

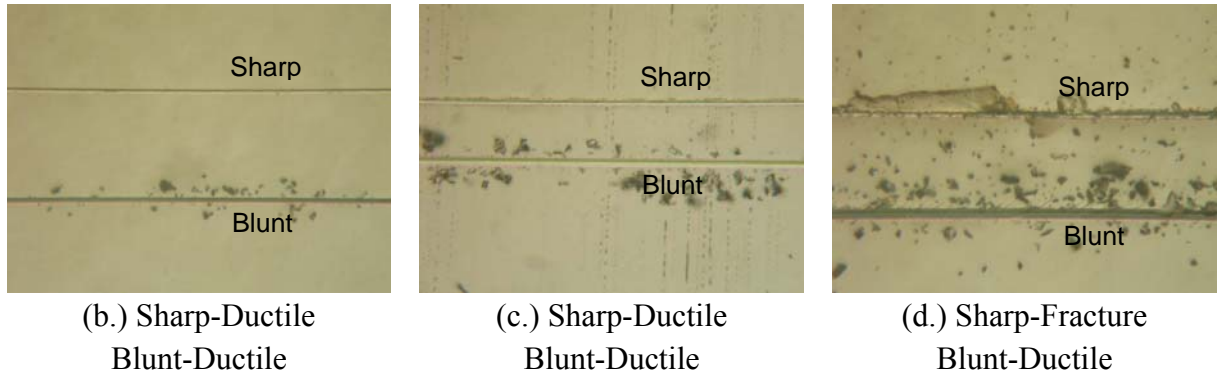
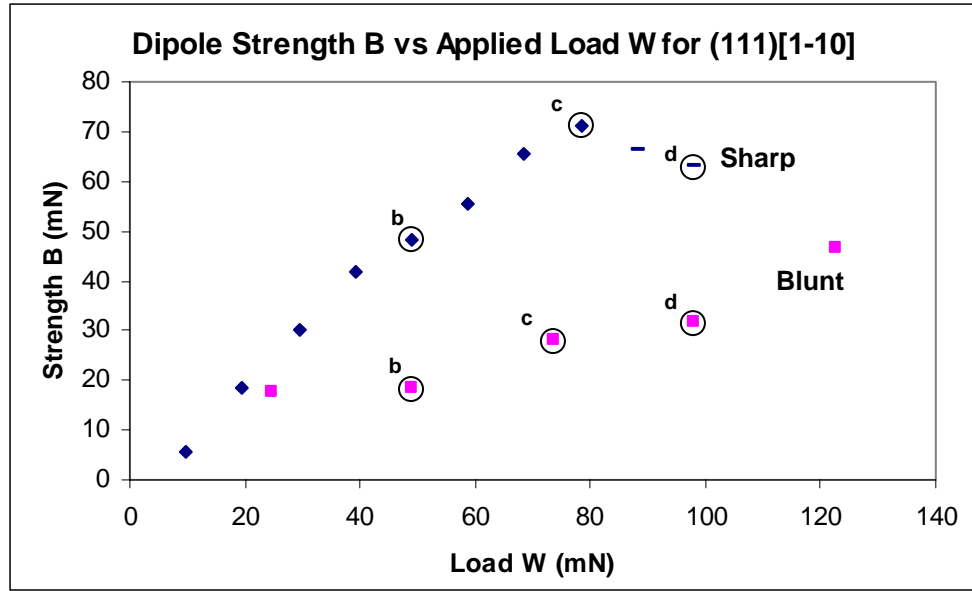
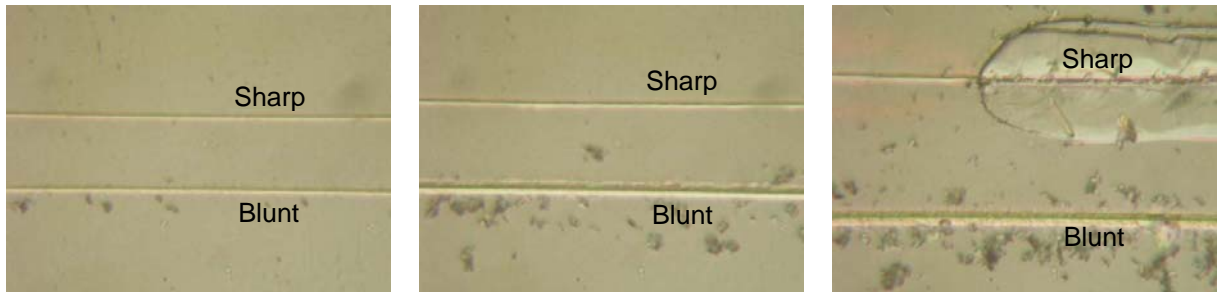


Figure 4.46. (a.) Graph of Dipole Strength B vs Scribe Load W comparing residual stress of sharp and blunt cutting for (100)[100] and (b.-d.) Micrographs corresponding to points encircled in (a.)

For (100)[100], scribing in the sharp direction created poor cutting behavior (a small ductile range) while scribing in the blunt direction created good cutting behavior (a large ductile range.) Sharp cutting produced a noticeably linear response in W vs. B within the ductile regime. Blunt cutting produced a similar linear response within the ductile regime, but the magnitude of the dipole strength is considerably less for similarly applied load.



(a.) Dipole Strength B vs Scribe Load W. Diamonds indicate no sign of fracture (purely ductile response) while dashes indicate presence of fracture.



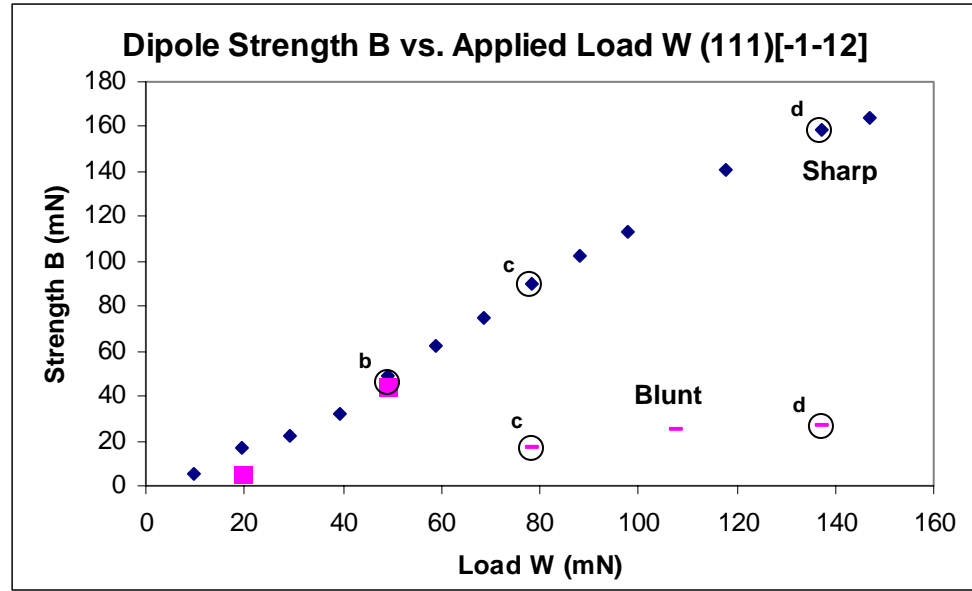
(b.) Sharp-Ductile
Blunt-Ductile

(c.) Sharp-Ductile
Blunt-Ductile

(d.) Sharp-Fracture
Blunt-Ductile

Figure 4.47. (a.) Graph of Dipole Strength B vs Scribe Load W comparing residual stress of sharp and blunt cutting for (111)[1-10] and (b.-d.) Micrographs corresponding to points encircled in (a.)

Similarly, for (111)[1-10], scribing in the sharp direction created poor cutting behavior (a small ductile range) while scribing in the blunt direction created good cutting behavior (a large ductile range.) Sharp cutting produced a noticeably linear response in W vs. B within the ductile regime. Blunt cutting produced a similar linear response within the ductile regime, but the magnitude of the dipole strength is considerably less for similarly applied load.



(a.) Dipole Strength B vs Scribe Load W. Diamonds indicate no sign of fracture (purely ductile response) while dashes indicate presence of fracture.

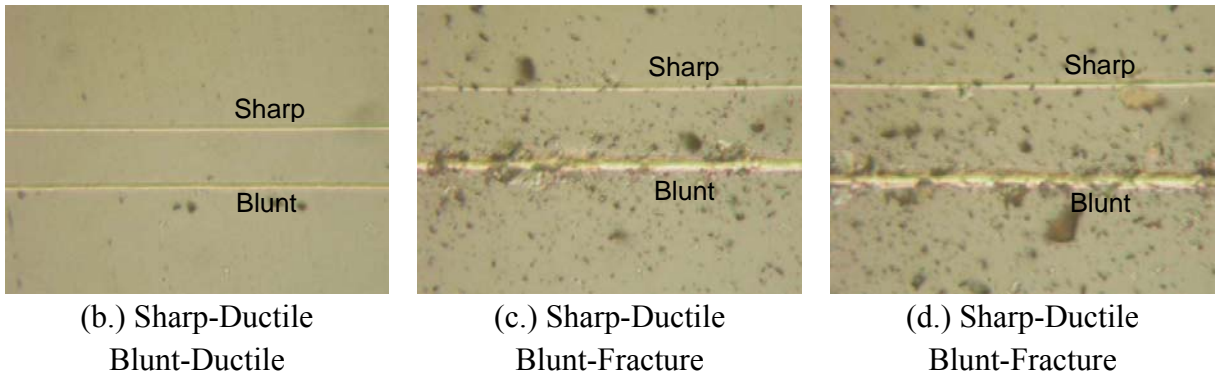


Figure 4.48. (a.) Graph of Dipole Strength B vs Scribe Load W comparing residual stress of sharp and blunt cutting for (111)[-1-12] and (b.-d.) Micrographs corresponding to points encircled in (a.)

Oppositely, for (111)[-1-12], scribing in the sharp direction created good cutting behavior (a large ductile range) while scribing in the blunt direction created poor cutting behavior (a small ductile range.) Sharp cutting produced a noticeably linear response in W vs. B within the ductile regime. It cannot be discerned from two points whether blunt cutting produced a similar linear response within the ductile regime; however the dipole strength B does increase with increasing applied load W for points in the ductile regime. With the onset

of fracture the magnitude of the dipole strength B dropped considerably and showed no observable dependence on the applied load W .

4.3.3 Raman Measurements of Scribe Regions and Debris

Raman was performed on scribes made with both geometries, showing sign of a peak that may correspond to a phase thought to be indicative of HPPT-induced plasticity. Figure 4.49 and 4.50 show typical Raman scans taken around the ductile scribe region for blunt and sharp scribes respectively. The scans were taken from outside of the scribe across to the center. These scans seemed to be typical of all those taken of the scribes made in the ductile regime, independent of orientation or scribing direction. Those presented here are for [100] direction cutting on a (100) wafer within the ductile regime.

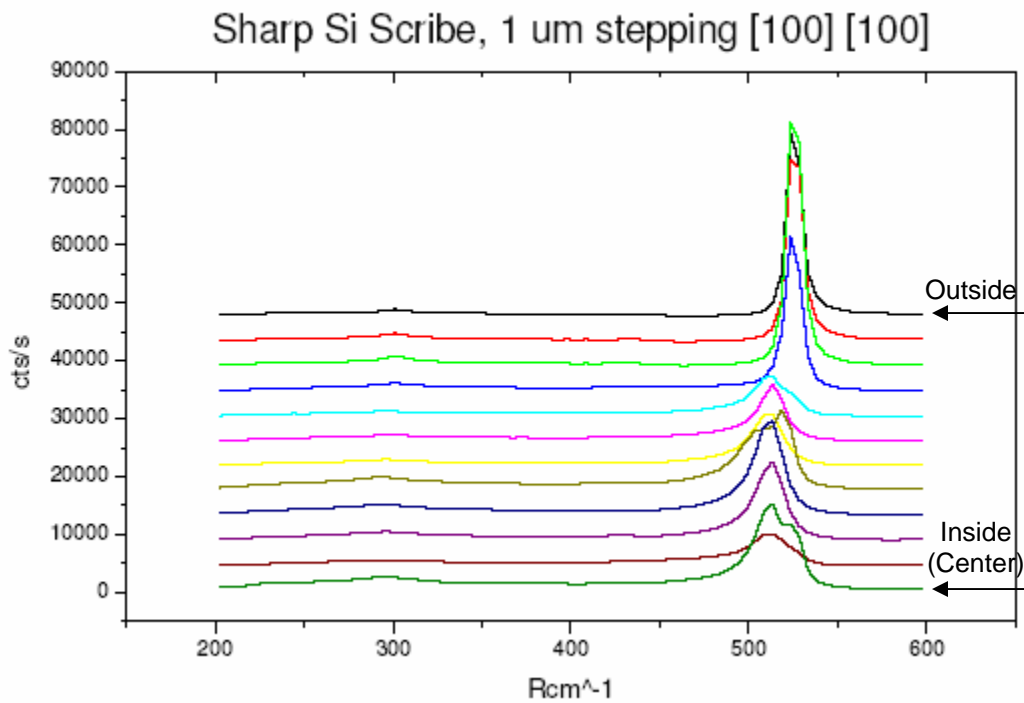


Figure 4.49. Typical Raman scans taken from the outside to the center of scribe region for the sharp geometry interaction on Si.

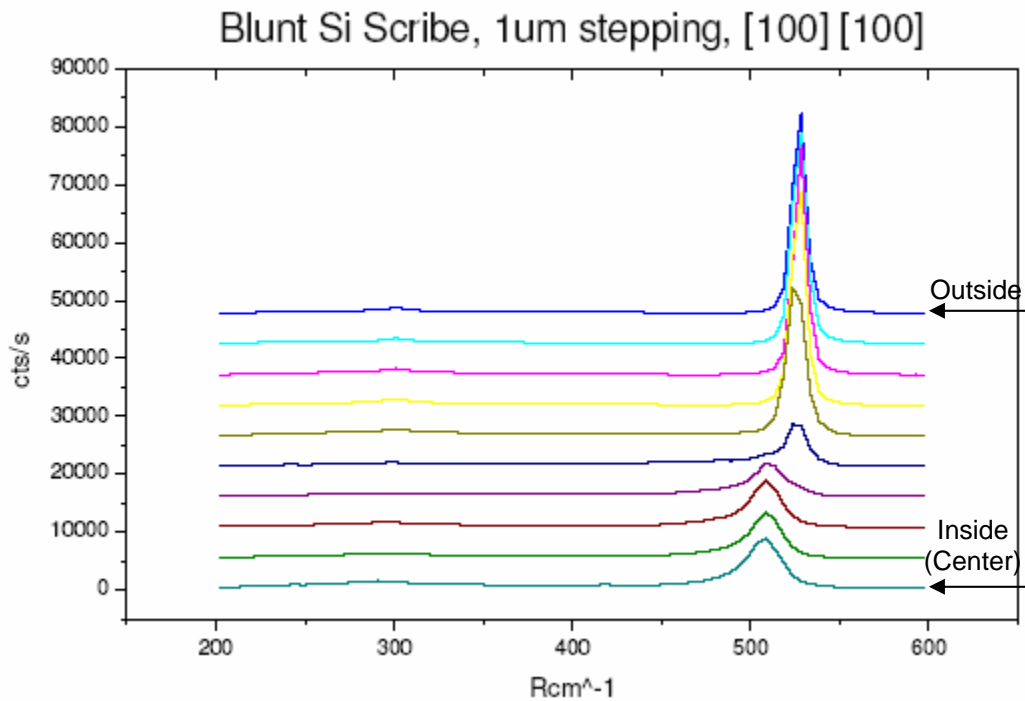


Figure 4.50. Typical Raman scans taken from the outside to the center of scribe region for the sharp geometry interaction on Si.

A peak shifted approximately centered on about 510 Rcm^{-1} (about $10\text{-}12 \text{ Rcm}^{-1}$ from the 521 Rcm^{-1} dc Si peak) consistently appears for scans taken within the scribe region perhaps indicating the presence of either dc Si nanocrystals under tensile stress within a less dense amorphous matrix or that of Si-IV, a meta stable crystalline phase.

A Raman scan of debris generated from blunt cutting in the ductile regime yielded the results shown in Figure 5.51(a.) at different laser level power. Figure 5.51(b.) shows the peak positions as a function of input power. At first thought to be a sign of nanocrystalline Si in an amorphous matrix, the results were shown to be heating effect as the peak shifted back towards 521 Rcm^{-1} when the power level was reduced.

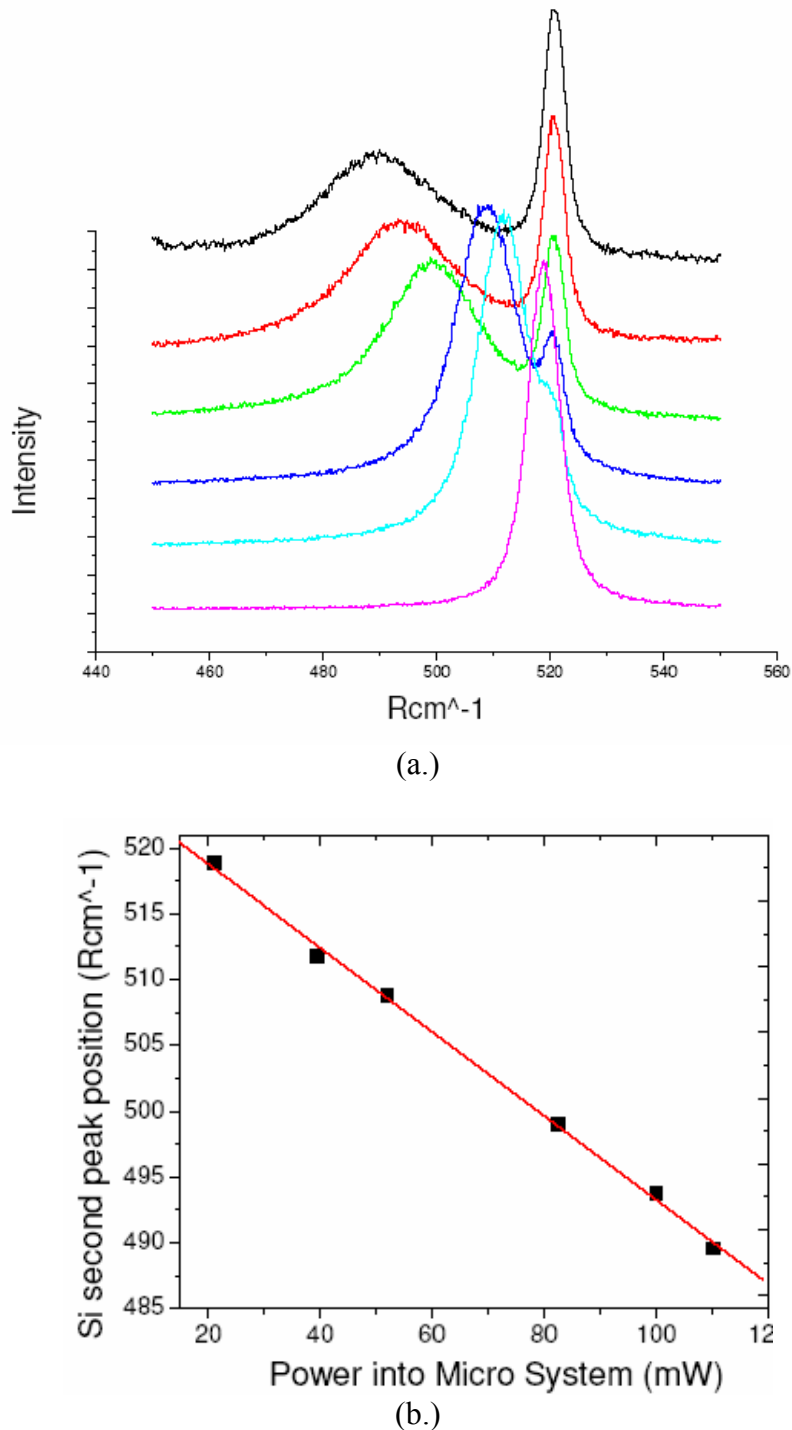


Figure 4.51. (a.) Raman spectra of Si debris taken at various power levels (decreasing from top) and (b.) graph of power level versus peak postion.

4.4 Discussion

4.4.1 Material Response to Scribing

Each crystallographic direction tested displayed some plasticity in scribing experiments at low loads. Ductile cuts made with the sharp geometry were all observed to generate no debris, a smaller depth of cut, and the presence of large pile ups along the sides of the scribe trace. By increasing the load applied to the tip, the dipole strength would increase linearly until a limit was reached. Because no material is removed it is assumed that the plastically generated material is fully pushed into the surrounding elastic matrix and constrained resulting in residual stress. The nature of the sharp geometry (picture a boat hull slicing through water) displaces the material in a “spreading” manner, perhaps driving flow of the plastic material into the surface and around the indenter (pile ups.) An illustration of the speculated profile of a scribe made with sharp indenter within ductile regime is shown in Figure 4.52.

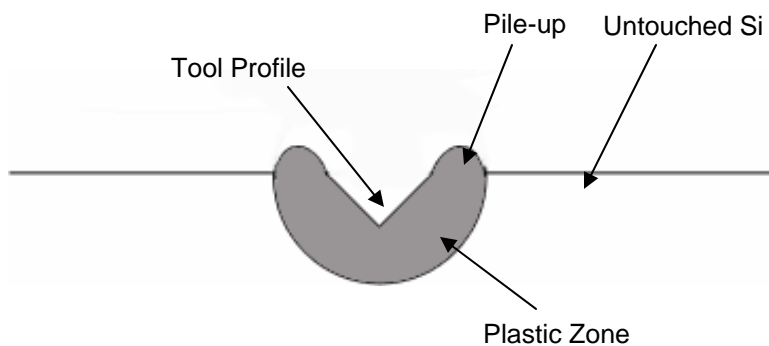


Figure 4.52. Speculated profile of scribe made with sharp indenter within ductile regime.

As the fracture threshold limit was reached, large, continuous pull outs thought to be due to lateral cracking are consistently present along scribes created above a particular

direction's threshold. The dipole strength would then drop slightly and then show little dependence on the applied load. This seems to corroborate reasonably with explanations (see section 3.1) presented by Lawn [17] and Ahn [20]. As a point force is applied to a surface a plastically deformed region forms beneath the force while the deformation scale is small. Translation of the asperity is preceded by the formation of the plastic zone. This makes sense because if this were not the case then cracking would precede the indenter as it were moved. As the load is increased the plastic region grows in size and the residual stress after release will be greater. At a critical limit of residual stress, the tensile stresses which are incurred in the elastic region surrounding the expanding plastic material initiate and propagate lateral cracking. This could partially explain the appearance of the continuous pull outs.

Ductile cuts made with the blunt geometry were all observed to generate considerable amounts of debris, a larger depth of cut, and the absence or reduction of pile ups along the side. By increasing the load applied to the tip, the dipole strength would increase approximately linearly until a limit was reached. Because material is removed it is assumed that the plastically generated material is only partially pushed into the surrounding elastic matrix and constrained resulting in less residual stress than that produced by sharp cutting. The nature of the blunt geometry removes some of the plastic material but leaves some behind as evident by the presence of residual stress (scribes also appear to have plastic material in SEM micrographs.) In addition to the presence of debris, the depth of cut for the blunt geometry is much greater, which can be partially explained by removal of material rather than displacement into the surface. An illustration the speculated profile of a scribe made with blunt indenter within ductile regime is shown in Figure 4.53.

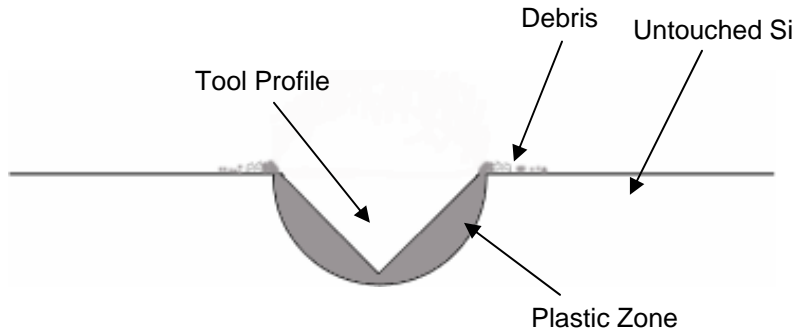


Figure 4.53. Speculated profile of scribe made with blunt indenter within ductile regime.

At the fracture threshold, large, continuous pull-outs seen during sharp cutting are replaced by small, disjunct pullouts. The author reasons that fracture observed may more likely be the result of tensile stresses induced by indenter itself on fracture planes, rather than as an effect of the residual stress created by the plastic zone. The fracture is very non-uniform, and randomized unlike the fracture created by sharp cutting. Because plastic material is removed, tensile stresses due to the expanding plastic zone do not rise as fast as those created by the indenter and fracture is primarily a result of the indenter. This may be further supported by the fact that there is a huge jump in depth of cut for directions where the blunt geometry creates ductile cuts at really low loads then fracture at mid to higher loads (poor cutting.)

4.4.2 Directional Dependency of Cutting Behavior

The directional dependence/tip geometry interaction on cutting behavior is not well understood at this point. It cannot be fully explained why the blunt geometry interaction seems to favor certain cutting directions while the sharp does not and vice-versa. However, based on the speculated cutting behavior presented in the previous paragraphs and a model

used in previous diamond turning research [26, 58], a qualitative explanation will be attempted.

A model developed by Blackley (see Appendix B) explained qualitatively the four-fold and three-fold symmetry exhibited by the (100) and (111) wafers during diamond turning operation (see page 19). The stress model shown in Figure 4.54 assumes a line force applied along an isotropic half-space boundary. The model assumes a region of tensile stress behind the tool producing mode I fracture resulting in pitting. Equation 4.3 gives the stress field where r is the distance from the line force and θ is the polar angle from the force direction. [26]

$$\sigma_{\pi} = -\frac{2P}{\pi * r} \cos \theta \quad (4.3)$$

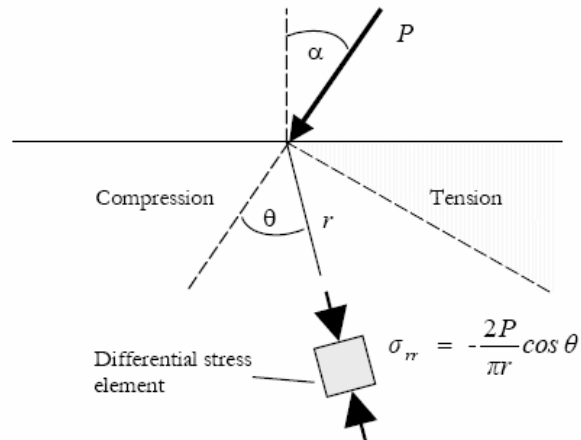


Figure 4.54 Line force loading P applied to an elastic half space. [26]

Using elastic theory, the dependence of pitting behavior based on stress state of particular orientation. The stress evaluations are done applying the proper rotation matrices to a fixed initial orientation of the crystal orientation and cutting direction to find the maximum tensile

stress resolved on the planes of easiest fracture. The maximum normal stress and tool-force angle is given by equation 4.4

$$\sigma_{\max} = \max\{\sigma_{ij}n_i n_j\} \quad (4.4)$$

where n_i is the unit vector normal to the assumed fracture plane and σ_{ij} is from equation 4.3.

The orientation dependence of σ_{\max} on a polar plot shows where the most favorable stress state for mode I fracture of a given fracture plane occurs.

The nature of the blunt geometry interaction is similar to that of diamond turning, for which the model was originally developed. A flat face at a negative rake angle plunging through the surface at a small depth of cut ($\sim 1\text{um}$). Increasing the load applied to the tip increases the depth of cut to a point where the deformation scale becomes too great to drive plastic flow (whether by HPPT or not) and fracture becomes more favorable. Because fracture was deemed to be the result of the stress state imposed by the action of the indenter, it is appropriate to apply the stress model developed by Blackley as a qualitative explanation. The model was changed slightly to better accommodate for the Dynatex scribing tips. Rather than use a two-dimensional line force, a three-dimensional point (localized) force is used. Figure 4.55 and 4.56 show the results of such a simulation for (100) and (111) orientation wafers assuming preferred fracture of the {111} (lowest energy) planes. A force vector from the surface of 30° is used as it is thought to accurately reflect the rake angle of the blunt face. The lobes indicate directions of preferred fracture, which match up with experimental results. For (100) orientation, $<110>$ directions fracture more easily, and for (111) orientation, $<112>$ directions fracture more easily.

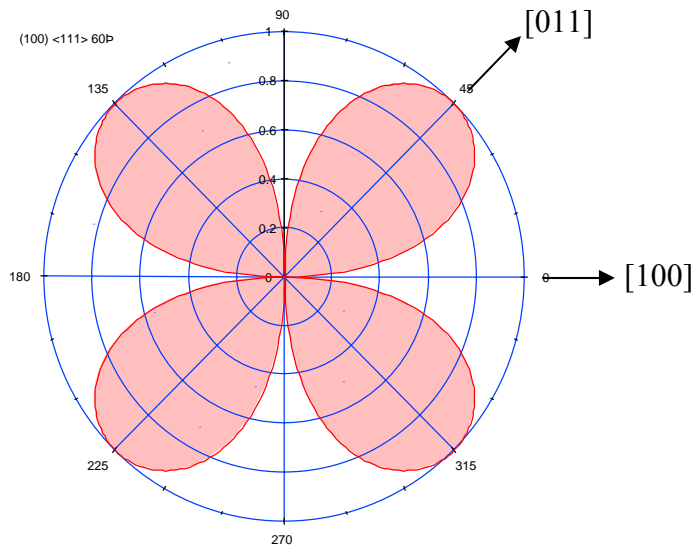


Figure 4.55. Point force stress model showing crystallographic dependence of fracture propensity for (100) surface as evaluated from maximum normal stress on $\{111\}$ planes. Correlation to blunt cutting behavior on a (100) surface is shown.

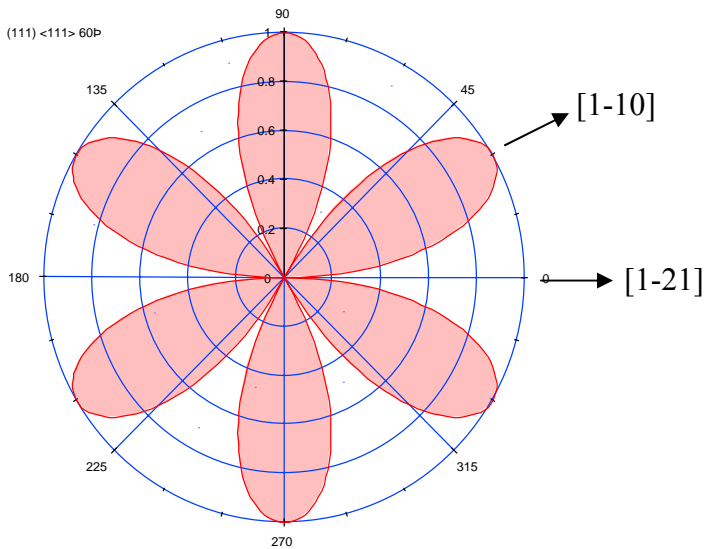


Figure 4.56. Point force stress model showing crystallographic dependence of fracture propensity for (111) surface as evaluated from maximum normal stress on $\{111\}$ planes. Correlation to blunt cutting behavior of a (111) surface is shown.

A similar qualitative discussion of the sharp interaction is more difficult due to the nature of the material response. As speculated the fracture during scribing with the sharp interaction is thought to be due to the residual stress imparted on the elastic matrix by the constrained plastic zone. The fracture is no longer thought to be due tensile stresses created behind the travel of the asperity (indenter or round nosed tool) but that of the residual stress remaining in from the plastic zone after the scribing operation. The model used by Blackley lacks capacity to fully account for this alternate stress state created by the material response. It does however provide some insight as to how a tensile stress state imparted (whether by the action of the asperity or by residual stress) on a specific set of fracture planes affects the fracture orientation dependencies.

Changing the expected fracture planes in a (100) orientation from {111} to {100} shifts the simulation pattern for the (100) orientation by 45°, as shown in Figure 4.57. The cutting direction with the greatest tendency towards fracture becomes [100] rather than [011], which seems to agree with results obtained from the sharp geometry cutting. Similarly, as shown in Figure 4.58, by switching the expected fracture planes from {111} planes to {110} planes in the simulation creates a pattern inversion, meaning the [1-10] direction becomes more susceptible to fracture rather than [11-2] or [-1-12] cutting directions. This matches well with observed cutting behavior.

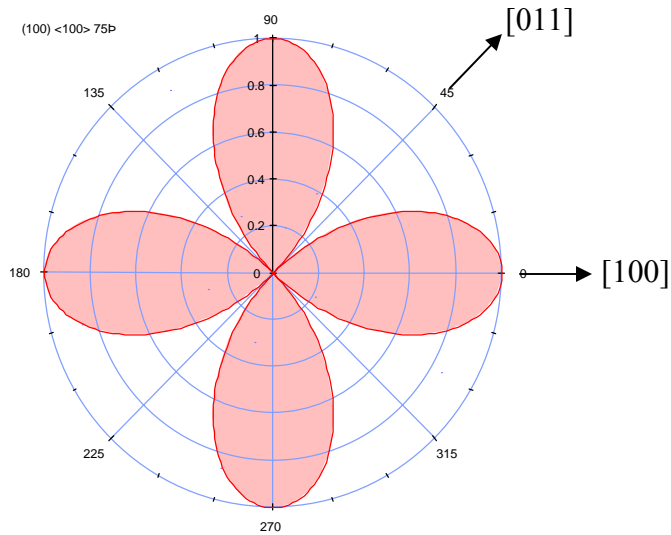


Figure 4.57. Point force stress model showing crystallographic dependence of fracture propensity for (100) surface as evaluated from maximum normal stress on {100} planes. Possible correlation to sharp cutting behavior on a (100) surface is shown.

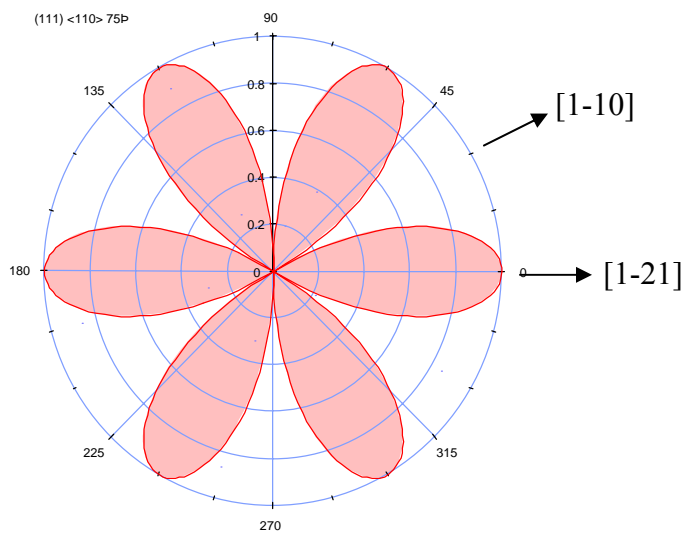


Figure 4.58. Point force stress model showing crystallographic dependence of fracture propensity for (111) surface as evaluated from maximum normal stress on {110} planes. Possible correlation to sharp cutting behavior on a (111) surface is shown.

There may be merit to the use alternate expected fracture planes to explain the behavior seen with the sharp geometry interaction. Several researchers speculate that

application of a point force to a brittle material creates median cracking below the plastic deformation zone, perpendicular to the surface. As the force is removed, the residual stress built up by the relaxation of the constrained plastic material is relieved by lateral cracking propagating from the site of median crack initiation. [17, 19, 20] Applying this argument to the present case would dictate the formation of a median crack between planes perpendicular to the orientation surface. By switching to the alternate planes in the simulation, the model predicts the correct direction dependence. Coincidentally, the alternate planes used in the simulation are perpendicular to the orientation surface. The author speculates that fracture is first initiated on these planes, facilitated by forces (due to the residual stress left by the expanding plastic zone) that act to separate these planes. While fracture may initiate on these planes, crack propagation may switch to a plane (or through several planes) of easier travel up to the surface in the form of lateral cracking. The point is that fracture could easily initiate between the planes used in the simulation, possibly explaining the noted behavior. Admittedly, the explanation given by the model depends on a parameter that can be altered to tailor the outcome of the simulation. However, based on how the material is thought to respond to the sharp interaction, the conjectures made about how and on which the planes the fracture could initiate may be viable for such a qualitative explanation.

4.4.3 Raman Measurement of Scribe Region and Debris

Results indicated the possibility of the existence of either tensile strained dc Si nanocrystals or that of Si-IV. Otherwise, no signature of peaks similar to those seen in other scratch testing experiments (Figure 4.59 [54]) appeared in the heavily plasticized scribe traces.

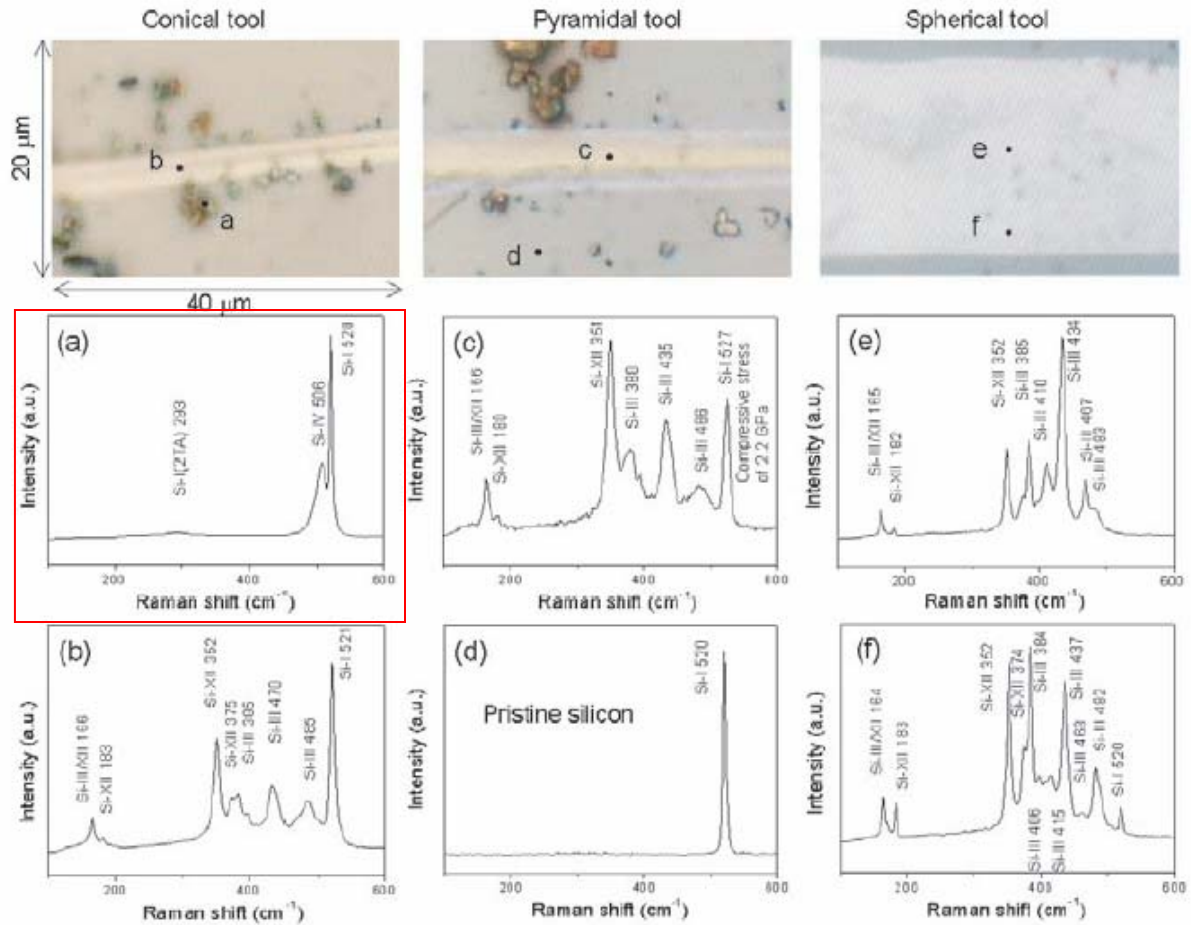


Figure 4.59. Raman spectra showing phases indicative of HPPT seen in other research for various indenter types. [54]

While the peak around 510 Rcm^{-1} has been noted in other investigations, it usually appears in the form of a double peak as shown encased in the box in the above figure. [50, 54] It is argued whether to assign this peak to a metastable crystalline Si-IV [56] or to nanocrystalline dc Si [57, 58] because it is thought that both can display a peak around this wavenumber. In either case, the assignment of this peak to either of these phases in this case is under some question. Due to the vastly different nature of the stress fields imposed by the two different geometries, it would be expected that differing Raman spectra would result. It is obvious that from Figure 4.59 that differing tip geometry creates differing Raman spectra. However, scribes made with both blunt and sharp geometries show almost exactly the same

spectrum. One would expect the sharp geometry, which is similar to a pyramidal type shape would yield a Raman spectrum close to that seen in (c.) of Figure 4.59. According to reference [54] the conical tool (spectrum shown in (a.) of Figure 4.59) may be similar in nature to the blunt geometry interaction creating a similar stress state and therefore the same remnant phase. This is only speculation because little else is known of the experimental conditions.

As the cause of this peak is highly disputed, the author offers other explanation. The first is that the phase transformation may not be occurring with the Dynatex tip due to the nature of the geometry tip. The plastic displacement could be by some other mechanism, for example, dislocations. This may be a reason why the more commonly seen indicative metastable crystal phases Si-III or Si-XII or amorphization are not seen. Regardless, even if the mechanism were by movement of large numbers of dislocations, it could be reasonable to expect presence of amorphized Si if not by back-transformation then through heavy shear and dislocation generation in the dc Si structure within the scribe region. The heavily plasticized nature of the scribe regions would lead us to believe that the material is dislocated and sheared enough to appear amorphous. But, a second, more likely explanation is detection proficiency of the Raman unit prevents detection of the more commonly seen phases and what is seen in Figures 4.49 and 50 may be due to something other than an alternate phase. The transformation zones are thought to be very small (on the order of a few hundred nanometers.) If the penetration depth of the laser is much greater than that of the depth transformation zone, or if the laser spot size (2-3 um) is slightly larger than the scribe width, the signal obtained from the transformed region may be insufficient for detection by the Raman unit. Again, it is reasonable to make this conclusion, because at the very least, the

nature of the material seen around in and around the scribe regions appears plastically generated. It is assumed that such material would be amorphous in nature, if not by a HPPT, then by extreme dislocation generation and motion by shear. Because no amorphization has been shown, it may be reasonable to assume that the Raman system cannot detect this small region. Sufficient data was not found to draw a distinct conclusion as to the occurrence of HPPT for scribing experiments.

Raman performed on debris created by scribing has not drawn any conclusions. Originally, the spectra shown in Figure 4.60 was seen and thought to be nanocrystalline Si in an amorphous matrix as found in debris and attributed by others (Figure 4.61.) [50, 54] As shown in Figure 5.51(a.), decreasing the power level shifts the second peak toward the dc Si peak at 521 Rcm^{-1} . The problems occurring with sample heating may have been originally misinterpreted as the presence of an alternate phase. Direct measurement with a Raman laser proved as a poor method. TEM analysis would be a viable option but collection of the debris for analysis would prove difficult as debris size is on the order of a few microns and very sparse.

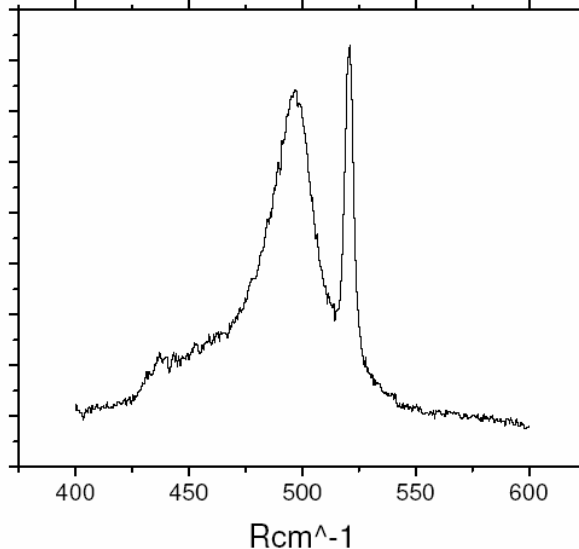


Figure 4.60. Raman spectra obtained for plastically generated debris matching that attributed by others to nanocrystalline Si in an amorphous matrix.

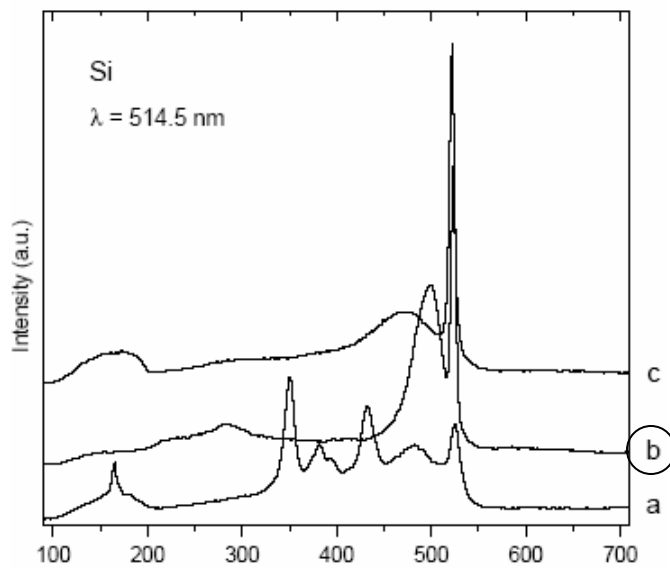


Figure 4.61. Raman spectra (b in figure) obtained for plastically generated debris found around a scribe and attributed by others to nanocrystalline Si in an amorphous matrix. [54]

4.5 Conclusions and Suggested Future Work

Scribing with two different tool geometry/surface interactions on single crystal silicon yielded unique material responses dependent on crystal orientation and cutting direction. At

low enough loads, a purely plastic response was created for both geometries noted in SEM observation. The sharp geometry interaction was shown to wedge plastically generated material into the surrounding elastic matrix at the surface generating residual stress and measurable deflection of the wafer samples. Fracture behavior was noted to occur as large continuous pull-outs of crystalline material surrounding the scribe region. It was speculated that the fracture was initiated in crystal planes perpendicular to the surface and propagated by wedging forces created by residual stress. Fracture may then change planes as cracks go to the surface to form the lateral pull-outs seen. A stress model was used to qualitatively show the directional dependence of tensile stress (created by the wedging forces) on the initiation planes. The blunt geometry interaction was shown to remove plastically generated material in the form of surface debris, resulting in less residual stress and measured deflection than that of the sharp interaction. Fracture behavior was noted to occur as small disjunct pull-outs of material thrown onto the surface surrounding the scribe. It was thought that the fracture was mainly to the forces induced by the indenter itself, rather than the built up residual stress. The stress model (originally developed for diamond turning) was used to show the directional dependence of tensile stress (and therefore fracture) induced on the planes by a point force used to represent the stress state imposed by the blunt indenter.

Raman measurements failed to provide solid evidence as to the presence of the β -tin transformation within the scribes created within the ductile regime. A disputed peak was found at 510 Rcm^{-1} , possibly indicating Si-IV or nanocrystalline dc Si, but no other more commonly seen indicative phases were found. Although Raman failed to detect any distinct signature of the transformation, it is thought to be due to the detection proficiency of the unit at such a small scale, rather than any transformation (whether β -tin \rightarrow amorphous, or directly

to amorphous) not occurring. Raman performed on the debris was shown to be plagued by heating problems, and no definitive conclusion could be drawn.

Suggested future work includes cross sectional TEM of the scribe regions for both sharp and blunt interactions. Diffraction can be used to definitively draw conclusions as to the structural nature of the plastically generated zone. Further Raman work should also be attempted as other research has drawn definitive conclusion using this characterization technique. Using a lower laser wavelength to reduce the penetration depth and keep the sampling volume closer to the surface may be appropriate. Additionally, *in-situ* scribing work should be attempted to show the presence of β -tin directly, rather than relying on finding indicative phases to show the transformation has occurred.

5. Diamond Turning of Silicon and Germanium

5.1 Scope and Objectives

The scope of this investigation is the study of the response of silicon and germanium to single point diamond turning (SPDT) and more specifically, to determine the presence of HPPT on the machined surface as well as within generated debris. SPDT is an ultra precision machining method in which nanometer surface finishes can be obtained using the cutting action of a single crystal diamond on positioning equipment of high stiffness and accuracy.

By SPDT in the ductile regime, the productivity of optical components and large-diameter substrates is improved greatly. The technology however is greatly restricted by the introduction of subsurface damage to the part with the removal of material. The mechanical, optical, and electrical properties are directly influenced by the depth and nature of the near surface damage. The mechanisms governing the material removal (a combination of microcracking, dislocation motion, and structure change- HPPT) in ductile-regime turning are not well understood. The work presented here is mainly focused on the appearance of amorphization (structure change) in a ductile-turned region. Secondary focus is placed on the characterization of surface finish and cutting behavior as a function of crystallographic orientation and cutting direction, feed rate, and rake angle.

During the investigation, (100), (110) and (111) silicon and germanium wafers are diamond turned under various conditions. The effects of crystallographic orientation and cutting direction, feed rate, and tool rake angle are considered. Machined surfaces are studied with Nomarsky optical microscopy to observe the fracture/ductile turning behavior in

relation to the various conditions. Interferometry methods are used to characterize surface finish of ductile-turned regions. Raman spectroscopy will be used to identify differences in structure between the untouched silicon (and germanium) and that within the machined to observe any structure change and relate it to the observed plasticity. It is hoped that either crystalline or amorphous phases of silicon that are indicative of β -tin phase transformation can be identified on the ductile-turned surface.

Unlike the previous section, experimental results and the discussion are combined into one section. The author deemed it easier to discuss certain aspects as the data is presented to keep clarity and brevity.

5.2 Aside: SPDT Material Removal in Si and Ge

Material is removed (chip formation) in SPDT by translating the tool in the feed direction at a desired depth while the part rotates on a high speed air spindle in the cutting direction (orthogonal to the feed direction and tool face.) Figure 5.1 [Adapted, 61] provides an illustration of the chip formation during SPDT.

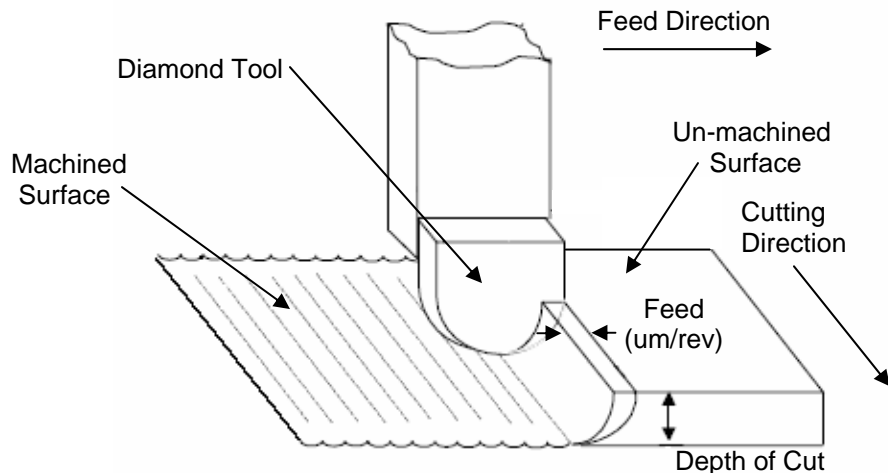


Figure 5.1. Illustration of chip formation during diamond turning pass. [Adapted, 61]

As a tool passes through the material it introduces an amount of microfracture damage into the uncut shoulder. Below a certain depth (dependent on the feed rate,) the material removal is ductile. As the feed rate is increased the damage was shown to move down the shoulder until a critical limit is reached where the damage cannot be cleaned up by subsequent passes. At this point fracture damage starts to appear in the turned surface. This is shown in Figure 5.2. [26]

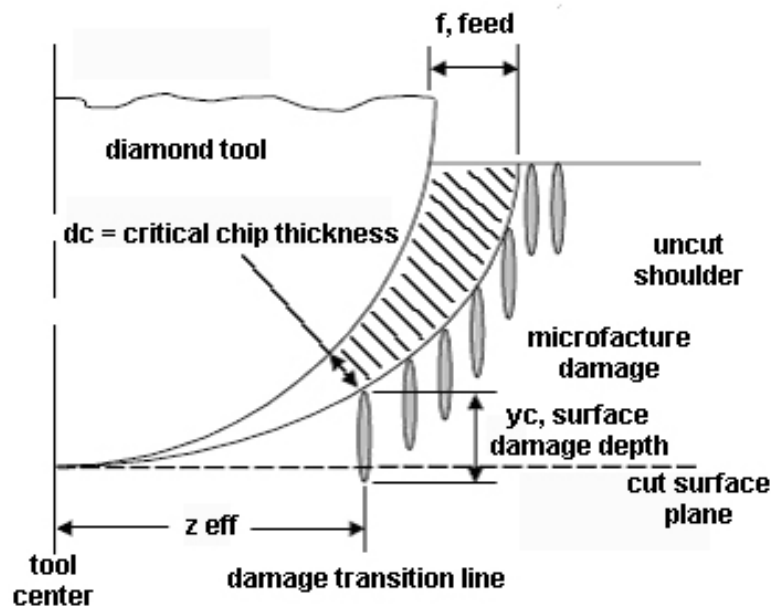


Figure 5.2. Diagram showing chip removal area and damage region. [26]

The surface generation of an ideal finish for a sharp round-nose tool appears in Figure 5.3. [62] The nose radius is repeated in the surface at a distance dictated by the feed rate.

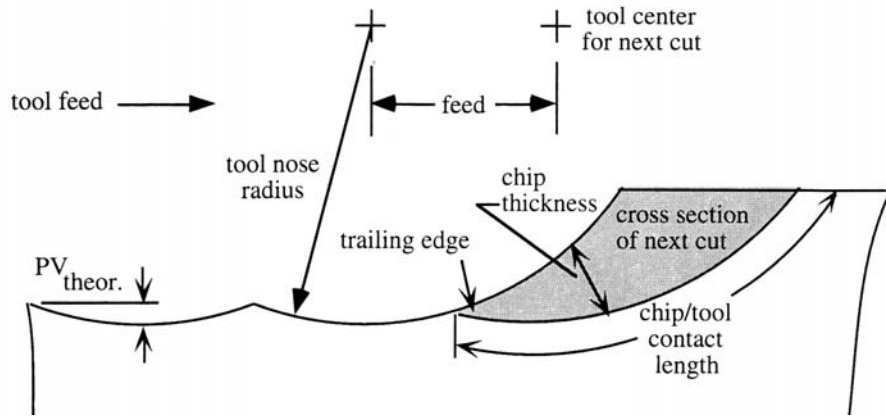


Figure 5.3. Theoretical diamond turned surface generation. [62]

Deviation of a turned surface from theoretical can happen for several reasons including spindle/slide vibration, tool geometry (sharpness of cutting edge, tool waviness, and damage) and chatter. [62] Based on the surface finish data, tool sharpness and damage seemed to be of interest to this investigation. The first phenomenon, shown in Figure 5.4 [62] is thought to be due to deformation of the work piece under the tool. [63, 64] As a result the surface springs back with relief of elastic stress creating a small area not ideally removed by the tool. The PV of the surface becomes greater than theoretical. [65] The second phenomenon of interest is the introduction of the profile of a damaged (or wavy) tool into the work piece. [66]

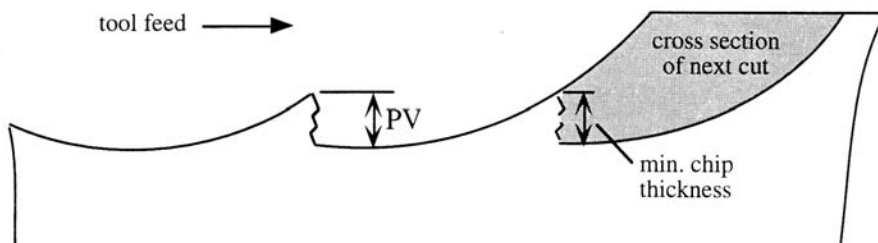


Figure 5.4. Variation of surface from theoretical due to deformation and spring back of surface. [62]

5.3 Aside: Materials Consideration- Germanium

The primary focus of investigation has been on silicon due to its high technological importance and dominance both as a substrate for microelectronic and micromechanical components, as well as its relative cheapness. Germanium (Ge,) while not as predominant as silicon, still finds application in similar fields. Specific to this investigation, germanium tends to reduce tool wear during machining when compared to silicon (most of the early work at the PEC was done on Ge.) As a result much of the diamond turning experimentation of this investigation has been done on Ge, and then transferred to Si. Due to its similarity of bonding and crystal structure to Si, Ge exhibits similar machining characteristics and dependencies. [24, 26] Most of the property information (crystal structure, valence numbers and bonding, anisotropic nature of mechanical properties) and theories (on contact process and brittle material response) presented in previous chapters can also be applied to Ge. Additionally, Ge is also said to undergo a similar phase transformation to metallic β -tin, facilitating plastic flow. [59] Despite the focus of this work on Si, for completeness, results for Ge are also discussed.

5.4 Experimental Setup

5.4.1 Diamond Turning

A Rank Pneumo ASG 2500 diamond turning machine (DTM) was used for conducting the diamond turning experiments. This DTM features hydrostatic bearing slide axes, an aerostatic bearing work piece spindle, and laser interferometer feed back. A PC based control system uses the laser interferometer reading as the feed back to drive the slides. The DTM's controller was built at Precision Engineering Center (PEC), North Carolina State University, Raleigh, NC. An image of the DTM is shown in Figure 5.5.



Figure 5.5. Rank Pneumo ASG 2500 DTM used in diamond turning experiments.

Experiments were conducted on both single crystal silicon and germanium. Silicon wafers (4 inch diameter, 525 um thickness) and germanium wafers (3 inch diameter, 1 mm thickness) were glued to a diamond turned aluminum block (cylindrical) with the block mounted on the vacuum chuck. A close-up view of a chucked wafer is shown in Figure 5.6. Lubrication/Coolant (Mobilmet Omnicron, Mobil) was provided at the tool tip by a low pressure spout (blue hose in Figure 5.6.)

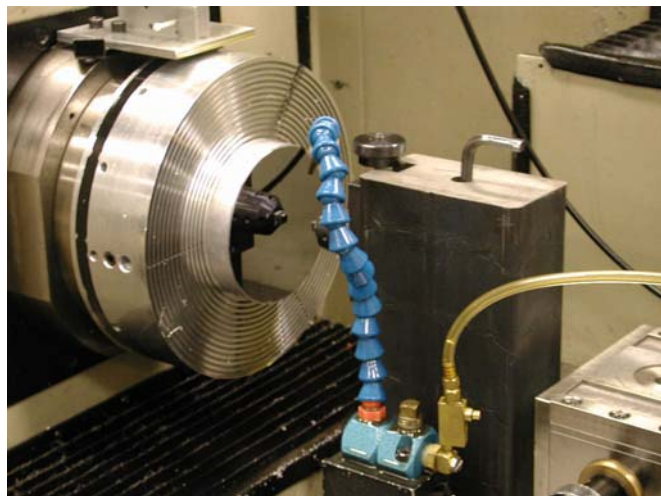


Figure 5.6. Close-up view of a wafer vacuum chucked to the DTM spindle.

Surfaces were turned with a -30° and -45° rake angle, 3mm radius, round-nosed diamond tool. Both tools had approximately a 6° clearance. The spindle rotation was held constant at 530 RPM to minimize system vibration (resulting in a cutting speed range of 0.55-2.22 m/s depending on position.) Wafers were first faced flat optically reflective (1-3 nm RMS) at a feed rate of 4 um/rev (within the ductile regime for all conditions) at a depth of cut of 20 um. For observation of the material response and surface finish measurements wafers were then turned at feed rates of 1, 2, 3, 5, 7, 10 and 15 um/rev at a depth of cut (DOC) of 2.5 um. For Raman characterization of turned surfaces, the following abbreviated experimental matrix (Table 5.1) was used, altering wafer orientation, tool rake angle, and feed rate (low/high.)

Table 5.1. Experimental matrix of 20 Raman scans for comparison of wafer orientation, tool rake angle, and feed rate (low/high.)

Ge	-30°	-45°
(100)	1um/rev 8um/rev	1um/rev 8um/rev
(110)	1um/rev 10um/rev	1um/rev 10um/rev
(111)	1um/rev 5um/rev	1um/rev 5um/rev
Si	-30°	-45°
(100)	1um/rev 5um/rev	1um/rev 5um/rev
(111)	1um/rev 5um/rev	1um/rev 5um/rev

5.4.2 Characterization

Optical Microscopy

Optical micrographs using a Nomarski filter were taken with an Olympus BH2-UMA to determine the quality and topography of the machined surface.

Surface Roughness

Surface finishes of the ductile-turned regions were measured using a Zygo New View 5600 white light interferometer. Surfaces were measured with the 50x objective. MetroPro, the software suite used to analyze the interferometer data, reports a measure of surface roughness by the root mean square (RMS) parameter and peak to valley (PV) values. Measurements were taken for from the center outward in regions within and outside the predicted fracture pattern area (further explained in Results section.)

Raman Spectroscopy

Characterization of the machined surface was accomplished with Macro-Raman spectroscopy done at room temperature using an ISA U-1000 scanning monochromator. Raman excitation was done with the 514.5 nm line of an Argon-ion laser, with a spot size of approximately 1mm in diameter. Raman spectra were taken in the 200-600 cm⁻¹ range which contains the characteristic peaks normally associated with crystalline, amorphous, and various metastable crystalline phases seen in other research. A spectral resolution of \approx 4 cm⁻¹ was utilized, and the laser power was \approx 5 mW.

5.5 Experimental Results and Discussion (Silicon Surfaces)

5.5.1 Machining Behavior/ Material Response

Parameter Effects

Figure 5.7 is an illustration of a (100) Si wafer face with machining bands made at the various feed rates indicated with a -30° rake angle tool. In this figure and those similar to it, the white areas indicate regions where no pitting was evident and the surface was completely ductile turned. The grey scale areas indicate regions of pitting (elastic removal) on the machined surface with the degree of severity increasing with scale darkness. The four-fold

fracture pattern symmetry (full pattern is overlaid on the figure) seen at mid/higher feed rates is consistent with previous research. [24, 26, 60]

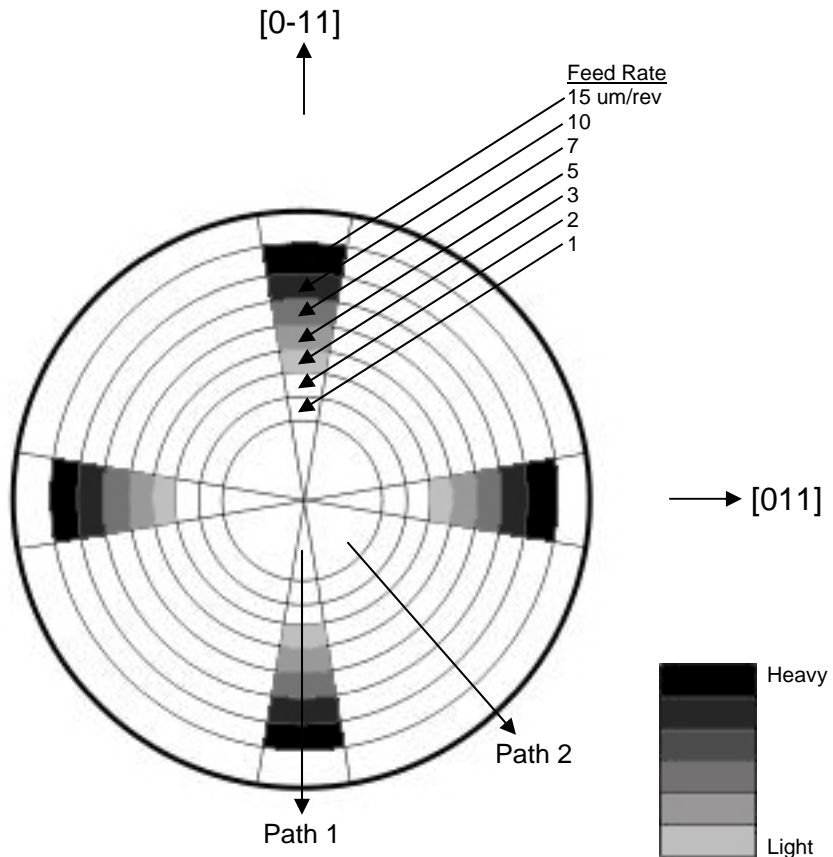


Figure 5.7. Illustration of fracture pattern on (100) Si machined with a -30° rake angle tool. White areas indicate no pitting. Grey scale indicates severity of pitting.

Figures 5.8 (a.) and (b.) are collages of Nomarski micrographs taken along paths 1 and 2 (two distinct regions of machining behavior,) respectively. The path indicates the direction along which micrographs were taken in each machining band. Path 1 is taken along regions where the cutting direction of the tool is oriented along the $<110>$ directions on the wafer face. Path 2 is along regions where the cutting direction is in the $<100>$ directions.

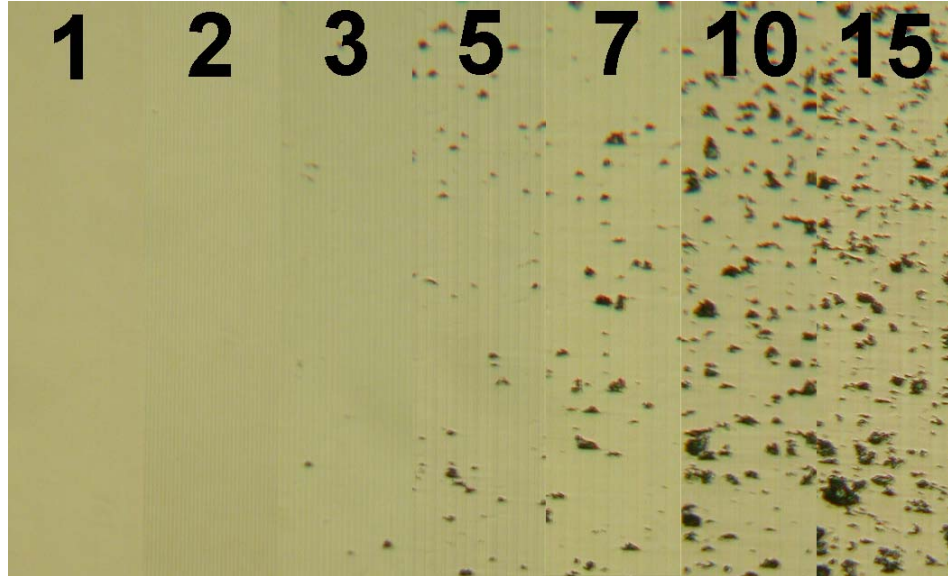


Figure 5.8(a.) Collage of micrographs depicting surface of (100) Si diamond turned at various feed rates (um/rev) with -30° rake angle tool. **(Path 1)**

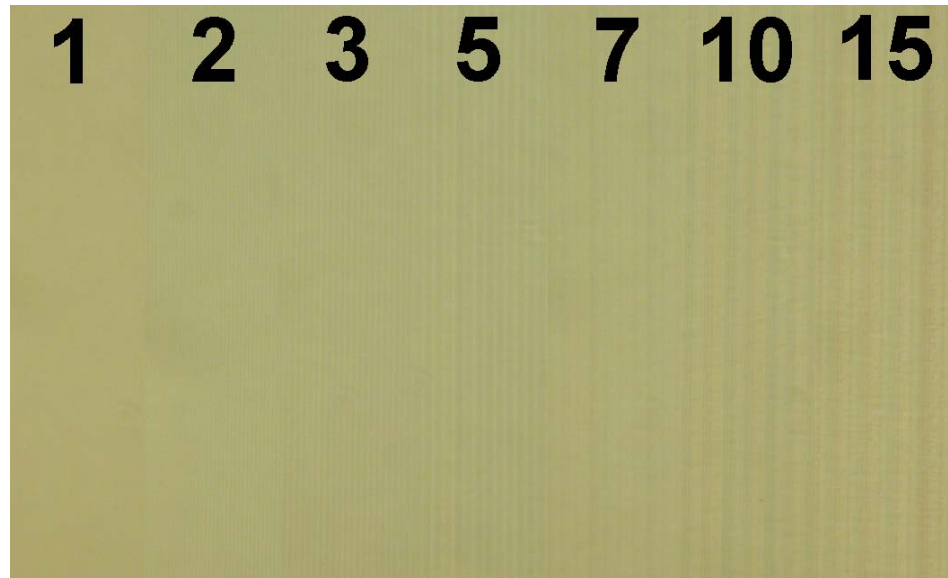


Figure 5.8(b.) Collage of micrographs depicting surface of (100) Si diamond turned at various feed rates (um/rev) with -30° rake angle tool. **(Path 2)**

Figure 5.8(a.) shows the progression of material response from purely ductile surface to a pitting response at higher feed rates. Path 1 sees the onset of pitting at 5 $\mu\text{m}/\text{rev}$, with pitting density increasing with feed rate. Path 2 remains ductile for the range of feed rates tested.

Figure 5.9 is an illustration of a (100) Si wafer face with machining bands made at the various feed rates indicated with a -45° rake angle tool. The four-fold fracture pattern symmetry (full pattern is overlaid on the figure) is seen again, but is slightly less severe than seen with the -30° tool.

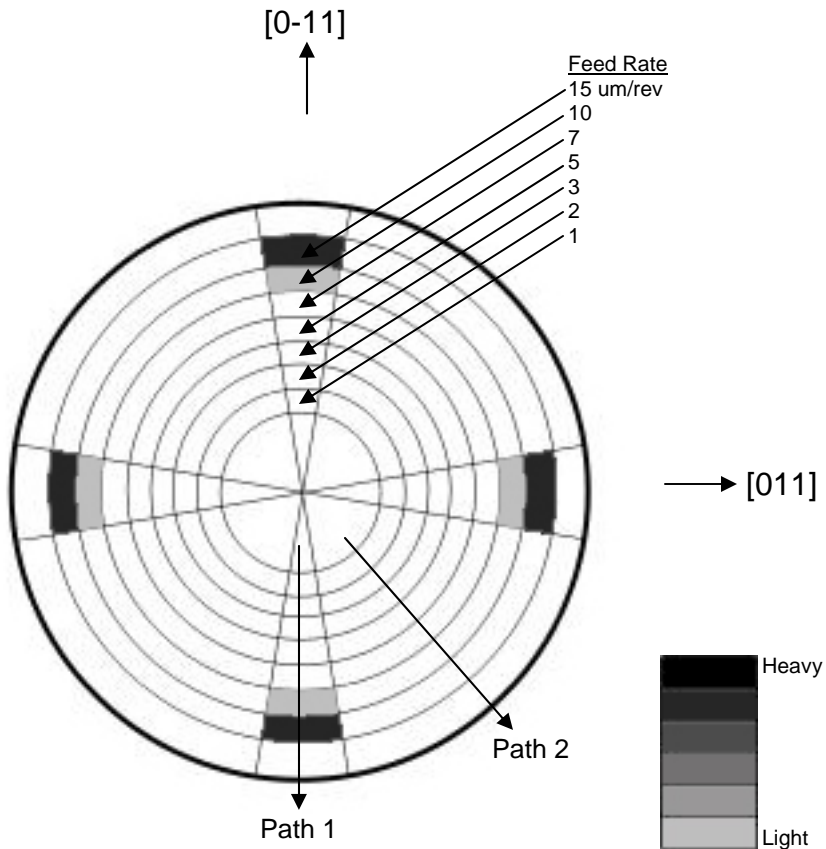


Figure 5.9. Illustration of fracture pattern on (100) Si machined with a -30° rake angle tool. White areas indicate no pitting. Grey scale indicates severity of pitting.

Figures 5.10 (a.) and (b.) are collages of Nomarski micrographs taken along paths 1 and 2 (two distinct regions of machining behavior,) respectively. Again, path 1 is taken along regions where the cutting direction of the tool is oriented along the $\langle 110 \rangle$ directions on the wafer face. Path 2 is along regions where the cutting direction is in the $\langle 100 \rangle$ directions.

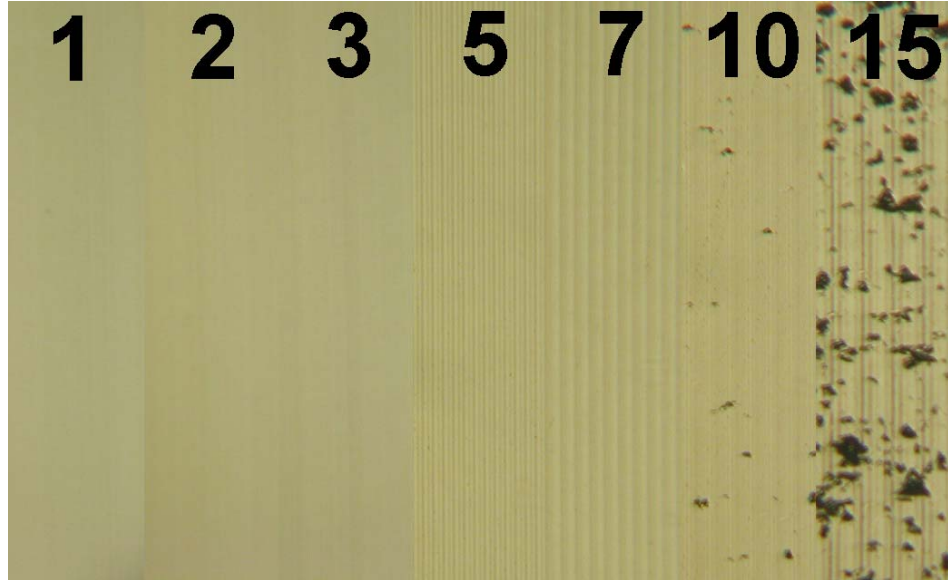


Figure 5.10(a.) Collage of micrographs depicting surface of (100) Si diamond turned at various feed rates (um/rev) with -45° rake angle tool. (**Path 1**)

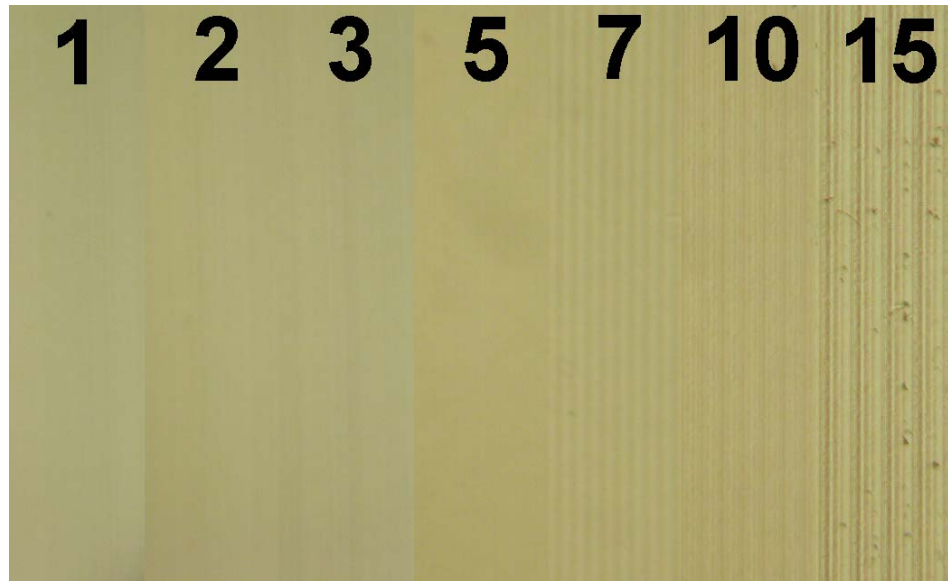


Figure 5.10(b.) Collage of micrographs depicting surface of (100) Si diamond turned at various feed rates (um/rev) with -45° rake angle tool. (**Path 2**)

Figure 5.10 (a.) shows the progression of material response from purely ductile surface to a pitting response at higher feed rates. Path 1 sees the onset of pitting at 10 um/rev, with pitting density increasing with feed rate. Path 2 remains ductile for the range of feed rates tested.

Figure 5.11 is an illustration of a (111) Si wafer face with machining bands made at the various feed rates indicated with a -30° rake angle tool. The three-fold fracture pattern symmetry (full pattern is overlaid on the figure) seen at higher feed rates is consistent with previous research. [24, 26, 60]

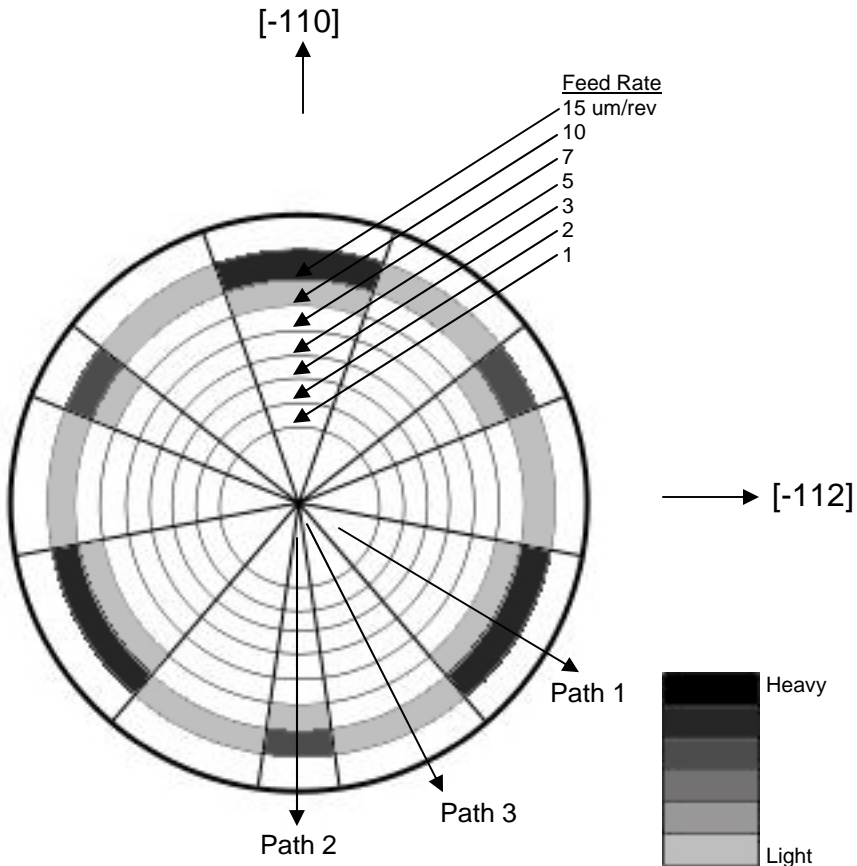


Figure 5.11. Illustration of fracture pattern on (111) Si machined with a -30° rake angle tool. White areas indicate no pitting. Grey scale indicates severity of pitting.

Figures 5.12 (a.), (b.) and (c.) are collages of Nomarski micrographs taken along paths 1, 2 and 3 (three distinct regions of machining behavior,) respectively. The path indicates the direction along which micrographs were taken in each machining band. Both path 1 and 2 are along regions where the cutting direction of the tool is oriented along $<112>$ directions, but due to the three-fold symmetry, for example, $[1\bar{1}2]$ will have a vastly different response

than [-1-12], the opposite cutting direction. Path 3 is along regions where the cutting direction of the tool is oriented along <110> directions.

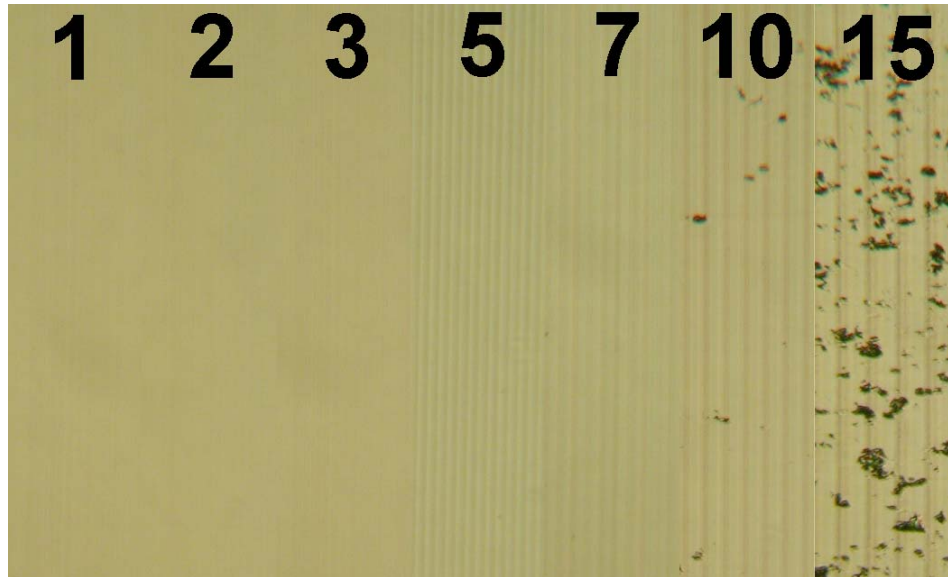


Figure 5.12(a.) Collage of micrographs depicting surface of (111) Si diamond turned at various feed rates (um/rev) with -30° rake angle tool. (**Path 1**)



Figure 5.12(b.) Collage of micrographs depicting surface of (111) Si diamond turned at various feed rates (um/rev) with -30° rake angle tool. (**Path 2**)

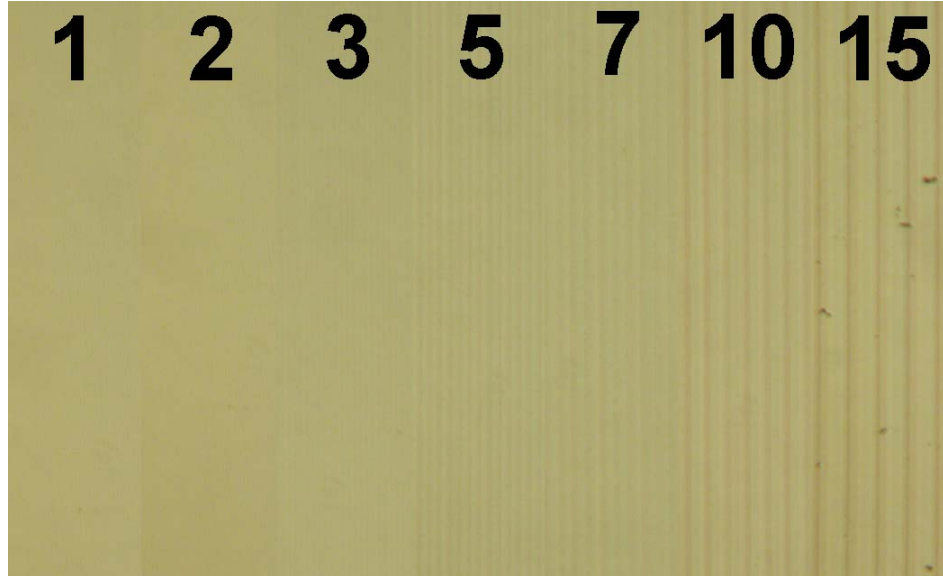


Figure 5.12(c.) Collage of micrographs depicting surface of (111) Si diamond turned at various feed rates (um/rev) with -30° rake angle tool. **(Path 3)**

Each of the figures shows the progression of material response from purely ductile surface to a pitting response at higher feed rates. Paths 1 and 2 see the onset of pitting at 10 um/rev, with pitting density increasing with feed rate. The density of pitting seems to be higher for path 1 at both feed rates. Path 3 sees a small amount of pitting at 15 um/rev.

Figure 5.13 is an illustration of a (111) Si wafer face with machining bands made at the various feed rates indicated with a -45° rake angle tool. The three-fold fracture pattern symmetry (full pattern is overlaid on the figure) is seen again but is less severe than for -30° .

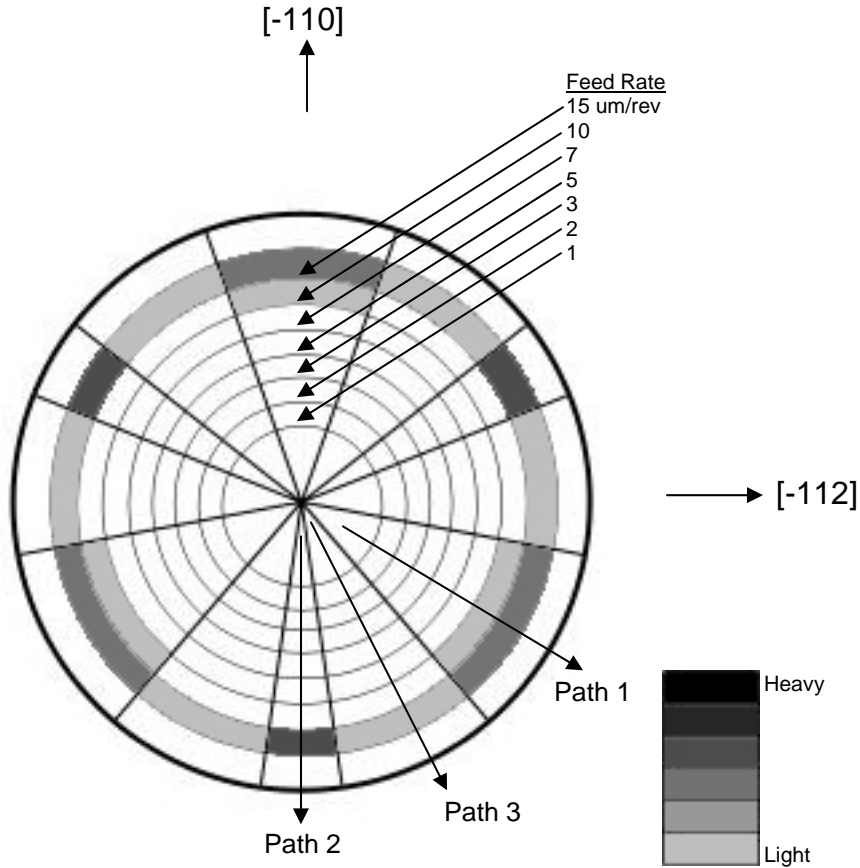


Figure 5.13. Illustration of fracture pattern on (111) Si machined with a -45° rake angle tool.
White areas indicate no pitting. Grey scale indicates severity of pitting.

Figures 5.14 (a.), (b.) and (c.) are collages of Nomarski micrographs taken along paths 1, 2 and 3 (three distinct regions of machining behavior,) respectively. Again, path 1 and 2 are along regions where the cutting direction of the tool is oriented along $<112>$ directions and path 3 is along regions where the cutting direction of the tool is oriented along $<110>$ directions.

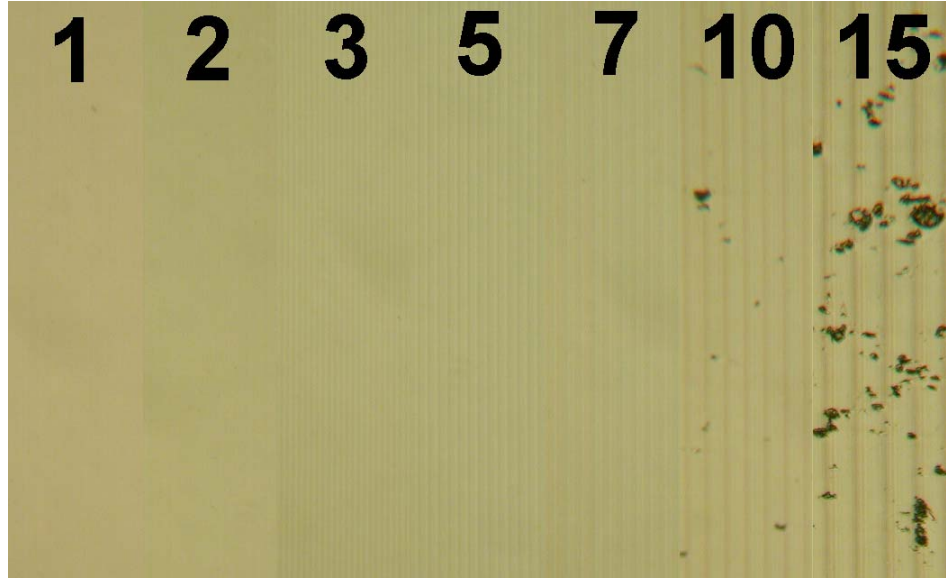


Figure 5.14(a.) Collage of micrographs depicting surface of (111) Si diamond turned at various feed rates (um/rev) with -45° rake angle tool. (**Path 1**)

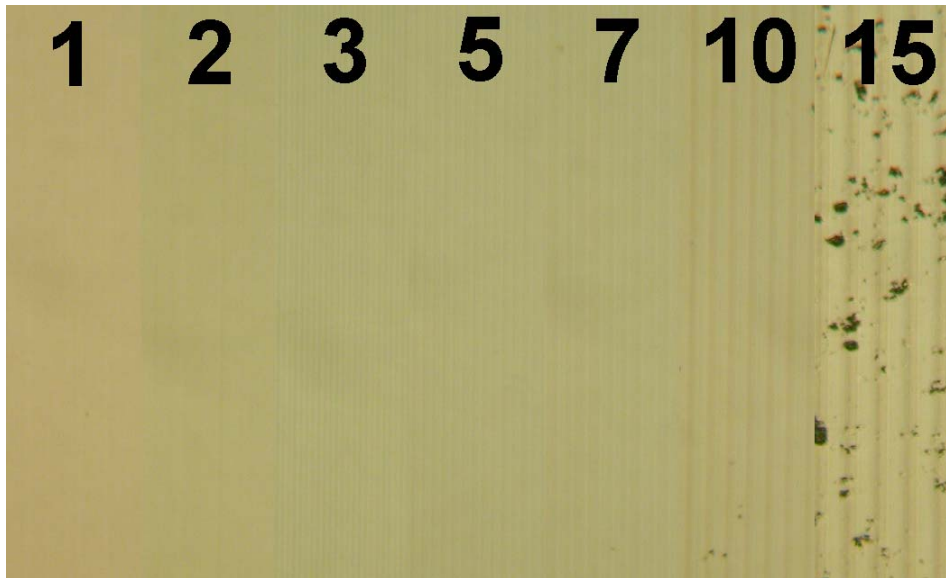


Figure 5.14(b.) Collage of micrographs depicting surface of (111) Si diamond turned at various feed rates (um/rev) with -45° rake angle tool. (**Path 2**)

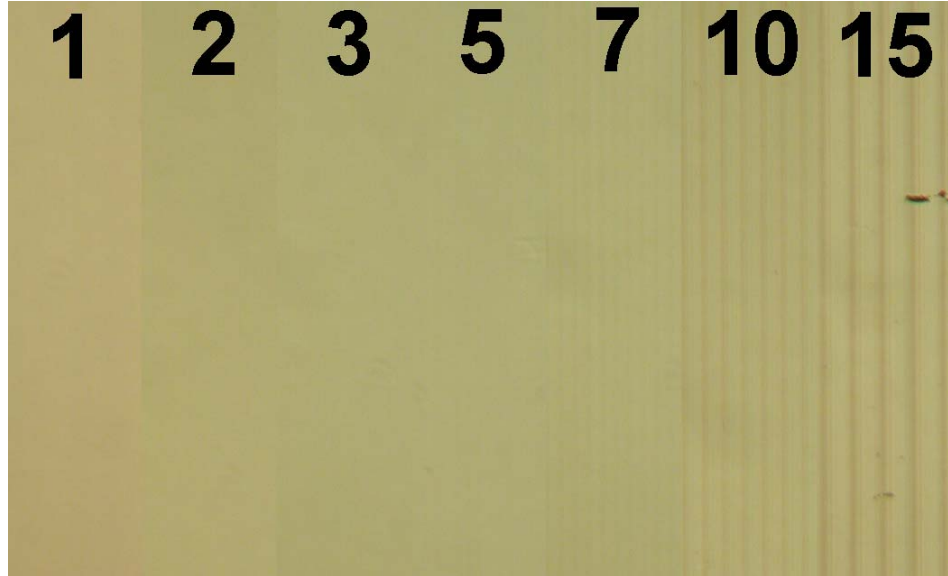


Figure 5.14(c.) Collage of micrographs depicting surface of (111) Si diamond turned at various feed rates (um/rev) with -45° rake angle tool. (**Path 3**)

Each of the figures shows the progression of material response from purely ductile surface to a pitting response at higher feed rates. Path 1 sees the onset of pitting at 10 um/rev, with pitting density increasing at 15 um/rev. Paths 2 and 3 see pitting at 15 um/rev. The density of pitting is to be higher for path 2 than 3.

The difference in the severity of pitting exhibited between the -30° and -45° is expected as the increase in hydrostatic stress with higher negative rake angle in the plastic deformation zone reducing the propensity for fracture to occur. [61]

Machining results achieved in this investigation generally matched those achieved in previous research. The four-fold and three-fold symmetry exhibited by the (100) and (111) wafers, respectively, can be explained by Blackley (see page 19 and 77 for discussions) using the crystal orientation dependence stress model. The simulation qualitatively shows on a polar plot the orientation dependence of propensity for pitting behavior by outputting an “orientation dependent stress factor.” This factor represents the most favorable stress state

for mode I fracture of the $\{111\}$ stress planes (those of lowest fracture energy for dc structure.) While the fracture mechanism could be determined solely by stress state alone (no preferred fracture plane,) the model used by Blackley assumes cleavage of these planes as the simulation fit the experimental observation correctly. The author refers the reader to Appendix B for a more detailed description. Figures 5.15 and 16 are stress orientation factors as a function of rotation around the crystal face for (100) and (111) orientations respectively as calculated by Blackley and corresponding experimental observation. [26, 61] Increased distance of the polar plot from the center indicates a higher tendency for that direction to display pitting behavior. The stress orientation factors demonstrate the four and three-fold symmetry exhibited by the machined wafers.

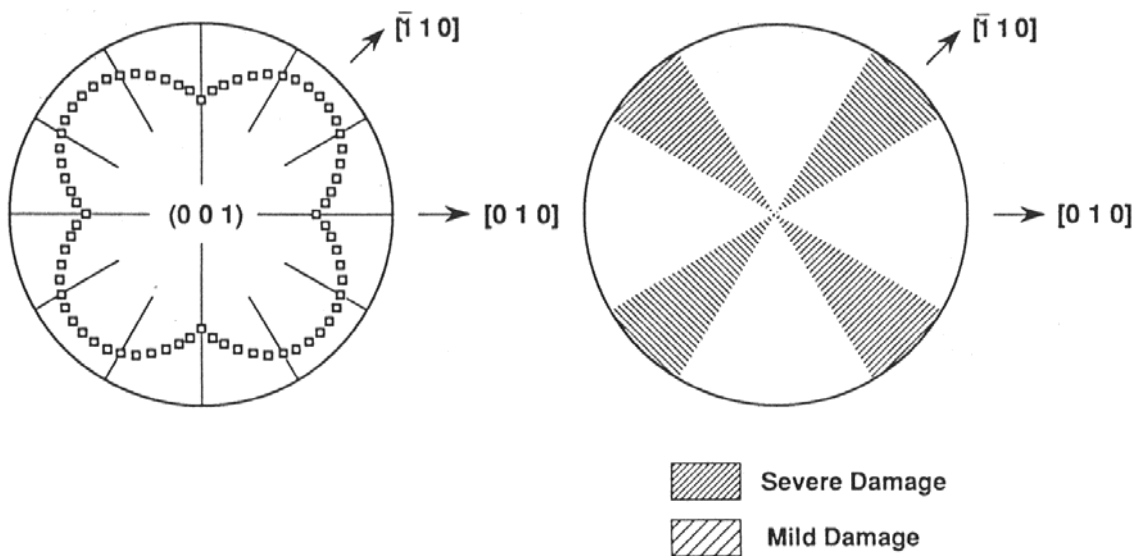


Figure 5.15. Stress orientation factor accompanied by a schematic representation of pitting damage observed by Blackley for (100) wafer. [26]

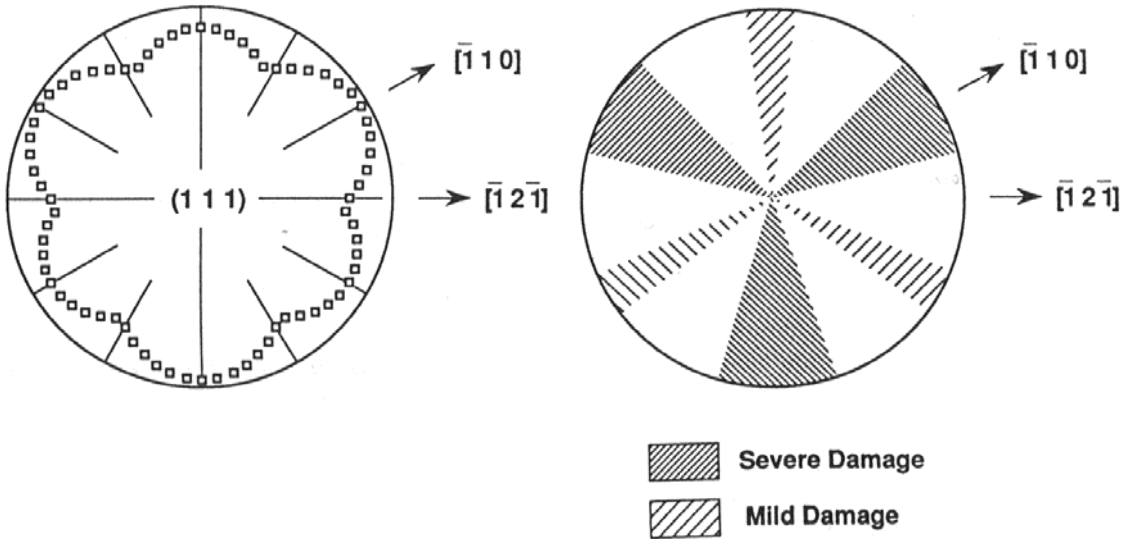


Figure 5.16. Stress orientation factor accompanied by a schematic representation of pitting damage observed by Blackley for (111) wafer. [26]

An anomaly noted during experimentation and by others (using vastly different tool geometries and conditions) [27, 67] was the rotation of the fracture pattern of (100) Si by 45° . This means that the cutting directions most susceptible to fracture go from $<110>$ to $<100>$. The rotation of the fracture pattern was noted (although it seemed to be rare) at one time or another for both the -30° and -45° tips. This is evident in the picture show in Figure 5.17.

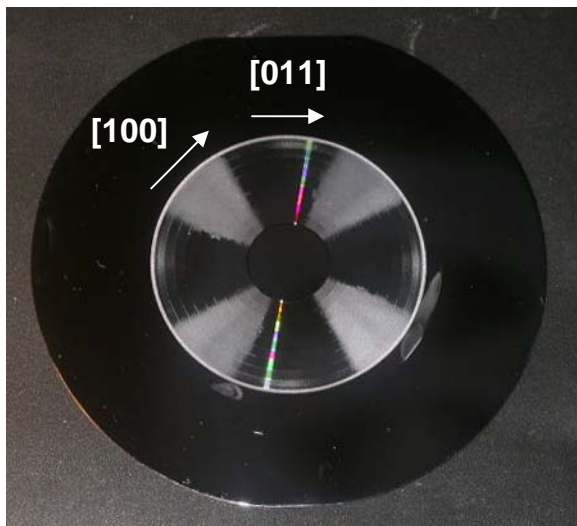


Figure 5.17. Digital image showing (100) Si wafer with fracture pattern shifted 45° from normal (previous results [24, 26, 60] with same tool.)

While this behavior is likely due to a changing stress state applied to the workpiece by the tool (perhaps as it changes shape with wearing or damage,) the actual material fracture mechanism responsible for the behavior is not well understood. However by adjusting the preferred fracture plane in the Blackley model to {110} rather than {111} gives similar shift in stress intensity factor. This is an empirical observation of the model behavior and does not necessarily indicate the validity of the assumption as the actual reason for the pattern shift. Also noted was that for the wafer shown in Figure 5.17, fracture occurred at a much lower feed rate (1 um/rev) than it did for the wafer shown in Figure 5.7.

Surface Finish Characterization

Four separate machining runs were performed on silicon for the two orientations ((100) and (111)) and two tool angles. Profiles shown are from the most ductile cut regions on the surface. All though RMS values are in the low nanometer range for ductile turned surfaces, the profiles are far from the theoretical predictions. Tool wear and starting tip conditions greatly affected the shape of the machined surface. Each machining run (one set of 7 feed rate bands) created a different profile affecting PV and RMS values. No comparison will be made between the machining runs as each has exhibited different behavior. However, surfaces with in a feed rate band had similar features seemingly independent of cutting direction. Most of the surfaces generated greatly deviated from an ideal surface.

Figure 5.18-5.20 show surface profiles of the (100) Si wafer turned with a -45° rake angle tool. The profile shape changes drastically as the feed rate decreases. In each figure, the surface profile is inconsistent with an ideal surface finish. (Figure 5.20 may appear as an ideal profile shape, but the PV at least one to two magnitudes of order too high to be ideal.)

This machining run has been affected by damage to the tool brought on by wear. (The damage may have incurred during a facing cut.) A pattern is repeated in the finished surface at a distance determined by the feed rate. As the feed rate decreases less of the tool radius influences the final surface, and as a result less of the damage pattern seen in the tool is ingrained in the part. Damage close to the tool center is repeated even at small feed rates creating features of similar width and height still seen as the feed rate approaches low values. The repeated features are circled in the figures.

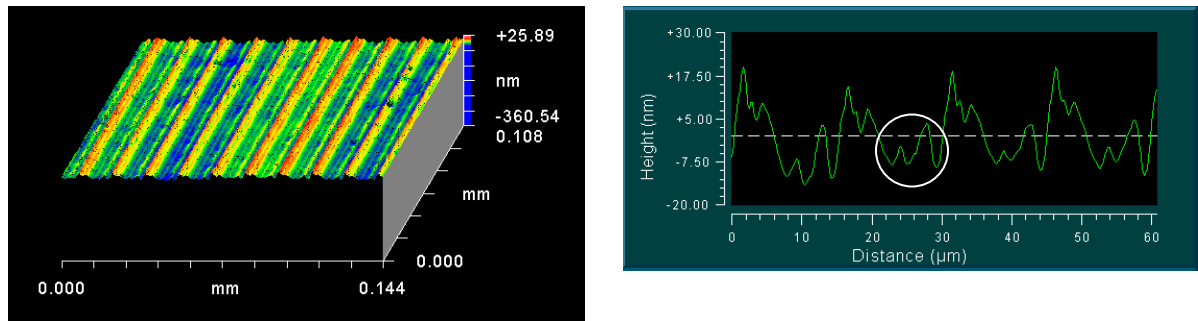


Figure 5.18. Profile of (100) Si surface machined at 15 $\mu\text{m}/\text{rev}$ feed with -45° tool. The encircled area due to tool damage is repeated in the next figure.

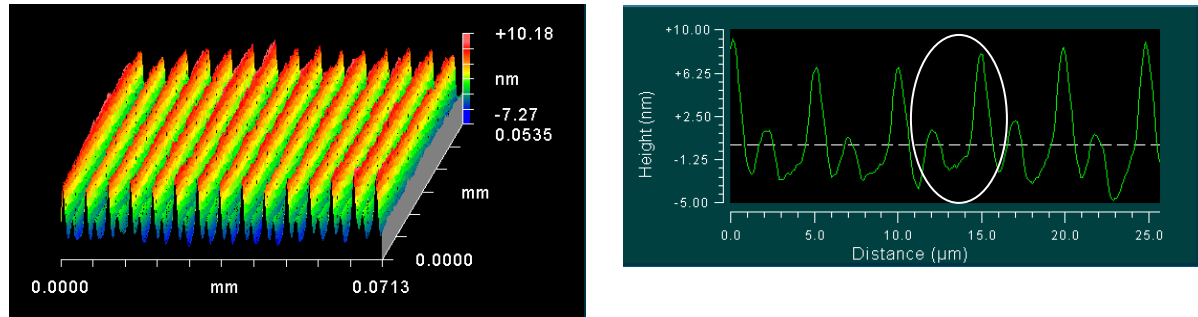


Figure 5.19. Profile of (100) Si surface machined at 5 $\mu\text{m}/\text{rev}$ feed with -45° tool. The encircled area is part of the patterned tool damage seen in the previous figure.

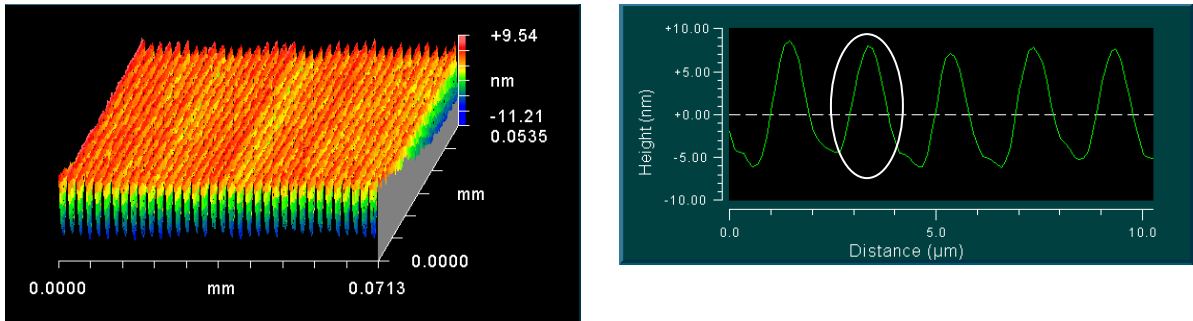


Figure 5.20. Profile of (100) Si surface machined at 2 $\mu\text{m}/\text{rev}$ feed with -45° tool. The encircled area is part of the patterned tool damage seen in the previous two figures.

Figures 5.21-5.23 show surface profiles of the (100) Si wafer turned with a -30° rake angle tool. The profile shape changes drastically as the feed rate decreases. Again, in each figure the surface profile is inconsistent with an ideal surface finish. The machining run was again affected by tool wear and subsequent damage that repeats itself in the surface. (5 $\mu\text{m}/\text{rev}$ contains surface features seen in 15 $\mu\text{m}/\text{rev}$) However this time, the feature seen in Figure 5.23 at 2 $\mu\text{m}/\text{rev}$ does not appear at any of the higher feed rates. This may be due to increased wear during the machining run which changed the shape of the damage in the tool between the 5 and 2 $\mu\text{m}/\text{rev}$ machining runs. The tool would have traveled an approximate 40-50 m between the two measurement points.

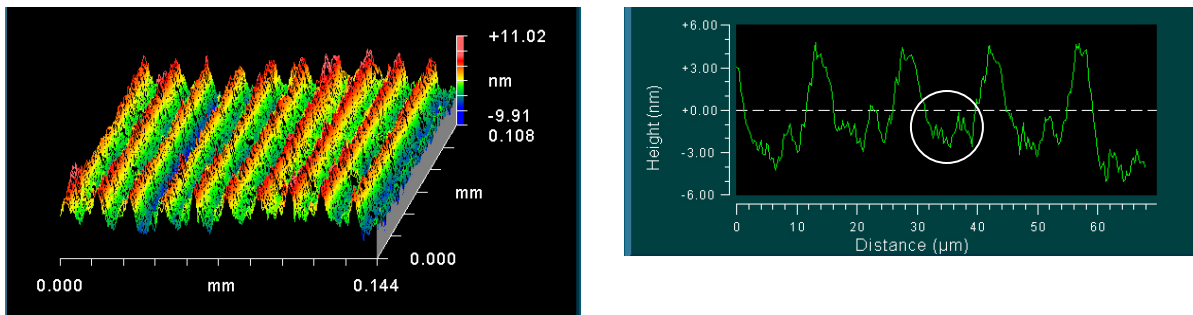


Figure 5.21. Profile of (100) Si surface machined at 15 $\mu\text{m}/\text{rev}$ feed with -30° tool. The encircled area due to tool damage is repeated in the next figure.

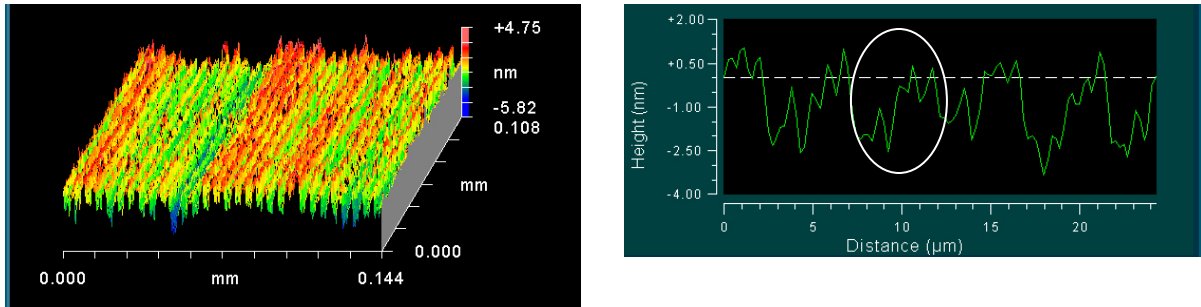


Figure 5.22. Profile of (100) Si surface machined at 5 $\mu\text{m}/\text{rev}$ feed with -30° tool. The encircled area is part of the patterned to tool damage seen in the previous figure.

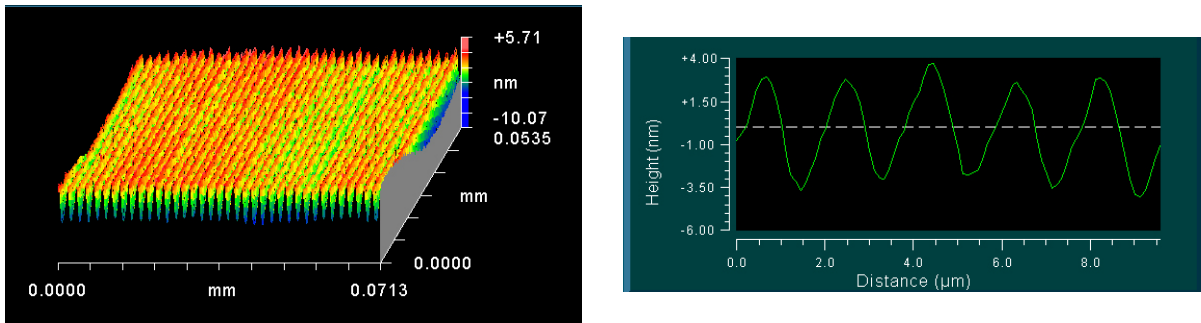


Figure 5.23. Profile of (100) Si surface machined at 2 $\mu\text{m}/\text{rev}$ feed with -30° tool. The features shown in the profile do not appear to be present at the higher feed rates, this may indicated that the damage may have been incurred between 5 and 2 $\mu\text{m}/\text{rev}$.

PV values will not be compared to theoretical values as the surface profiles are not ideal shape. The profiles contain markings and peaks due solely to damage of the tool tip.

Figure 5.24-26 show surface profiles of the (111) Si wafer turned with a -45° rake angle tool. In each figure the surface profile is inconsistent with a theoretical surface finish as the PV values are much greater than theoretical. This may be due deformation and elastic spring back resulting in larger PV values (non-ideal material removal.) This machining run did not seem to be affected by tool damage that plagued the previous two examples.

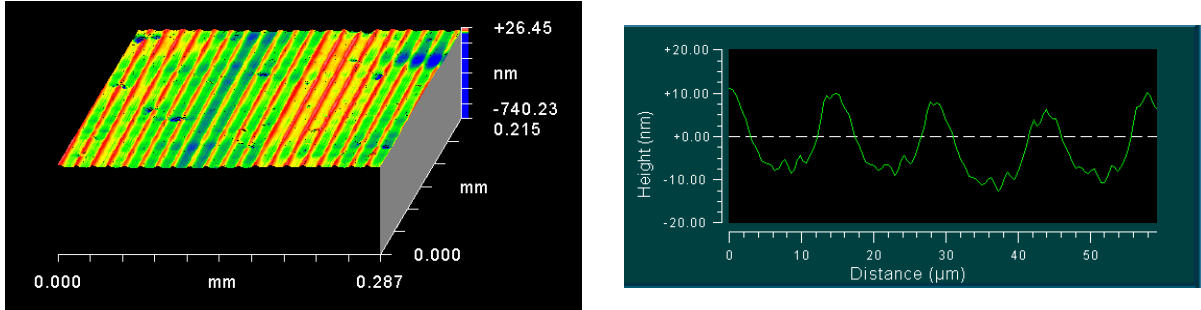


Figure 5.24. Profile of (111) Si surface machined at 15 um/rev feed with -45° tool.

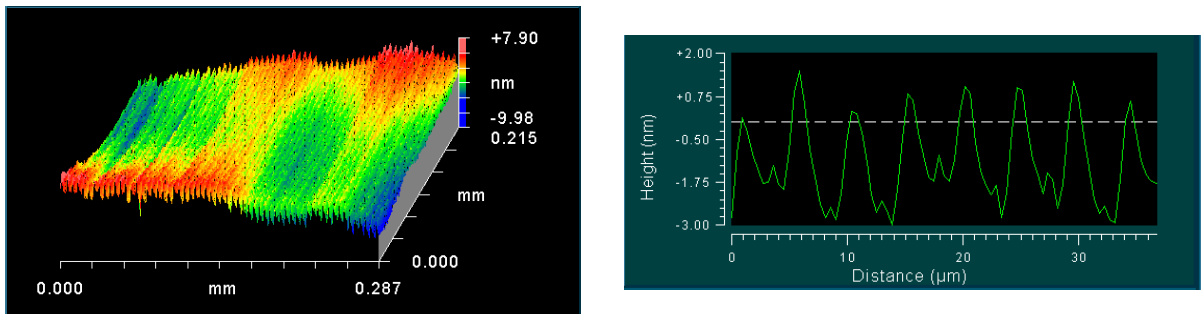


Figure 5.25. Profile of (111) Si surface machined at 5um/rev feed with -45° tool.

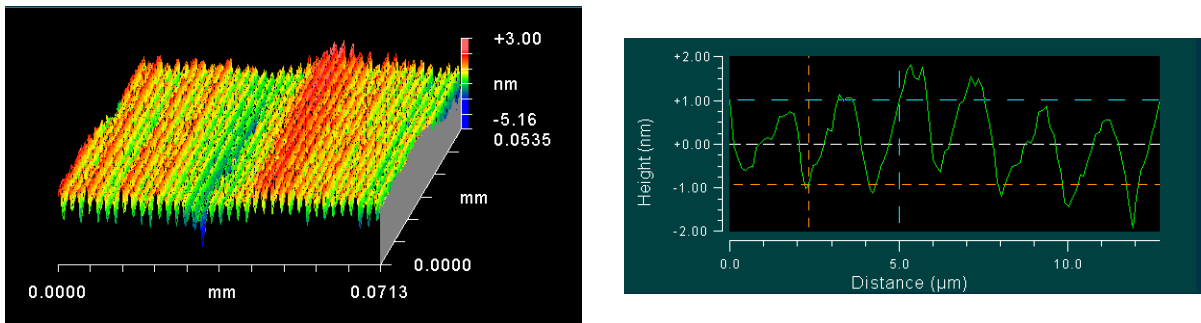


Figure 5.26. Profile of (111) Si surface machined at 2um/rev feed with -45° tool.

Figures 5.27-29 show surface profiles of the (111) Si wafer turned with a -30° rake angle tool. In each figure the surface profile is inconsistent with a theoretical surface finish as the PV values are much greater than theoretical. This also may be due deformation and elastic spring back resulting in larger PV values (non-ideal material removal.) This

machining run did not seem to be affected by tool damage that plagued the machining runs of the (100) wafers.

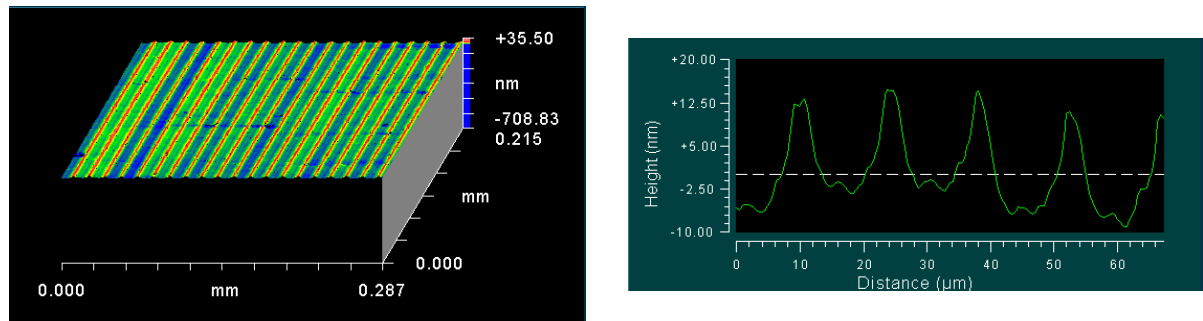


Figure 5.27. Profile of (111) Si surface machined at 15 $\mu\text{m}/\text{rev}$ feed with -30° tool.

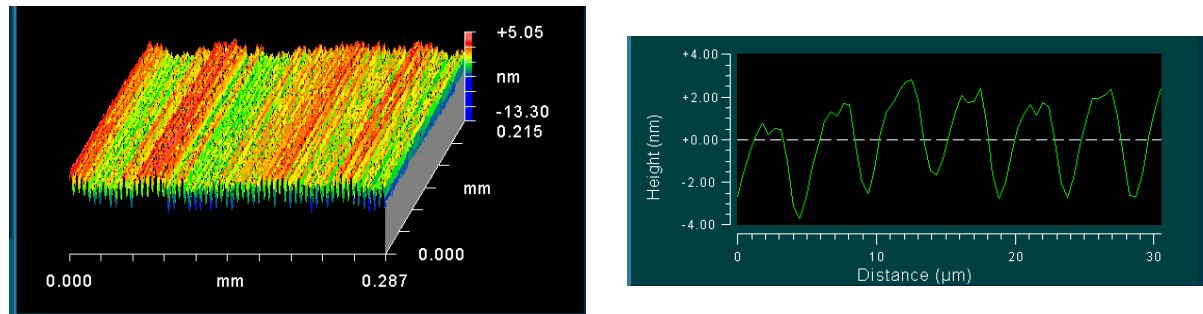


Figure 5.28. Profile of (111) Si surface machined at 5 $\mu\text{m}/\text{rev}$ feed with -30° tool.

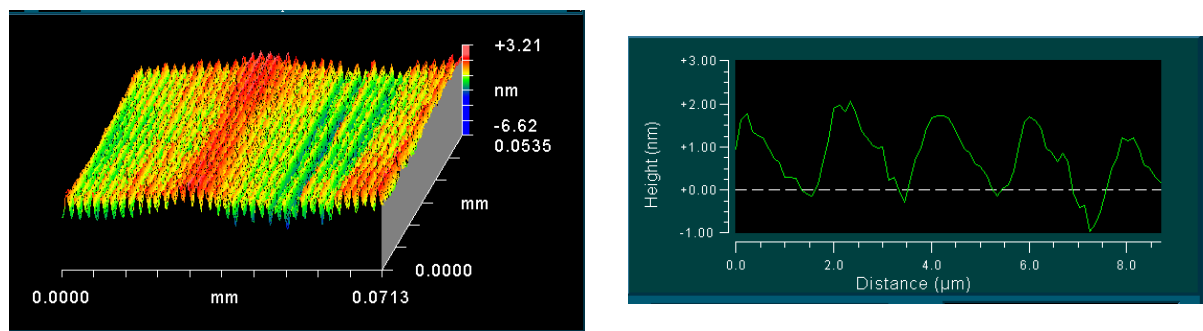


Figure 5.29. Profile of (111) Si surface machined at 2 $\mu\text{m}/\text{rev}$ feed with -30° tool.

Because the (111) wafers appear to have not been influenced by tip damage and resemble that of an ideal surface, comparison of PV values to a theoretical surface is appropriate. Figure 5.30 shows the comparison of PV achieved in the surface with that from Equation 5.1 where PV is peak to valley height (nm), f is the feed rate (um/rev), R is the tool radius and α is the rake angle. As expected, the achieved PV is higher than the theoretical.

$$PV \approx \frac{f^2}{8R} \cos \alpha \quad (5.1)$$

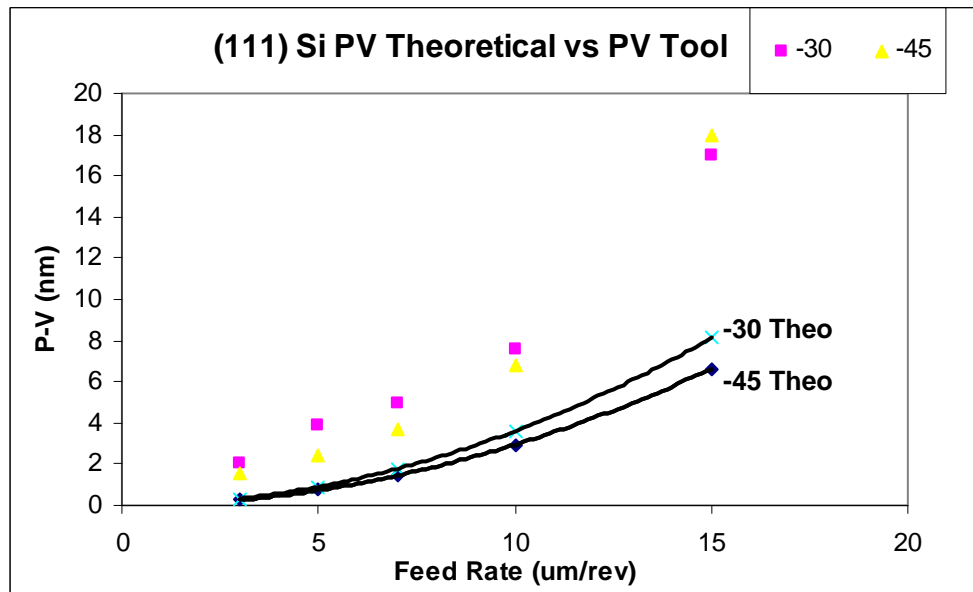


Figure 5.30. Comparison of PV values achieved during machining experiments of (111) Si with those obtained theoretically with Equation 5.1.

Though the features of the profiles between machining runs differ greatly, Figures 5.31-34 sum up the RMS values achieved for each. No comparison is appropriate between the runs as profile (chip shape) generation differed among the runs due to tip condition. The RMS values obtained for (100) with a -45° tool are greater than those achieved than both (111) machining runs as that run differs the greatest from ideal due to tip damage. Even

though -30° on (100) also appeared to suffer influence of a damage tip, the influence was much more negligible. It is apparent though that RMS and surface shape profile did not vary greatly between machining directions within a feed rate band. The two paths in each key indicate the direction along which measurements were taken in each machining band corresponding to those in the previous section (see Figures 5.7, 5.9, 5.11, 5.13.) Two distinct machining regions were measured for each orientation. The dashes indicate where pitting was substantial enough to influence the measurement.

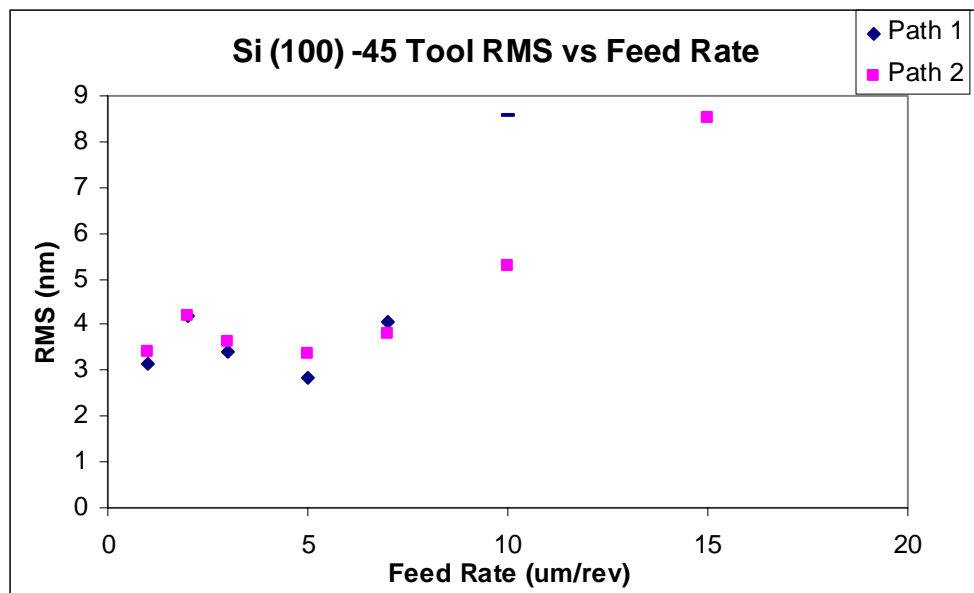


Figure 5.31. RMS versus feed rate and machining direction for a (100) Si wafer machined with a -45° rake angle tool.

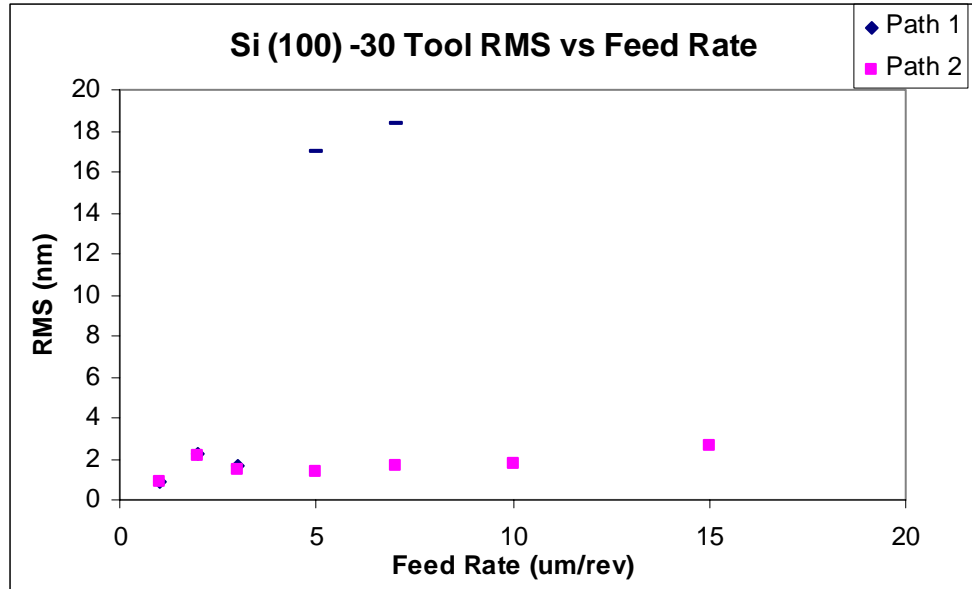


Figure 5.32. RMS versus feed rate and machining direction for a (100) Si wafer machined with a -30° rake angle tool.

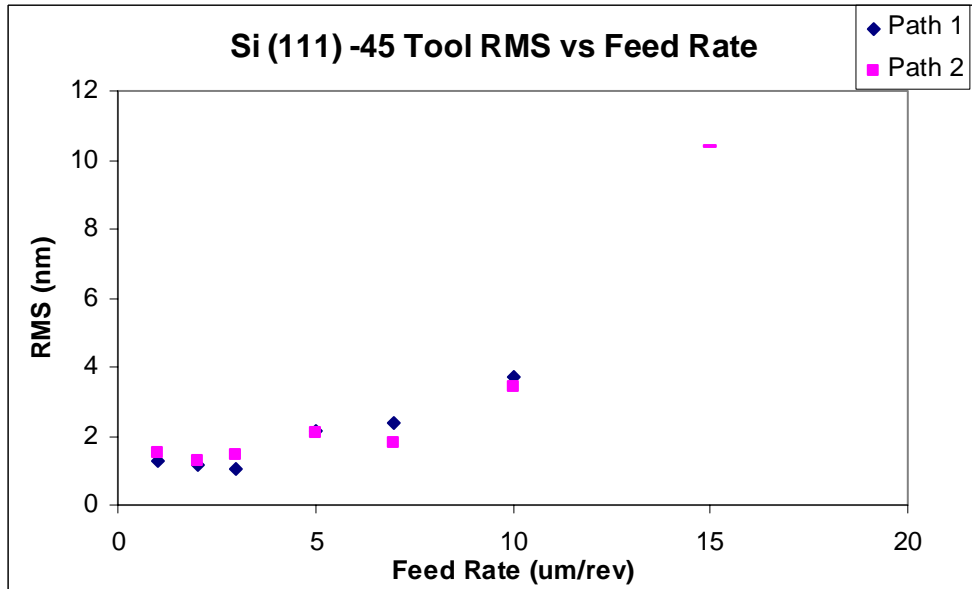


Figure 5.33. RMS versus feed rate and machining direction for a (111) Si wafer machined with a -45° rake angle tool.

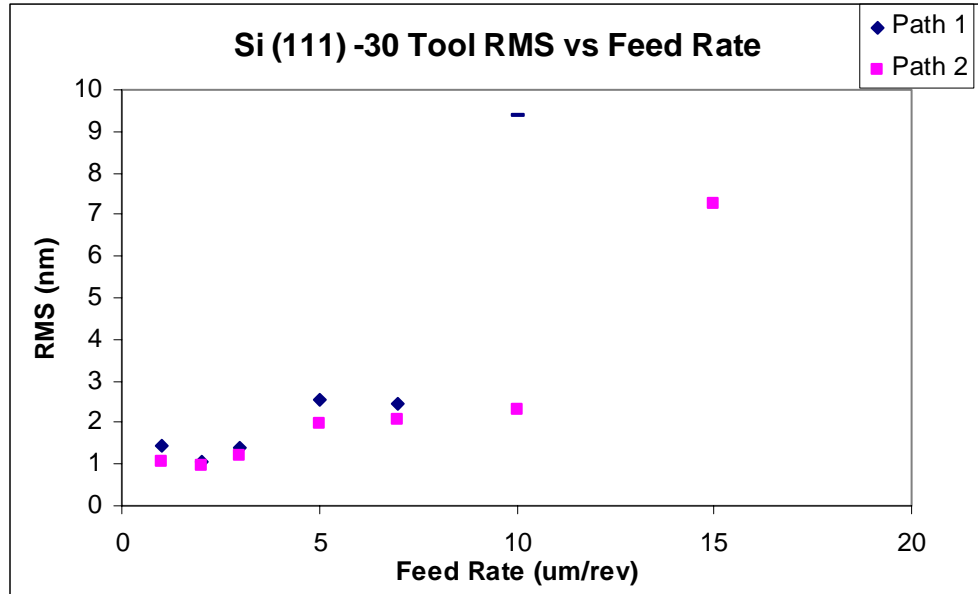


Figure 5.34. RMS versus feed rate and machining direction for a (111) Si wafer machined with a -30° rake angle tool.

Despite problems with tip wear, low RMS values ($<10\text{ nm}$ at 15 um/rev) were achieved where cutting was within the ductile regime. The introduction of fracture to the surface in the more susceptible cutting directions seemed to be the only limiting factor to using large feed rates for machining.

5.5.2 Raman Measurement of Machined Surface

Figure 5.35 shows the several Raman spectra taken on a ductile turned (100) surface machined with a -30° tool at various feed rates. The measurements were taken in the region where the cutting direction with the greatest propensity for ductile turning, $\langle 100 \rangle$. It is apparent that at each feed rate tested that there is a thin layer of amorphized material (resulting in the broadened peak at 480 Rcm^{-1}) at the surface, below which the material is dc crystalline (521 Rcm^{-1}). Laser power was altered to check if the noted peak was due to sample heating rather than amorphization. The peak did not shift, indicating that amorphous material does exist. There is a clear trend of increasing amorphous/dc crystalline

intensity as a function of decreasing feed rate. While intensity is an arbitrary value, it holds as a comparison of peak ratios. As the laser may penetrate through the amorphous layer, sampling of the underlying dc crystalline occurs. The observed trend may indicate that the thickness of the amorphous layer decreases with increasing feed rate in this case.

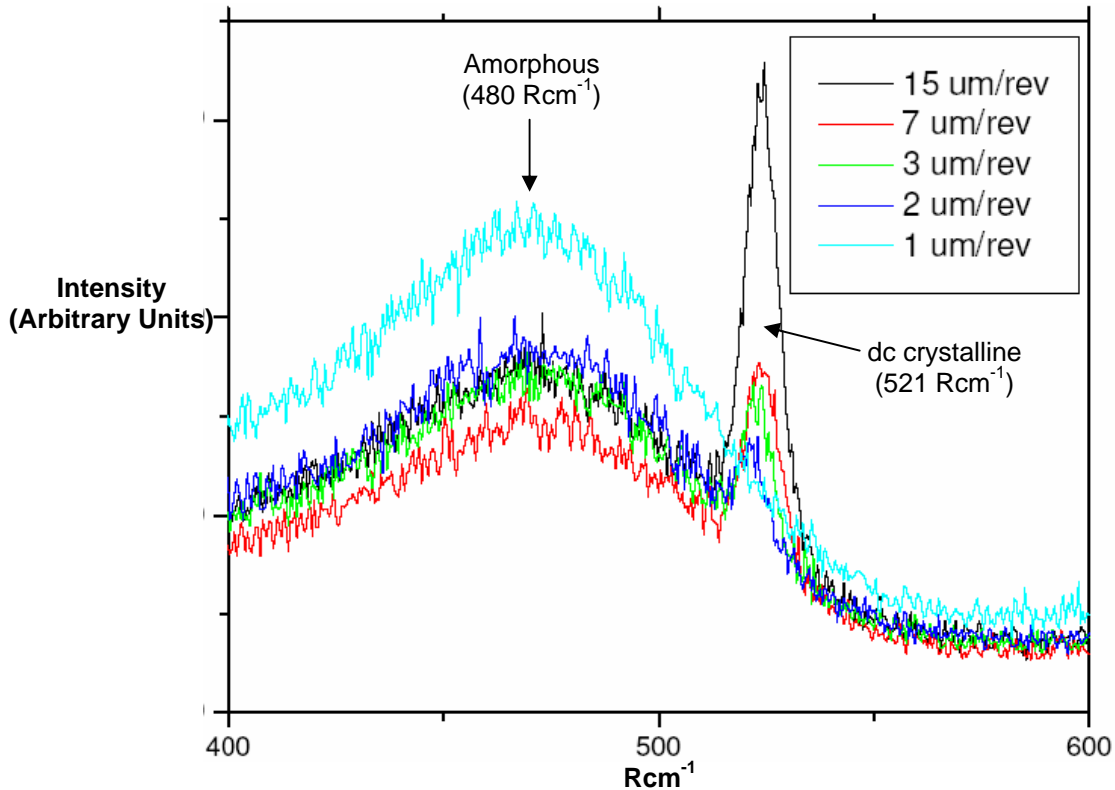


Figure 5.35. Raman spectra taken of a ductile turned (100) Si surface at various feed rates machined with a -30° tool.

Figure 5.36 shows the Raman spectra of the same wafer machined with a -45° tool at two different feed rates, 1 and 5 um/rev taken along the same direction, <100>. It is much less evident in this figure of an indication of an amorphized layer. There appears to be a slight broadened peak at 480 Rcm⁻¹ for the 1um/rev feed rate which seems to be absent at 5 um/rev feed rate. The conclusion could be drawn from the spectra that an amorphous layer exists at the surface for areas machined with a 1 um/rev feed rate, but not so for the higher feed rate. The amorphous layer still likely exists at the higher feed rate due to the ductile

nature of the material removal, but it may be too thin for the detection proficiency of the Raman unit.

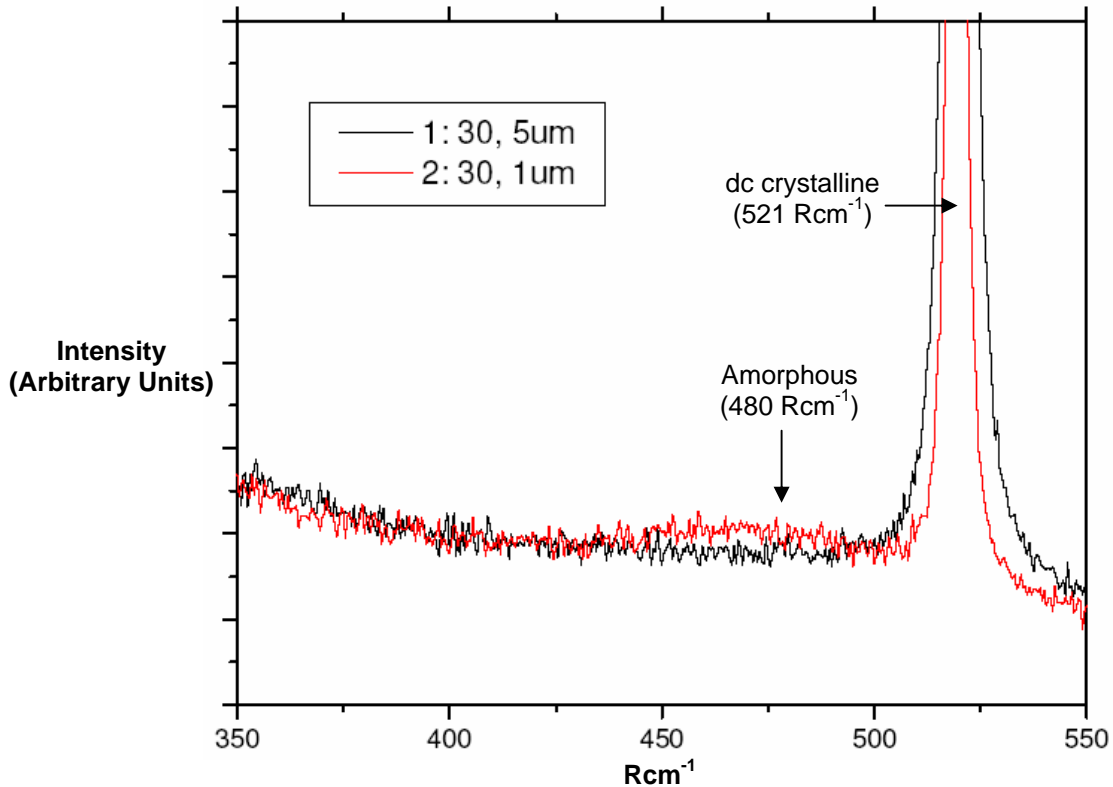


Figure 5.36. Raman spectra taken of a ductile turned (100) Si surface at two feed rates machined with a -45° tool.

A comparison of the ratio of amorphous to crystalline intensity between the two tools at 1 and 5 um/rev feed rates could show that the amorphized layer for the -30° is much thicker than that of the -45°. It is however imprudent to account this solely to the difference in rake angle. Little is known about the tip condition at the time it machined the measured areas. Silicon wears the tip aggressively thus making it difficult to know the sharpness of the tool, or whether damage was incurred. Because the machining forces are highly dependent on the condition of the tip, the stress states imposed on the materials will differ largely. This may result in different material accommodation mechanisms, specifically the size of the transformation zone, making comparison between machining runs difficult.

Figure 5.37 is Raman spectra taken of two different machining runs (one with a -30° rake angle tool, the other with -45°) at 1 and 5 $\mu\text{m}/\text{rev}$ feed rates for a (111) wafer. Measurements were taken along the $<112>$ direction (where cutting would be in a $<110>$ direction.) No definitive conclusion can be drawn as to the existence of the amorphized layer for this orientation as it is difficult to substantiate a peak at 480 Rcm^{-1} . Again it is thought that the amorphous layer may still be present (as ductile regime material removal was achieved for these conditions,) but too thin to be capably detected. As a result no conclusion can be drawn and a comparison of the transformation zone thicknesses between wafer orientations cannot be made.

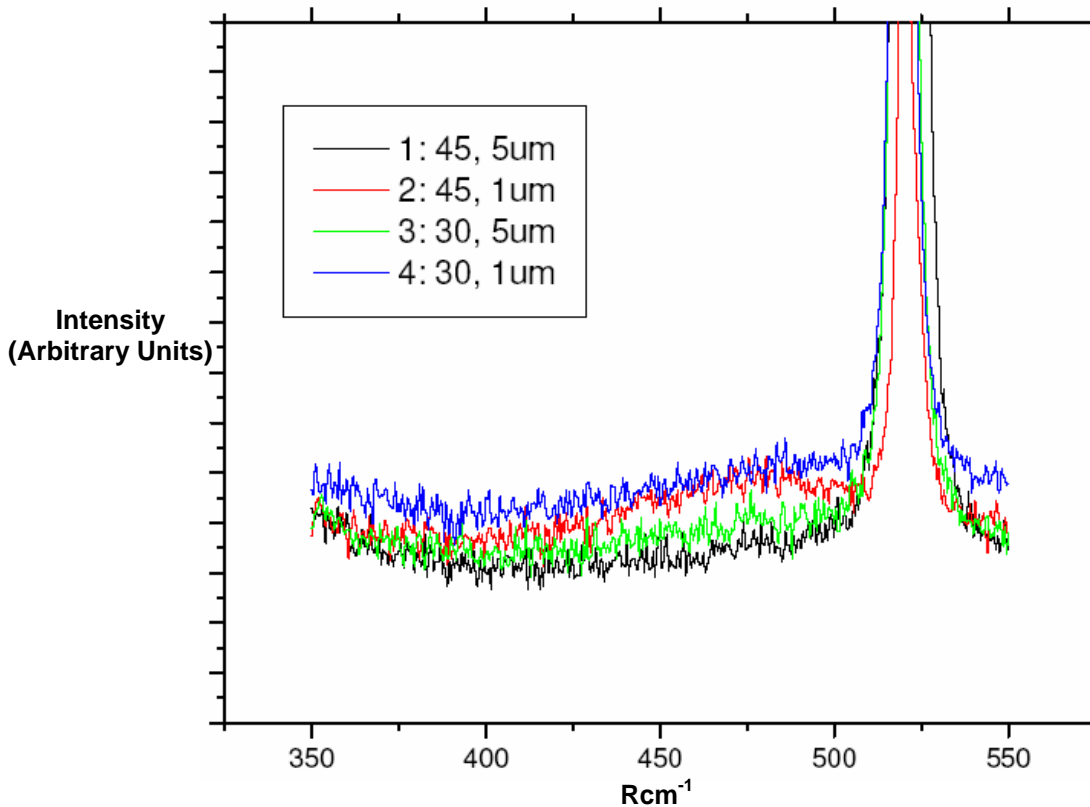


Figure 5.37. Raman spectra taken of a ductile turned (111) Si surface at two feed rates machined with -30° and -45° tools.

5.6 Experimental Results and Discussion (Germanium Surfaces)

5.6.1 Machining Behavior/ Material Response

Parameter Effects

Figure 5.38 is an illustration of a (100) Ge wafer face with machining bands made at the various feed rates indicated with a -30° rake angle tool. The four-fold fracture pattern symmetry (full pattern is overlaid on the figure) seen at higher feed rates is consistent with previous research. [24, 26, 60]

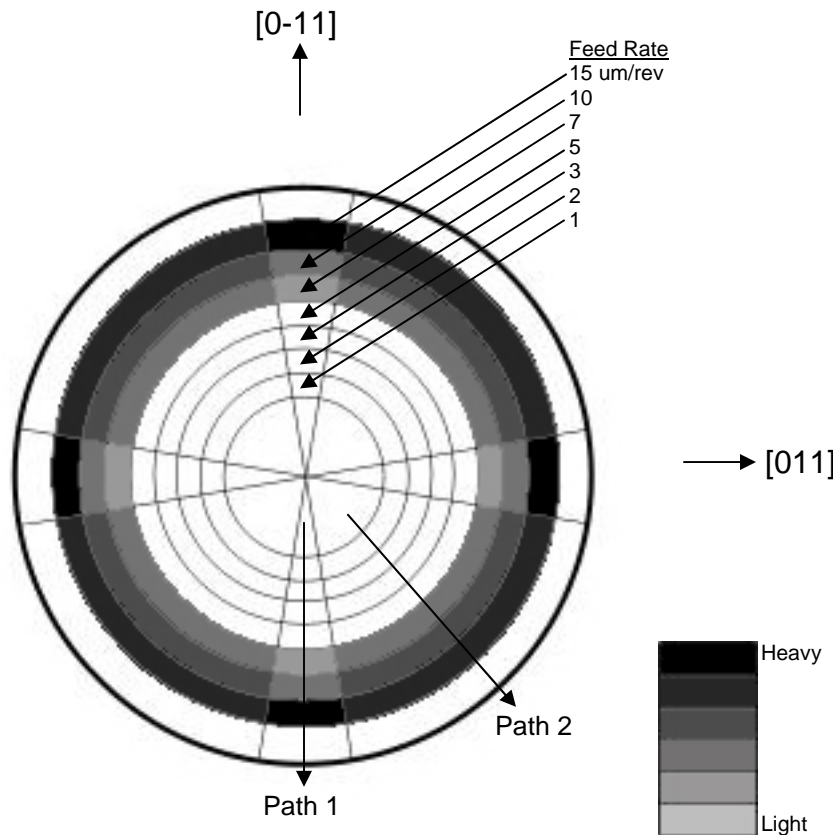


Figure 5.38. Illustration of fracture pattern on (100) Ge machined with a -30° rake angle tool. White areas indicate no pitting. Grey scale indicates severity of pitting.

Figures 5.39 (a.) and (b.) are collages of Nomarski micrographs taken along paths 1 and 2 (two distinct regions of machining behavior,) respectively. Path 1 is taken along regions thought to be where the cutting direction of the tool is oriented along the $<110>$ directions on

the wafer face. Path 2 is thought to be along regions where the cutting direction is in the <100> directions. (The assignment of directions is based on previous work, as there were no wafer flats. Also, a diffraction method for identification was not available.)

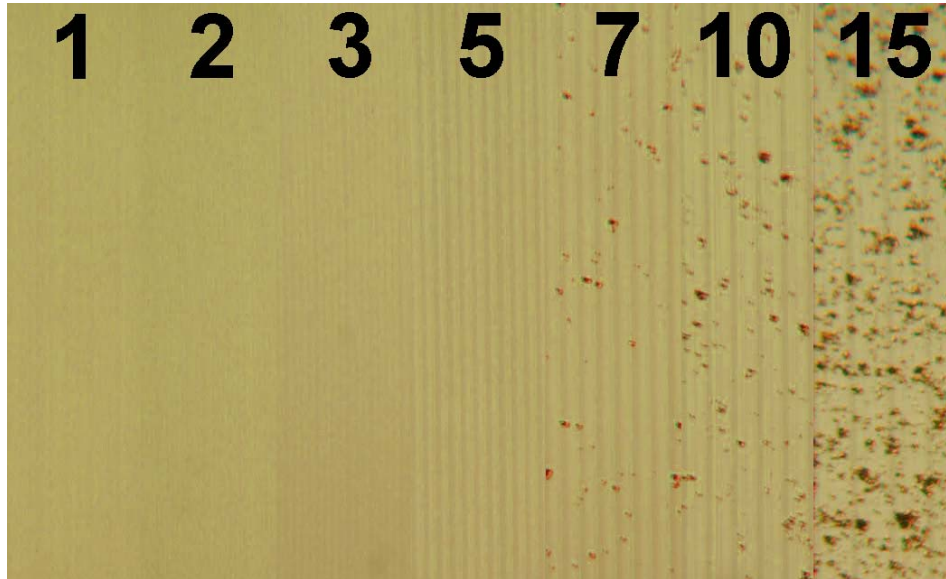


Figure 5.39(a.) Collage of micrographs depicting surface of (100) Ge diamond turned at various feed rates (um/rev) with -30° rake angle tool. (**Path 1**)

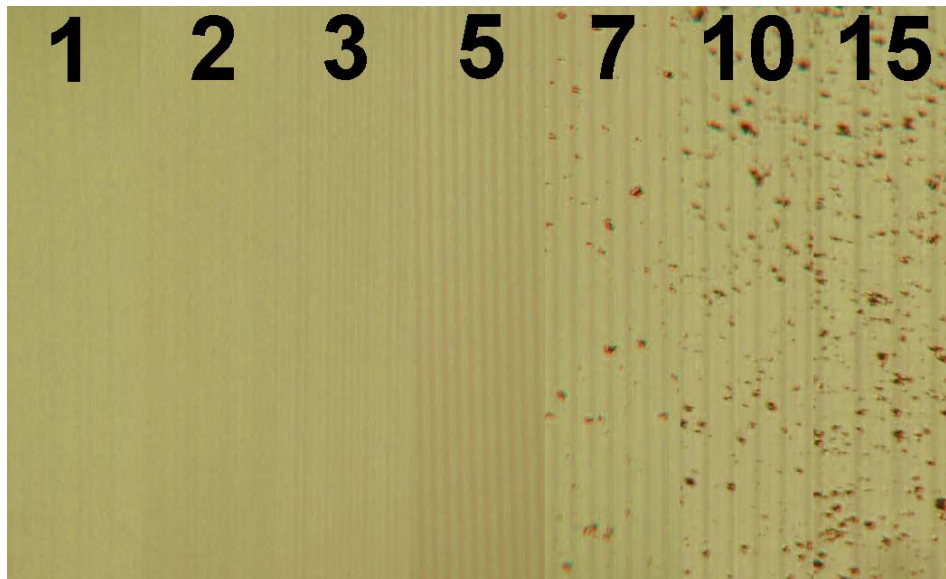


Figure 5.39(b.) Collage of micrographs depicting surface of (100) Ge diamond turned at various feed rates (um/rev) with -30° rake angle tool. (**Path 2**)

Figures 5.39 (a.) and (b.) show the progression of material response from purely ductile surface to a pitting response at higher feed rates. Both paths see the onset of pitting at 7 $\mu\text{m}/\text{rev}$, with pitting density increasing with feed rate. The density of pitting seems to be higher for path 2 at 7 and 10 $\mu\text{m}/\text{rev}$, but at 15 $\mu\text{m}/\text{rev}$ the pitting becomes more severe in path 1.

Figure 5.40 is an illustration of a (100) Ge wafer face with machining bands made at the various feed rates indicated with a -45° rake angle tool. The four-fold fracture pattern symmetry (full pattern is overlaid on the figure) is seen again, but not until a feed rate of 15 $\mu\text{m}/\text{rev}$.

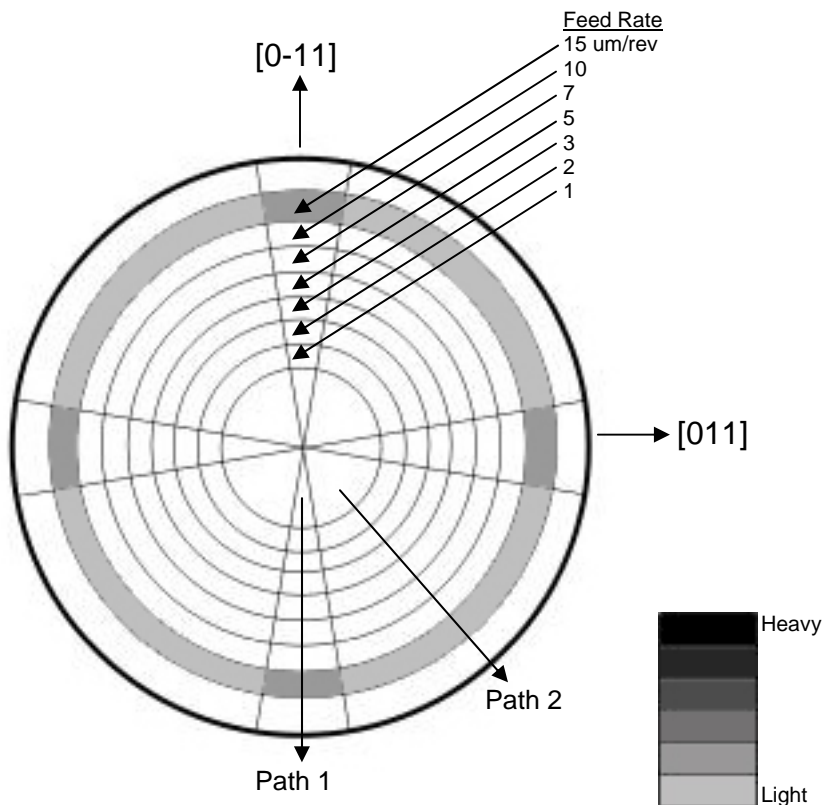


Figure 5.40. Illustration of fracture pattern on (100) Ge machined with a -45° rake angle tool. White areas indicate no pitting. Grey scale indicates severity of pitting.

Figures 5.41 (a.) and (b.) are collages of Nomarski micrographs taken along paths 1 and 2 (two distinct regions of machining behavior,) respectively. Again, path 1 is taken along regions thought to be where the cutting direction of the tool is oriented along the $<110>$ directions on the wafer face. Path 2 is thought to be along regions where the cutting direction is in the $<100>$ directions.

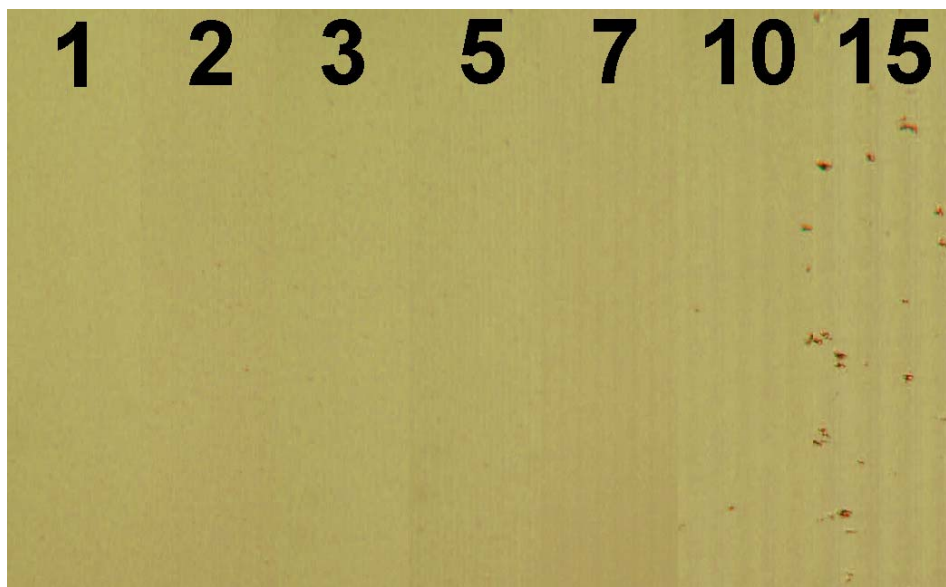


Figure 5.41(a.) Collage of micrographs depicting surface of (100) Ge diamond turned at various feed rates (um/rev) with -45° rake angle tool. (**Path 1**)

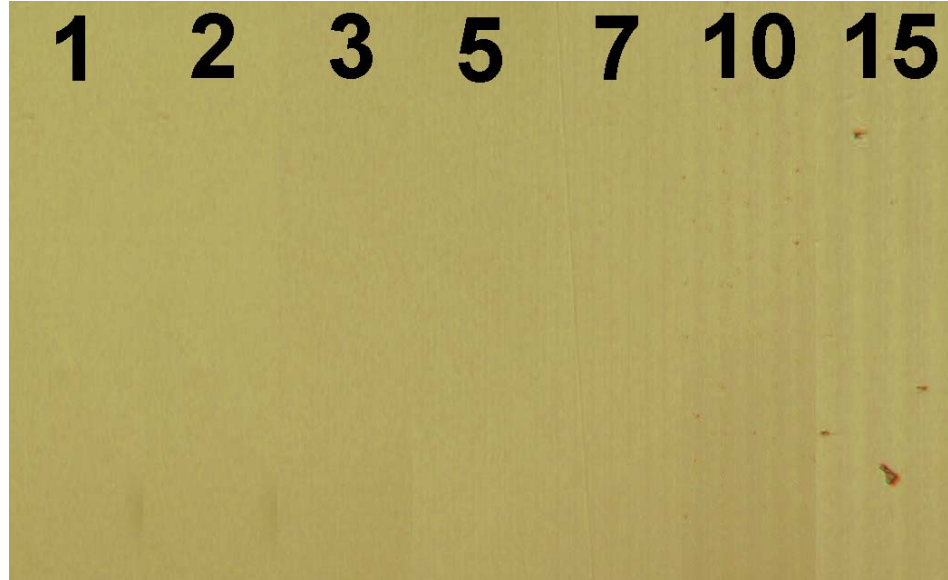


Figure 5.41(b.) Collage of micrographs depicting surface of (100) Ge diamond turned at various feed rates (um/rev) with -45° rake angle tool. (**Path 2**)

Figures 5.41 (a.) and (b.) show the progression of material response from purely ductile surface to a pitting response at 15 um/rev. The density of pitting is higher at 15 um/rev along path 1 than path 2.

Figure 5.42 is an illustration of a (110) Ge wafer face with machining bands made at the various feed rates indicated with a -30° rake angle tool. The two-fold fracture pattern symmetry (full pattern is overlaid on the figure) seen at higher feed rates is consistent with previous research. [24, 26, 60]

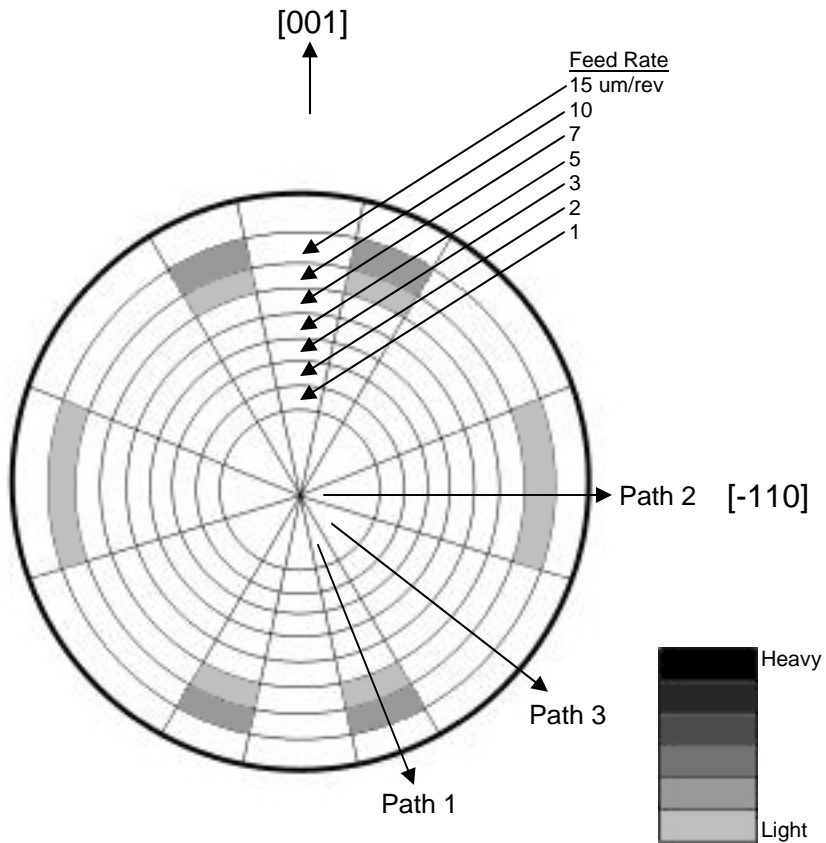


Figure 5.42. Illustration of fracture pattern on (110) Ge machined with a -30° rake angle tool. White areas indicate no pitting. Grey scale indicates severity of pitting.

Figures 5.43 (a.) and (b.) are collages of Nomarski micrographs taken along paths 1 and 2 (two distinct regions of machining behavior,) respectively. Path 1 is taken along regions thought to be where the cutting direction of the tool is oriented along the $<111>$ directions on the wafer face. Path 2 is thought to be along regions where the cutting direction is in the $<100>$ directions. Path 3 is though to be along regions where the cutting direction is in the $<112>$ directions.

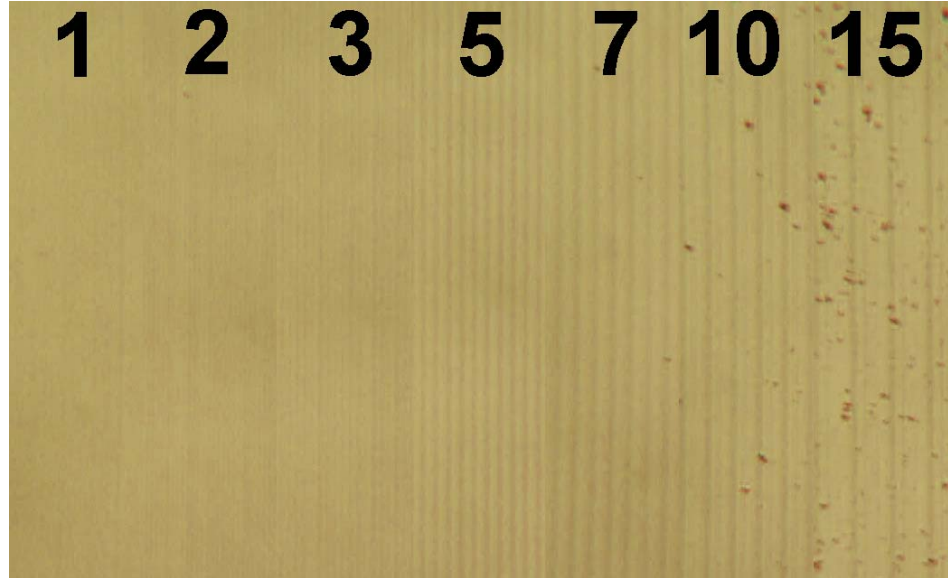


Figure 5.43(a.) Collage of micrographs depicting surface of (110) Ge diamond turned at various feed rates (um/rev) with -30° rake angle tool. (**Path 1**)

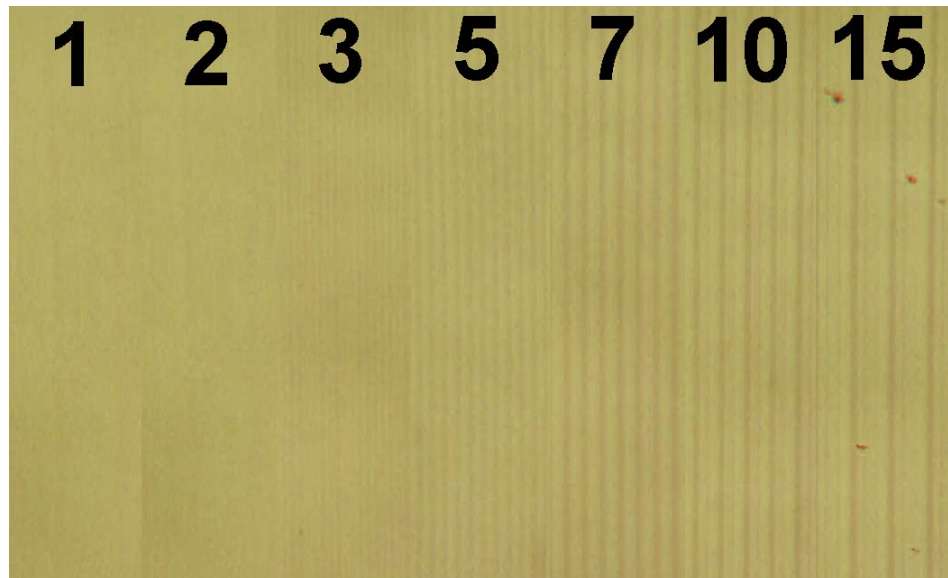


Figure 5.43(b.) Collage of micrographs depicting surface of (110) Ge diamond turned at various feed rates (um/rev) with -30° rake angle tool. (**Path 2**)



Figure 5.43(c.) Collage of micrographs depicting surface of (110) Ge diamond turned at various feed rates (um/rev) with -30° rake angle tool. (**Path 3**)

Figures 5.43 (a.) and (b.) show the progression of material response from purely ductile surface to a pitting response at higher feed rates. Pitting occurs along path 1 at 10 um/rev and increases in severity at 15 um/rev. Small amounts of pitting occur only at 15 um/rev along path 2. The density of pitting is higher at 15 um/rev along path 1 than path 2.

Figure 5.44 is an illustration of a (110) Ge wafer face with machining bands made at the various feed rates indicated with a -45° rake angle tool. The four-fold fracture pattern symmetry (full pattern is overlaid on the figure) is seen again at a feed rate of 15 um/rev.

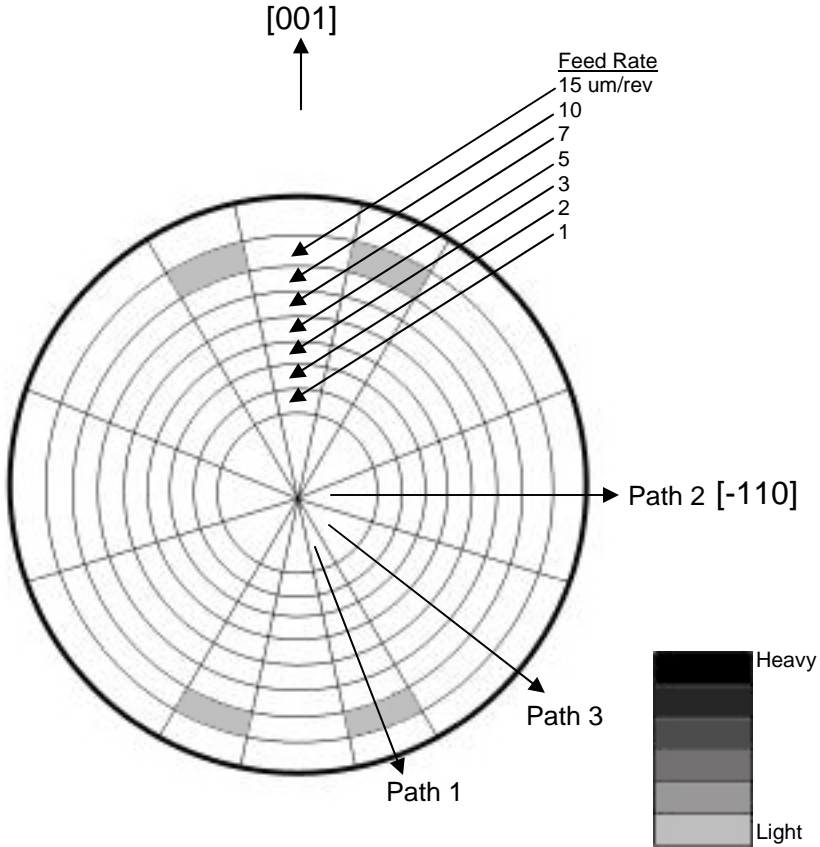


Figure 5.44. Illustration of fracture pattern on (110) Ge machined with a -45° rake angle tool. White areas indicate no pitting. Grey scale indicates severity of pitting.

Figures 5.45 (a.) and (b.) are collages of Nomarski micrographs taken along paths 1 and 2 (two distinct regions of machining behavior,) respectively. Again, path 1 is taken along regions thought to be where the cutting direction of the tool is oriented along the $<111>$ directions on the wafer face. Path 2 is thought to be along regions where the cutting direction is in the $<100>$ directions. Path 3 is thought to be along regions where the cutting direction is in the $<112>$ directions.

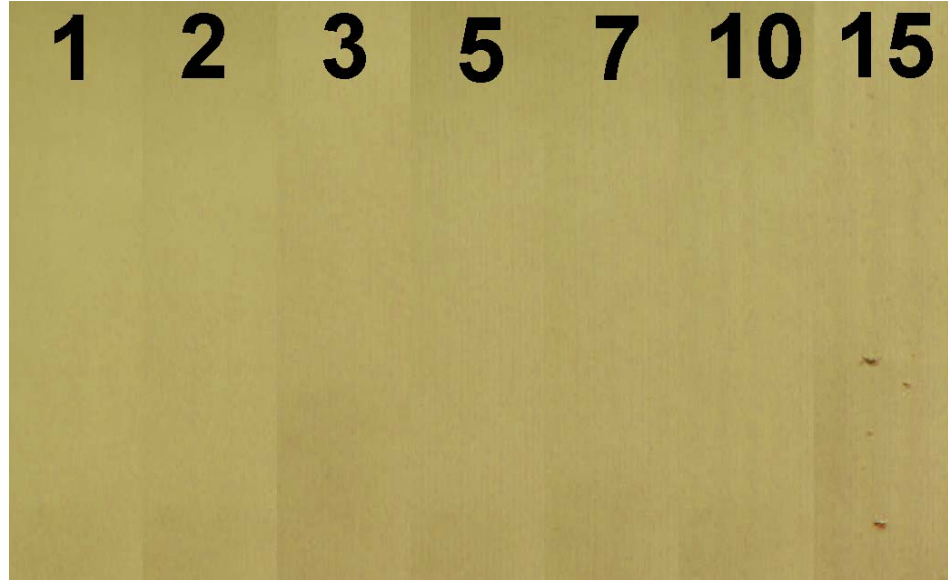


Figure 5.45(a.) Collage of micrographs depicting surface of (110) Ge diamond turned at various feed rates (um/rev) with -45° rake angle tool. (**Path 1**)

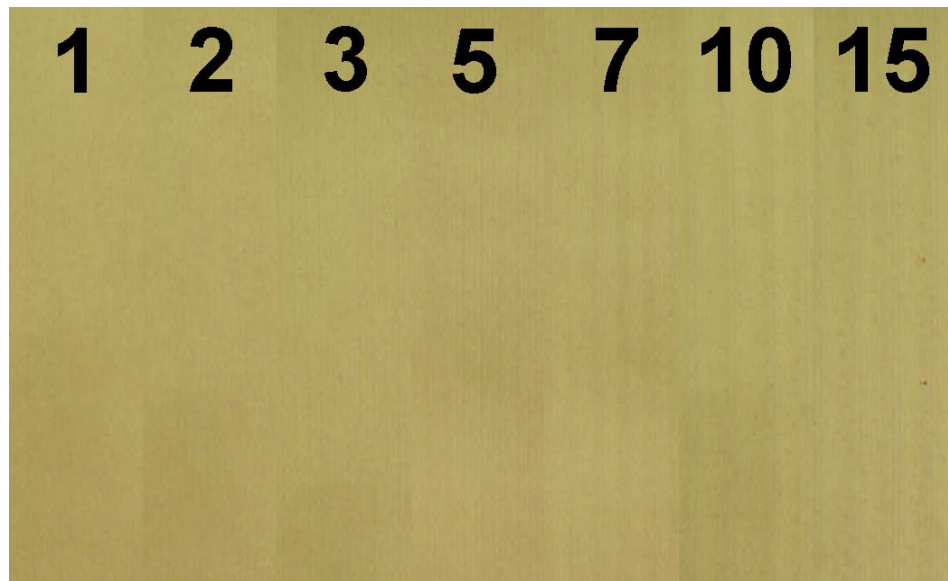


Figure 5.45(b.) Collage of micrographs depicting surface of (110) Ge diamond turned at various feed rates (um/rev) with -45° rake angle tool. (**Path 2**)

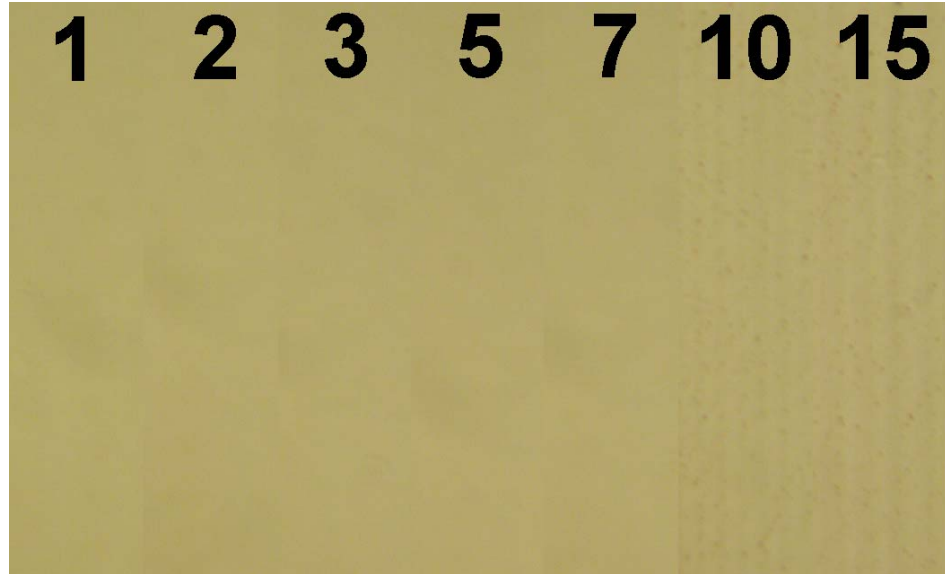


Figure 5.45(c.) Collage of micrographs depicting surface of (110) Ge diamond turned at various feed rates (um/rev) with -45° rake angle tool. (**Path 3**)

Figures 5.45 (a.) and (b.) show the progression of material response from purely ductile surface to a small pitting response at 15 um/rev along path 1. Feed rates above those tested would result in increased presence of pitting.

Figure 5.46 is an illustration of a (111) Ge wafer face with machining bands made at the various feed rates indicated with a -30° rake angle tool. The three-fold fracture pattern symmetry (full pattern is overlaid on the figure) seen at higher feed rates is consistent with previous research. [24, 26, 60]

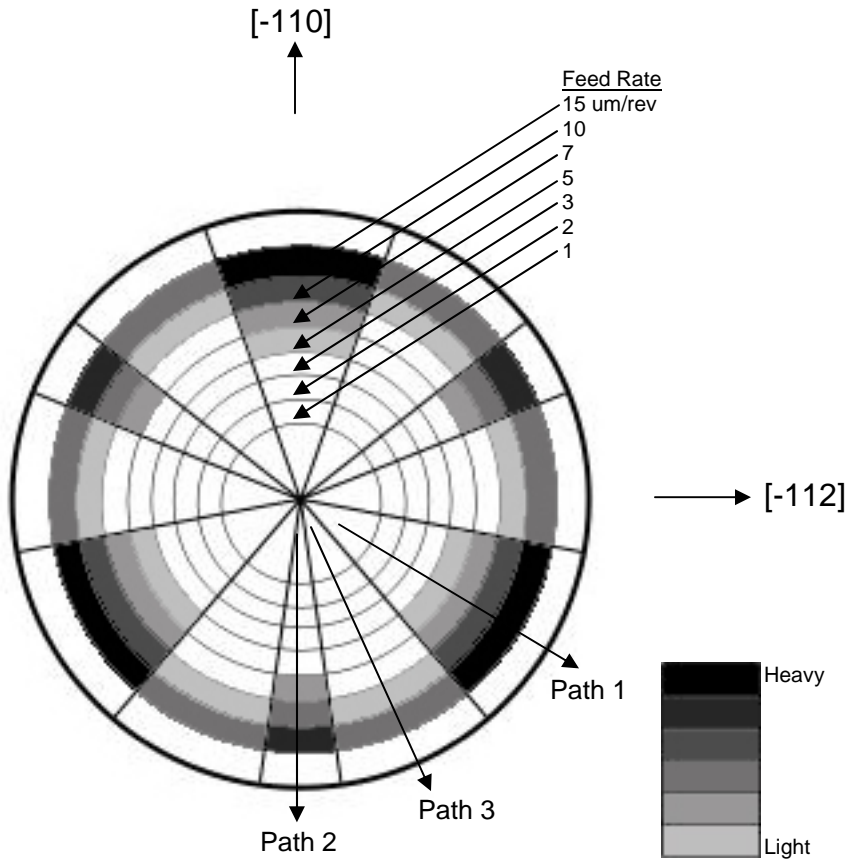


Figure 5.46. Illustration of fracture pattern on (111) Ge machined with a -30° rake angle tool. White areas indicate no pitting. Grey scale indicates severity of pitting.

Figures 5.47 (a.) and (b.) are collages of Nomarski micrographs taken along paths 1 and 2 (two distinct regions of machining behavior,) respectively. Both path 1 and 2 are along regions where the cutting direction of the tool is oriented along $<112>$ directions, but due to the three-fold symmetry, for example, [11-2] will have a vastly different response than [-1-12], the opposite cutting direction. Path 3 is along regions where the cutting direction of tool is oriented along $<110>$ directions.

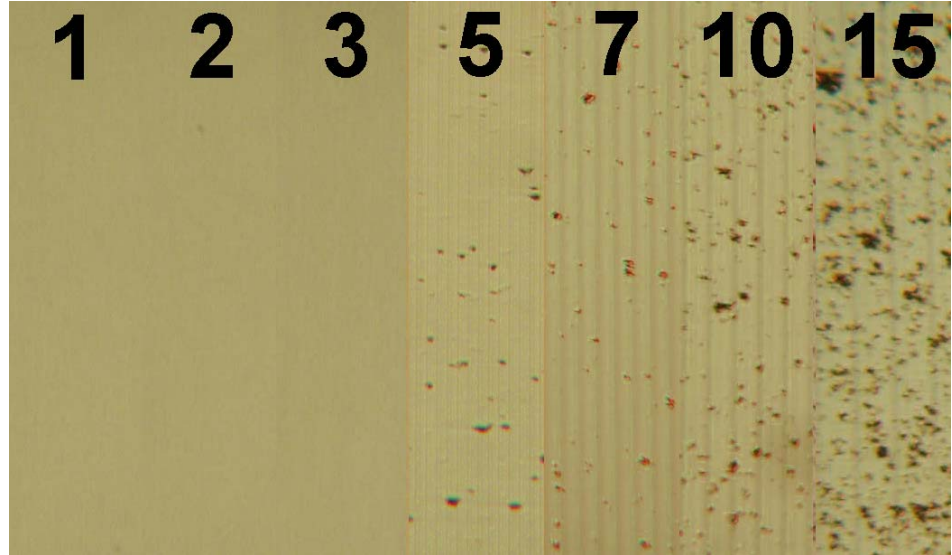


Figure 5.47(a.) Collage of micrographs depicting surface of (111) Ge diamond turned at various feed rates ($\mu\text{m/rev}$) with -30° rake angle tool. **(Path 1)**

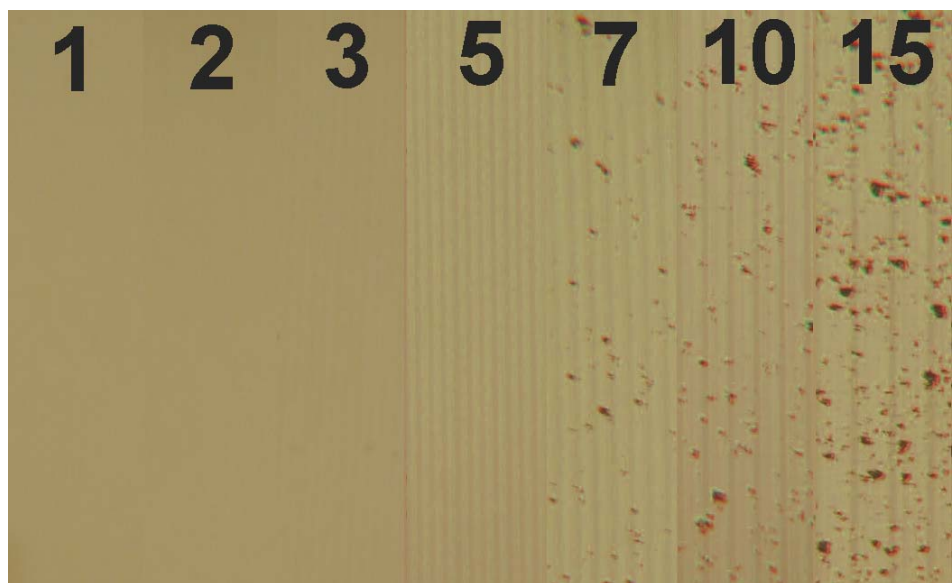


Figure 5.47(b.) Collage of micrographs depicting surface of (111) Ge diamond turned at various feed rates ($\mu\text{m/rev}$) with -30° rake angle tool. **(Path 2)**

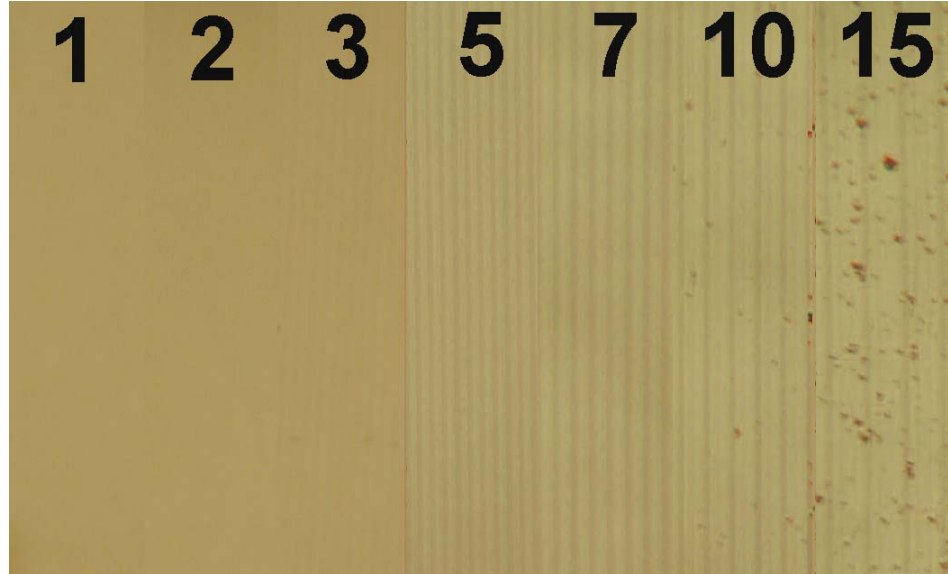


Figure 5.47(c.) Collage of micrographs depicting surface of (111) Ge diamond turned at various feed rates (um/rev) with -30° rake angle tool. (**Path 3**)

Figures 5.47 (a.) and (b.) show the progression of material response from purely ductile surface to a pitting response at higher feed rates. Path 1 sees the onset of fracture at 5 um/rev, path 2 sees the onset of pitting at 7 um/rev, and path 3 sees the onset of pitting at 10 um/rev; each with pitting density increasing with feed rate. The density of pitting seems to be highest for path 1, slightly less for path 2, and the least for path 3 for equivalent feed rates.

Figure 5.48 is an illustration of a (111) Ge wafer face with machining bands made at the various feed rates indicated with a -45° rake angle tool. The three-fold fracture pattern symmetry (full pattern is overlaid on the figure) is seen again at higher feed rates.

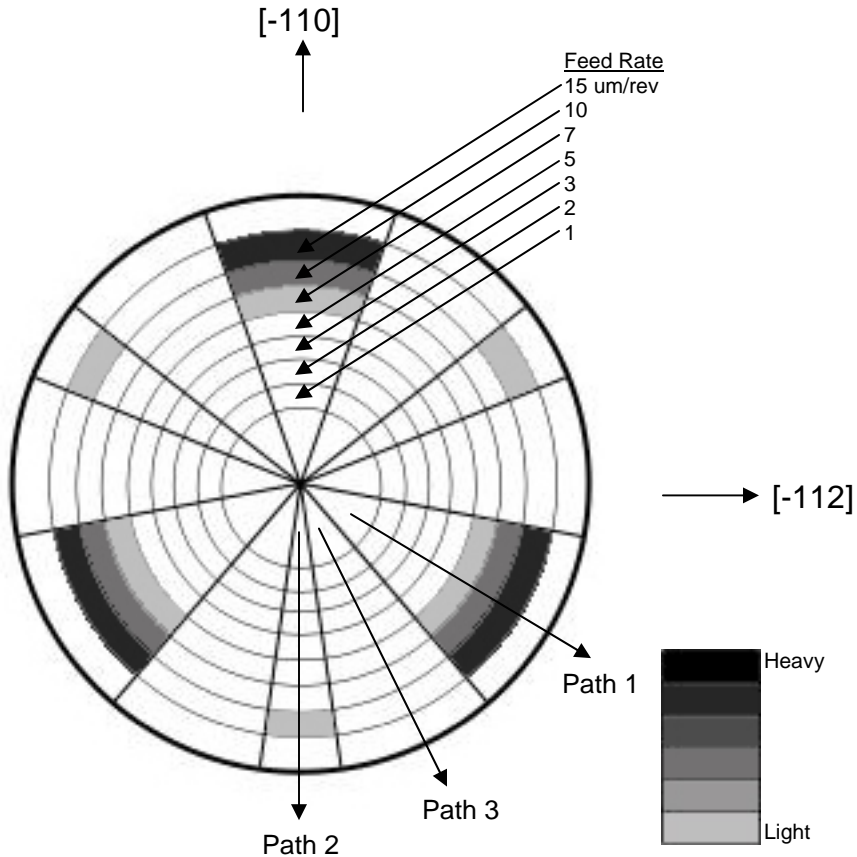


Figure 5.48. Illustration of fracture pattern on (111) Ge machined with a -45° rake angle tool. White areas indicate no pitting. Grey scale indicates severity of pitting.

Figures 5.49 (a.), (b.) and (c.) are collages of Nomarski micrographs taken along paths 1, 2 and 3 (three distinct regions of machining behavior,) respectively. Again, path 1 and 2 are along regions where the cutting direction of the tool is oriented along $\langle 112 \rangle$ directions and path 3 is along regions where the cutting direction of the tool is oriented along $\langle 110 \rangle$ directions.

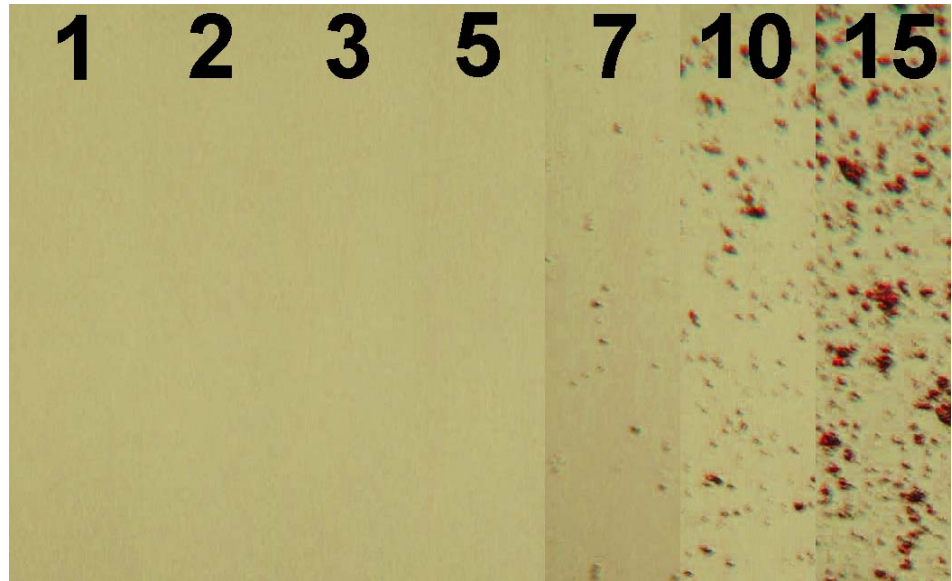


Figure 5.49(a.) Collage of micrographs depicting surface of (111) Ge diamond turned at various feed rates (um/rev) with -45° rake angle tool. (**Path 1**)

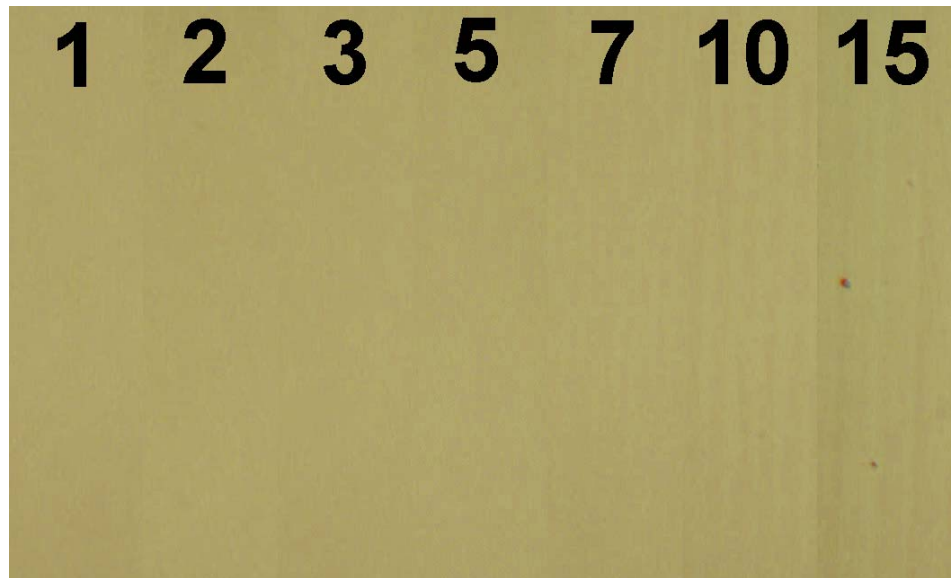


Figure 5.49(b.) Collage of micrographs depicting surface of (111) Ge diamond turned at various feed rates (um/rev) with -45° rake angle tool. (**Path 2**)

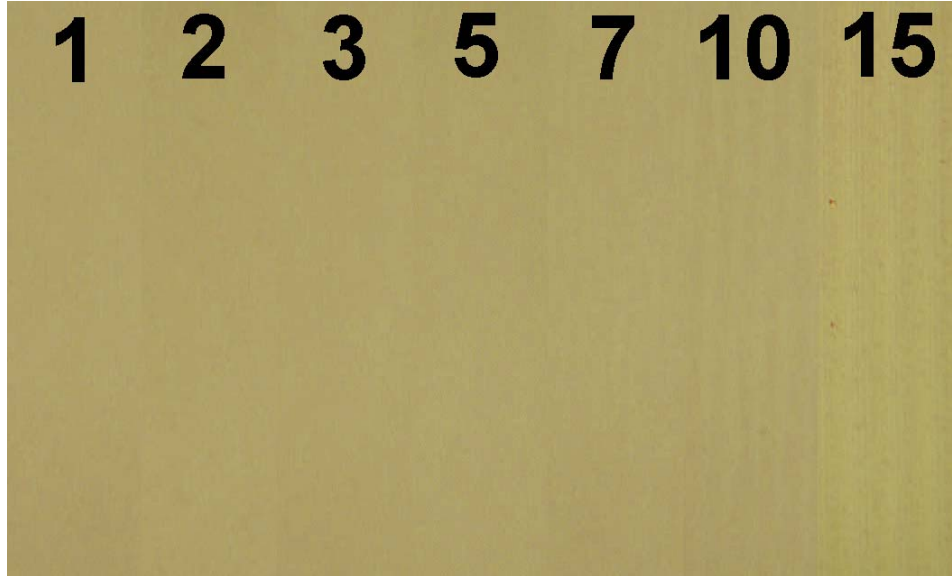


Figure 5.49(c.) Collage of micrographs depicting surface of (111) Ge diamond turned at various feed rates (um/rev) with -45° rake angle tool. **(Path 3)**

Figure 5.49 (a.) shows the progression of material response from purely ductile surface to a small pitting response at 7 um/rev along path 1. Increasing feed rate created high density pitting along this path. A few random pits were seen at 15 um/rev along path 2. Path 3 remains purely ductile through the range tested.

The fracture pattern symmetries for (100), (110) and (111) can again be interpreted by the crystal orientation/stress model proposed by Blackley. The stress orientation factor plots corroborate well with the behavior seen during machining of these orientations. Figure 5.50 is stress orientation factors as a function of rotation around the crystal face for the (110) orientation and corresponding observation by Blackley. [26, 61]

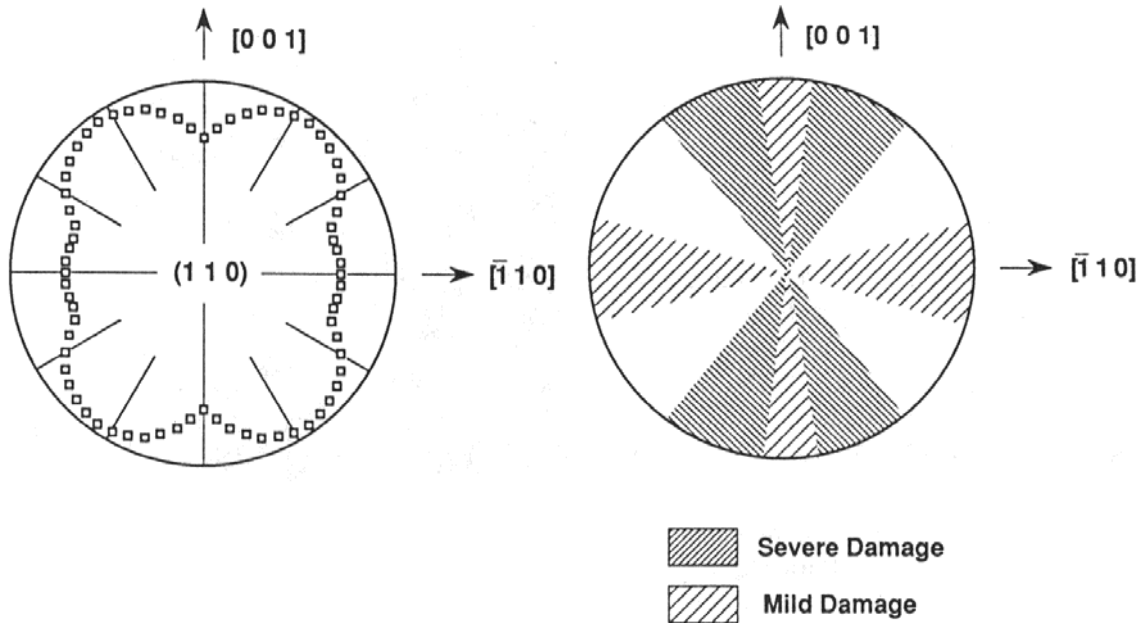


Figure 5.50. Stress orientation factor accompanied by a schematic representation of pitting damage observed by Blackley for (110) wafer. [26]

Surface Finish Characterization

Typical profiles for Ge machined in the ductile regime with a -45° rake angle tool for a high and low feed rate are shown in Figures 5.51 and 5.52. As Ge is not plagued by the same tool wear considerations as Si, comparison of the feed profiles among the orientations is permitted. The same sharpening was used for the machining of all three orientations tested. It is assumed that tool wear may have only slightly changed the tip condition among the three machining runs done with this sharpening. As a result similar feed rates yielded similar profile characteristics among the different cutting directions on a given orientation, as well as among the different orientations (three different machining runs.)

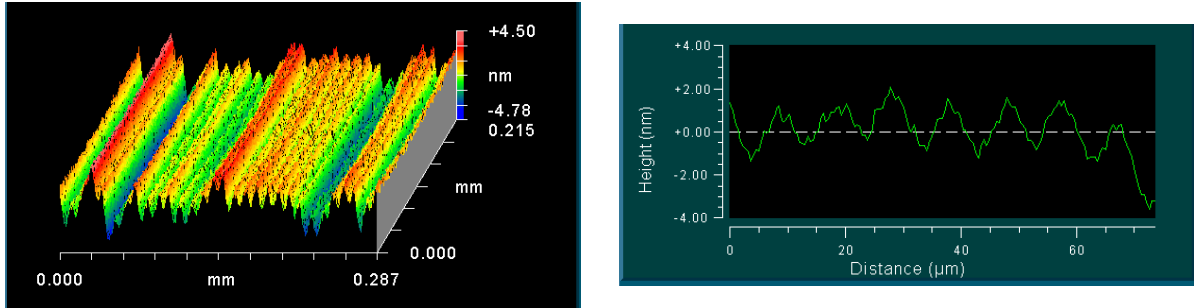


Figure 5.51. Typical profile of Ge surface machined at high feed with -45° tool. (10 $\mu\text{m}/\text{rev}$ feed)

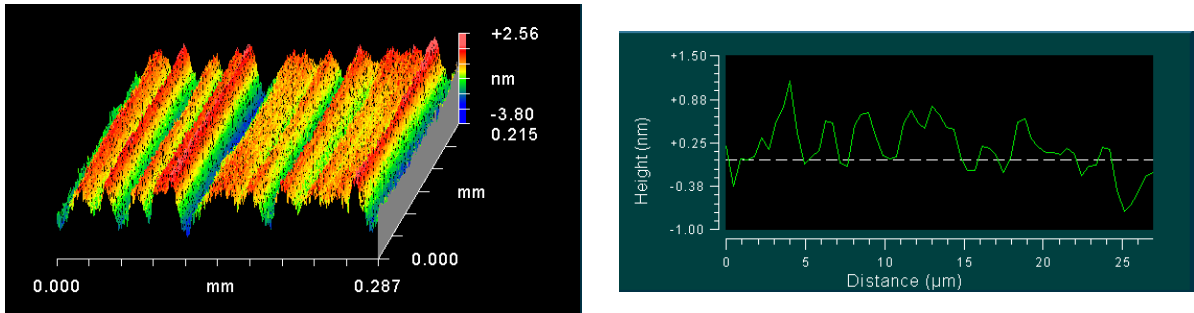


Figure 5.52. Typical profile of Ge surface machined at low feed with -45° tool. (5 $\mu\text{m}/\text{rev}$ feed)

The profiles show distinct feed marks (cusps) at higher feed rates which disappear to local surface variation as feed rate decreases. The feed cusps are regularly repeated at a distance corresponding to the feed rate going from a few nanometers in PV at high feeds (15-7 $\mu\text{m}/\text{rev}$) to indistinguishable values at lower feed rates (5-1 $\mu\text{m}/\text{rev}$). While the surfaces generally did not display features similar to a theoretical surface, the PV values matched pretty closely for all orientations tested (see Figure 5.56) The surfaces were pretty ideal (but not theoretical) for those turned with such low RMS. Unlike silicon, all the profiles seemed to lack features that may be attributed to heavy damage incurred on the tip.

Due to the similarity of machined surface profiles among the cutting directions and orientations, a comparison between PV and RMS values can also be made. Figures 5.53-56 show graphs of RMS values versus feed rate for (100), (110) and (111), respectively, turned with a -45° rake angle tool. The two paths in each key indicate the direction along which measurements were taken in each machining band corresponding to those in the previous section (see Figures 5.38, 5.40, 5.42, 5.44, 5.46, 5.48). Two distinct machining regions were measured for each orientation. The dashes indicate where pitting was substantial enough to influence the measurement.

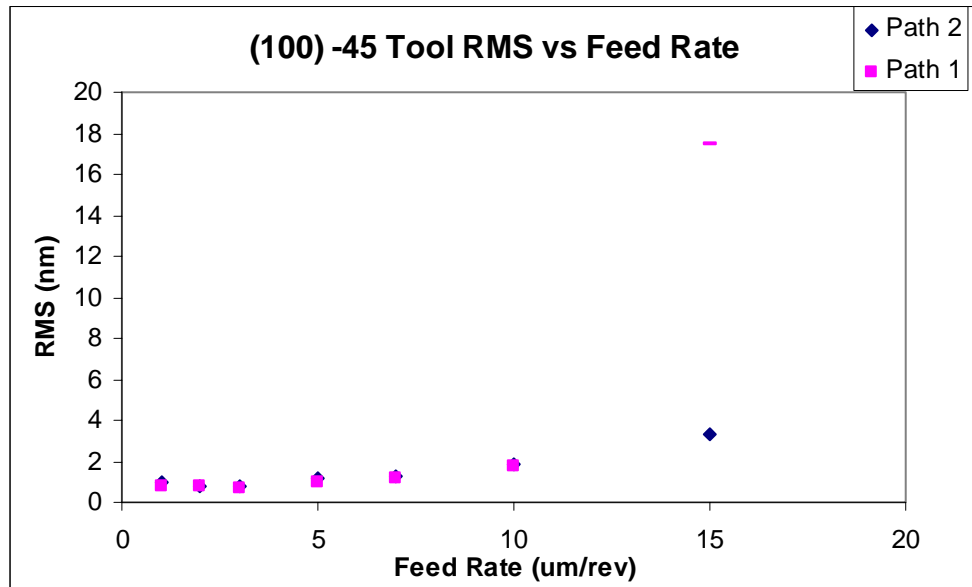


Figure 5.53. RMS versus feed rate and machining direction for a (100) Ge wafer machined with a -45° rake angle tool.

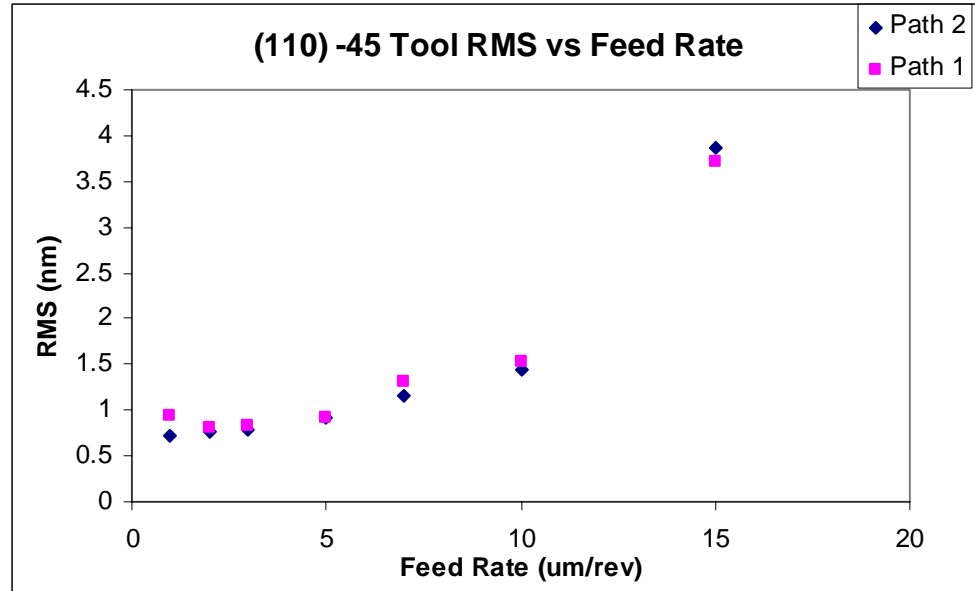


Figure 5.54. RMS versus feed rate and machining direction for a (110) Ge wafer machined with a -45° rake angle tool.

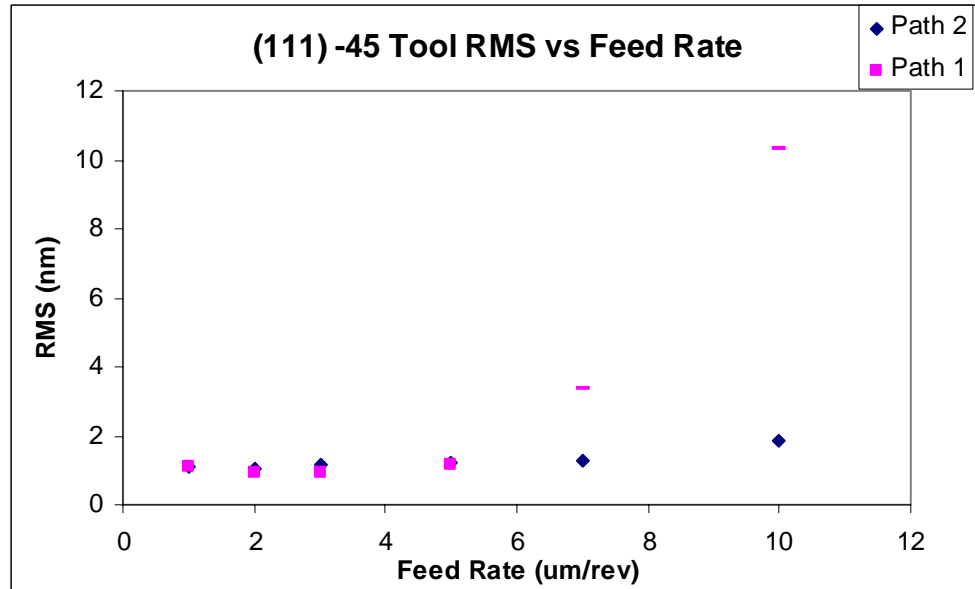


Figure 5.55. RMS versus feed rate and machining direction for a (111) Ge wafer machined with a -45° rake angle tool.

Low RMS values were obtained on the order of a few nanometers where ductile regime machining was observed. From the graphs it is apparent that the measurement path (and

therefore cutting direction) bares little dependence on RMS value when surfaces are ductile. RMS values increase with feed rate as expected. Figure 5.56 shows that in addition to RMS independence on cutting direction for a given wafer, there is little variation in RMS among the three different orientations machined.

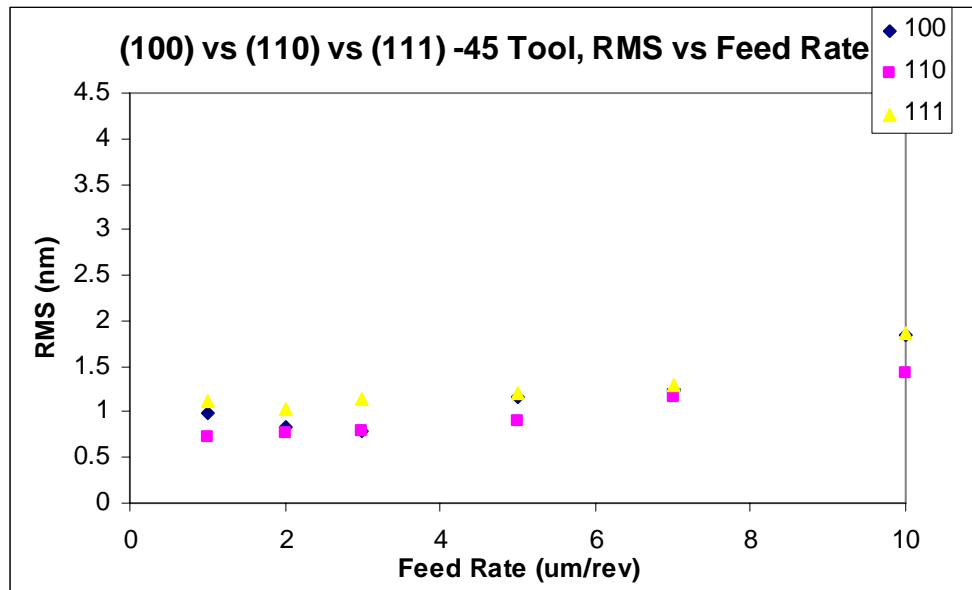


Figure 5.56. RMS versus feed rate and machining direction for as a function of wafer orientation wafer machined with a -45° rake angle tool.

Typical profiles for Ge machined in the ductile regime with a -30° rake angle tool for different feed rates are shown in Figures 5.57 and 5.58. Again similar feed rates yielded similar profile characteristics among the different orientations (three different machining runs.)

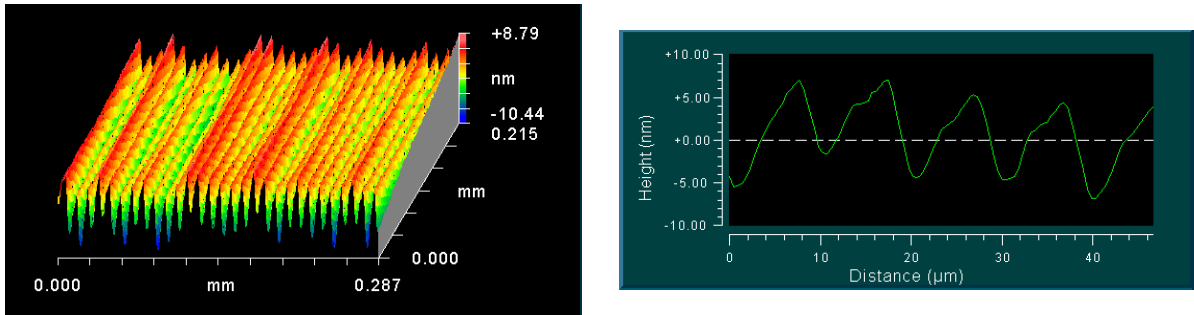


Figure 5.57. Typical profile of Ge surface machined at high feed with -30° tool. (10 $\mu\text{m}/\text{rev}$ feed)

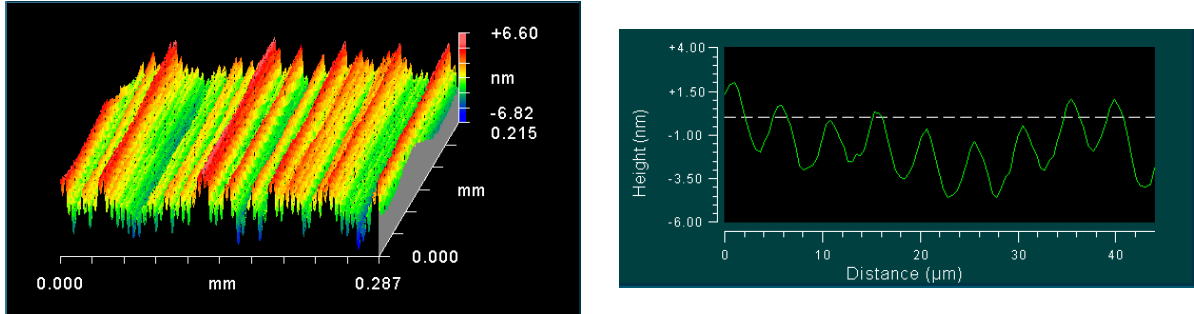


Figure 5.58. Typical profile of Ge surface machined at low feed with -30° tool. (5 $\mu\text{m}/\text{rev}$ feed)

The profiles show distinct feed marks at higher feed rates which disappear to decrease in size as feed rate decreases eventually getting indistinguishable. The feed cusps are regularly repeated at a distance corresponding to the feed rate going from several nanometers in PV at high feeds (15-5 $\mu\text{m}/\text{rev}$) to indistinguishable values at lower feed rates (3-1 $\mu\text{m}/\text{rev}$). The feed marks appear ideal (but not theoretical) in shape, but have feed cusps appear that have a much greater PV value for similar feed rates compared to surfaces machined with the -30° rake angle tool. This difference may be due the deformation under the work piece causing surface spring back, effectively increasing the PV ratio.

Due to the similarity of machined surface profiles among the cutting directions and orientations, a comparison between PV and RMS values can also be made. Figures 5.59-62 show graphs of RMS values versus feed rate for (100), (110) and (111), respectively, turned with a -30° rake angle tool. Again, the two paths in each key indicate the direction along which measurements were taken in each machining band corresponding to those in the previous section. Two distinct machining regions were measured for each orientation. The dashes indicate where pitting was substantial enough to influence the measurement.

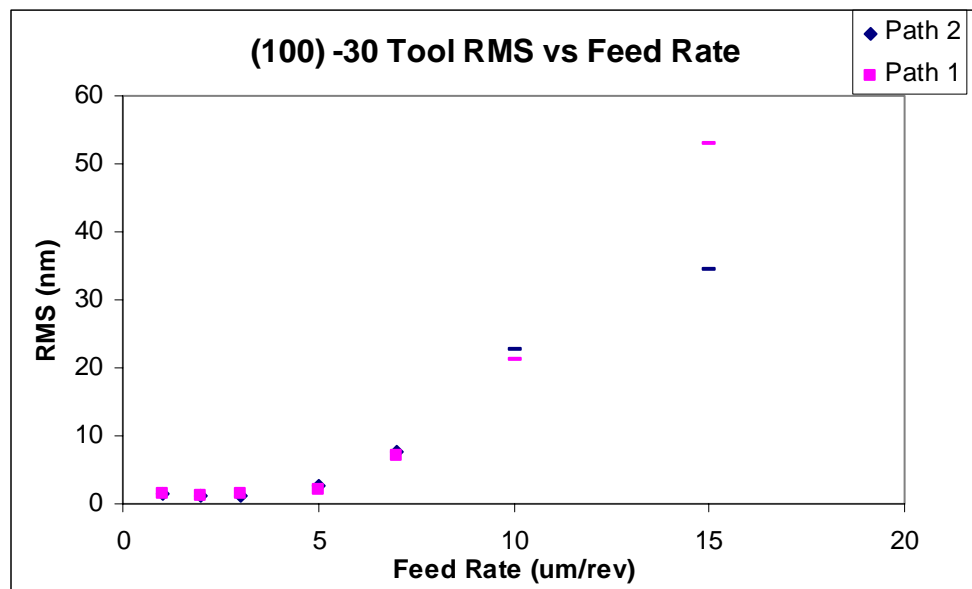


Figure 5.59. RMS versus feed rate and machining direction for a (100) Ge wafer machined with a -30° rake angle tool.

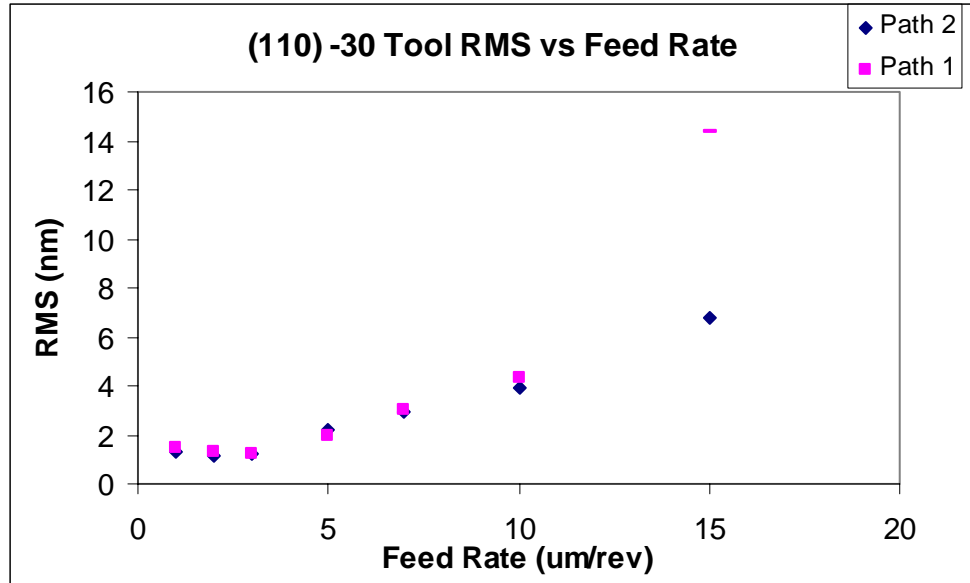


Figure 5.60. RMS versus feed rate and machining direction for a (110) Ge wafer machined with a -30° rake angle tool.

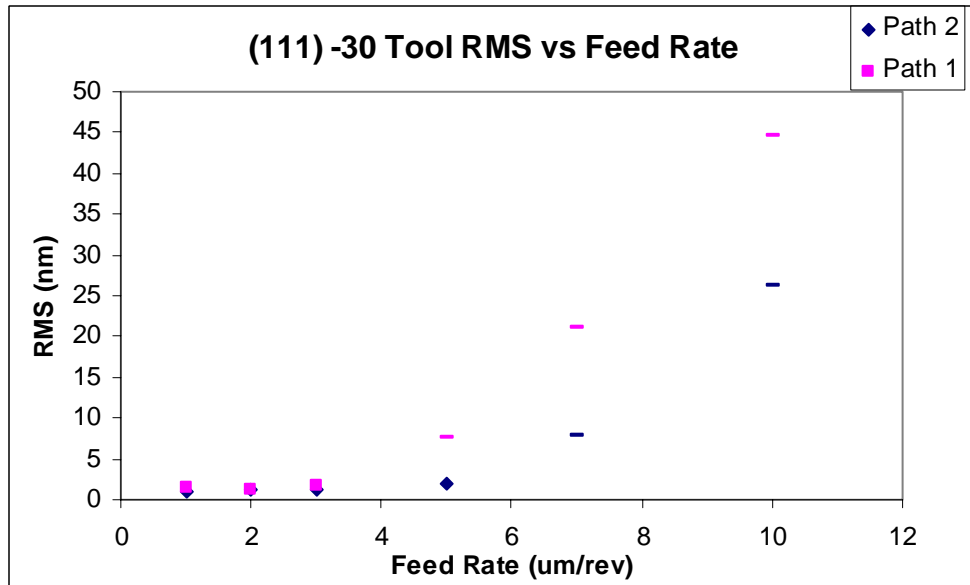


Figure 5.61. RMS versus feed rate and machining direction for a (111) Ge wafer machined with a -30° rake angle tool.

Low RMS values were obtained on the order of a few nanometers where ductile regime machining was observed. From the graphs it is again apparent that the measurement path

(and therefore cutting direction) bares little dependence on RMS value when surfaces are ductile. RMS values increase with feed rate as expected. Figure 5.62 shows that in addition to RMS independence on cutting direction for a given wafer, there is little variation in RMS among the three different orientations machined for the -30° rake angle tool as well.

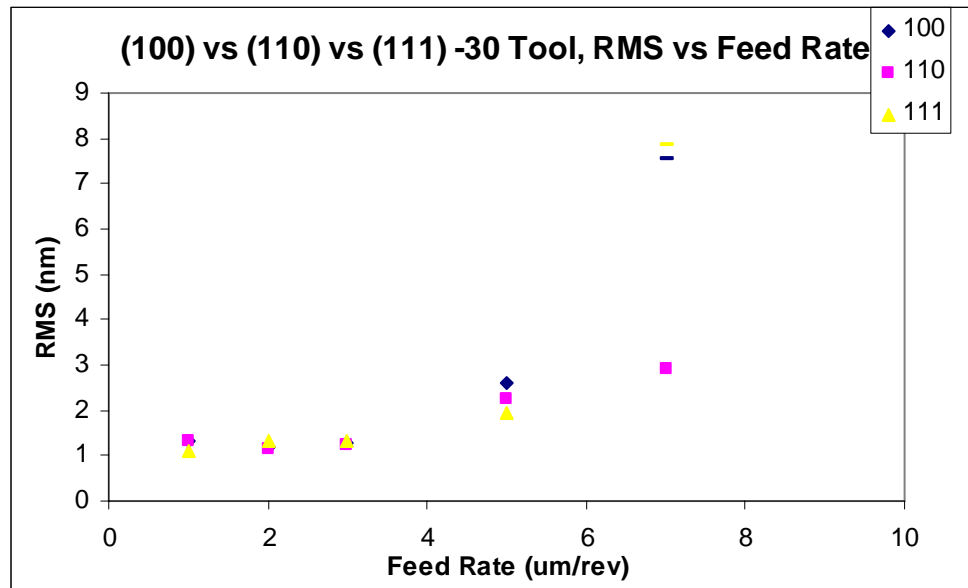


Figure 5.62. RMS versus feed rate and machining direction for as a function of wafer orientation wafer machined with a -45° rake angle tool.

Shown in Figure 5.63 for both tools is the comparison of the PV values measured from the profiles to those obtained theoretically from equation 5.1. Only the upper end feed rates are shown as they are the only values that could be decisively measured from the surface profile. At lower feed rates, the PV become to small to distinguish.

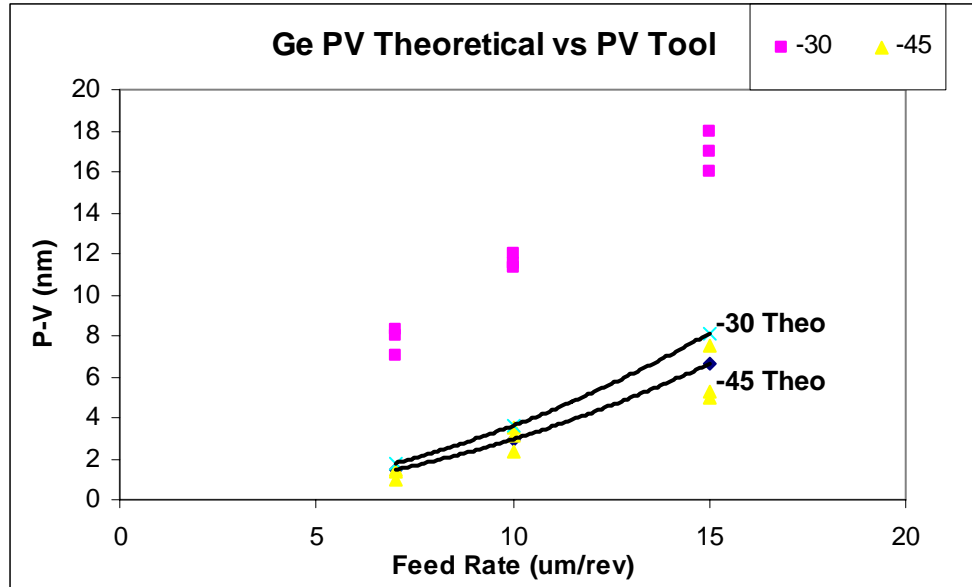


Figure 5.63. Comparison of PV values achieved during machining experiments of different Ge orientations with those obtained theoretically with Equation 5.1.

PV values measured for the -45° tool seem to correspond well with those determined from equation 5.1, where values for the -30° tool seems to be almost double that value. This is seen by comparing Figures 5.51 and 5.52 with Figures 5.57 and 5.58 for similar feed rates. The difference PV values is thought to be due to non-ideal removal of the material (in the form of deformation and elastic spring back) during machining with the -30° tool.

Low RMS values (<8nm at 15 um/rev) were achieved where cutting was within the ductile regime. The introduction of fracture to the surface in the more susceptible cutting directions seemed to be the only limiting factor to using large feed rates for machining. Ge tended to machine much better than the Si as surface effects due to damaged tools were not seen. As a result, Ge surface profiles were closer to ideal and had lower RMS values for similar feed rates.

5.6.2 Raman Measurement of Machined Surface

Figure 5.64 is Raman spectra taken of two different machining runs (one with a -30° rake angle tool, the other with -45°) at 1 and 8 $\mu\text{m}/\text{rev}$ feed rates for a ductile turned (100) wafer. The measurements were taken along the direction with the greatest propensity for ductile turning, $<100>$. It is apparent that for both feed rates tested that there is a thin layer of amorphized material (resulting in the broadened peak at 270 Rcm^{-1}) at the surface, below which the material is dc crystalline (300 Rcm^{-1}). This is very evident for the 8 $\mu\text{m}/\text{rev}$ scans, but slightly more difficult to see for the 1 $\mu\text{m}/\text{rev}$ scans.

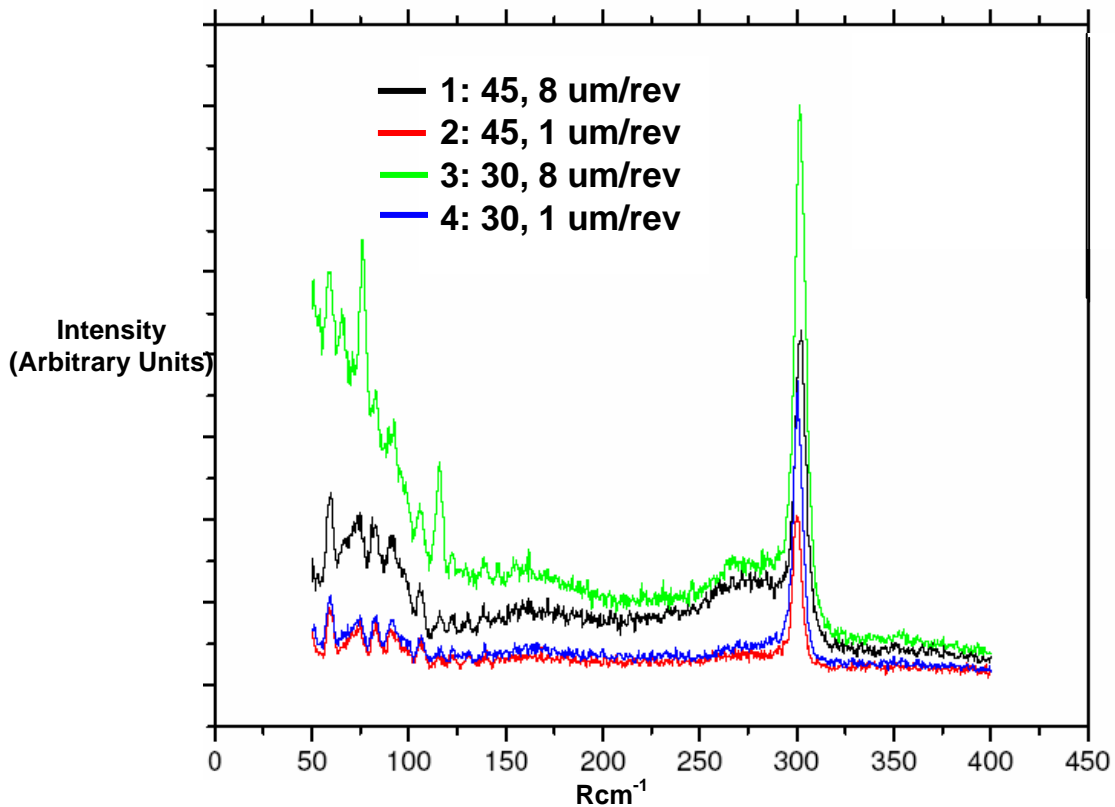


Figure 5.64. Raman spectra taken of ductile turned (100) Ge surface at two feed rates machined with a -30° and -45° tool in separate machining runs.

No definitive trend can be noted because at the low feed rates, the signal proved to be pretty weak in comparison with the higher rates. It is difficult to estimate the ratio of amorphous/crystalline intensity thereby giving no decisive trend of layer thickness as a

function of feed rate. Comparison between tools may be inappropriate because little is known about the condition of the tool at the time of machining.

Figure 5.65 is Raman spectra taken of two different machining runs (one with a -30° rake angle tool, the other with -45°) at 1 and 10 $\mu\text{m}/\text{rev}$ feed rates for a ductile turned (110) wafer. Measurements were taken along the $<110>$ direction (where cutting would be in a $<100>$ direction.) It appears that for measurements 1, 2, and 3 that there is some signature of an amorphous layer as indicated by the slight bump at 270 Rcm^{-1} . The fourth measurement shows little indication of such a feature, but again it does not rule out the possibility of an amorphous layer being present. The only definitive conclusion for this orientation is that amorphization is noted during machining of Ge.

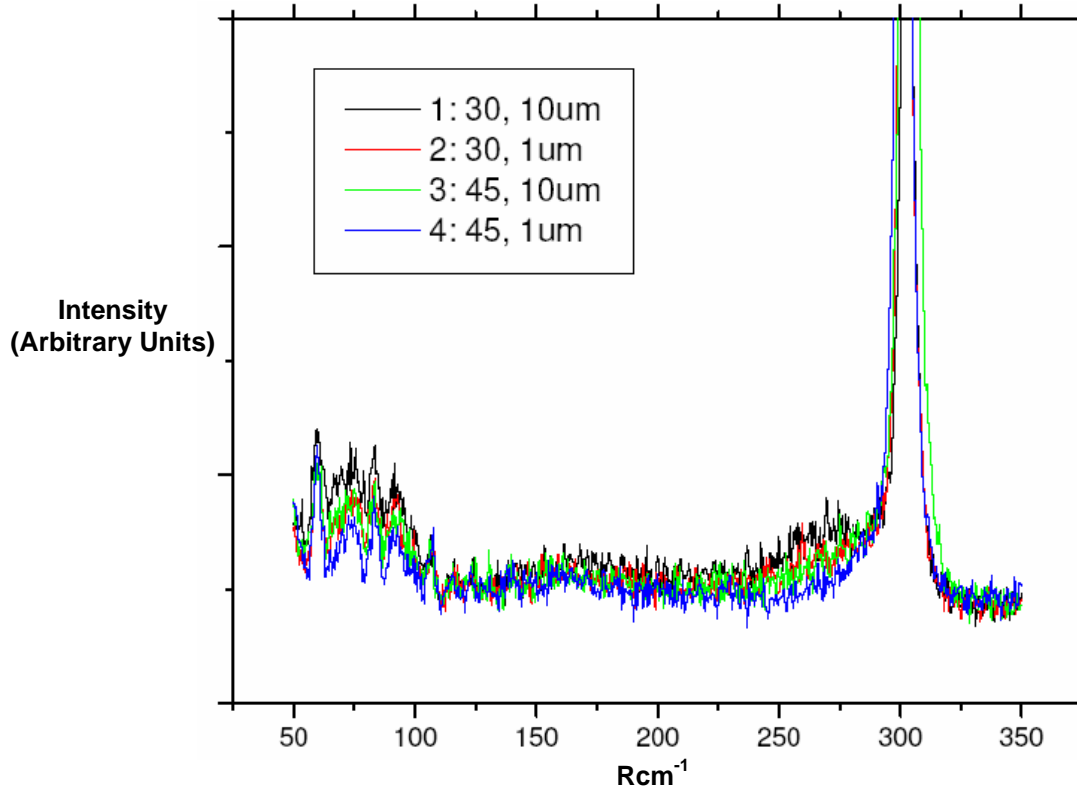


Figure 5.65. Raman spectra taken of ductile turned (110) Ge surface at two feed rates machined with a -30° and -45° tool in separate machining runs.

Figure 5.66 is Raman spectra taken of two different machining runs (one with a -30° rake angle tool, the other with -45°) at 1 and 5 $\mu\text{m}/\text{rev}$ feed rates for a ductile turned (111) wafer. Measurements were taken along the $<112>$ direction (where cutting would be in a $<110>$ direction.) No definitive conclusion can be drawn as to the existence of the amorphized layer for this orientation as it is difficult to substantiate a peak at 270 Rcm^{-1} . Again it is thought that the amorphous layer may still be present (as ductile regime material removal was achieved for these conditions,) but too thin to be capably detected.

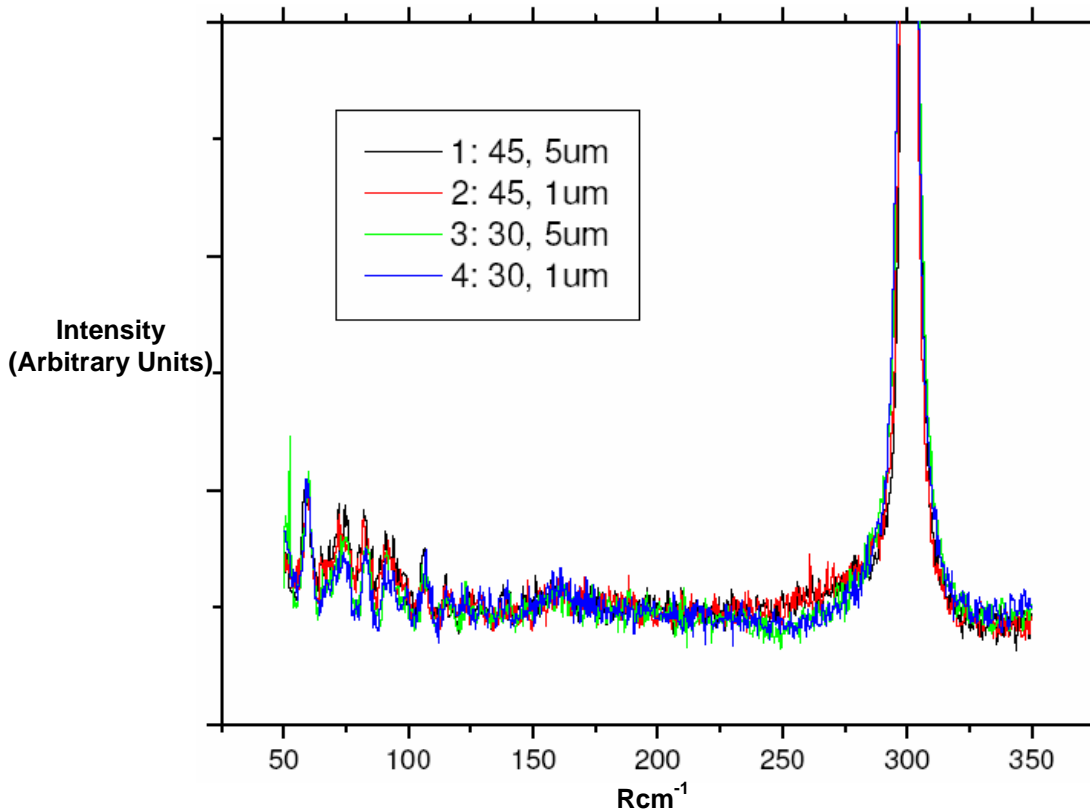


Figure 5.66. Raman spectra taken of ductile turned (111) Ge surface at two feed rates machined with a -30° and -45° tool in separate machining runs.

5.7 Experimental Results and Discussion (TEM analysis of Si and Ge Debris)

TEM analysis done on chips generated during machining in the ductile regime with the -45° tool on (100) Si and Ge indicated that the chips were of dc structure. Figures 5.67 and 5.68 are a TEM image of a Si chip generated in the ductile regime (2 $\mu\text{m}/\text{rev}$ feed rate, 2.5 μm depth of cut) and its corresponding diffraction pattern indexed as dc structure crystalline Si. (Crystallinity is noted by distinct diffraction ring formation, while amorphous is noted by “halo-ed,” diffuse rings.) TEM work and diffraction indexing was performed by staff at Oak Ridge National Laboratory (ORNL.)

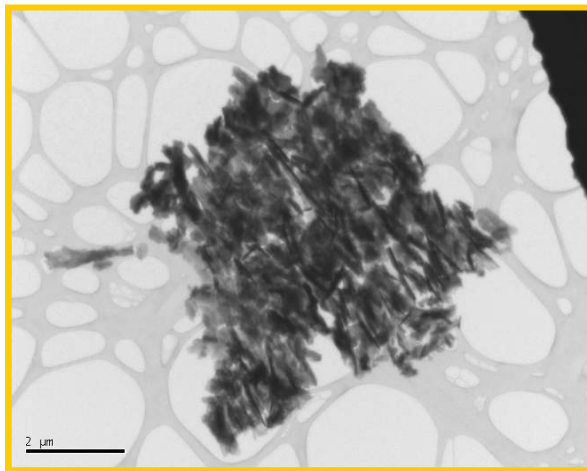


Figure 5.67. TEM image of Si chip generated in the ductile regime. [ORNL] Bar = 2 μm

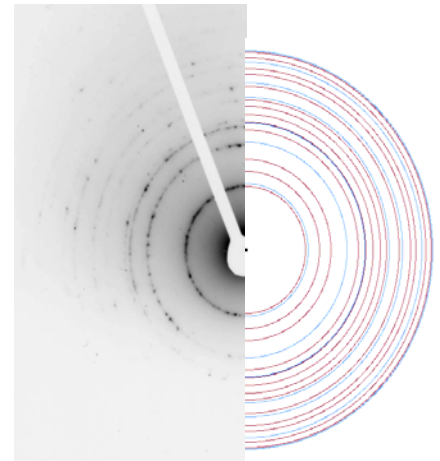


Figure 5.68. Diffraction pattern of Si chip indexed as crystalline dc-Si. [ORNL]

Figures 5.68 and 5.69 are a TEM image of a Ge chip generated in the ductile regime and its corresponding diffraction pattern indexed as dc structure crystalline Ge.



Figure 5.69. TEM image of Ge chip generated in the ductile regime. [ORNL] Bar = 0.5 μm

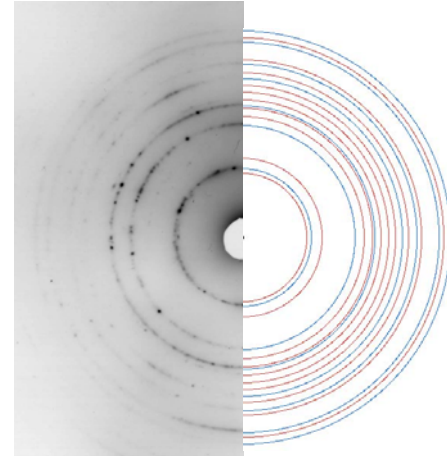


Figure 5.70. Diffraction pattern of Ge chip indexed as crystalline dc-Ge. [ORNL]

Comparison of the chip morphologies both in TEM observation and observation of its generation during cutting demonstrates that Si chips are smaller (1-4 μm) and tend to cluster together in small groups, while Ge chips are long (20+ μm), thin ($\sim 1 \mu m$ wide) spiraling chips. As Si cut in the ductile regime (characterized by surface finish) it was apparent that the generate chips were a very fine dust that when touched would smear, similar to that of pencil lead. A fine dust was left at the tool tip after machining. Ge chips on the other hand were very fine, and continuous, having a consistency similar to a spider web. This created a clumping of chips together at the tool tip.

It is difficult to note the ductile mode removal of the observation of Si chips as they do not form ribbon-like chips as expected. It was however distinctly noted that the surfaces created by the operation where ductile in nature (no observed pitting, repeated patterning of feed marks,) leading the author to believe removal was ductile. Ge chips however do appear continuous and ribbon like in nature similar to that seen in chip formation of turnable metals.

Despite the amorphous nature of the machined surfaces, there is not indication of amorphous material in the TEM diffraction experiments. This could possibly be due to recrystallization of this material with the high temperatures created at high speed machining. The chips are thin (on the order of tens of nanometers) and unattached to a medium that could conduct heat away. As a result high temperatures may be present creating rapid crystallization of the amorphized material. Jasinevicius *et al.* found results that may prove the validity of this statement. Small regions of crystallized Si domains where found in the very near surface among the amorphized in the transformed layer using careful TEM diffraction of the machined surface. [68] This may indicate that heating of the material at the tool tip could create regions where recrystallization of the amorphous layer could occur.

5.8 Conclusions and Suggested Future Work

Optical quality, low RMS surfaces where created by single point diamond turning single crystal Si and Ge wafers in the ductile regime. This was evident by the absence of fracture damage in the machined surfaces and the generation of continuous chips. Large radius, high negative rake angle tools where used at low feed rates (1-15um/rev) and small depth of cut (2.5 um) to generate these surfaces.

Feed rate seemed to be the limiting factor for generating a damage free surface. At increasing feed rates, certain directions on a wafer face initiated fracture at before others, creating symmetric damage patterns on the surface. The damage patterns for the various wafer orientations tested ((100), (110) and (111)) were explained qualitatively by an orientation stress model used in previous research. [26, 61] For (100) orientation wafers, an anomalous shift in the fracture pattern was noted for some early machining runs. This is not

fully understood, but was explained qualitatively by switching the favored fracture planes in the model.

The RMS (and PV) value of ductile turned surfaces was limited by the effect of the condition of the tool tip. While tips were freshly sharpened, experimental preparation (i.e. part touch off and preliminary facing cuts) perhaps dulled the tips enough to result in non-ideal material removal (deformation under the tool and elastic spring back.) This was evident by higher-than-theorized PV values, and machining profiles that did not fit theoretical shape (but were similar to realistic expectations) as measured by interferometry techniques. Both Si and Ge machining runs experienced this. Additionally, machining runs on Si were plagued by tip wear and damage considerations as evident by the repeated patterns of tip damage features into the part surface. Despite these various problems, surfaces turned within the ductile regime had RMS values in the range of <1 nm to 10nm increasing with feed rate.

Ge tended to machine much better than Si. This is due to the aggressive wear on the diamond tip imposed by the Si work piece. The effect of tip wear on fracture behavior as well as on the quality of a ductile turned is not fully understood. In addition it was noted that a higher negative rake angle (-45° versus -30°) provided improved machining for both materials.

Raman measurements of the turned surfaces for various machining conditions yielded some result indicating the presence of a near-surface amorphous layer. The presence of this layer is though to be the sign of a rapid back transformation from the β -tin metallic phase. While the Raman measurements did not always clearly indicate the existence of this layer for some of the conditions yielding a ductile turned surface, it is thought that the layer may still

be present but thin enough to escape detection by the unit. The condition of the tip was also thought to play a large role in the formation of this zone, creating difficulty in comparison of parameters between machining runs (i.e. rake angle, and crystallographic orientation.)

TEM results showed that the chips studied by diffraction are thought to be of dc crystal structure. Si chips generally showed a morphology of smaller (1-2 um) clustered chips, while Ge showed larger (20+ um) spiraling, continuous chips. Despite the amorphous nature of the near surface machine regions, TEM failed to show direct evidence of the amorphous nature of the chip. It is thought that intense local heating during machining may cause recrystallization of the amorphized material as the thin chips lack cannot dissipate heat quickly.

Suggested future work includes further Raman work on ductile turned surfaces with a more systematic test of the effect various conditions such as feed rate, cutting direction, cutting speed, lubricant, etc. Cross sectional TEM of a turned surface could give a better idea of the size of the transformation region and additionally, information (i.e. dislocation slip, microcracking) about the underlying dc crystalline region. Force measurements during cutting could give some indication of the magnitude of the pressure being exerted on the material during chip formation.

6. References

1. J.D. Plummer, M.D. Deal and P.B. Griffin. “Silicon VLSI Technology: Fundamentals, Practice, and Modeling.” Prentice Hall, New York, 2000.
2. Yury Gogotsi, Guohui Zhou, Sang-Song Ku and Sabri Cetinkunt. *Semicond. Sci. Technol.* **16** (2001) 345–352.
3. D. C. Thompson and J.A. Patten. *1998 ASPE Spring Topical Meeting on Silicon Machining* (Carmel-by-the-Sea, CA: ASPE.)
4. Liangchi Zhang and Irena Zarudi. *International Journal of Mechanical Sciences.* **43** (2001) 1985–1996.
5. V. Domnich and Y. Gogotsi. *Rev. Adv. Mater. Sci.* **3** (2002) 1-36.
6. Israel Institute of Technology, Israel, <http://phycomp.technion.ac.il/~nika/>.
7. B. Lawn. “Chapter 8: Indentation Fracture.” *Fracture of Brittle Solids- 2nd Edition*. Cambridge University Press, Cambridge, 1993.
8. K. Faber and K. Malloy. *The Mechanical Properties of Semiconductors*. Academic Press, Inc., California, 1992.
9. William Callister, Jr. *Materials Science and Engineering: an Introduction*, 4th e., John Wiley and Sons, Inc., New York, 1997.
10. P.J. Hesketh, C. Ju and S. Gowda, J. Electrochem. Soc. **140** (1993) 1080.
11. J.J. Wortman and R.A. Evans. *J. Appl. Phys.* **36** [1] (1965) 153.
12. J.F. Nye. *Physical Properties of Crystals*. Oxford University press, London, 1957.
13. V. Kaajakari. “Silicon as an Anisotropic Mechanical Material.” http://www.kaajakari.net/~ville/research/tutorials/elasticity_tutorial.pdf.
14. F. Ebrahimi and L Kalwani. *Mat Sci Eng.* **A268** (1999) 116.
15. C.A. Brookes and R.P Burnand. “Chapter 15: Hardness Anisotropy in Crystalline Solids.” *The Science of Hardness Testing and Its Research Applications*. American Society for Metals, Ohio, 1971.
16. K. Nihara, R. Morena and D.P.H. Hasselman. *J. Mater. Sci. Lett.* **2** (1983) 221.

17. B. Lawn. "Chapter 8: Indentation Fracture." *Fracture of Brittle Solids- 2nd Edition.* Cambridge University Press, Cambridge, 1993.
18. K. Kendall. *Proc. Roy. Soc. London, Series A* **361** (1978) 245.
19. M. Swain. *Proc. Roy. Soc. London, Series A* **366** (1979) 575.
20. Y. Ahn, T.N. Farris and S. Chandrasekar. *Mech. of Mat.* **29** (1998) 143.
21. S.S. Chaing, D.B. Marshall and A.G. Evans. *J. App. Phys.* **53** [1] (1982) 298.
22. E.H. Yoffe. *Phil. Mag. A.* **46** [4] (1982) 617.
23. K.L. Johnson. *Contact Mechanics.* Cambridge University Press, Cambridge, 1985.
24. P.N. Blake and R.O Scattergood. *J. Amer. Ceram. Soc.* **73** (1990) 949.
25. T. Bifano. PhD Thesis. North Carolina State University. 1988.
26. W. S. Blackley and R.O. Scattergood. *J. Eng. Ind.* **116** (1994) 263.
27. T. Shibata, S. Fujii, E. Makino and M. Ikeda. *Precision Eng.* **18** [2] (1996) 129.
28. J.A. Patten, H. Cherukuri and Jiwang Yan. High Pressure Phase Transformations of Semiconductors and Ceramics, NSF Research Project DMR-0203552.
29. V.I. Trefilov and Y.V. Milman. *Sov. Phys. Dokl.* **8** (1964) 1240.
30. J.J. Gilman. *J. Appl. Physics.* **39** (1968) 6086.
31. T. Figielksi. *Phys. Stat. Sol.* **4** (1971) 773.
32. V.I. Nikitenko and V.G. Eremenko. *Phys. Stat. Sol.* **14** (1972) 317.
33. D. J. Rowcliffe and M.J. Hill. *J. Mater. Sci.* **9** (1974) 1569.
34. V. Gridneva, Y.V. Millman and V.I. Trefilov. *Phys. Stat. Sol.* **9** (1972) 177.
35. D.R. Clarke, M.C. Kroll, P.D Kirchner and R.F Cook. *Phys. Rev. Lett.* **60** (1988) 2156.
36. M.C. Gupta and A.L. Ruoff. *J. Appl. Phys.* **51** (1980) 1072.

37. G.M. Pharr, W.C. Oliver, R.F. Cook, and P.D. Kirchner. *J. Mater. Res.* **7** (1992) 961.
38. D.L. Callahan and J.C. Morris. *J. Mater. Res.* **7** (1992) 1614.
39. T.F. Page, W.C. Oliver and C.J. McHargue. *J. Mater. Res.* (1992) 450.
40. Y.Q. Wu and Y.B. Xu. *J. Mater. Res.* **14** (1999) 2431.
41. A.B. Mann, D. van Heerden and T.P. Weihs. *J. Mater. Res.* **15** (2000) 1754.
42. J.E. Bradby, J.S. Williams and P. Munroe. *J. Mater. Res.* **12** (2001) 1500.
43. J.E. Bradby, J.S. Williams and P. Munroe. *Appl. Phys. Lett.* **77** (2000) 3749.
44. Kailer, Y.G. Gogotsi and K.G. Nickel. *J. Appl. Phys.* **81** (1997) 3057.
45. Y. Gogotsi and M.A. Gardner. *Microscopy and Analysis.* **41** (2000) 11.
46. E.R. Weppelmann, J.S. Field, and M.V. Swain. *J. Mater. Sci.* **30** (1995) 2455.
47. N. V. Novikov, S.N. Dub, Y.V. Milman and I.V. Grindeva. *Journal of Superhard Materials.* **18** (1996) 32.
48. V. Domnich, Y. Gogotsi and S. Dub. *Appl. Phys. Lett.* **76** (2000) 2214.
49. D.L. Callahan and J.C. Morris. *J. Mater. Res.* **9** (1994) 2907.
50. B. N. Tanikella, R.O. Scattergood, R.J. Nemanich, A.T. Sowers and A.H. Somasekhar. *Appl. Phys. Lett.* **69** (1996) 2870.
51. J. Morris, D. Callahan, J. Kulik, J. Patten and R.O. Scattergood. *J. Amer. Cer. Soc.* **78** [8] (1995) 2015.
52. T. Shibata, A. Ono, K. Kurihara, E. Makino and M. Ikeda. *Appl. Phys. Lett.* **65** [20] (1994) 2553.
53. J. Yan. *J. Appl. Phys.* **95** [4] (2004) 2094.
54. Y. Gogotsi, G. Zhou, S.S. Ku and S. Cetinkunt. *Semicond. Sci. Tech.* **16** (2001) 345.
55. B. Austin. M.S. Thesis, *Scribing of Brittle Materials*, North Carolina State University, 2000.

56. G. Weill, J.L. Mansot, G. Sagon, C. Carbone and J.M. Besson. *Semicond. Sci. Technol.* **4** (1989) 280.
57. X. S. Zhao, Y. R. Ge, J. Schroeder and P. D. Persans. *Appl. Phys. Lett.* **65** (1994) 2033.
58. J. Zi, H. Buscher, C. Falter, W. Ludwig, K. Zhang and X. Xie. *Appl. Phys. Lett.* **69** (1996) 200.
59. V. Domnich and Y. Gogotsi, "Pressure-induced phase transformations in semiconductors under contact loading." *Frontiers of High-Pressure Research II: Application of High Pressure to Low Dimensional Novel Electronic Materials.* Kluwer Academic Publishers, Dordrecht, 2001.
60. R.M. Tidwell. M.S. Thesis. North Carolina State University. 1991.
61. W.S. Blackley. M.S. Thesis. North Carolina State University. 1990.
62. C. Arcona. PhD. Thesis. North Carolina State University. 1996.
63. K. Bitans and R.H. Brown. *Int J Mach. Tool Des. and Res.* **5** (1965) 155.
64. T. Moriwaki. N. Sugimura and S Luan. *Annals of the CIRP.* **42** [1] (1993) 75.
65. J.A. Bailey and G Boothroyd. *J. Eng. Ind.* **90** (1968) 54.
66. J.S Taylor, C.K. Syn, T.T. Saito and R.R. Donaldson. *Opt. Eng.* **25** [9] (1989) 451.
67. N. P. Hung and Y. Q. Fu. *Int. J. Adv. Manuf. Tech.* **16** (2000) 871.
68. R.G. Jasinevicius, F. J. dos Santos, P.S. Pizani, J.G. Duduch, A.J.V. Porto. *J. of Non-Crystalline Sol.* **272** (2000) 174.

Appendix A

RESIDUAL STRESS BEND EFFECT DUE TO DIAMOND-TIP SCRIBING OF AN Al_2O_3 -TiC COMPOSITE CERAMIC

B. W. Austin
IBM Corporation
Fishkill NY 12524

T. Randall and R. O. Scattergood
Materials Science and Engineering Dept.
North Carolina State University
Raleigh, NC 27695-7907

ABSTRACT

A system consisting of a microhardness tester and a motorized stage was used to produce controlled diamond scribes on Al_2O_3 -TiC ceramic samples. A bending distortion is produced as a result of the residual stresses generated by the scribing operation. The change in sample shape was measured using an optical profilometer. Data from the measurement tool were analyzed using computer software to extract the net bending effect. An analytical model for the bend effect based on the residual stresses due to line-force dipoles was developed. The adjustable parameter in the model, dipole strength, was determined using bend-angle measurements. The predicted bend-displacement profiles were compared with measured profiles and the agreement was excellent. Although fracture could be observed along the flanks of scribe traces, this did not appear to diminish the residual stress intensity produced over the range of scribe loads used. The line-force dipole model has application for process analysis or as a benchmark for the verification of detailed elastic-plastic models of scribe-induced deformation.

INTRODUCTION

Indentation methods for the study of fracture processes in ceramic materials have been the subject of many investigations. Comprehensive reviews are available [1-3]. Scribing using sharp diamond tips is related to single indentations in that the loading conditions are spatially localized. The stress fields produced by indentation or scribing can be distinguished as those present during the loading-unloading cycle and those remaining after the loads are removed, i.e., the residual stress fields. Both types of stresses can contribute to the fracture processes that result. Various models have been developed to describe indentation-type stresses.

In the case of single indentations, the elastic-plastic analysis of Chiang et. al. [4] stands as a pioneering study of the detailed deformation mechanisms that control both the loading-unloading stresses and the residual stresses. Phenomenological models based on single or dipole point forces have also been developed. Among these, the model developed by Yoffe [5] stands as a pioneering study for the loading-unloading and residual stresses produced for single indentations. Force dipole models can be quite useful because they produce an approximate, closed-form solution for the stress fields. However, a direct measurement of the parameters that dictate the scale of the stresses or stress-intensity factors in force-dipole models is difficult. In the work reported here, a force-dipole model for the residual stresses resulting from scribing is developed. By making scribes on plate samples, and measuring the bend deflections resulting from the bending moment produced by the residual stresses, a dipole-strength parameter can be determined experimentally. This provides a unique way to calibrate the force dipole model. The procedure can be used to investigate the effects of loading conditions and material response on scribing, as evidenced by concomitant changes in the dipole strength parameter. This approach can also provide benchmarks for the verification of more detailed elastic-plastic models for scribing. In the following, the procedure for measuring the residual stress bend-effect is presented along with the line-force dipole model. The focus material for the experimental work was an Al_2O_3 -TiC ceramic composite. For comparison, some preliminary data on silicon is also presented.

EXPERIMENTAL PROCEDURE

A Zwick microhardness tester shown in Fig. 1a was used as the platform for the scribing tests. To produce a scribe at a constant speed, a motorized translation stage was fixed to the base of the hardness tester. The system was fixtured so that the direction of motion of the stage could be aligned with the cutting direction for a Dynatex V4-64 diamond scribing tool shown in Fig. 1b. This is a three-faced pyramidal diamond tool used in the semiconductor industry for scribing. For the tests done here, the Dynatex tool shank was mounted such the cutting edge made an angle of approximately 3.3° from the Al_2O_3 -TiC (AITiC) material surface, as is shown in Fig. 1c. The normal force on the scribing tip was controlled by placing weights on the loading pan of the microhardness tester. The normal force W ranged from 0.3 to 1.7 N.

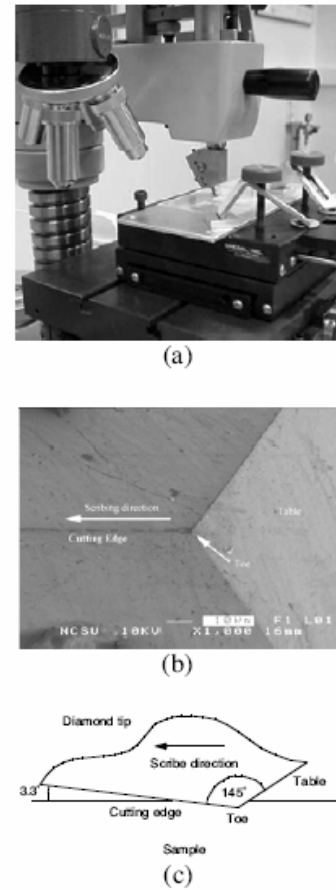


Figure 1. (a) Scribing setup. (b) Dynatex V4-64 diamond scribing tool. The angle between the faces defining the cutting edge is 90° . (c) Schematic of the scribe-tip geometry.

Higher loads caused excessive wear and chipping damage on the scribing tip. SEM observations of the tip edge were made during the tests and the tip was replaced whenever damage or excessive wear was observed.

The AlTiC ceramic used for the tests contained 65 vol% Al_2O_3 and 35vol% TiC. The microstructure consists of polycrystalline Al_2O_3 with a grain size of about 1 μm and TiC particles about 1 μm in diameter. The samples used for the scribing tests were polished AlTiC rectangular plates measuring approximately 1.0 mm x 1.0 mm x 0.3 mm. The spacing between the scribes was approximately 0.2 mm. For standard tests, three scribes were made across the width of a sample on the polished side with the middle scribe centered on the sample span. A Zygo New View non-contacting optical profilometer was used to measure the 2D surface height profiles of the test samples. Measurements were taken before and after scribing. To capture the intrinsic bend effect, profilometer data taken before scribing must be subtracted from the data taken after scribing. This was accomplished by importing both sets of data into a file and aligning fiducial marks. The initial data were subtracted from the final data, point by point, using the JMP software package. Any remaining tilt was removed from the data by the software. The sample surfaces on the measurement side need to have an optical quality surface finish. Details are reported in [6]. Fig. 2 shows a typical example of the 2D profilometer data obtained using three scribes per sample. The scribe traces were made on the top surface of the samples and the bending occurs downward. The steep craters present in Fig 2 occur at the three scribe positions. These are due to drop-out of the optical profilometer signal at the high-slope regions adjacent to scribe traces. As a final step, 1D profiles were extracted from the 2D data in order to obtain a simple representation of the bend-displacement profiles orthogonal to the scribe direction.

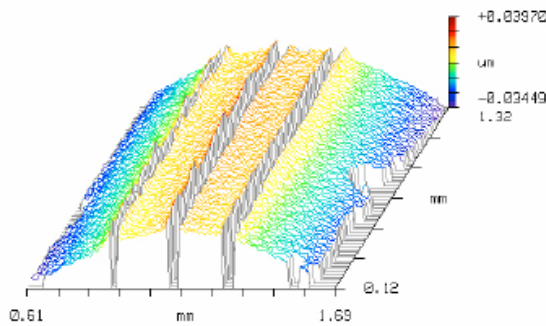


Figure 2. Optical profilometer data for a scribed sample.

BEND-EFFECT MODEL

The action of the residual stresses produced along a scribe trace using a scribe (normal) load W can be modeled as the line-force dipole shown in Figure 3a. The dipole forces act outward from the scribe trace because the elastic unloading of the plastically deformed and compressed material produces outward wedging forces on the surrounding restraining elastic material. A pair of orthogonal dipole forces acting on the surface of an elastic half space was introduced by Yoffe [5] as a model for the residual stresses due to single indentations. Ahn, et. al. [7] analyzed the stresses due to scribing as the superposition of a row of overlapping

Yoffe-type indentation dipole force pairs. For scribing across the width of a plate sample, superposition of the dipole force pairs is mathematically equivalent to a line force dipole because the dipole forces oriented along the trace mutually cancel, as is indicated in Figure 3b. Line-force dipole stresses for an isotropic elastic half space can be readily obtained from standard elasticity solutions. The dipole forces in Fig. 3 will produce a bending moment around the scribe direction in a finite-size plate sample. The bend deflection and bend angle along the plate length, $0 \leq x \leq L$, are denoted as $\delta(x)$ and $\phi(x)$, respectively.

For the analysis of the bend effect in finite-size plates, imagine that the $2L \times h \times b$ plate shown in Fig. 3 is extracted from the elastic half-space. The finite-body stress solution requires that the stress-field tractions due to the line-force dipole vanish on the plate free surfaces. If the plate thickness h is reasonably small compared to its length $2L$, the stresses acting on the plate edges are negligible and their effects can be ignored. However, the stresses acting on the bottom surface of the plate cannot be ignored. Since there is no resultant force due to dipoles, the equilibrium configuration can be approximated by applying reversed stresses to the bottom of the plate and then solving a beam-bending problem using these stresses as loading functions. This procedure will insure equilibrium of forces and moments acting on any cross section of the plate. For internal stress fields, this has been shown to be a very good approximation to the exact finite-body solution [8]. It is important to include both the normal and shear stresses for the beam loading functions since these have comparable magnitudes for the bending effect. The detailed analysis is given in the Appendix. FEM calculations were made which showed that the bend effect predicted by this approach is within a few percent of an exact, finite-body numerical solution [6]. The beam-bending solutions for a single scribe centered on the plate in Fig. 3 are given by eq. [1] (also see eq. [A6]). E is the elastic modulus ($E = 405$ GPa for AlTiC), h is the plate thickness, $B = Fa$ is the line-force dipole strength parameter and $X = x/h$ is the normalized distance along the plate. B is the adjustable parameter in the model and is represented here in the infinitesimal dipole limit, i.e., $B = Fa = \text{constant}$ in the limit where $a \rightarrow 0$ as $F \rightarrow \infty$. Since the problem can be treated as simple (plane strain) bending of a rectangular beam, the results are independent of the plate width b .

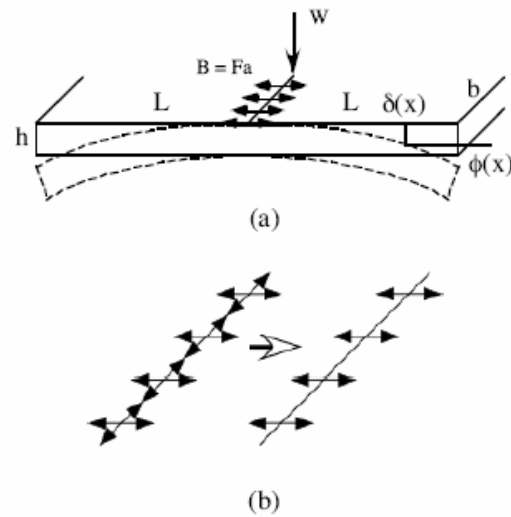


Figure 3. (a) Line-force dipole and the parameters used to describe the bend effect. (b) Superposition of a row of Yoffe-type orthogonal (crossed) dipole force pairs produces a line force dipole.

$$\begin{aligned}\phi(X) &= -\frac{6B}{\pi Eh^2} \left[\tan^{-1}(X) + \frac{X}{1+X^2} \right] = \frac{6B}{\pi Eh^2} f(X) \\ \delta(X) &= -\frac{6B}{\pi Eh} [X \tan^{-1}(X)] = \frac{6B}{\pi Eh} g(X)\end{aligned}\quad (1)$$

The bend-effect equations for multiple scribe traces are easily obtained from the superposition of the single-scribe functions in eq. (1), suitably offset in the X coordinate to account for the change of scribe position. The scribing geometry considered in the Appendix is a central scribe surrounded by specified number of equally spaced scribes on either side of the central one. The normalized bend angle $f(X)$ and bend displacement $g(X)$ functions are plotted in Fig. A4 for single and multiple scribes. Multiple scribes increase the overall deflection due to the bend effect and thereby reduce scatter in the measured profilometer data. Three scribes per sample were used as the standard test in this study, and this gave very reproducible data.

The key parameters for scribing tests are the material, the scribe-tip geometry and the normal load W applied during scribing. Scribing speed was found to be a second order effect over the range of speeds tested here, 50 to 250 $\mu\text{m/s}$, and the testing was done at a nominal speed of 100 $\mu\text{m/s}$. Values of B as a function of W are a direct measure of the intensity of the residual stresses produced by a scribe load W for given scribing conditions.

To judge the overall effectiveness of the line-force dipole model, the measured bend profiles are compared to the model predictions.

RESULTS AND DISCUSSION

The dipole strength parameter B was determined at each scribe load by comparing measured data for the average bend angle ϕ per scribe with model predictions using the procedure described in the Appendix. The ϕ vs W test data obtained for scribing AlTiC are shown in Fig. 4. The reproducibility of the results was very good, as long as the diamond tips remained undamaged.

The B vs W curve shown in Fig. 5 was obtained from the bend-angle data in Fig. 4. The curve fit through the data points in Fig. 5 is a second-order polynomial, B

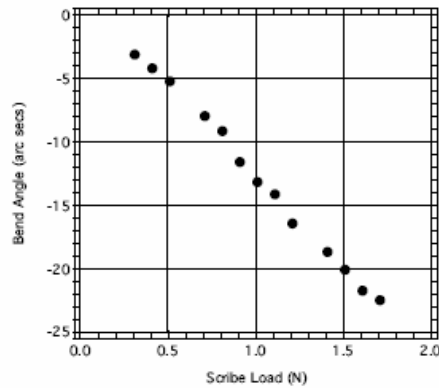


Figure 4. Bend angle ϕ vs. scribe load W data obtained for AlTiC.

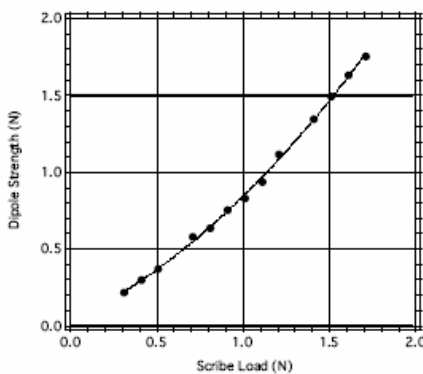


Figure 5. Dipole strength B vs. scribe load W for AlTiC.

$= 0.0332 + 0.516W + 0.291 W^2$. This can be viewed as the “calibration curve” for the line-force dipole model for given diamond tool geometry, scribing conditions and material. The effectiveness of the model can be demonstrated by comparing the measured bend profiles with predicted profiles derived using the calibration curve. Fig. 6 a-c shows typical examples of measured (solid) and predicted (dashed) bend profiles for low, medium and high values of the scribe load W . The large spikes on the measured profiles are due to the profilometer drop outs at the scribe positions.

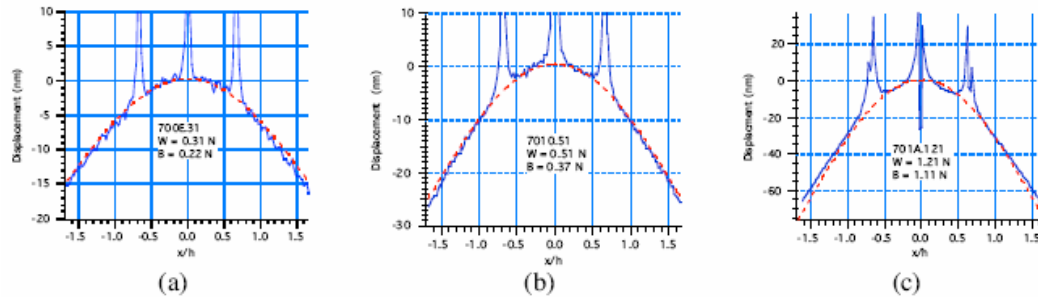


Figure 6. Measured (solid) and predicted (dashed) bend profiles for the following test conditions: (a) $W = 0.31 \text{ N}$, $p = 0.2 \text{ mm}$, $2L = 1.1 \text{ mm}$ and $h = 0.3 \text{ mm}$. (b) $W = 0.51 \text{ N}$, $p = 0.2 \text{ mm}$, $2L = 1.2 \text{ mm}$ and $h = 0.3 \text{ mm}$. (c) $W = 1.21 \text{ N}$, $p = 0.2 \text{ mm}$, $2L = 1.0 \text{ mm}$ and $h = 0.3 \text{ mm}$.

The bend profiles have the appearance of a plastic hinge around the region of the scribe traces. The measured profiles are matched to a high degree of accuracy by the model. This was the case for the profiles obtained over the entire range of scribe loads tested. As further comparison, the bend profiles shown in Fig. 7 a-b were also obtained. These were done using test conditions that were different from the standard three-scribe tests used to obtain the calibration curve in Fig. 5 (different sample dimensions and five scribes per sample). Excellent agreement is again obtained. Note that the magnitude of the bend deflections is in the nanometer range for the scribing conditions and sample sizes used.

Fig. 8 a-c shows SEM micrographs of the scribe traces for samples corresponding to the test conditions and displacement profiles shown in Fig. 6. With increasing scribe load W , the scribe widths become larger and there is an increasing amount of fracture damage evident along the flanks of the scribe traces. However, because of the relatively high toughness of the AlTiC ceramic samples ($K_{IC} = 4.2 \text{ MPa}\cdot\text{m}^{1/2}$), extensive chipping due to lateral

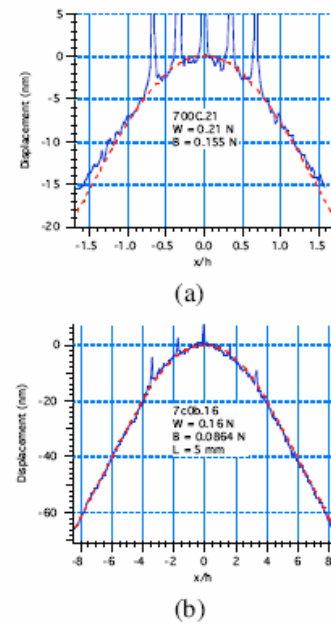


Figure 7. Measured (solid) and predicted (dashed) bend profiles for the following test conditions: (a) $W = 0.21 \text{ N}$, $p = 0.1 \text{ mm}$, $2L = 1.0 \text{ mm}$ and $h = 0.3 \text{ mm}$. (b) $W = 0.16 \text{ N}$, $p = 0.5 \text{ mm}$, $2L = 5.2 \text{ mm}$ and $h = 0.3 \text{ mm}$.

cracking is not evident. The central regions of the scribes still retain significant amounts of ductile-like deformation. This is most clearly evidenced in the dipole strength results shown in Fig. 5. There is no break or leveling-off in the dipole-strength curve that would indicate, for example, the onset of a severe fracture/chipping process. The latter would remove large amounts of the plastically deformed material from the scribe zone, thereby reducing the capacity to store residual stresses. One might expect this kind of change to occur at a sufficiently large value of the scribe load. However, loads beyond 1.8 – 2 N could not be used for the scribing tests on AlTiC because of catastrophic damage to the scribe tips. During the initial phases of the testing, a noticeable leveling-off did appear for the B vs. W curve in Fig. 5 when the scribe load was in the range of 2 N or higher, but it was determined that this effect results from scribing with a badly fractured diamond tip. The blunt nature of the fractured scribe tip significantly affects the deformation processes and this was reflected in a reduced dipole strength.

The line-force dipole model has several important ramifications for the study of residual stresses produced by scribing. The dipole strength parameter B gives a simple characterization of the scale of the residual stress as a function of the loading conditions, tool geometry and materials. This is a scaling parameter, in the spirit of Yoffe's original suggestion for the use of force dipoles to model indentation stress fields [1, 5]. Scribing processes are more complex and difficult to model than indentation processes. The approach presented here provides an experimental means to characterize the residual stresses produced by scribing in terms of a force-dipole strength parameter B. This should be a useful benchmark to compare with more detailed elastic-plastic models of scribing. Such comparisons were not within the scope of this study.

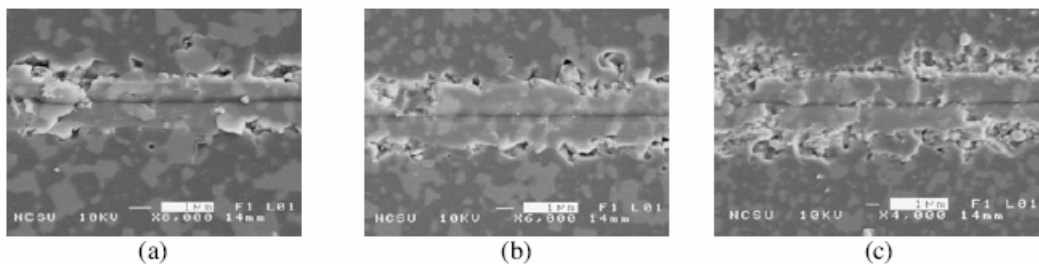


Figure 8. SEM micrographs of the scribe traces corresponding to conditions a-c in Fig. 6, respectively.

A noteworthy feature of the line-force dipole model was observed in our recent, preliminary work on the scribing of silicon wafer samples [9]. Evidently, because of the low toughness of silicon compared to AlTiC, the B vs. W curve for silicon in Fig. 9 shows a clear break-point at the onset of fracture (arrow). The latter was established visually using optical microscopy and AFM. The break-point corresponds to a critical load for the onset of a ductile-brittle transition during scribing of silicon. Based on these preliminary results, one can anticipate that the force-dipole bend effect model could be a useful technique to determine critical

loads for fracture transitions in brittle materials as a function of the tool geometry and scribing conditions. In turn, this would provide critical load or critical depth parameters relevant for ductile-regime machining and precision grinding of ceramics [10-12]. Although not attempted in this study, there is also the possibility for developing a bend-effect model appropriate for linear rows of widely spaced (single) indentations in order to determine dipole strength parameters for residual stresses due to these types of indentation processes.

Finally, it should be mentioned that the bend effect for AlTiC has a unique application. This material is used for the manufacture of hard-disk read-write heads. Among other methods, diamond-tip scribing has been used to produce nano-scale curvature adjustments during the manufacture of the heads, which in current generation have dimensions close to the sample dimensions, 1mm x 1mm x 0.3 mm, used for the work reported here. During the manufacturing process, scribes are made on a non-functional region of the read-write head in order to tailor the curvatures for optimization of the aerodynamic (flying-height) performance [13]. A line-force dipole model can serve as the basis of a process model for predicting the bending deflections for controlled curvature adjustments during manufacturing [14].

CONCLUSIONS

A line-force dipole model gives an excellent representation of the bend-effect produced in rectangular plates by the scribe-induced residual stresses. Characterization of these stresses in terms of a dipole strength parameter will be useful for analyzing the scribing process and as a benchmark for comparing to more detailed elastic-plastic models. Based on preliminary results for silicon, it also appears that trends in the dipole strength parameter as a function of scribe load can be used as an indicator of ductile-brittle transitions for specified scribing conditions.

APPENDIX

Consider a line-force dipole acting on the surface of an elastic half-space shown in Fig. A1. The line-force dipole lies along the z-axis. The forces act outward because the plastically displaced subsurface material formed will, upon

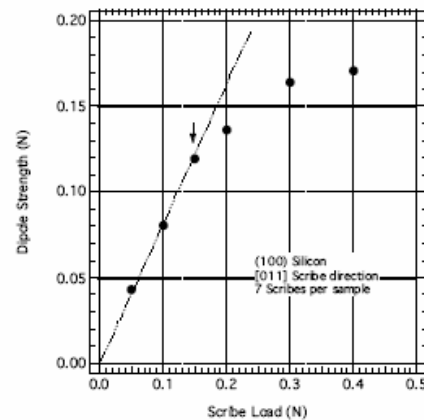


Figure 9. Dipole strength B vs. scribe load W curve for silicon for the same setup, Dynatex scribing tool and scribing geometry used for AlTiC (Fig. 1). $2L = 1\text{ cm}$, $h = 0.5\text{ mm}$, $a = 0.1\text{ mm}$ and seven scribes per sample. (100) crystal surface normal, [011] scribing direction. $E = E_{(100)} = 150\text{ GPa}$. The arrow indicates the onset of fracture as observed by optical and AFM microscopy.

unloading, push outward on the surrounding elastic material. This is the action that produces a bend effect for diamond-tip scribing. Note that other types of “scribing processes”, for example focused-laser melting, could reverse the sign of these residual-stress forces [13,15].

The stresses needed to describe the bending effect for plate scribing are σ_{yy} and σ_{xy} . The stresses due to a single line force of magnitude F (N/m), acting at the origin in the positive x direction, are given by Johnson [15] as follows

$$\sigma_{yy}(x,y) = -\frac{2F}{\pi} \frac{xy^2}{(x^2 + y^2)^2} \quad (A1)$$

$$\sigma_{xy}(x,y) = -\frac{2F}{\pi} \frac{x^2y}{(x^2 + y^2)^2}$$

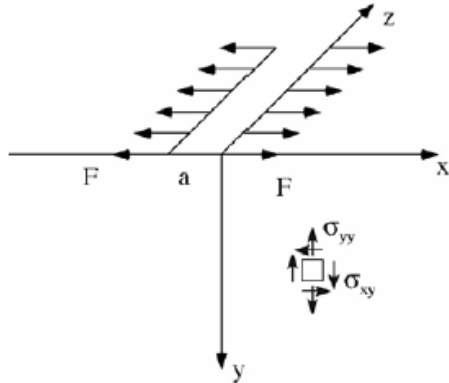


Figure A1. A single line force per unit length acting at the origin on the surface of an elastic half space produces a 2D stress field σ_{ij} . The line-force dipole field is obtained by the superposition of the two oppositely directed line forces shown where a is the spacing.

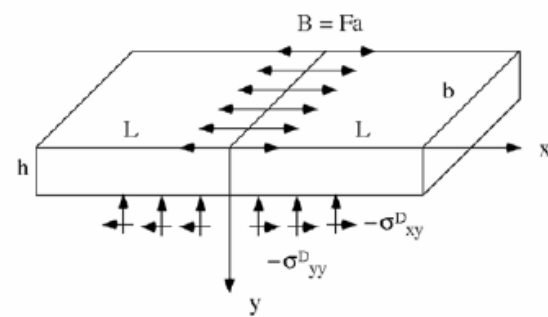


Figure A2. The finite plate is "cut out" from the elastic half space. The reversed dipole half-space stresses are applied to the bottom surface as indicated. Equilibrium of moments is obtained by allowing the plate to undergo bending with these stresses acting as the loading functions.

In order obtain the line-force dipole stress field, consider an oppositely directed line force F acting at $x = -a$ in Fig. A1. The dipole stresses are the superposition of the stresses due to the two line forces. The infinitesimal line-force dipole stresses are obtained by taking the limit $a \rightarrow 0$ and $F \rightarrow \infty$ such that $B = Fa$ remains finite. B is defined as the dipole strength (N). The infinitesimal line-force dipole stresses, σ_{yy}^D and σ_{xy}^D , can be obtained from the derivatives of eq. [A1] as follows

$$\begin{aligned} \sigma_{yy}^D &= -a \frac{\partial \sigma_{yy}}{\partial x} = \frac{2B}{\pi} \frac{y^2(-3x^2 + y^2)}{(x^2 + y^2)^3} \\ \sigma_{xy}^D &= -a \frac{\partial \sigma_{xy}}{\partial x} = \frac{4B}{\pi} \frac{xy(y^2 - x^2)}{(x^2 + y^2)^3} \end{aligned} \quad (A2)$$

For the analysis of the bending effect due to scribe-induced residual stresses, consider a finite plate with a scribe along its centerline (z axis) “cut out” from the half-space as shown in Fig. A2. The finite-body stress solution requires that the stress field due to the line-force dipole vanish on the plate surfaces. If the plate thickness h is relatively small compared to its length $2L$ and width b , the magnitude of the half-space stresses, σ_{yy}^D and σ_{xy}^D , acting on the plate edges is negligible and their effects can be ignored. However, the stresses (tractions) acting on the bottom surface of the plate cannot be ignored. Since there is no resultant force due to the line-force dipole, the equilibrium configuration can be approximated by applying the reversed stresses, $-\sigma_{yy}^D$ and $-\sigma_{xy}^D$, to the bottom of the plate and then solving a simple (plane strain) beam-bending problem with these stresses as the loading functions. However, this will not produce an exact solution for the stress distribution within the finite plate because there remains a self-equilibrated distribution of tractions along the free surfaces. Nevertheless, FEM calculations showed that the bending effect calculated by this procedure was within a few percent of the exact solution [6].

The required beam-bending equations are based on Fig. A3. It is important to note that both the normal and shear tractions must be taken into account when calculating the slope and deflection of the plate. For a single, central scribe across the width b of the plate in Fig. A2, the beam equations are obtained from the equilibrium of the shear force $V(x)$ and moment $M(x)$ acting on an element Δx of the plate

$$\begin{aligned}\frac{dV}{dx} &= -q(x) \\ \frac{dM}{dx} &= V(x) - \tau(x)\frac{h}{2}\end{aligned}\quad (A3)$$

$q(x)$ and $\tau(x)$ are the normal and tangential beam loading functions, respectively. These are obtained from the reversed half-space stresses given in eq. [A2] using the value $y = h$

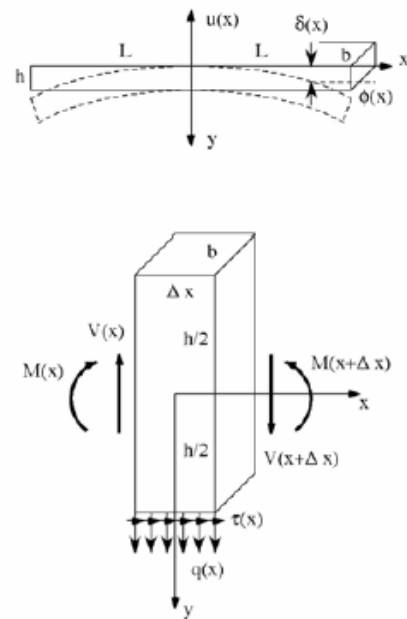


Figure A3. Top) Geometry used to describe the plate bending effect. Bottom) Shear forces and moments on a section Δx due to the normal and shear loading functions $q(x)$ and $\tau(x)$.

$$q(x) = -b\sigma_{yy}^D(x, h) = -\frac{2Bb}{\pi} \frac{h^2(-3x^2 + h^2)}{(x^2 + h^2)^3} \quad (A4)$$

$$\tau(x) = -b\sigma_{xy}^D(x, h) = -\frac{4Bb}{\pi} \frac{hx(h^2 - x^2)}{(x^2 + h^2)^3}$$

Let $u(x)$ denote the beam displacement due to bending. By convention, downward displacements and negative slopes are considered to be negative displacements and angles. The bend (tangent) angle $\phi = du/dx$ and the deflection $\delta = u$ (Fig. A3) are obtained by integration of the moment-curvature equation [6]

$$EI \frac{d^2u}{dx^2} = M(x) \quad (A5)$$

E is the elastic modulus and $I = bh^3/12$. The final results are independent of the beam width b and can be obtained in closed form as follows.

$$\phi(X) = -\frac{6B}{\pi Eh^2} \left[\tan^{-1}(X) + \frac{X}{1+X^2} \right] = \frac{6B}{\pi Eh^2} f(X) \quad (A6)$$

$$\delta(X) = -\frac{6B}{\pi Eh} \left[X \tan^{-1}(X) \right] = \frac{6B}{\pi Eh} g(X)$$

$X = x/h$ is the normalized distance along the plate (beam). The bend-angle and displacement functions, $f(X)$ and $g(X)$, defined in eq. [A6] are shown in Fig. A4; the deflection is symmetric with respect to the beam center, $X = 0$. The bend-angle function $f(X)$ approaches the value $-\pi/2$ when X increases. The deflection function $g(X)$ becomes essentially linear as $f(X)$ approaches $-\pi/2$. This means that the bending effect appears as a localized "hinge" where the outer regions of the sample are simply carried downward by the bend-effect in the region containing the scribes.

The bending effect for multiple scribes across the width of a plate sample can be obtained from the superposition of the single-scribe functions in eq. [A6]. This assumes that the scribes are sufficiently widely spaced so as not to interact. If $2n+1$ scribes are made on a plate such that n equally spaced scribes lie each side of the center scribe at $X = 0$, the bend angle and deflection functions will be as follows

$$\phi_{2n+1}(X) = \frac{6B}{\pi Eh^2} \sum_{j=-n}^n f(X + jA) = \frac{6B}{\pi Eh^2} (2n+1)f_{2n+1}(X) \quad (A7)$$

$$\delta_{2n+1}(X) = \frac{6B}{\pi Eh} \sum_{j=-n}^n g(X + jA) = \frac{6B}{\pi Eh} (2n+1)g_{2n+1}(X)$$

p is the spacing between adjacent scribes and $A = p/h$ is the normalized scribe spacing. The average bend angle or displacement functions per scribe are defined as

$$\begin{aligned} f_{2n+1}(X) &= \frac{1}{2n+1} \sum_{j=-n}^n f(X + jA) \\ g_{2n+1}(X) &= \frac{1}{2n+1} \sum_{j=-n}^n g(X + jA) \end{aligned} \quad (\text{A8})$$

The general form of the functions $f_{2n+1}(X)$ and $g_{2n+1}(X)$ is shown in Fig. A4 for a single scribe, three scribes ($n = 1$) and five scribes ($n = 2$) with a scribe spacing $A = 2/3$ ($p = 2h/3$). When X increases, $f_{2n+1}(X)$ approaches the single-scribe function $f(X)$ whereas $g_{2n+1}(X)$ is shifted to a smaller value than $g(X)$. Because of this behavior, the bend angle has been used in this study for calibration of the dipole strength. The method adopted here to evaluate B was to make measurements of the average bend angle per scribe, which is defined to be the total bend angle divided by the number of scribe traces. As seen in Fig. A4, the bend angle function $f_{2n+1}(X)$ asymptotes to a constant value for sufficiently long plate samples. This means that the outer regions of the beam are simple carried along as straight sections by the localized plastic hinge. Therefore, the opposing outer regions of bend profiles were fit to straight lines in order to calculate overall bend angles. The dipole strength parameter B is determined by equating the measured angle to the predicted angle given by eq. [A7]. If the sample L is too small to reach the straight-line asymptote for the bend-profile arms, the measured and predicted angles can be equated at a suitable mean measurement position [6].

ACKNOWLEDGMENTS

The authors are indebted to Professor Jeff Eischen, North Carolina State University, for critical comments on the development the bend-effect model and also for the FEM verification calculations. The authors gratefully acknowledge the support provided by IBM, Data Storage Division, San Jose CA, and the NSF, Award No. DMR-0203552. The research was conducted at the Precision Engineering Center, North Carolina State University.

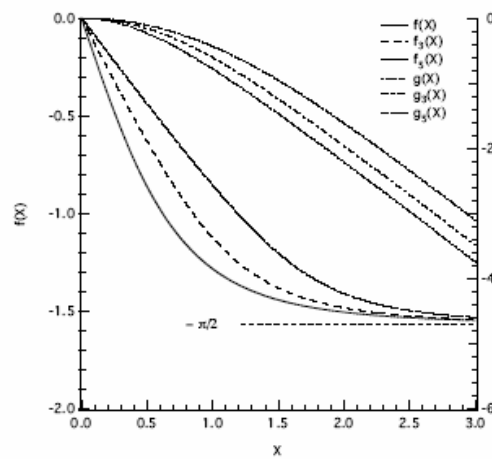


Figure A4. Plot of the normalized bend angle and deflection functions for a single scribe, $f(X)$ and $g(X)$, three scribes, $f_3(X)$ and $g_3(X)$ and five scribes, $f_5(X)$ and $g_5(X)$, using $A = a/h = 2/3$.

REFERENCES

1. R. F. Cook and G. M. Pharr, "Direct Observation and Analysis of Indentation Cracking in Glasses and Ceramics", *J. Am. Ceram. Soc.*, 73 [4], 787 (1990).
2. B. Lawn, "Fracture of Brittle Solids", 2nd Edition, Cambridge Solid State Science Series (1993).
3. B. R. Lawn, "Indentation of Ceramics with Spheres – A Century after Hertz", *J. Am. Ceram. Soc.*, 81 [8], 1977 (1998).
4. S. S. Chiang, D. B. Marshall and A. G. Evans, "The Response of Solids to Elastic-Plastic Indentation. I. Stresses and Residual Stresses", *J. Appl. Phys.*, 53(1), 298 (1982).
5. E. H. Yoffe, "Elastic Stress Fields Caused by Indenting Brittle Materials", *Phil. Mag. A*, vol. 46, no. 4, 617 (1982).
6. B. W. Austin, MS Thesis, North Carolina State University, 2000.
7. Y. Ahn, T. N. Farris and S. Chandrasekar, "Elastic Stress Fields Caused by Sliding Microindentation of Brittle Materials", Proc. of the Int. Conf. On Machining of Advanced Materials, S. Jahanmir, ed., NIST Spec. Publ. 847, 71 (1993).
8. R. O. Scattergood and U. F. Kocks, "Dislocation Pair Interaction in a Finite Body", NBS Special Publication 317, vol. II, 1179 (1970).
9. T. Randall, MS Thesis, North Carolina State University, in progress (2003).
10. W. S. Blackley and R. O. Scattergood, "Ductile-Regime Machining Model for Diamond Turning of Brittle Materials", *Precision Engineering*, [13], 95 (1991).
11. T. G. Bifano, T. A. Dow and R. O. Scattergood, "Ductile-Regime Grinding: A New Technology for Machining Brittle Materials", *J. of Engr. for Industry* [113], 184 (1991).
12. K. W. Sharp, M. H. Miller and R. O. Scattergood, "Analysis of the Grain Depth-of-Cut in Plunge Grinding", *Precision Engineering*, [24], 220 (2000).
13. C. Tam, C. C. Poon, L. Crawforth, and P. M. Lundquist, "Stress On The Dotted Line", Data Storage No. 6, 29 (1999).
14. B. M. Love, MS Thesis, North Carolina State University, 2001.
15. K. L. Johnson, "Contact Mechanics", Cambridge Univ. Press, p.17 (1985).

Appendix B

Crystal Orientation Dependence of Machining Damage—A Stress Model

Winston S. Blackley and Ronald O. Scattergood*

Precision Engineering Center, North Carolina State University, Raleigh, North Carolina 27695-7918

The pitting damage occurring along preferred crystal orientations observed after single-point diamond turning of brittle materials dictates a limiting feed rate at which the material can be machined. Using elasticity theory, the orientation dependence of the pitting can be qualitatively explained. Calculations based on a line-force stress model predict the orientation dependence of the damage symmetry. The results are in good agreement with machining tests for a series of germanium single-crystal wafers. [Key words: stress, machining, crystals, orientation, modeling.]

I. Introduction

MUCH of the germanium machined in the optics industry is polycrystalline. When diamond turned, grains with different crystal orientation exhibit strikingly different machining characteristics. Some grains present a nearly perfect optical reflecting surface while others show signs of pitting due to fracture damage. The feed rate for the machining process will be limited by pitting on a few critically oriented grains. Several previous papers have noted the effect of crystal orientation on machining damage,^{1,2} but no rationalization of the effect was given.

A method of simulating the stresses for diamond turning has been developed.^{3,4} Maximum normal stresses were calculated from the elastic solution for a line force P applied along an isotropic half-space boundary. Equation (1) gives the stress field where r is the distance from the line force and θ is the polar angle measured from the force direction.⁵ The only non-zero stress component is the radial stress σ_r .

$$\sigma_r = -\frac{2P}{\pi r} \cos \theta \quad (1)$$

As shown schematically in Fig. 1, σ_r can be a tensile stress in the region behind the tool for oblique tool force angles $\alpha > 0$, i.e., for $\theta > 90^\circ$. Ramalingham and Lehn⁶ have shown that the line-force stress field in Eq. (1) is a good approximation to the actual cutting stresses in orthogonal machining.

In order to avoid singularities, it is assumed throughout that $2P/\pi r = 1$ in Eq. (1); therefore only the angular dependence of the tool-force stresses is considered here. It is further assumed that mode I fracture processes lead to pitting so that tensile stresses are the relevant components. To simulate the diamond-turning process and propensity for pitting damage, the orientation factors describing the maximum normal stress on {111} planes were evaluated. In diamond cubic structures such as germanium, these are the planes of lowest fracture energy. The stress evaluations were done by fixing an initial orientation for the crystal surface and cutting direction. The tool-force stress field is given from Eq. (1) as a

D. Clarke—contributing editor

radial stress in this reference frame. Changes in cutting direction are equivalent to rotations about the normal to the crystal surface, and plane or direction indices are obtained from appropriate rotation matrices. The maximum normal stress for a given cutting direction and tool-force angle is obtained from

$$\sigma_{max} = \max \{\sigma_{\theta} n_i n_j\} \quad (2)$$

where σ_{θ} follows from Eq. (1) and n_i represents a unit normal to {111} planes in the rotated frame (summation convention applied). The maximum in Eq. (2) is taken over all angles θ and all {111} planes n_i for given cutting direction and tool force inclination angle α . σ_{max} thus represents the most favorable stress state for mode I fracture for unit value of $2P/\pi r$. At given α , the orientation dependence of σ_{max} can be displayed as a polar plot of stress orientation factor vs ω where ω measures cutting direction from a fixed datum on a given crystal plane. Calculations were carried out for (100), (110), and (111) surface planes using $\alpha = 90^\circ$. Smaller values of α produce similar results, but with lower amplitudes.

II. Experimental Results

Germanium crystals in (100), (110), and (111) surface orientations were machined under conditions where the amount of pitting damage appeared equivalent for all orientations. Orientation of each of the machined wafers was determined by X-ray diffraction using the Laue method.⁷ The tool used for each of these cuts had a 3.175-mm radius, -30° rake angle, and 6° clearance angle. Several tests were made for each orientation. Further details on the procedures are available elsewhere.⁴

Machined (100) germanium wafers exhibit pitting damage having a simple fourfold symmetry. A polar plot of the calculated stress orientation factor is shown in Fig. 2(A) along with a schematic representation of the typical pitting damage observed in machining tests (B). Reference orientations are in-

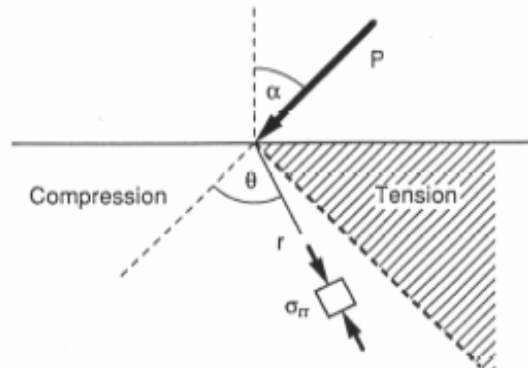


Fig. 1. Line force loading P applied to an elastic half space. The angles α and θ are measured as shown. For $\alpha > 0^\circ$, radial tension occurs in the region behind the tool (shaded) where $\theta > 90^\circ$.

Manuscript No. 197586. Received June 1, 1990; approved August 8, 1990. Supported by the Office of Naval Research and the industrial affiliates of the Precision Engineering Center of North Carolina State University.

*Member, American Ceramic Society.

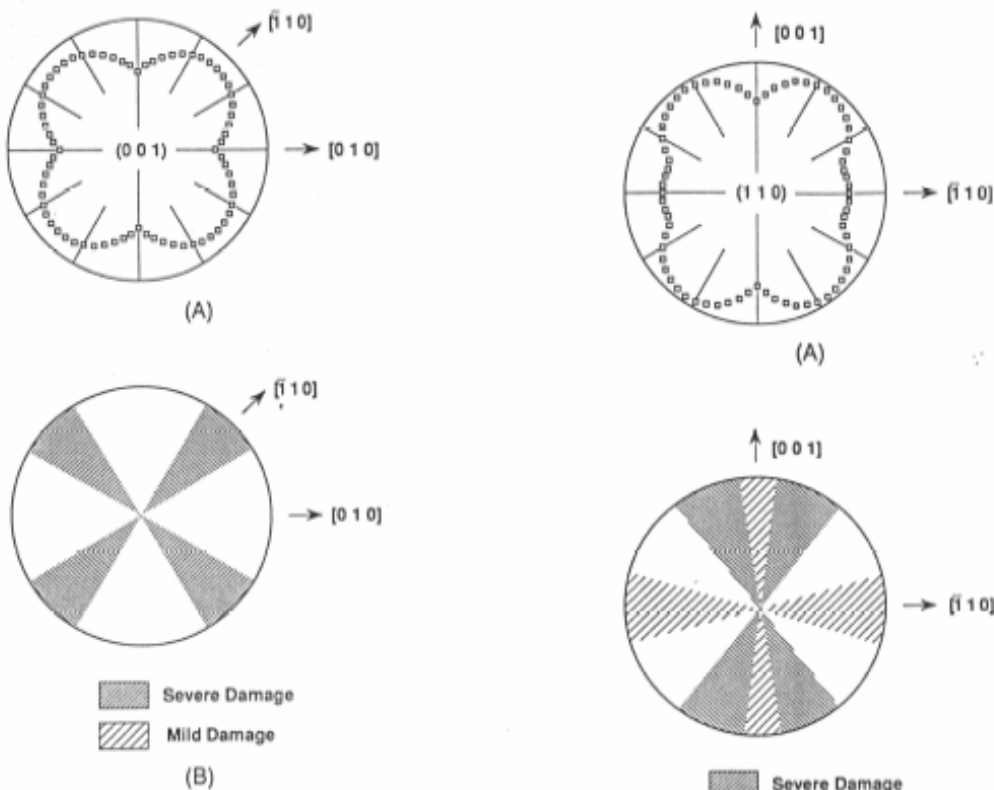


Fig. 2. (A) σ_{max} vs ω for diamond turning of (100) single-crystal wafer. (B) Schematic representation of the pitting damage observed on machined wafers.

dicated on the figures. A macrophotograph of an actual machined (100) wafer is shown in Fig. 3. The fourfold pitting damage arms observed on the machined wafers lie along $\langle 110 \rangle$ directions, in good agreement with the calculated maxima in the stress orientation factor shown in Fig. 2. The extent and intensity of the pitting damage will depend upon the machining conditions, in particular the tool feed rate.^{1,4}

Pitting damage on machined (110) germanium wafers shows a different and more subtle symmetry than (100) wafers. The polar plot of the calculated stress orientation factor in Fig. 4

Fig. 4. (A) σ_{max} vs ω for diamond turning of (110) single-crystal wafer. (B) Schematic representation of the pitting damage observed on machined wafers.

(A) shows twofold symmetry with a pair of primary maxima lying about 30° from a $\langle 001 \rangle$ direction. A pair of shallower maxima lie along $\langle 110 \rangle$ directions. Careful observation of pitting damage on samples machined under various conditions and feed rates revealed the damage patterns shown schematically in Fig. 4 (B). A macrophotograph of a machined (110) wafer is shown in Fig. 5. Severe damage occurs along



Fig. 3. Macrophotograph of (100) germanium single-crystal wafer.



Fig. 5. Macrophotograph of (110) germanium single-crystal wafer.

arms lying about 30° from $\langle 100 \rangle$, consistent with the predictions. As indicated in Fig. 4, arms of less severe damage (smaller, less dense pits) were observed along $\langle 110 \rangle$ directions and along $\langle 100 \rangle$ directions, the latter lying between the pair of severe damage arms at 30° inclination from $\langle 100 \rangle$. In earlier work, Blake¹ reported a single pair of damage arms lying along $\langle 100 \rangle$ directions for machined $\langle 110 \rangle$ wafers. Evidently, his machining conditions were such that the 30° arms merged into what appeared to be a wide, single arm of severe damage along $\langle 100 \rangle$.

Machined $\langle 111 \rangle$ wafers exhibit a threefold damage symmetry. The polar plot of stress orientation factor shown in Fig. 6(A) reveals dominant maxima lying along $\langle 110 \rangle$ directions with maxima of slightly less amplitude along the reverse direction. The proper indexing for these directions in a $\langle 111 \rangle$ surface is indicated in the figure. In view of the similarity of the stress amplitudes along positive and negative $\langle 110 \rangle$ directions, the symmetry appears to be quasi-sixfold. The observed damage is shown schematically in Fig. 6(B) and also in the macrophotograph in Fig. 7. Three arms of severe damage occur along $\langle 110 \rangle$ in agreement with the stress orientation factor maxima. Arms of less severe damage occur along the

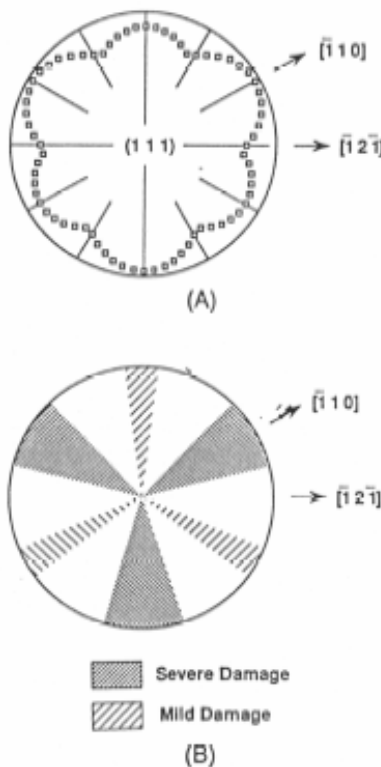


Fig. 6. (A) σ_{\max} vs ω for diamond turning of $\langle 111 \rangle$ single-crystal wafer. (B) Schematic representation of the pitting damage observed on machined wafers.



Fig. 7. Macrophotograph of $\langle 111 \rangle$ germanium single-crystal wafer.

negative to these $\langle 110 \rangle$ directions. The latter arms are much less intense than the former and do not scale proportionally with the calculated stress maxima.

III. Conclusions

Pitting damage observed on machined germanium single-crystal wafers depends on the cutting direction. The orientation dependence can be attributed to the maximum amplitude of the resolved tensile stresses on $\{111\}$ cleavage planes. This changes with cutting direction because of change in crystal orientation with respect to the principal stress axes. Evaluation of tensile stress orientation factors using the solution for a line force on an elastic half space provides a simple method to qualitatively predict the crystal directions where pitting damage will appear. The maxima in the stress orientation factor show agreement with the observed damage arms on machined germanium wafers. The patterns reflect the underlying symmetry of the crystal surface plane. The results support the assumption that tensile stresses behind the tool tip are responsible for the observed fracture damage.

References

- ¹P. N. Blake and R. O. Scattergood, "Ductile-Regime Machining of Germanium and Silicon," *J. Am. Ceram. Soc.*, 73 [4] 949-57 (1990).
- ²D. J. Decker, J. M. Grandjean, and J. M. Bennet, "Optical and Surface Characteristics of Diamond-Machined Infrared Windows"; p. 293 in *Science of Ceramic Machining and Finishing*, NBS STP 562, National Bureau of Standards, Washington, D.C.
- ³R. O. Scattergood; pp. 30 JTUC1-I in *Optical Fabrication and Testing—1990 Technical Digest Series*, Optical Society of America, Monterey, CA, 1990.
- ⁴W. S. Blackley, "Single Point Diamond Turning of Brittle Materials"; M.S. Thesis, North Carolina State University, Raleigh, NC, 1989.
- ⁵S. P. Timoshenko and J. N. Goodier, *Theory of Elasticity*; p. 97. McGraw-Hill, New York, 1970.
- ⁶S. Ramalingham and L. L. Lehn, "A Photoelastic Study of Stress Distribution During Orthogonal Cutting," *J. Eng. Ind.*, May, 527 (1971).
- ⁷B. D. Cullity, *Elements of X-ray Diffraction*; p. 233. Addison-Wesley, Reading MA, 1978. □